Faculty of Science and Engineering
Department of Spatial Sciences

Determination of Tide Height Using Global Navigation Satellite Systems

Faisal Alsaaq

This thesis is presented for the Degree of
Doctor of Philosophy
of
Curtin University

August 2017

Declaration

To the best of my knowledge and belief this thesis contains no material previously published by any other person except where due acknowledgement has been made.

This thesis contains no material which has been accepted for the award of any other degree or diploma in any university.

Signature:  Date: August 31, 2017

Abstract

Hydrographic surveys, which may include establishing critical water level and depth data, rely on the availability of tide information that allows raw sounding observations to be benchmarked to a common (chart) datum. This is usually related to specific long-term tide information obtained from tide gauge observations and/or tide predictions using local, regional or global tide models. There may well be situations in which access to tide gauge stations is denied (in conflict zones, for example) and it is not possible to establish a temporary tide gauge. In addition, because tide gauge stations are usually located on coastlines or islands, they do not necessarily represent tidal behaviour in the open ocean. Terrestrial tide gauge stations may also be subject to long-term vertical land movement in geologically active regions, which may be interpreted as sea-level change or tide behaviour change.

An emerging method for tide estimation is based on Global Navigation Satellite Systems (GNSS) positioning of the sea surface. With increased availability and sophistication of the continuous stream of data from satellite-based systems, precise GNSS vertical positioning at cm-level accuracy has the potential to replace traditional tide gauge observations, especially in remote areas. This offers the prospect of lower costs both in money and time, as well as a reworking of the logistical requirements in marine surveying. This thesis contains an assessment of the potential of GNSS-derived water-level heights for determining the tide signal independently of, but in conjunction with, physical tide gauge observations. Two GNSS positioning techniques, post-processed kinematic (PPK) and precise point positioning (PPP), were assessed for their applicability to nearshore and offshore environmental settings.

To extract the tide signature from GNSS-derived water-level heights, the suitability of four filtering methods was examined: the moving average, Savitzky–Golay, Gaussian and Butterworth filters. These are used to eliminate the high-frequency components of the signal generated by waves, and to assess dynamic draft, and measurement uncertainties. The performance of each filter was evaluated by comparing the amplitude and phase of the four major tidal harmonic constituents M2, S2, K1 and O1 determined by fast Fourier transform (FFT) for the unfiltered and filtered water level

signals. In particular, in every case the focus was on amplitude damping over various filter window lengths.

The GNSS heights of the water level were estimated from data gained over two 30-day periods of continuous (1 Hz sampling) GPS (Global Positing System) and GLONASS (GNSS of the Russian Federation). Data was collected by a Fugro Starpack GNSS receiver for both nearshore and offshore environments.

For the nearshore environment, the receiver was installed on a floating pontoon at Hillarys Boat Harbour in Western Australia. Sea level heights recorded by a tide gauge at Hillarys Boat Harbour were used as a reference to evaluate the effectiveness of the GNSS-derived water level heights in monitoring the tide signal.

In the offshore environment, the data were collected by a survey vessel that had been used to support the search for the wreckage of an aircraft believed to have been lost in the Indian Ocean. This section includes a discussion of the challenges presented by the offshore environment: the effect of vessel movements on GNSS-PPP water level height estimation and extraction of tide information, and the effect of non-tidal motion (wave activity and the attitude of the vessel) during height observations.

The study found that there was a close agreement between the unfiltered GNSS tide information and tide gauge observations, documented as almost identical amplitudes of the tidal harmonic constituents. Regarding the filter performance, the main finding was that the Savitzky–Golay filter suffers considerably less from damping of the tidal harmonic constituents than the other filters. The maximum damping effect of the Savitzy–Golay filter for PPP (using a window length of 360 minutes) was 1–2 mm nearshore and 7 mm offshore. The Savitzy–Golay and Gaussian filters both met current International Hydrographic Organization (IHO) standards for Special Order hydrographic surveys when considering damping effects only.

Short-term tide modelling and prediction using GNSS-derived water level heights nearshore and offshore were investigated using the four principal tidal harmonic constituents. The predictions used the extracted tidal harmonic constituents and predicted the tide for 1 to 29 days. The Root Mean Square Error (RMSE) values between the daily predicted tides and the smoothed GNSS-water level heights for each day showed that the predictions were reasonably accurate after low-pass filtering. The

GNSS-derived nearshore and offshore predictions were particularly successful for four days ahead of tide gauge observations.

The results demonstrate the benefit of GNSS-derived water level heights for detecting anomalous sea level variations such as seismic sea waves (tsunami), and can be used to monitor real-time water-level observations for tsunami early warning systems using short-term tide predictions, for example up to one day or more where a threshold level between 2 to 8 cm can be set. For a better prediction (i.e., improved filtering performance), a lower threshold can be prescribed, which would enable small tsunami to be detected.

Finally, the results imply that GNSS water height measurement can play a major role as a replacement for tide gauges by estimating tides in real time for hydrographic surveying, marine geodesy and physical oceanography and it is very useful for natural hazard warning systems.

Acknowledgements

First of all, I would like to thank Allah for giving me the opportunity, power and help to complete this thesis. Without God‘s will and blessing, I would not have been able to finish this research.

I would like to express the deepest appreciation to Associate Professor Michael Kuhn for providing invaluable advice, and support. His guidance helped me in all the phases of the research and writing of this thesis. Without his supervision and constant help this thesis would not have been possible. I would also like to thank Prof. Jon Kirby for his help and support at a crucial point in the final phase of this thesis. I would also like to thank Dr. Ahmed El-Mowafy for his suggestions and comments.

In addition, I would like to thank academic and administrative staff at the Department of Spatial Sciences for all their help and support, especially to Lori Patterson, for her assistance with formatting and editing. I wish to express my warmest thanks to Dr Amir Khodabandeh, Dr Nandakumaran Nadarajah, Nathan Agutu, Christopher Ndehedehe and Hasan Alssaedi for their assistance, friendship and emotional support.

I would like also to thank the King AbdulAziz University-Faculty of Maritime Studies for providing me with a scholarship to continue my postgraduate research in order to gain a PhD. Heartfelt thanks go to Dr Salem Alharbi and Dr Rifat Abdullah for their support and assistance. Thanks also be extended to all my colleagues at Hydrographic survey Department and Faculty of Maritime Studies.

I wish also to express my sincere appreciation to Fugro Survey Pty Ltd., Western Australia for providing the GNSS observation and tide gauge data used in this study. I am extremely thankful to Paul Kennedy, Romeo Pellicioli, Stephen Fewings and Ken Eddy for providing help and encouragement in times of need. I would also like to acknowledge Ron Furness for his invaluable assistance with contacting Fugro.

Special thanks and appreciation must go to my mother, Noda Alshahrani for her prayer, support and patience. I would especially like to express my gratitude to my lovely wife, Abeer Alshahrani, and my children Jana, Fay, Rawa and Jaser. Thank you for your prayers, sacrifices and patience. I would also like to acknowledge my sisters, brothers and friends for all their support.

Dedication

To my late father, who always wanted me to become a great stature, May GOD bless his soul, and to my family who have suffered from my absence.

Table of Contents

List of Figures

List of Tables

Abbreviations

AHD	:	Australian Height Datum
AIC	:	Akaike Information Criterion
ANTT	:	Australian National Tide Tables
APC	:	Antenna Phase Centre
ARP	:	Antenna Reference Point
AWGN	:	Additive White Gaussian Noise
BEIDOU	:	Chinese Global Navigation System (China)
C/A	:	Coarse Acquisition
CD	:	Chart Datum
CORS	:	Continuous Operating Reference Stations
CSRS	:	Canadian Spatial Reference System
CWT	:	Continuous Wavelet Transform
DGPS	:	Differential GPS
DHI	:	Danish Hydraulic Institute
DOY	:	Day of Year
EGM2008	:	Earth Gravitational Model 2008
FFT	:	Fast Fourier Transform
FOC	:	Fully Operational Capability
GALILEO	:	European Satellite Navigation System (Europe)
GATED	:	GPS-Aided Tsunami Early Detection
GEO	:	Geostationary Earth Orbit
GITEWS	:	German Indonesian Tsunami Early Warning System
GLONASS	:	Global Navigation Satellite System (Russia)
GNSS	:	Global Navigation Satellite Systems
GPS	:	Global Positioning System
GRS80	:	Geodetic Reference System 1980
IGS	:	International GNSS Service
IGSO	:	Inclined Geosynchronous Orbit
IHO	:	International Hydrographic Organization
IMU	:	Inertial Measurement Unit
IOC	:	Intergovernmental Oceanographic Commission
IOV	:	In-Orbit Validation

ISSH	:	Instantaneous Sea-Surface Heights
ITRS	:	International Terrestrial Reference System
LAT	:	Lowest Astronomical Tide
LINZ	:	Land Information New Zealand
LSSA	:	Least Squares Spectral Analysis
MBES	:	Multi-beam Echo Sounder
MEO	:	Medium Altitude Earth Orbit
MGEX	:	Multi-GNSS Experiment
MHHW	:	Mean Higher High Water
MHW	:	Mean High Water
MLLW	:	Mean Lower Low Water
MLW	:	Mean Low Water
MSL	:	Mean Sea Level
MWR	:	Microwave Radiometer
NAVIC	:	Navigation with Indian Constellation
NAVSTAR	:	NAVigation System with Time And Ranging
NLN	:	National Levelling Network
NOAA	:	National Oceanic and Atmospheric Administration
OZSS	:	Quasi-Zenith Satellite System (Japan)
PCTMSL	:	Permanent Committee on Tides and Mean Sea Level
PPK	:	Post-Processed Kinematic
PPP	:	Precise Point Positioning
READI	:	Real-Time Earthquake Analysis for Disaster mitigation network
RINEX	:	Receiver Independent Exchange
RMS	:	Root Mean Square
RMSE	:	Root Mean Square Error
RTK	:	Real Time Kinematic
SBP	:	Sub-Bottom Profiler
TBC	:	Trimble Business Centre
THU	:	Total Horizontal Uncertainty
TPU	:	Total Propagated Uncertainty
TVU	:	Total Vertical Uncertainty
UTC	:	Universal Time Coordinated
VAV	:	Tidal analysis software (include reference)
WGS84	:	World Geodetic System 1984

Chapter 1:

Introduction

1.1 Background

Advances in space technology have led to a significant increase in the use of global navigation satellite systems (GNSS) and remote sensing systems in oceanographic applications, including ocean surface monitoring, ocean surface kinematic measurements, remote sensing, and the determination of oceanographic parameters such as wave height and current speed (Tay, Coatanhay, Maussang, & Garello, 2010). Progress in computer hardware and software has allowed the development of accurate GNSS kinematic relative positioning solutions with centimetre accuracy. These are now standard products available for a wide range of applications; however, most of them are able to achieve centimetre accuracy only when they are relatively close to a reference station. Decimetre accuracy can be achieved for longer distances between reference stations (Marreiros, 2012). GNSS is often used because of its capacity to estimate three-dimensional positions (horizontal position and height). The vertical, height or depth, dimension is of particular interest in hydrography because the parameters in question, such as sea floor, tide and water level requiring a rigorous vertical definition. In this regard GNSS offers the advantage to directly reference hydrographic parameter, both horizontally and vertically, to a mathematically and geometrically defined reference ellipsoid which does not require further external information.

Tidal data derived from tide gauge stations is an important aspect of hydrographic surveying. Such information is used to reduce raw water depth

observations to a common datum (e.g., chart datum). Data recorded by tide gauges mounted on piers close to the survey area are typically used to derive tide reductions, and the (chart) datum can in many cases be transferred from an existing datum nearby. However, in many situations, hydrographic surveyors do not have access to local tide gauges and/or are not able to establish a temporary tide gauge for any number of reasons. Indeed, since the spatial distribution of tide gauge stations is limited to coastlines or islands in the open ocean, the information they record does not necessarily represent the open ocean adequately.

Another limitation of tide gauge stations is their susceptibility to vertical land motion in geologically or tectonically active regions, and their data may be interpreted as sea level change. Relatively rapid vertical land motion (e.g. rates at a few mm/year) may occur on a large scale (e.g., due to post-glacial rebound) or on a local scale, for example land subsidence due to groundwater extraction (Peltier, 2004; Shennan & Horton, 2002). The conventional method of monitoring vertical tide gauge movement is by levelling to appropriate benchmarks; however, levelling has its spatial and temporal limitations as it usually only captures local movements and is performed in epochs (annually or even less frequently) and therefore may not capture short-term (e.g., seasonal, permafrost etc.) changes.

GNSS technology can be used to mitigate these problems; GNSS positioning measures all vertical movement, whether local or large-scale, and offers better temporal coverage when continuous tracking is done. GNSS can also continuously monitor tide gauge movement in real time. Importantly, GNSS monitoring of vertical stability may be readily automated (Dawidowicz, 2014).

Hein et al. (1990) were among the pioneers of measuring sea levels using GNSS signals by installing a GNSS antenna and receiver on top of a buoy and continuously measuring its horizontal and vertical position. Their work revealed technical issues related to technology availability at that time, including the need for the receiver position to be close to a land-based reference station to achieve centimetre-level accuracy; the need for additional sensors to account for the dipping and tilting of the buoy; and the need for the reduction of multiple signals reflected by the ocean surface to achieve centimetre-level accuracy (IOC, 2006). GNSS buoys are commonly used

today for the calibration of satellite altimetry and in tsunami detection and warning systems (Cheng, 2004; Kato et al., 2005; Kuo et al., 2012).

Satellite altimetry is now known to be a powerful tool for the study of the oceans, currently attaining centimetre accuracy when monitoring sea level height in the open ocean. It is also widely used in sea-level and various oceanography-related research and applications (Fu & Cazenave, 2000; Fu et al., 1994). However, altimetry data in coastal regions may be compromised for two main reasons: (i) land contamination of the signal coming from the large radiometer footprint invalidates the wet tropospheric correction that is computed from the onboard microwave radiometer (MWR) measurements, and (ii) global ocean tide models do not adequately account for local tidal effects (Fernandes et al., 2010), although re-tracking algorithms have made a significant contribution to the development of altimetry data-processing techniques in coastal zones (Vignudelli et al., 2011).

In some altimetric missions, satellite orbits pass over static tide gauges and GNSS stations mounted on offshore oil rigs or on platforms close to coastline and harbours, but they are infrequent and limited to a single position. As the accuracy of kinematic GNSS for offshore applications has improved, GNSS-equipped buoys have been developed for determining instantaneous sea-surface heights (ISSH). These were initially used for calibration or validation, and consequently they were deployed at locations on the ground tracks of altimeter satellites (Marreiros, 2012).

Several recent projects for measuring the height of the sea surface have been conducted using a vessel with a GNSS antenna. Some studies did no accurate modelling of the squat or the antennae height (Bouin et al., 2009), and no corrections were applied for height changes due to the ship's attitude (Jürgenson, Liibusk, & Ellmann., 2008); however, one series of experiments that took the ship's attitude into account was conducted by Chang, Lee and Tsui (2002), who showed that heights corrected for the ship's attitude were significantly more accurate than uncorrected heights (Härting, Berndt, , & Reinking., 2007; Härting & Reinking, 2002).

New applications have been developed from these initial ideas and studies; these utilise highly accurate vertical GNSS positioning at sea for anchoring or manoeuvering floating platforms, hydrographic surveying, control of maritime works, and sea level

measurement. The use of precise kinematic GNSS relative positioning for vertical control in hydrographic surveys is now common (IHO, 2005). High-vertical-accuracy GNSS is used to position hydrographic data-acquisition platforms, relating bathymetric observations and elevations of conspicuous land features directly to the Earth's ellipsoid. Models are then used to translate those observations to other datums (Dodd & Mills, 2011).

GNSS has also been used to monitor sea surface variations for tsunami detection (Schöne et al., 2011). For example, tsunami forecast systems using GNSS observations are operated by the National Oceanic and Atmospheric Administration (NOAA) (Tang, Titov & Chamberlin, 2009; Tang et al., 2012) and the Japan Meteorological Agency (JMA) (Tsushima et al., 2011). These forecast systems are reliable but are relatively slow, because a tsunami typically takes tens of minutes to reach the nearest offshore stations (Tang et al., 2012; Tsushima et al., 2011; Wei et al., 2013). A number of studies have suggested the use of seismic and/or geodetic observations, as well as offshore tsunami observations, to facilitate rapid and reliable forecasting (Melgar & Bock, 2013, 2015; Rodkin & Tikhonov, 2014; Tsushima et al., 2014). The use of shipborne GNSS at anchor has also been proposed for natural hazard and sea level monitoring (Saito & Kubo, 2016). Kinematic PPP height positioning has been used to estimate the initial tsunami height offshore (Inazu, Waseda, Hibiya & Ohta, 2016; El-Mowafy & Deo, 2017)

For precise (cm-level accuracy) marine positioning, GNSS relative positioning is typically limited to areas on the coast where reference stations can be mounted; PPP offers a very promising alternative, as it allows worldwide coverage for offshore applications, and improves GNSS precision positioning capability from dm- down to cm-level accuracy in remote areas (El-Mowafy Deo, & Kubo, 2017). Therefore PPP has the potential to reduce the cost and logistical requirements in hydrographic surveying. There may be a broad range of oceanographic applications and studies if cm-level accuracy were to be extended to oceanic regions (Marreiros, 2012); for example, direct georeferencing of shipborne or buoy sensors, ship dynamics determination, sea level and wave height determination, atmosphere sensing and motion compensation. However, at present most of these applications are restricted to coastal areas within the range of one, or a network of, reference stations, because of

the limits to the baseline length required to reliably solve for integer ambiguities and guarantee cm-level accuracy.

One important aspect is the possibility of using GNSS-derived water level heights from which the tide can be modelled across global oceans. Tidal analysis and prediction are essential for various applications, such as safe navigation and the reduction of hydrographic survey data. Since tides are a periodic phenomenon, they can be modelled by various periodic functions, such as sinusoidal functions. To conduct a reliable tidal analysis and prediction, the (main) tidal frequencies must be reliably known. Many tidal frequencies have been proposed, based on tidal theory. In most cases, these expand the tide-generating potential harmonically by different methods, using the ephemerides of the main celestial bodies such as the Moon and Sun (Cartwright & Edden, 1973; Cartwright & Tayler, 1971; Doodson, 1921; Hartmann & Wenzel, 1994; Kudryavtsev, 2004; Qin-Wen, 1987, 1989; Tamura, 1987, 1993). These studies have largely been physics-based (e.g., astronomically) and no tide observations are used. These methods assume that the tidal frequencies are known but their amplitudes are unknown.

Other studies have analysed sea level heights by using Fourier and wavelet transforms in order to extract tidal frequencies. Flinchem and Jay (2000) and Jay and Kukulka (2003), who considered tidal time series to be non-stationary, introduced the continuous wavelet transform (CWT) method to extract tidal information. The method complements harmonic analysis and Fourier methods. Ducarme et al. (2006b) used the Akaike information criterion (AIC) method, which is based on maximum likelihood (Sakamoto et al., 1986) to reveal the non-tidal components in tidal residues by reducing all estimated tides using VAV software (Venedikov et al., 2005). Based on the NormPeriod code, Pytharouli and Stiros (2012) applied spectral analysis to the time series of the astronomical tide (smoothed tide time series). Capuano, De Lauro, De Martino, and Falanga (2011) applied independent component analysis (ICA) (Hyvärinen, Karhunen, & Oja 2001) to determine the nonlinear, independent components of tidal motion. Finally, Amiri-Simkooei, Zaminpardaz, and Sharifi (2014), using least-squares harmonic estimation (LS-HE), estimated tidal frequencies from a mathematical and statistical approach. Common to all of these methods is the use of sea level observations (e.g., from tide gauge observations).

1.2 Problem statement

The water level height observed by GNSS or tide gauge stations contains both low- and high-frequency variations. This is particularly the case for GNSS-derived water level height observations on a boat or a buoy where the GNSS antenna is exposed to a very dynamic environment. The high-frequency signal is mainly caused by waves and dynamic draft variations, and measurement uncertainties during data collection. Such variations are considered here as noise when focusing on the low-frequency tide signals with essentially semi-diurnal and diurnal periods. Hence, a filtering technique is subsequently required to reduce or remove the high-frequency signals and obtain the low-frequency tide signals. The tidal constituents are then derived from a filtered data set.

There is little current research on the use of filtering techniques to extract, model and predict tides; the present study addresses this gap. The ideal filter in this context is one that optimises for a flat amplitude response and has zero phase distortion. The flat amplitude response is important in order to prohibit any contaminating effects (e.g., attenuation ripple) from entering the filtered tidal series. Zero phase distortion is important to ensure no delay or phase offsets that might introduce errors, both in hydrographic height determinations and in oceanographic constituent analysis (Wert, Dare, & Clarke, 2004).

In this thesis, a major focus is set on extracting the tidal signature from GNSS-derived water level height observations, including the efficient use of filtering techniques. The GNSS positioning methods are currently well established and they are thoroughly discussed in the literature, hence, there will be a limited description of the used GNSS methods. Primarily, this work will assess the suitability of practical filtering methods to extract the tide signal from GNSS observations of the water level height in two, quite different, types of water area (nearshore and offshore). The study will use 30 days of continuous GNSS measurements (GPS and GLONASS) for each case with a sampling rate of 1 Hz, then re-sampled at 1 minute intervals. The moving average, Savitzky–Golay, Gaussian and Butterworth low-pass filters are implemented and assessed as to their effectiveness in eliminating the high-frequency water height components, which, in the present context are: wave amplitude, dynamic draft and measurement uncertainties. The amplitude and phase of the four major tidal harmonic

constituents M2, S2, K1 and O1 are determined by fast Fourier transform (FFT) for the unfiltered and filtered water level signals. The emphasis is on amplitude damping over different filter window lengths. Tide modelling and prediction are carried out for nearshore and offshore GNSS-derived water level heights.

1.3 Research objectives

This research seeks to develop, implement and study data filtering to enable obtaining accurate tide information at sea from GNSS data. The objective is to provide an efficient replacement for tide gauge observations and to examine the use and performance of suitable GNSS positioning techniques for this purpose, either post-processed kinematic (PPK) or precise point positioning (PPP), along with the most appropriate filtering technique. The specific objectives are:

- Evaluate different GNSS positioning information accessed on a marine platform (vessel or buoy) to obtain the required height information at sub-decimetre accuracy that are compatible with current methods and in accordance with the standards set by the International Hydrographic Organization (IHO).
- Evaluate filtering techniques for extraction of low-frequency tide signals from GNSS height observations received on a marine platform, for the purpose of reducing or suppressing high-frequency signals of the measured water height caused by platform motion, including heave, pitch, roll, long-term draft and dynamic draft.
- Assess the capability of smoothed GNSS vertical solution in providing tidal signal offshore and the level of accuracy obtained in this case.
- Tide modelling and prediction using GNSS height data, both nearshore and offshore including an assessment of the use of filtering techniques to provide improved tide predictions.

1.4 Significance and benefits of the research

The availability and use of GNSS-derived water level heights for tide determination provides significant benefit in hydrography and related disciples, since it complements and/or replaces tide gauge observations, especially in areas of sparse tide gauge coverage, and in the open ocean. The operational flexibility of precise positioning using GNSS in hydrography would be significantly improved by the success of this

technique, and result in considerable savings in time, cost and labour. Another important benefit is its capability to act as an additional sensor for tsunami early warning systems.

The significance of this thesis is summarised as follows:

- Study the ability of using GNSS height data as an efficient replacement for tide gauge observations. The thesis will evaluate the use of GNSS on nearshore and offshore marine platforms to obtain precise estimates of sea surface height, and implement techniques for extracting the tide signals while taking all platform motion into account.
- Examine and compare performance of potential filtering methods applied to GNSS data to suppress the high-frequency water level variations and extract the low-frequency tide signals.
- Tide modelling and prediction using GNSS-derived water level heights in both nearshore and offshore environments for tide monitoring and tsunami detection.

1.5 Outcomes of this research

The research outcomes will play an important role in hydrographic surveying, marine geodesy and physical oceanography, as they will permit precise positioning in extensive ocean areas where such activity has not previously been possible.

The outcomes of the research are summarised as follows:

- This study will provide an efficient method of using a short period of GNSS observations to replace tide gauge data for tide estimation at the survey location, which in turn will result in savings in time, cost and labour.
- The assessment of the accuracy of the GNSS positioning techniques in a marine environment and make recommendations as to the best approach for tide estimation from GNSS observations.
- Determine the most appropriate filtering techniques for reducing noise and measurement error of the GNSS-estimated water heights and thereby optimise the accuracy of tide monitoring and prediction.
- The establishment of tide modelling and prediction at the location of the GNSS water level height observations will provide tidal information to mariners and

many other participants in nearshore activities, and have a direct application in offshore, such as for oil rigs and tsunami early warning systems.

1.6 Thesis structure

This thesis comprises six chapters to address the research objectives. They are summarised as follows:

Chapter 1 (this chapter) introduces the research background and sets out the problem statement on the use of GNSS for tide determination. The objectives of the research and its significance are outlined. The outcomes of the research and the research design are presented.

Chapter 2 discusses the theory behind tidal forces and motions to the detail required for this thesis. This is provided in an attempt to understand the behaviour of a natural phenomenon as dynamic and complex as tidal heights which will help in the subsequent chapters in studying, modelling and predicting tide. The chapter also provides brief overviews of the GNSS technologies and error sources, and describes the precise positioning techniques that were used in this research program. The concept of the determination of tidal height/water level from shipborne GNSS is described.

Chapter 3 describes in detail the analysis of the GNSS-derived water level heights observed at a sheltered harbour site, as an example of nearshore environment. Since the data used in this study were collected before its commencement, only post-processing GNSS methods were employed. Hence, GNSS positioning techniques such as post-processed kinematic (PPK) and precise point positioning (PPP) are examined and compared to traditional tide gauge observations. Spectral analysis is used to determine the amplitude of the four major tidal harmonic constituents. Four filtering methods are tested for their ability to eliminate high-frequency noise and maintain the low-frequency tide signal from GNSS data. In addition, this chapter discusses the results in the context of IHO standards.

Chapter 4 focuses on studying and analysing offshore GNSS-derived water level heights, following the same scenario as described in Chapter 3, but taking into account the difference between the nearshore and offshore environments. The chapter presents a comparison between GNSS-derived water level heights in the two environments and

the appropriate measures needed in case of estimating tides from GNSS in the offshore environment.

Chapter 5 discusses short-term tide modelling and prediction of tide using GNSS heights based on nearshore (PPK and PPP) and offshore (PPP) GNSS-derived water level heights. This chapter discusses how this information may be used for the detection of anomalous sea level variations such as those caused by a tsunami.

Chapter 6 provides a summary of the major findings and the limitations of the research in relation to the stated objectives. Finally, recommendations on possible avenues for future research are suggested in light of the results obtained in this work.

Chapter 2:

Background

2.1 Introduction

Tides are the periodic motion of the waters of the sea caused by variations in the attraction forces exerted by the Sun and the Moon and the rotation of the Earth (Cartwright, 2000). Accurate knowledge of tidal heights may be vital to mariners, fishermen and hydrographers, even seaplane pilots; a high tide may allow a vessel to clear an obstruction that is not navigable at low tide.

The basic forces affecting tidal movement on Earth are the gravitational forces generated by the Sun and the Moon and to a much lesser extent other planets. This chapter contains an overview of the forces affecting tides and their principal constituents that need to be modelled, as well as the factors that influence the simulation model for predicting tides.

The chapter also provides a brief overview of GNSS technologies and their error sources, and various precise positioning techniques that are used in this thesis. However, a full and thorough explanation of the GNSS service is not given here. Extensive descriptions of basic GNSS architecture and methodologies can be found in the literature (e.g. Hofmann-Wellenhof, Lichtenegger & Wasle, 2008, Hofmann-Wellenhof, Lichtenegger, & Collins, 2012; Misra & Enge, 2006; Strang & Borre, 1997). A list of some GNSS-related publications is given in the reference section at the end of this thesis.

The aim of this study is to extract the tidal information from GNSS-derived water level height data. To better analyse tide information, however, a deeper understanding of tidal mechanics is required. The following serves as an introduction to these mechanics.

2.2 Tidal mechanics

'Tides' refer to the familiar predominantly twice-daily rise and fall of the sea surface (Ross, 1995). Together with its rotation and path around the Sun, tides are among the Earth's most predictable phenomena. It is a geophysical phenomenon that occurs as a result of the gravitational attraction of the Sun, Moon and, to a much lesser extent, of the other planets acting upon the Earth. The Moon orbits the Earth while the Earth simultaneously rotates around its axis and orbits the Sun. These motions explain the period, amplitude and phase of the major tidal harmonic constituents observed throughout the Earth's oceans.

2.2.1 Physical phenomenon of tides

According to Ross (1995), tides are very long-period waves that move in a vertical motion through the oceans due to the combined gravitational forces that the Moon, Sun and other planets exert upon the rotating Earth. Ocean tides move around the Earth towards coastlines, where they appear as recurring rising and falling of the ocean surface. Due to the fact that tides are periodic in nature, the magnitude and frequency of the tide at any given location is largely determined by the size and shape of the ocean basin and local coastal conditions (Haigh, 2017); 'high tide' refers to the crest of the tidal wave, while 'low tide' is the trough, or the lowest part of the tidal wave. The difference in height between high and low tide is referred to as the tidal range.

Tidal currents are horizontal movements of water, often associated with the terms 'flood' and 'ebb'. Tidal currents are usually related to the rise and fall of the tide (Ross, 1995). The incoming tide along coastal bays and estuaries is called the flood current, while the outgoing tide is referred to as the ebb current. The weakest flood and ebb currents ('slack tides') usually occur prior to or around the time of the high and low tides. By contrast, the strongest currents occur between the flood and ebb currents (Parker, 2007). Tidal currents are relatively weak in the open ocean, but they may travel at several kilometres per hour close to estuary entrances, narrow straits and inlets (Ross, 1995).

2.2.2 Tide generating forces

Here the tide generating forces are described first for the equilibrium tide model assuming the Earth is fully covered by water, e.g. no interactions between oceans and land masses exist. The superposition of the gravitational attraction forces from the Moon and Sun and the centripetal forces that occur because of the revolution of the Earth around the centres of gravity in the Earth–Sun and Earth–Moon systems cause tidal-generating forces (Hicks & Szabados, 2006). This is illustrated in Figure 2.1, in which the Moon orbits around the Earth, and the Earth and Moon rotate about a common point (same principle can be used for the Earth-Sun system). Since the Earth has about 82 times more mass than the Moon, this common point, called the common axis of revolution, is inside the Earth but not at the Earth's centre (Pugh, 1987). In order to maintain the rotation of the Moon system on a stable orbit, a centripetal force is required to balance the gravitational attraction between the Earth and the Moon.

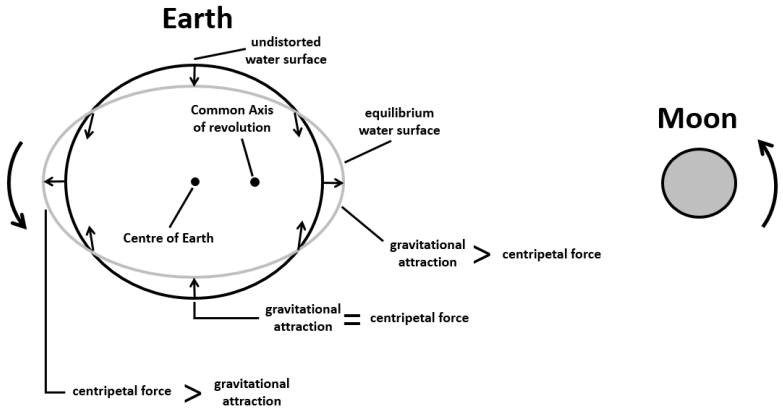

Figure 2.1: Principle of the tidal forces within the Earth-Moon system

The gravitational force on the Earth's surface (e.g. undistorted water surface for the equilibrium tide model) varies according to Newton's law of gravitation, which states:

$$F_g = \frac{GMm}{r^2} \tag{2.1}$$

where F_g is the force of attraction between the two objects; M is the mass of the Earth; m is the mass of the Moon; r is the distance between a point on the Earth's surface and the centre of the Moon; and G is the universal gravitational constant. In Equation 2.1 the Earth and Moon are treated as spherical bodies with homogenous mass distributions, e.g. their respective gravitational attractions are modelled by point

masses. At the centre of the Earth, gravitational attraction force tends to pull the Moon towards the Earth, while centripetal force tends to keep the Moon in its orbit as they both revolve around the common axis of revolution. This is the fundamental physical requirement for orbital motion, e.g. both are considered to be on a stable orbit. When any point on the Earth's surface is closest to the Moon, the gravitational attraction of the Moon is slightly larger than that at the centre of the Earth due to the smaller distance from the Moon, and therefore greater in magnitude than the opposing centripetal force, resulting in a force towards the Moon. Meanwhile, on the opposite side of the Earth, the centripetal force is greater than the Moon's gravitational attraction due to the increased distance from the Moon (see Figure 2.1). As a result of these imbalances between the gravitational and centripetal forces, two tidal bulges form at locations nearest and farthest from the moon (Pugh, 1987). In a similar way, the Sun also produces tide-raising forces upon the Earth's oceans: a tide-raising force is generated at the closest point on the surface of the Earth to the Sun. This force is only about 46 % of that from the Moon (Tomczak, 2007).

The semi-diurnal 'tidal bulge', which is typically oriented at an angle to the equator (e.g. accounting for the inclinations of the Moon's orbit and Earth's equatorial plane with respect to the ecliptic), produces the semi-diurnal components of the tide. The direction of the tide-producing force at the Earth's equator is vertically upwards towards the Moon. Thus, on the side of the Earth facing the Moon at the equator, the centripetal force is smaller than the gravitational force. Away from the equator but still on the side of the Earth facing the Moon, the small tide-producing force is still approximately directed towards the Moon, but it is no longer perpendicular to the Earth's surface (see Figure 2.1). The horizontal components of the differential forces are the main tide-generating forces. These components are parallel to the Earth's surface and they move the body of water in a horizontal direction towards the equator until an equilibrium position is established (Bowditch, 2002). Thus two tidal bulges occur: one centred around the point that is vertically under the Moon's orbit, and one on the opposite side of the Earth (Parker, 2007).

When the rotation of the Earth completes its lunar cycle of 24 hours and 50 minutes, because of the two bulges of water that lie on the equator, and because the declination of the Moon is assumed here to be 0°, there are two high tides during the interval of one day: one high tide when the Moon is overhead and the other after 12 hours and 25

minutes when the Moon is on the other side of the Earth. There is also a low tide between each high tide. At the equator, the theoretical range of these equilibrium tides is typically less than 1 metre as depicted in Figure 2.2 (Bowditch, 2002).

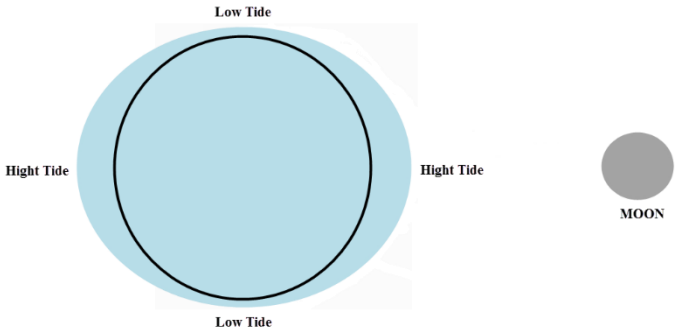

Figure 2.2: Theoretical equilibrium of the Moon's differential gravitational forces

Figure 2.3 shows the maxima in the tide-generating force (crests) and the minima (troughs) for a semi-diurnal tide. The horizontal axis in the figure represents time and the vertical axis represents the relative magnitude of the tide-generating force. For example, when the Moon is overhead at noon, the first crest occurs. The minimum tidal force occurs at the trough, six hours later, followed by the maximum tide (the second crest) which occurs at midnight. This is then followed by another trough at dawn and then back to the noon crest. From this component of the total tide, the vertical departure of the curve is the range that the tide-generating forces are trying to cause in the waters (Hicks & Szabados, 2006).

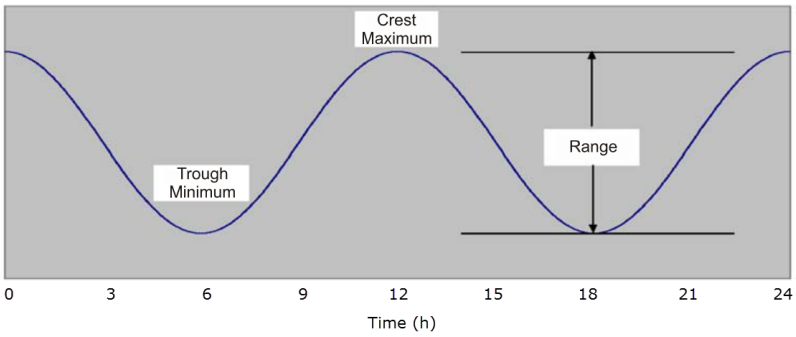

Figure 2.3: Constituent tide curve example (Hicks & Szabados, 2006)

2.2.3 Tidal variations

As discussed above, ‘tidal range’ refers to the height difference between consecutive high and low tides, which varies from place to place and over time. While this variation partly results from the wind and weather, the main cause is the periodic phenomena

due to the relative positions of the Sun, Moon and Earth. These phenomena are discussed in more detail in this section.

2.2.3.1 Lunar phase effects: Spring and neap tide

While the Moon has a key influence on the Earth's tides, the Sun also produces significant tidal forces. Solar tides are usually expressed as a variation of lunar tidal patterns and not as a separate set of tides. At the period of the new or full Moon, when the Sun, Moon and Earth are in alignment (see Figure 2.4), the solar tide and lunar tide coincide, producing spring tides: extra-high high tides and extra-low low tides. As shown in Figure 2.4, in the Moon's first and third quarters (approximately one week after the Spring tides), when the Sun and Moon are positioned at 90° to each other, lower 'neap' tides occur as the solar tide partly cancels out the lunar tide. Therefore, two Spring tides and two neap tides occur in each lunar month (Sumich & Morrissey, 2004).

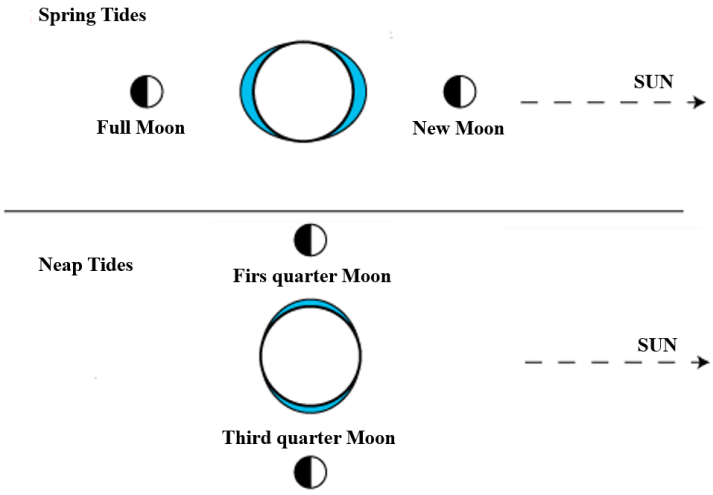

Figure 2.4: Spring and neap tides (NOAA, 2005)

2.2.3.2 Parallax effects of the Moon and Sun

There are various tidal frequencies that result from the complex nature of the Moon's orbit around the Earth and Earth's orbit around the Sun. If the Moon–Earth and Earth–Sun orbits were circular and occurred in the plane of the Earth's equator, there would only be two tidal frequencies and the tides could be predicted from two semidiurnal tidal harmonic constituents (M2 and S2, defined in Section 2.2.4). However, both orbits are elliptical and also occur at angles to the Earth's equatorial plane. Therefore,

the distance between the Moon and the Earth varies throughout each month, and the distance between the Earth and the Sun varies throughout the year. All these modulate the tidal forces, resulting in tidal energy being spread out among a much greater number of frequencies in addition to M2 and S2 (Stewart, 2008).

As illustrated in Figure 2.5, when the Moon is at the perigee (nearest the Earth), the lunar tidal forces are higher than they usually are. This occurs once a month. When the moon is at its apogee (farthest from the Earth), the lunar tidal force is smaller and the tidal range is less than average. This occurs about two weeks after the perigee. Likewise, at the perihelion (Earth is closest to the sun at around 2 January each year), the tidal range increases. In contrast, at the aphelion (Earth is farthest from the sun at around 2 July each year), the tidal range is reduced (Parker, 2007).

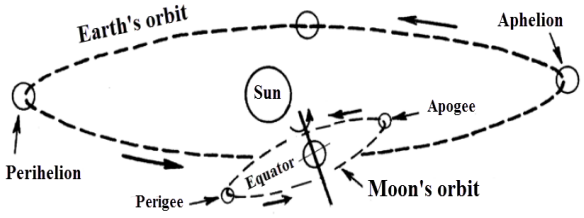

Figure 2.5: Orbits of the Moon around the Earth and of the Earth plus Moon around the Sun (modified from Dean, 1966)

The combination of lunar and solar parallax inequalities together with spring and neap tides creates another variation of the tidal range. When perigee, perihelion, and either the new or full Moon coincide at around the same time, considerably increased tidal ranges result. On the other hand, when apogee, aphelion, and first- or third-quarter Moon occur at around the same time, the tidal range is considerably smaller (Gill & Schultz, 2001).

2.2.3.3 Lunar declination effects: The diurnal inequality

As illustrated in Figure 2.6, the plane of the Moon's orbit lies at an angle of 5.145° to the ecliptic, which is inclined to the plane of the Earth's equator at an angle of 23.27° (Hicks & Szabados, 2006). The Moon's nodes are the two locations where the Moon crosses the ecliptic: the ascending node where the Moon crosses the ecliptic from south to north, and descending node where the Moon crosses from north to south (Hicks & Szabados, 2006). This causes diurnal inequality in the tides. Its cycle is the nodical

month of 27.212 days because it depends on the revolution of the Moon in its orbit around the Earth. The declinational effect is greater than that of the Sun (Hicks & Szabados, 2006); however, the orientation of the Moon's orbit also fluctuates. The perigee rotates for a period of 8.85 years (known as the lunar equinox precession). In addition, the plane of the Moon's orbit revolves around the Earth's axis of rotation once every 18.613 years. Both of these processes result in variations in the distance between the Earth and Moon, and each has a significant effect on the tidal range (Hicks & Szabados, 2006).

Figure 2.6 depicts the regression of the Moon's nodes which is the long-term deviation in tide range due to a slowly varying change in orientation of the Moon's orbit (dashed ellipse). Equatorial tides refer to tides that occur when the Moon is almost directly above the equator. Tropic tides refer to tides that occur when the Moon is near its maximum northern or southern declination.

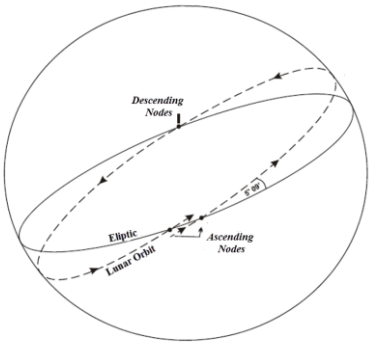

Figure 2.6: Regression of the Moon's nodes (NOAA, 2005)

2.2.4 Tidal harmonic constituents

The relationships between the tidal frequencies and the periodicities of the orbital motions of the Earth, Sun and Moon are called the harmonic constituents. Harmonic constituents are in the form of an amplitude for the height and phase angle for the time relation (Parker, 2007). Harmonic constituents are used when studying tides and for future tide prediction. Each constituent is typically designated using one or more letters, and a number. "M" stands for Moon and "S" stands for Sun: for example, the principal lunar semidiurnal constituent is designated M2; the principal solar semidiurnal constituent is designated S2. The number "2" indicates two complete tidal cycles in each astronomic cycle day (semidiurnal constituents). Their tidal period "T"

refers to the time between cycle maxima, and describes the constituents. S2 has a period of 12.00 solar hours; M2 has a period of 12.42 solar hours (Hicks & Szabados, 2006).

Doodson (1921) found that the celestial driving forces for the tides are based upon the six fundamental frequencies listed in Table 2.1, which are a result of interactions between the Earth, Moon and Sun. The lunar day, or the interaction between the Earth and the Moon as the Earth makes one complete rotation in relation to the Moon, is the first frequency (f_1). The second frequency (f_2) relates to the lunar month, which is the time required for the Moon to make one full orbital revolution around the Earth with respect to the Sun. The solar year, which is the time required for the Earth to make a full orbital revolution around the Sun, gives rise to the third frequency (f_3). The movement of the intersection between the Earth's celestial equator and the orbit of the Moon (precession of the lunar equinoxes; see Section 2.2.3.3), results in the fourth frequency (f_4). The movement of the Moon's orbit with respect to the ecliptic (the plane of the Earth's orbit) results in the fifth frequency (f_5). Finally, the movement of the intersection point of the Earth's celestial equator and the ecliptic (precession of the solar equinoxes) results in the sixth frequency (f_6). The fundamental frequencies along with their period and source are given in Table 2.1.

Table 2.1: Defined fundamental tidal frequencies (Doodson, 1921, modified by Stewart, 2008)

	Frequency (°/hour)	Period		Source
f_1	14.49205211	1	lunar day	Local mean lunar time
f_2	0.54901653	1	month	Moon's mean longitude
f_3	0.04106864	1	year	Sun's mean longitude
f_4	0.00464184	8.847	years	Longitude of Moon's perigee
f_5	–0.00220641	18.613	years	Longitude of Moon's ascending node
f_6	0.00000196	20 940	years	Longitude of Sun's perigee

Doodson's expansion provides a sophisticated decomposition of the tidal constituents into groups with similar frequencies and spatial variation. Using this expansion, each constituent of the tide has a frequency, such that:

$$f = n_1 f_1 + n_2 f_2 + n_3 f_3 + n_4 f_4 + n_5 f_5 + n_6 f_6 \qquad (2.2)$$

where the integers n_i are the Doodson numbers: n_1 = 1, 2, 3 (where n1=1 stands for diurnal, and n1=2 for semi-diurnal) and n_2 to n_6 are between −5 and +5. To avoid negative numbers, Doodson added five to $n_2 \ldots n_6$. Each tidal wave that has a particular frequency designated by its Doodson number is known as a tidal constituent, or is sometimes referred to as a partial tide (Stewart, 2008).

If the ocean covered the whole Earth with no continents, the ocean would be in equilibrium with the tidal potential (Cartwright, 2000). In such a case, the largest tidal constituents would have amplitudes such as those shown in Table 2.2. Each constituent is made up of combinations of the different fundamental frequencies. The sixth frequency is usually omitted because of its long period (Stewart, 2008). The harmonics are divided into two main groups, either semidiurnal or diurnal. Within these groups there are small modulations of the central frequency, which create hundreds of lower-amplitude constituents. As examples, the principal diurnal and semidiurnal tidal harmonic constituents are listed in Table 2.2 along with their associated Doodson integer numbers.

Table 2.2: Doodson's numbers used for the principal semidiurnal and diurnal harmonic constituents (modified from Stewart, 2008)

Tidal Species	Name	n1	n2	n3	n4	n5	Equilibrium amplitude (m)	Period (hr)
Semidiurnal n1 = 2								
Principal lunar	M2	2	0	0	0	0	0.242334	12.4206
Principal solar	S2	2	2	-2	0	0	0.112841	12.0000
Lunar ecliptic	N2	2	-1	0	1	0	0.046398	12.6584
Lunisolar	K2	2	0	0	0	0	0.030704	11.9967
Diurnal n1 = 1								
Lunisolar	K1	1	1	0	0	0	0.141565	23.9344
Principal lunar	O1	1	-1	0	0	0	0.100514	25.8194
Principal solar	P1	1	1	-2	0	0	0.046843	24.0659
Elliptic lunar	Q1	1	-2	0	1	0	0.019256	26.8684

2.2.5 Types of tide

In order to classify tidal signals, three types of tides are considered: semidiurnal, diurnal and mixed tides (Hicks & Szabados, 2006). When both high tides and both low tides of each tidal day are approximately equal in height, the tide is considered to be

semidiurnal (i.e., two high tides and two low tides per day). Diurnal high tides and low tides occur only once each tidal day. When there is a relatively large diurnal inequality (i.e., a large difference in the two high and/or low tides of each tidal day), the tide is considered to be a mixed tide.

The amplitudes of the major harmonic constituents M2, S2, K1 and O1 (see Table 2.2) are used for most of the tide signal around the world. The most common tide classification uses the "form factor", F, defined as F = (K2 + O2) / (M2 + S2), where the ratio classifying the tide as semidiurnal, mixed mainly semidiurnal, mixed mainly diurnal, or diurnal are given in Table 2.3 (Tomczak, 2007).

Table 2.3: Form factor F used for tide classification

Tide type	F
Semidiurnal	0.0 to 0.25
Mixed semidiurnal	0.25 to 1.5
Mixed diurnal	1.5 to 3
Diurnal	Greater than 3

2.2.6 Harmonic analysis

A harmonic analysis of a tide series highlights the presence or absence of significant harmonic constituents. In this study, the four major tidal harmonic constituents M2, S2, K1 and O1, representing a combination of the lunar and solar tide, have been considered. Harmonic analysis refers to the mathematical process of examining one harmonic constituent at a point in time from an observed time series (Schureman, 1958). Two parameters are typically derived for each tidal constituent by harmonic analysis of an observed water-level time series. The first is the amplitude, which is the vertical distance between the mean tide level and the crest of the corresponding sine/cosine curve. The second value is the phase lag, or epoch, which is the time between the maximum astronomic event to the first maximum of the corresponding harmonic constituent of the tide; in most cases it is expressed as an angle (in degrees) with respect to one complete cycle (360°) of the cosine curve of that harmonic constituent (IHO, 2005).

Typically, parameters for about 36 harmonic tide constituents are estimated when the sea level data for a single month is analysed (Haigh, 2017). When data for one year is analysed, the amplitudes and phases for 68 harmonic tide constituents are produced. It should be noted, however, that the amplitudes of many of these constituents are in most cases very small, being a few millimetres or less. As the amount of scatter or noise in the sea level measurements can affect these values, the reliability of such results is questionable. Therefore, meaningful values are usually acquired for the most significant 20 to 30 tide constituents only (Haigh, 2017).

Mathematically, the variations between the lunar and solar tide-producing forces, such as those that occur due to changing phase, distance and declination, are considered to be separate constituent forces. The harmonic analysis of observations shows the response of each constituent of the tide to its corresponding force. This response remains constant at any one point. Each constituent is represented by harmonic constants, which are in the form of a phase angle for the time relation and an amplitude for the height (Parker, 2007).

In general the observed water level $h(t)$ at time t is expressed by simple harmonic terms in the following form (Hicks & Szabados, 2006):

$$h(t) = z_o + \sum_{i=1}^{N} f_i \, H_i \cos\,(\omega_i t + (v_i + u_i) - \varphi_i) \qquad (2.3)$$

where z_0 is the datum shift between the mean tide level and the selected datum; H_i is the amplitude for constituent i; ω_i is the constituent frequency (or angular frequency as given for each harmonic constituent, e.g. Table 2.2); t is time; φ_i is the phase of the tidal harmonic constituent (by convention, phases of the equilibrium tide are expressed relative to the Greenwich meridian); f_i is the nodal amplitude; v_i is the phase angle at time zero; and u_i is the nodal angles within an 18.6-year cycle. In Equation 2.3 the summation is performed over N tidal harmonic constituents. Least-squares spectral analysis (LSSA) algorithms are then used to solve for H_i and φ_i, the tidal constants for that location (Pugh, 1987). The nodal correction functions f_i and u_i are basically designed to account for long-period astronomical cycles.

Harmonic analysis methods make use of least-squares fit in order to determine the relative phase and amplitude of each angular frequency (or angular speed) in the tidal

response. These denote compression of the data in the complete tidal time series. In order to understand the characteristics of tidal dynamics, this data may be compared with similar data at other locations. Alternatively, it can be used to create a synthetic time series for tidal effects at other times for prediction purposes (Foreman, 1996).

2.2.7 Tidal prediction

In chapter 5, the thesis provides a model for tidal prediction. The model is designed to obtain the tidal harmonic constituents from GNSS height observations and use that information to build tide prediction. This section explains the tidal predictions.

Tidal predictions are representations of the tide as they are predicted based on tidal observations recorded at a tide gauge (Parker, 2007). For precise prediction, the observed readings used to generate them must also be precise. Tidal predictions are usually based on the analysis of sea level measurements taken over a period of at least one year. Using this standard, the average variations in mean sea level that occur due to seasonal variations and different meteorological conditions are calculated and included in the predictions. These variations are not replicated from year to year, however. Ideally, therefore, observations and analysis of sea level measurements should cover a span of several years (Haigh, 2017).

There are many methods available for obtaining tide predictions. All such predictions are made on the basis of reconstructing the tidal signature of a given area for a given time using the calculated tidal harmonic constituents. Traditionally, tidal predictions are performed when enough information is available, for instance at ports where tide gauges have been set up. The observed tide is then broken down into its harmonic constituents using harmonic analysis as shown in Section 2.2.6. The harmonic constituents are used to reconstruct the tidal signal, which in turn is used to predict future tides. As the propagation and modification of the tide along a coastline changes considerably, the prediction is only valid at the location of the tide gauge. While interpolations between gauges may be made, they are usually assumed to be linear, which is not necessarily true (Church, 2008). Therefore, the ability to accurately predict tides in a given area is or would be a valuable tool for works related to the sea surface.

2.2.8 Tidal datums

A datum is a reference from which linear measurements are made. It consists of a physical point, line or surface. It may also be an invisible point, line or surface that is positioned by statistical treatment of the numerical values of a particular natural phenomenon. Datums are indicated as references for either vertical or horizontal measurements.

A tidal datum can be regarded as a reference sea level that is statistically constructible using sea-level observations. The datum is used as a reference for describing and measuring vertical positions near the Earth's surface (Fok, 2012). A 'sounding datum' is the sea-level datum to which soundings are referred to. A 'chart datum' is the datum to which depths on a chart are referred to. Finally, a 'tidal datum' is a sea-level datum when it is defined in terms of a certain phase of a tide (NOAA, 2001). Tidal datums are based on water-level observations from a water-level measurement system (e.g. tide gauge). They are then transferred by differential levelling on land between the tide measurement system and a local benchmark. Tidal datums can function as vertical references to measure local water levels or water depths. Tidal datums are also important to establish state-owned land, privately owned land and the territorial sea baseline from which other high-seas boundaries are established (e.g. territorial seas, contiguous zones and exclusive economic zones) (NOAA, 2001).

There are numerous types of tidal datums, including mean lower low water (MLLW), mean low water (MLW), mean sea level (MSL), mean higher high water (MHHW), mean high water (MHW) etc. (see Figure 2.7). For example, the tidal datum of MLLW refers to the average of the lower low water heights (or only low height) of each tidal day observed over the National Tidal Datum Epoch defined by the Centre for Operational Oceanographic Products and Services (CO-OPS) (Hicks & Szabados, 2006). In some countries, including Australia and the UK, the lowest astronomical tide (LAT) is usually used as chart datum. LAT is defined as the lowest level which can be predicted to occur under any astronomical condition and under average meteorological conditions (Pugh, 1987).

To determine tidal datums, a period of 19 years of tide observations is recommended because it approximates the full 18.6-year node cycle. This is the period required for the regression of the Moon's node to complete 360° of longitude (Hicks & Szabados,

2006). Tide gauges installed on land, which are fixed stations near the coast, are traditionally used to measure the coastal sea level.

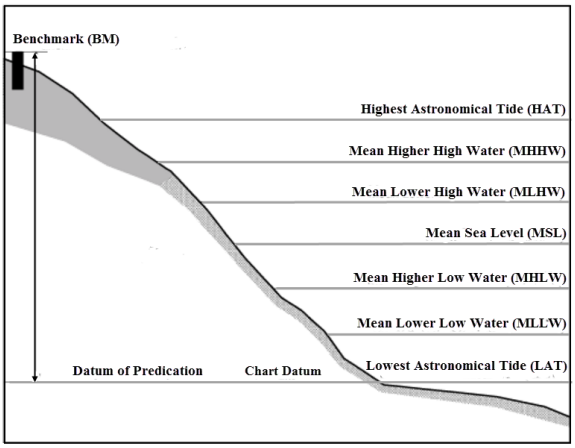

Figure 2.7: The principal tidal datums related to a beach profile (modified from The State of Queensland – Department of Transport and Main Roads, 2016)

Common to all tide measuring devices is the fact that the station must be connected to a reference network of benchmarks that have an accurate geodetic position location and height. A station benchmark does not remain constant over extended periods of time due to the fact that the Earth's surface moves as a result of a range of natural processes, such as seismic and plate tectonic activity, or human-related activity. Therefore, sea level measurements must be segregated from land height variations due to vertical land movements.

In most cases, tide gauge benchmarks are defined in terms of a National Levelling Network (NLN). The vertical datum used for the NLN is typically based on tide gauge observations defining mean sea level (MSL). Ideally, it is recommended that tide gauges be equipped with a GNSS receiver to continuously monitor land movement. The GNSS antenna position should be accurately determined in three dimensional geodetic coordinates. The position should be linked to the tide gauge benchmark by regular levelling, on at least an annual basis (IOC, 2006).

2.2.9 Tide observations

In the past, a recorder driven by a float in a stilling well was utilized in the majority of water level measuring systems. The function of a stilling well was to calm the waters around the water level sensor. Installed inside the stilling well, a float was attached by

a wire from the recording unit above. Prior to the use of computer technology, water level data was recorded on a constant running pen and ink strip chart. These records were collected on a monthly basis and sent to headquarters for manual processing (Pugh, 1987). Today, recordings are usually done through an electronic readout system.

An alternative approach to tide observation is to choose a fixed point below the sea surface and measure the pressure, then convert it to a water level height based on knowledge of the water density and local value of acceleration due to gravity. Such a device is called a pressure gauge. It is possible to deploy these systems off the coast, as well as work in offshore areas where mounting a stable tide gauge station is not possible. Pressure gauges are prone to a relatively high level of inaccuracy because the calculated water depths are a function of sea water density, which is greatly affected by salinity, temperature and ambient atmospheric pressure. To correct for these and attain a higher level of precision, additional measurements of atmospheric pressure, water column temperature and salinity are required (Pugh, 1996).

Various acoustic tide gauges have been developed which function by measuring the travel time of acoustic pulses reflected vertically from the sea surface. Theoretically, this type of measurement can be made in open air using an acoustic transducer that is mounted vertically above the sea surface; however, in certain conditions the reflected signals may be lost. Therefore, to ensure continuity and reliability of the gauge, the sensor is located inside a tube that gives some degree of surface stilling and protects the equipment (NOAA, 2005). In some sensors, a narrow vertical tube which further constrains the acoustic pulses is contained inside the outer tube. While the outer tube does not completely filter out wave action, by averaging a number of measurements, the desired filtering can be achieved. Although they are quite accurate (~1 cm at 2σ) and robust, this system is much more costly than traditional and simple mechanical measurement methods (Aarup et al., 2006).

Radar tide gauges use a relatively new technique. It is similar to acoustic systems, but uses electromagnetic waves at radar frequencies. This system is easy to operate and has the features of an acoustic sensor but overcomes their main disadvantage their high dependence on air temperature (Hicks & Szabados, 2006). The gauge must be mounted so that between the gauge mounting and the sea surface, there are no restrictions or

reflectors in the path of the radar beam. Radar gauges are cost-effective and, compared to other systems, the engineering work required to install them is relatively simple (Aarup et al., 2006).

While these systems work well for most part, they are typically spatially limited and often have a sparse distribution. Furthermore, users have no access to tidal data from the local tide gauges, nor to land where temporary gauges can be established. Thus, the GNSS technique has been developed rapidly to support tidal observations, and is used to monitor height variations of a vessel or a buoy. Using GNSS heights for tide measurement is important as it can complement and/or replace tide gauge observation in areas of poor coverage of tide gauges, or in the open sea. This method is described in detail in Chapters 3 and 4 of this thesis.

2.3 Global Navigation Satellite Systems (GNSS)

To extract tide information from sea-surface heights determined by GNSS, the critical components of the GNSS concept, GNSS error sources and a complete appreciation of the evolution of both the technology and methods used to minimise system limitations are reviewed in the following.

2.3.1 The GNSS concept

Global navigation satellite systems (GNSS) enable autonomous geospatial positioning, navigation and time-transfer information. GNSS positioning is based on trilateration, which determines the position of a point by measuring distances to a set of satellites of known coordinates (Hoffman-Wellenhof, Lichtenegger, & Wasle, 2008). The calculations can allow for errors in the three-dimensional coordinates of the antenna position and the receiver clock, provided sufficient (typically more than four) satellites are tracked simultaneously and their positions are accurately known (El-Rabbany, 2002; Wells et al., 1986). The distance from an antenna to a satellite is usually obtained from two GNSS observables: pseudoranges (code observations) and carrier-phase observations. The intention is to provide the position of any given location in the world using coordinates defined in a geocentric earth-fixed reference frame such as the International Terrestrial Reference Frame (ITRF).

There are currently four operational GNSS offering global coverage. The Global Positioning System (GPS) (or NAVSTAR GPS, as it is officially called) was the first

fully operational GNSS. A comparable system is GLONASS, a Russian space-based navigation system. GALILEO is a civilian-controlled European system which offers accurate and guaranteed global positioning services (European Commission, 2016). Finally, there is the Chinese government-funded GNSS BeiDou. Some countries have been developing regional coverage, such as the Quasi-Zenith Satellite System (QZSS) from Japan, and the Navigation with Indian Constellation (NAVIC) (Montenbruck et al., 2017). All of these are intended to be operable in conjunction with other GNSS for improved accuracy.

Table 2.4 shows the constellations of GNSS as of August, 2017. The GPS constellation consists of 31 operational satellites in six near-circular orbital planes, which are evenly spaced at an inclination of 55° with respect to the equator and a 12-hour period. The system is currently made up of three different blocks of satellites IIR, IIR-M and IIF. All blocks transmit the legacy (L1 C/A) signal and encrypted P(Y) signal on L1/L2 (Block IIF), including the L5 signal. These are most widely used by present GPS users (Montenbruck et al., 2017). The orbital altitudes are approximately 20 200 km above the Earth, so that there are at least four satellites simultaneously above the horizon anywhere on Earth, 24 hours a day (Hoffman-Wellenhof, Lichtenegger, & Wasle, 2008).

The GLONASS constellation is mainly composed of GLONASS-M+ satellite and two GLONASS-K1 satellites. It contains 24 operational satellites in all. These are distributed into three equally spaced orbital planes, each containing eight evenly spaced satellites at an inclination of 64.8°. The altitude of the orbits is 19 100 km; orbital period is 11 h 15 min 44 s (Hoffman-Wellenhof, Lichtenegger, & Wasle, 2008). These two GNSS satellites systems (GPS and GLONASS) were used in the research for this thesis. More descriptions of the basic GNSS satellite systems is available at http://igs.org/mgex and in Hofmann-Wellenhof, Lichtenegger, and Wasle (2008).

Table 2.4: Status of navigation satellite systems as of August 2017. MEO = medium altitude Earth orbit; IGSO = inclined geosynchronous orbit; GEO = geostationary Earth orbit; IOV = in-orbit validation; FOC = fully operational capability (Montenbruck et al., 2017)

System	Block	Signals
GPS	IIR	L1 C/A, L1/L2 P(Y)
	IIR-M	L1 C/A, L1/L2 P(Y), L2C, L1/L2 M
	IIF	L1 C/A, L1/L2 P(Y), L2C, L1/L2 M, L5
GLONASS	M	L1/L2 C/A & P
	M+	L1/L2 C/A & P
	K	L1/L2 C/A & P
BeiDou-2	MEO	B1, B2, B3
	IGSO	B1, B2, B3
	GEO	B1, B2, B3
BeiDou-3	MEO	B1, B1, B2, B3ab
	IGSO	B1, B1, B2, B3ab
Galileo	IOV	E1, E6, E5a/b/ab
	FOC	E1, E6, E5a/b/ab
QZSS	I	L1 C/A, L1C, L1 SAIF, L2C, L6 LEX, L5
NAVIC	IGSO	L5/S SPS & RS
	GEO	L5/S SPS & RS

2.3.2 GNSS observation errors

GNSS measurements are affected by noise and errors. The errors depend on their nature and source, since they may be satellite-related, signal-propagation-related, and/or receiver-related. Satellite errors can be minimised by calculated corrections that are transmitted to the user. Signal propagation errors can be reduced by receiver design, implementation of a differential processing strategy, and atmospheric modelling. Receiver errors can also be handled directly by the user, taking into account site selection and receiver design. All observation errors correspond to one parcel in the observation equation, and can be divided into three main groups: receiver, satellite and frequency-dependent. The errors are summarised as follows (Marreiros, 2012, El-Rabbany 2002):

- Satellite-dependent effects: Antenna offset and antenna phase centre variations.
- Relativistic effects: Frequency effect, path range effect and the effect of Earth's rotation.
- Signal propagation effects: Ionosphere propagation, neutral atmosphere propagation and multipath.

- Receiver-dependent effects: Clock error, antenna offset and antenna phase centre variations.
- Carrier phase windup effect.

Table 2.5 summarizes the errors affecting single-receiver delta phase processing based on rigorous orbit / clock correction data. Further information on GNSS observation errors can be found in the cited literature, as in Misra and Enge (2006), Hofmann-Wellenhof, Lichtenegger, and Wasle (2008), and Marreiros (2012).

Table 2.5: Common magnitudes of GNSS error types (adopted from Misra & Enge, 2001)

Common Error Sourse	Error size
Satellite orbit	~ 2 m
Satellite clock	~ 2 m
Ionospheric delay	~ 2 – 10 m at zenith
Tropospheric delay	~ 2.3 – 10 m at zenith
Receiver noise	Code: 0.25 – 0.5 m Carrier phase: 1 – 2 mm
Multipath	In a clean environment, Code: 0.5 – 1 m Carrier: 0.5 – 1 cm

2.3.3 Height determination using GNSS

GNSS provide the position of a point in a three-dimensional geocentric Cartesian system (X, Y, Z). The GNSS height determined uses ellipsoidal height. This height does not refer to the height system that is used in practice (e.g. the orthometric height). 'Ellipsoidal height' refers to the reference ellipsoid that is used (e.g., WGS84 in the case of GNSS), whereas 'orthometric height' refers to the geoid, which is an equipotential surface of the Earth's gravity field; for practical purposes it is very close to the global mean sea level (MSL), e.g. deviates globally by about ± 2 m. Figure 2.8 shows the geometric relationship between the two heights. The vertical relationship between the ellipsoid, geoid and topography is:

$$H = h_{GNSS} - N_{geoid} \tag{2.4}$$

where H is the orthometric height (referred to the geoid); h_{GNSS} is the ellipsoidal height provided by GNSS (referred to as the 'used ellipsoid'); N_{geoid} is the geoid height, also known as the geoid-ellipsoid undulation. The orthometric height (H), also called height

above mean sea level, can be obtained by subtracting the geoid height (N_{geoid}) from the GNSS-derived ellipsoidal height (h_{GNSS}). N is positive (+) when the geoid is above the ellipsoid, and negative (–) when it is below (NRCAN, 2016).

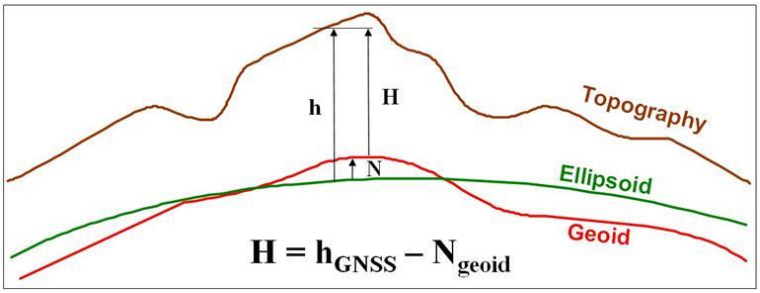

Figure 2.8: Relation between ellipsoidal, orthometric and geoid heights

2.3.4 GNSS positioning techniques

GNSS augmentation techniques have been developed to eliminate or reduce the error sources discussed in the previous section. Multipath errors cannot be reduced using these techniques, and continue to be a significant potential source of GNSS bias. The various augmentation techniques used in this thesis are described in the following sections and are broadly divided into *relative* and *absolute* categories.

2.3.4.1 Relative techniques

The relative positioning technique requires a reference station at a precisely known location so that the measurement error to each GNSS satellite can be reduced by calculating the difference between the measurements of the user, and the reference. The basis for the efficacy of the relative technique relies on the assumption that the observation errors at the user location are similar to those at the reference station. With increasing distance between them, this assumption becomes less valid and positional accuracy decreases; this is termed spatial de-correlation. To increase robustness, multiple reference stations may be used to gather data (Hofmann-Wellenhof, Lichtenegger, & Wasle, 2008; Misra & Enge, 2006).

Various relative techniques have been developed. The techniques used in this thesis are briefly described in the following.

- ***Real time kinematic (RTK)***

RTK is a differential positioning real-time technique which utilises a reference station whose coordinates are known. It is occupied by one receiver which determines the coordinates of unknown points that are visited by a rover receiver. The technique uses phase measurements, and processing is carried out in real time. It produces computed coordinates at the visited points (at cm level accuracy), meanwhile continuing to occupy it for a few seconds (El-Mowafy, 2000, 2012). Using data links, it transmits the reference station coordinates and measurements to the rover to process the data in real time.

An alternative to single-station RTK is to use network RTK, which uses a network of permanent GNSS receivers so that data from all stations is pooled and RTK corrections or raw data may be generated for a mobile user.

- ***Post-processed kinematic (PPK)***

PPK is a post-processing positioning method in which satellite measurements of a sufficient length (typically more than one hour) at the rover are stored. These can then be later processed with measurements from a reference station in a relative mode. PPK relies on the collection of continuous and simultaneous code and carrier-phase at both the rover and reference receivers.

2.3.4.2 Absolute techniques

This method is commonly referred to as stand-alone GNSS, as it relies solely on the signal from the GNSS satellites and the receiver station. Where GNSS augmentation is incorporated with absolute techniques, the method does not require local reference stations to determine differential corrections as the relative positioning technique does. Rather, it uses the data from a network of GNSS reference (tracking) stations to model and correct for errors in the satellite navigation data.

- ***Precise point positioning (PPP)***

PPP is an absolute method which utilizes augmented data in the form of satellite clock and orbit corrections (Abd Rabbou and El-Rabbany, 2015; El-Mowafy ,Deo, & Rizos, 2016; 2017). These corrections are able to improve the accuracy of the standard navigation messages that are broadcast by the satellite. The augmentation data is

derived from a global network of GNSS tracking stations. A single set of globally valid orbit and clock corrections is generated for the entire GNSS constellation and broadcast to the PPP user. For this reason, the technique is not subject to spatial de-correlation.

2.4 Determination of water level heights from shipborne GNSS

In the past, tide reductions were usually derived from data recorded by tide gauges mounted on piers close to the survey area. The chart datum could often be transferred from an existing datum nearby. Tide gauge stations are limited in their spatial distribution since they are usually restricted to coastlines and open ocean islands, and therefore cannot adequately represent global oceans (Dodd & Mills, 2011). One of the most significant features in hydrography today, the use of GNSS with a vertical positioning accuracy corresponding to the required standard allows hydrographers to reference their depths directly to the reference ellipsoid (e.g. WGS84 used by GPS), thereby completely circumventing the tidal reduction process. However, the ellipsoidal height difference measured by the GNSS cannot be mathematically transformed to the geoid or a tidal surface without first defining the transformation function (e.g. requires knowledge of the geoid height or its approximation by mean sea level, cf. Section 2.3.3). This function requires the measurement of a time series of water level heights, and derivation of a mean value or tidal datum thereof. Essentially, GNSS uses an ellipsoidal 'ruler' to measure a physical phenomenon, in this case the tide (DeLoach, 1995).

The use of GNSS-derived water level heights on a platform (e.g. vessel) eliminates the traditional requirement of using personnel in the field to establish a tide pole and then stay on site to conduct tide observations. It is therefore safer, quicker and allows a more efficient use of personnel and resources (Bisnath et al., 2004). The continuous sampling of the data logger (e.g. GNSS receiver) facilitates a greater sampling density and a more precise dataset than was possible with the traditional methods. However, it is highly restricted to the time of the observations, which can be major limitation when trying to derive reliable tide signals that require a longer time period (e.g. months or longer as recommended by IHO standards).

Shipborne GNSS techniques collect the direct GNSS signals to estimate the GNSS tide, as illustrated in Figure 2.9. The GNSS height h_{GNSS} provides the ellipsoidal height

of the antenna, and the offset (ΔZa) from the water level (*WL)* to the antenna is then removed. Further, corrections for vessel motion and attitude (heave, pitch, roll, long-term draft and dynamic draft *DD*) reduce the GNSS ellipsoidal height measurements to the static water level which is the unperturbed water level where all dynamic effects have been removed. These corrections, including antenna offset ΔZa, must then be translated to the vessel reference point (*RP)*, which then translates the GNSS height directly to the GNSS tide referenced to the ellipsoid (Dodd, Mills, Battilana & Gourley, 2010). Moreover, the sources of GNSS tide error should be carefully analysed, as discussed in this chapter.

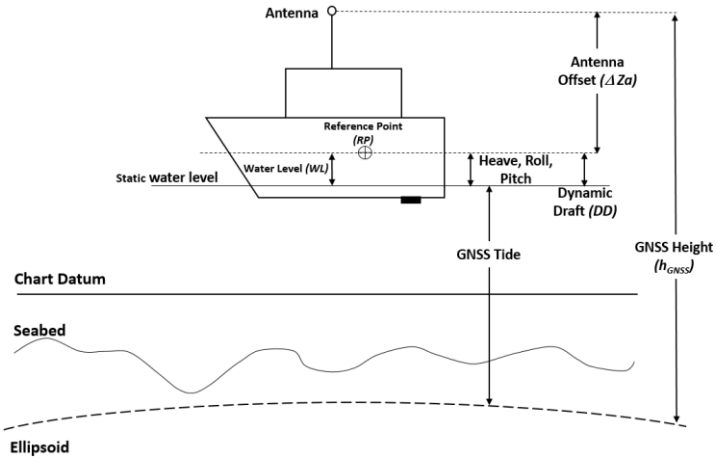

Figure 2.9: Vertical components relating the GNSS-determined position to seabed level and sounding data (modified from Dodd, Mills, Battilana, & Gourley, 2010, and CARIS, 2009)

The relationship between GNSS height and GNSS tide, as shown in Figure 2.9, is given by:

$$GNSS\ Tide = h_{GNSS} - \Delta Za \pm Heave \pm Roll \pm Pitch \pm DD + WL \qquad (2.5)$$

where

- h_{GNSS} is the GNSS height (vertical distance from the ellipsoid to the receiving antenna's phase centre).
- ΔZa is the antenna offset, the vertical distance between the antenna's phase centre and the vessel reference point (RP).
- *Heave* is the short-term vertical movement of the vessel with respect to the static water level measured from the RP.

- *Roll* is the short-term vertical movement related to the side-to-side movement of the vessel.
- *Pitch* is the short-term vertical movement related to the lifting at the bow and lowering at the stern of the vessel.
- *DD* is dynamic draft, the change in the vessel's vertical position due to velocity changes measured with respect to the static water level measured from the RP.
- *WL* is water level, e.g. vertical offset between the static water level and the RP.

2.5 International Hydrographic Organization (IHO) vertical standards

The IHO has developed a set of standards of allowable tolerances for vertical control that may be used during hydrographic surveys. Vessel position and GNSS height are considered to be independent measurements, each with its own degree of uncertainty owing to different equipment and techniques used to measure these variables. The total vertical uncertainty (TVU) is the component of total propagated uncertainty (TPU) calculated in the vertical dimension, and refers to the depth that includes all uncertainties e.g. observation and reduction on a survey vessel. Uncertainty propagation refers to the sum of the effects of measurement uncertainties from all sources and the uncertainties of derived or calculated parameters (IHO, 2008). Once all of the contributing measurement uncertainties, both random and systematic, have been included in the uncertainty propagation, it results in the TPU. The total horizontal uncertainty (THU) is calculated in the horizontal plane and is not relevant to the content of this thesis.

Hydrographic surveys are classified according to the importance of safety of surface navigation (IHO, 2008). Special Order hydrographic surveys deal with areas where ships may need to navigate with minimum under-keel clearance. Harbours, berthing areas, and critical areas of shipping channels are prime examples of areas that may warrant Special Order surveys. For areas where the sea is sufficiently shallow, Order 1a surveys are carried out: these note natural or artificial features on the seabed of concern to the type of surface shipping that typically travels in the area but where the under-keel clearance is not as critical as in the case of Special Order surveys. Order 1a surveys may be limited to water shallower than 100 metres. Meanwhile, Order 1b surveys may be required for areas with a depth of up to 100 metres, in cases where under-keel clearance is not considered to be an issue for the type of surface shipping expected to travel in the area. Specifications for Order 2 surveys apply in areas that are

deeper than 100 metres. As shown in Table 2.6, IHO Standards (fifth edition) specify the maximum allowable THU and TVU for the four survey orders.

The accuracy of tide measurement in reducing hydrographic surveys are specified in IHO Special Publication S44 (IHO, 2008). For Special Order surveys, the total measurement error of tidal heights should not exceed ± 5 cm at 95% confidence level, and ± 10 cm for other surveys (IHO, 2008). Within this thesis these specifications for the tidal heights are used as a general reference when assessing the tidal signal extracted from GNSS-derived water level heights. In practice, IHO Orders 1 and 2 are commonly required for offshore operations, while inshore port and harbour surveys where under-keel clearance is critical are required to meet IHO Special Order specifications. Table 2.6 shows the position (horizontal and vertical) tolerances as a function of Survey Order based on IHO Special Publication S44 in (IHO, 2008). The TVU includes all errors in positioning and propagation, where it roughly equates the fixed 'a' value for each order to the allowable positioning error.

Table 2.6: IHO positioning standards (IHO Spec. Pub. No. 44, 2008)

Order	Special	1a	1b	2
Area descriptions	Areas where under-keel clearance is critical	Areas shallower than 100 metres; under-keel clearance is less critical but there may be features of concern to surface shipping	Areas shallower than 100 metres; under-keel clearance is not considered to be an issue for the type of surface shipping expected to transit the area	Areas generally deeper than 100 metres; general description of the sea floor is considered adequate
Maximum allowable THU 95% confidence level	2 m	5 m + 5% of depth	5 m + 5% of depth	20 m + 10% of depth
Maximum allowable TVU 95% confidence level	a = 0.25 m b = 0.0075	a = 0.5 m b = 0.013	a = 0.5 m b = 0.013	a = 1.0 m b = 0.023
Depth accuracy is calculated from +/- $\sqrt{(a^2 + (b * depth)^2}$.				

2.6 Chapter summary

In this chapter, the basic concepts of tidal mechanics and its physical phenomena were discussed. The tidal generating forces which result from gravitational interactions

between the Sun, Moon and Earth were also discussed. The tidal harmonic constituents were described in detail, as was the relationship between the tidal frequencies and the periodicities of the orbital motions of the Earth, Sun and Moon. Methods of tidal prediction were also briefly presented. In addition, the conventional methods used to collect tidal observations were introduced.

A brief overview of GNSS concepts was presented, and the GNSS observation errors that affect the accuracy of GNSS measurements were given. The GNSS positioning techniques that are used in this thesis were described. The concept of the determination of tidal height/water level from shipborne GNSS was explained. The last section provided some insight on the standards provided by the IHO for the vertical components including the tide.

The next chapter will cover the first objective of this research: the analysis of GNSS-derived water level heights observed at a sheltered harbour site (nearshore area) to extract the tidal signal. GNSS positioning techniques such as post-processed kinematic (PPK) and precise point positioning (PPP) are examined and compared to traditional tide gauge observations. Further, the different low-pass filters to be used to suppress high-frequency water level variations and for the extraction of low-frequency tide signals are introduced.

Chapter 3:

Nearshore GNSS-derived Water Level Heights

3.1 Introduction

This chapter focuses on the analysis of GNSS-derived water level heights observed at a sheltered harbour site. It addresses studies on the suitability of GNSS-water level heights to replace traditional tide gauge observations. To this end, the results of commonly used GNSS positioning techniques in post mission such as Post-Processed Kinematic (PPK) and Precise Point Positioning (PPP) are examined and compared with traditional tide gauge observations. The tide gauge observations form here a reference by providing independent and widely accepted water level observations. While for the coastal location, PPK is considered as a suitable GNSS positioning technique due to the close proximity to available reference stations, the study also includes the PPP that does not require any reference station in close proximity. PPP has been included here to provide some benchmark information for its use at offshore sites at a considerable distance from the nearest coastline as will be discussed in Chapter 4. To estimate tides from GNSS heights, different low-pass filters are analysed for their ability to suppress high-frequency water level variations and to extract low-frequency tide signals.

The chapter describes the study site, data collection and processing strategies, and presents and analyses the results. The characteristics of the GNSS-derived water level heights and tide gauge observations are examined separately then compared, and finally their suitability for extracting tide signals is analysed. For this study, Hillarys

Boat Harbour located in Western Australia was selected as a well-controlled coastal environment. Results from this site serve as a representative example for the comparison to observations from traditional tide gauge stations often installed in sheltered harbour areas.

In this chapter, the study location and data collection are described in detail. GNSS data processing in PPK, PPP solutions, and in static setup will be discussed. The relation between tide gauge and GNSS heights and their reduction to a common datum from a direct comparison between GNSS-derived water level heights and traditional tide gauge records are defined and discussed. Spectral analysis is used to extract the main tidal constituents: the amplitude and phase of the four major tidal harmonic constituents (M2, S2, K2, and O1) from the GNSS (PPK), (PPP) and tide gauge (TG) data. Four different low-pass filters were implemented to eliminate high-frequency components due to wave and the dynamic draft; these are moving average, Savitzky–Golay, Gaussian and Butterworth filters. These low-pass filters are described in detail in this chapter.

3.2 Location of the study and data collection

3.2.1 Location at Hillarys Boat Harbour

In this study, the GNSS data used were collected by a multi-GNSS receiver installed by Fugro Survey Pty. Ltd, Australia on a floating pontoon at Hillarys Boat Harbour located on the Western Australian coast (see Figure 3.1). The pontoon was newly constructed and not in service at the time of observation and as such no disturbances due to common marine traffic were present. The movement of the pontoon was considered to be mainly due to water movement. As the pontoon was located in a sheltered harbour area (i.e., a controlled environment), effects due to sea swell and other short-term variations were largely reduced. As such, the selected study site can be considered as a suitable benchmark that can serve as a reference for other more dynamic off-shore sites. In addition, the site is well suited for a comparison between GNSS-derived water level heights and tide gauge heights, as both the pontoon and the tide gauge are located in the same sheltered harbour area.

Figure 3.1: GNSS antenna and receiver for the nearshore study. (Top) Installation of the GNSS antenna and receiver. (Bottom) Pontoon used to install the GNSS antenna and receiver at Hillarys Boat Harbour, Western Australia (Kennedy, 2011)

A high-performance Trimble Zephyr Geodetic antenna was connected to a Fugro Starpack GNSS receiver, which included an internal Trimble BD982 engine (Kennedy, 2011). GPS and GLONASS code and carrier phase observations on the L1 and L2 frequencies were recorded continuously for 30 days from August 1 to August 31, 2011 at 1 Hz sampling rate. The 1 Hz GNSS data were processed to obtain GNSS-derived water level heights, which were resampled at 1 min intervals (see Section 3.3) for direct comparison with the tide gauge observations provided with a 1 min sampling rate.

3.2.2 Traditional tide gauge observation at Hillarys

The tide gauge observations for this study were obtained from the Hillarys tide gauge station located in the same harbour area in close proximity to the GNSS antenna (as shown in Figure 3.2. The tide gauge was located approximately 348 m southeast of the

GNSS observation station. Hillarys tide gauge station is part of the SeaFrame station's network operated by the National Australian Tide Gauge Network (http://www.bom.gov.au/marine/).

The tide gauge station used is an Aquatrak Aqualogger 4100 (PCTMSL, 2005), an acoustic tide gauge. The water level is measured by sending an acoustic pulse down a small pipe within the environmental tube. The two-way travel time through the air between the transmitter/receiver and the water surface below is measured and converted to sea level height observations (Ronai, 2006). The nominal tide gauge accuracy is one centimetre in all-weather conditions, as required for standard port predictions in Australia, which is provided by tide gauge stations of the Global Sea Level Observing System (GLOSS) network (Tomczak, 2007). Importantly, the tide gauge is located in the same harbour basin without any major structures between it and the GNSS observation station (as depicted in Figure 3.2), thus they should experience the same longer-term water movements. The tide gauge observations are provided as 1-minute averages of 60 one-second observations. The 1-minute averages are referred in time to the mid-point of the 60 second interval, where the first value for each day refers to the time at 30 seconds after midnight.

Figure 3.2: Hillarys tide gauge (red dot) and GNSS observation stations (yellow dot) (Fugro, 2014)

3.3 GNSS data processing

The data acquired by the GNSS receiver is first converted to the standard RINEX (Receiver Independent Exchange) format files. The RINEX files consist of (e.g. Gurtner & Estey, 2013):

- The observation data file containing the pseudorange and carrier phase observations for each of the satellites tracked by the GNSS receiver. Here GPS and GLONASS satellites are tracked on the L1 and L2 signals.
- The navigation file containing the navigation message broadcast by the satellites.

As mentioned earlier, two kinematic GNSS post-processing techniques were applied since the data used was collected prior to conducting this study. The first technique is post-processed kinematic (PPK) (described in Section 3.3.1) which combines code and carrier phase observations with that of a base station located at a distance of approximately 25 km. The second method is using precise point positioning (PPP) (described in Section 3.3.2) which uses the International GNSS Service (IGS) final precise orbit and clock corrections and does not require direct access to a reference station. In order to examine the performance of these GNSS positioning techniques for kinematic positioning of a marine platform, height results were later compared to traditional tide gauge water heights (Section 3.5). Furthermore, to evaluate the two kinematic GNSS positioning techniques, a static baseline test was first conducted to evaluate the accuracy levels of both techniques.

3.3.1 PPK Processing

PPK is a post-processing technique based on the differencing of original code and/or carrier phase observables from a reference station receiver, and one or more roving GNSS receivers (Wert, et al., 2004). Only when using carrier phase observations and solving for the integer ambiguities, this technique provides high relative accuracy (e.g. a few mm in a static environment and cm-level in a kinematic environment) (Awange, 2012).

The IGS station CUT0 was used as the reference station (RS) (http://www.igs.org/). It is located at Curtin University, approximately 24.8 km from the GNSS observation station at Hillarys. It comprises a Trimble GNSS receiver (Figure 3.3). The commercial software package Trimble Business Centre (TBC) was used to process the GNSS data in PPK mode. For this study, TBC was configured in the kinematic mode, i.e. output positions every epoch, using 30 days of continuous L1 and L2 GPS and GLONASS measurements, adopting an elevation cut-off angle of 10° and a sampling rate of 1 Hz. Outputs of the PPK processing were geodetic latitude, longitude and ellipsoidal heights with respect to WGS84. The GNSS data was resampled to 1 minute

centred on the minute synchronized with tide gauge data for direct comparison, since the latter was provided with a 1-minute sampling rate.

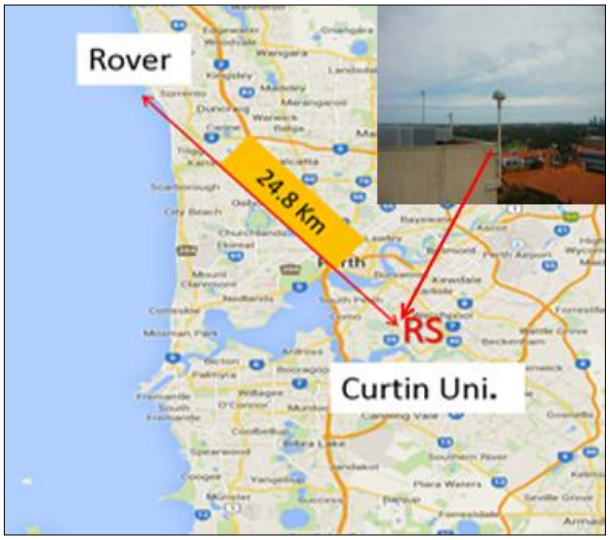

Figure 3.3: Location of GNSS observation station and reference station at Curtin University

3.3.2 PPP Processing

The PPP technique provides an attractive alternative to PPK as it does not require a local reference station but relies on precise satellite orbit and clock correction data. PPP uses code and carrier phase observations at the rover station only, and provides a centimetre to decimetre level accuracy (Hofmann-Wellenhof, Lichtenegger, & Wasle, 2008; Kouba and Heroux, 2001; Strang and Borre, 1997). Currently the IGS provides several precise satellite orbit and clock products that vary in latency and accuracy. The IGS satellite orbit and clocks are provided in SP3c format at 15-min intervals, and CLK (RINEX extension to handle clock information) at 30 s intervals. In this study, the IGS final products of GPS and GLONASS were used together with their observations.

The RINEX files were processed using the Canadian Spatial Reference System (CSRS) Precise Point Positioning (PPP) service, known as CSRS-PPP (http://webapp.geod.nrcan.gc.ca/geod/tools-outils/ppp.php). The service allows for the upload of RINEX files with options for static or kinematic modes. The static option produces one corrected averaged single point, while the kinematic option produces a corrected time series of positions. The CSRS-PPP provides position results with respect to either NAD83 (CSRS) the standard Canadian national reference frame or

the global ITRF2008 reference frame which is compatible with the WGS84. For this study, the kinematic processing mode and ITRF2008 reference system were selected. A transformation correction for datum compatibility with PPK results and their heights with tide gauge heights was applied.

3.3.3 PPK and PPP Expected Differences

In order to first demonstrate the differences in the heights achievable by the PPK and PPP positioning methods, a baseline test was performed with approximately the same distance between the rover and the reference station (i.e., ~ 25 km). For this experiment the rover antenna was static and dual-frequency GNSS measurements were processed in kinematic mode in exactly the same way as the GNSS-derived water level height were determined (Sections 3.2.1 and 3.2.2). A Trimble GNSS R10 receiver was employed to collect GNSS observations in the static mode on July 17, 2015, at Kwinana Beach, forming an approximately 25 km baseline from the Curtin base station (see Figure 3.4). Observation data were continuously recorded every second over a 3.5 hours period and processed in TBC for PPK and CSRS-PPP for PPP using the same processing technique and parameters. Thus the only difference from the GNSS-derived water level height observations at Hillarys was the test setup.

Figure 3.4: The static GNSS station setup at Kwinana Beach in Western Australia

Figure 3.5 (top) illustrates the evaluations of PPK and PPP for the time series of the solution obtained at each epoch for the static baseline setup. The first 15 minutes were excluded in PPK and PPP due to the convergence time of the PPP solution. In these first few minutes the PPP results exhibit considerably larger variations (m-level),

which demonstrate the time it takes for the PPP to initialize for phase ambiguties, where code and carrier phase observations on L1 and L2 were used to solve the integer ambiguity. The PPK and PPP height results appear to follow a similar trend. However, the PPP solution seems to exhibit some small but systematic deviations compared to the PPK results. This is attributable to small, unaccounted for biases, or the use of float ambiguities in PPP. The difference between PPP and PPK static setup is shown in the bottom panel of Figure 3.5. The mean of the difference was -2 cm and the standard deviation was 6.6 cm, which agrees with the literature in terms of accuracy of float ambiguity PPP.

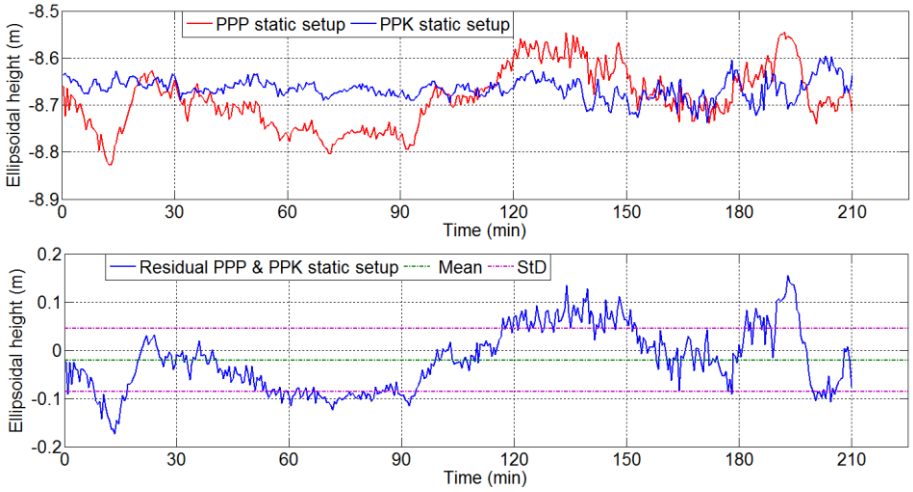

Figure 3.5: Static evaluation (top) and residual (bottom) of PPP and PPK static setup

The standard deviation for the PPK- and PPP-derived GNSS heights, indicated here by σ_{tech}, for the positioning technique used (σ_{PPK} and σ_{PPP}) were σ_{PPK} = 2.2 cm and σ_{PPP} = 3.1 cm, respectively. The key aspect of the baseline experiment is the possibility of quantifying the precision level of the GNSS positioning technique when used without any influence from the dynamic character of high-frequency water-level changes. Therefore, in Section 3.5.1, these values are used to provide an overall error budget when exposing the GNSS antenna to the dynamic environment at Hillarys Boat Harbour test.

3.4 Relation between tide gauge and GNSS heights

Before making direct comparisons between GNSS-derived water level heights and traditional tide gauge heights, it is important to reduce them to a common datum. While GNSS-derived water level heights are computed as ellipsoidal heights relative to the

WGS84 ellipsoid, the tide gauge heights are given relative to the chart datum used at Hillarys Boat Harbour. In this study, the Australian Height Datum (AHD) was used as the common reference datum, both for the heights obtained from GNSS and from tide gauge observations. The AHD is the vertical datum used in Australia and its zero level is based on mean ocean level observed at 32 tide gauge stations located around Australia (Roelse, Granger, & Graham, 1975).

At the location of the GNSS antenna, the height difference between the ellipsoidal height and AHD height is given by the geoid height denoted as N_{AHD}. The geoid height at Hillarys was computed using the AUSGeoid09 model, which is accurate to ~0.03 m across most of Australia (Brown, Featherstone, Hu, & Johnston, 2011). This ellipsoid-geoid separation was added to all original GNSS height observations at the antenna phase centre denoted as h_{GNSS} to convert them to AHD heights, that is $H_{GNSS,\,AHD}$ (as shown in Figure 3.6). The geoid height at Hillarys is negative since the ellipsoid is located above the geoid. In addition, the antenna offset (ΔZa) between the GNSS Antenna Phase Centre *(APC)* and waterline measured as 3.418 m was subtracted from all h_{GNSS} values. Using differential spirit levelling, this offset was obtained from the height of the Antenna Reference Point (ARP) above the pontoon deck measured as 2.746 m, the height of the pontoon deck above the water surface, measured as 0.588 m and the offset between the APC and ARP given as 0.084 m, thus the offset between the APC to the waterline is 3.418 m with an estimated measurement accuracy of ± 0.005 m. The final reduction procedure is summarized by:

$$H_{GNSS,AHD} = h_{GNSS} - \Delta Za \pm N_{AHD} \tag{3.1}$$

Observations at the tide gauge stations are referred to the chart datum at Hillarys, denoted here as $Tide_{CD}$. The offset between the chart datum (tide gauge zero) and AHD at the Hillarys tide gauge station denoted as CD_{offset} is 0.763 m (BOM, 2015) (see Equation 3.2). This offset was subtracted from all tide gauge observations $Tide_{\mathrm{CD}}$ to shift them relative to the AHD as depicted in Figure 3.6, where:

$$Tide_{AHD} = Tide_{CD} - CD_{offset} \tag{3.2}$$

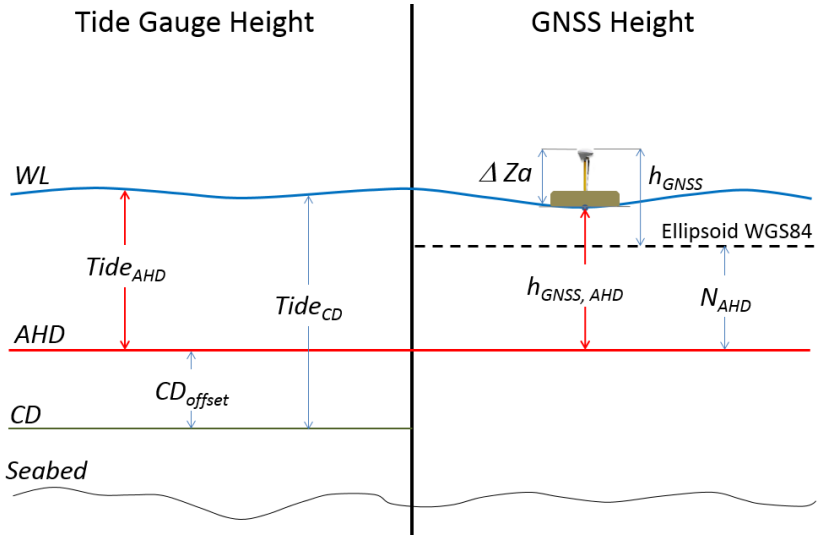

Figure 3.6: Datum connections between GNSS-derived water level heights and tide gauge observations. In this study the AHD has been used as common datum for all observations

3.5 Analysis of GNSS-derived water level and tide gauge heights

In order to evaluate the characteristic of the GNSS-derived water level heights and tide gauge observations, their respective statistical properties were analysed in more detail. For this, firstly the individual datasets were examined before providing comparisons between them.

3.5.1 Individual analysis of GNSS-derived water level heights

The GNSS-derived water level height based on PPK and PPP for Hillarys Boat Harbour test area are depicted in Figures 3.7 and 3.8 (upper panels). The figures clearly show the diurnal tide, which ranges between approximately + 0.6 m and – 0.4 m. The PPP results show more variation than the PPK as expected, due to the use of float ambiguities and reliance on orbit and clock corrections. These also produce some uncertainty in the PPP solution, and some errors that are usually cancelled in PPK (see Section 2.3.2) have to be taken into account. The mean values for the 30-day data for PPK and PPP were 0.8 cm and 4.8 cm respectively. The difference between the original data and smoothed (long-wavelength) heights using a moving average filter with a 100-minute window length are shown in Figures 3.7 and 3.8 (lower panels). PPP results show a larger maximum range of errors than the PPK, e.g. –0.1 to 0.2 m for PPP and ± 0.1 m for PPK. The mean of the residuals for PPK was 0.12 mm, and 40 mm for PPP.

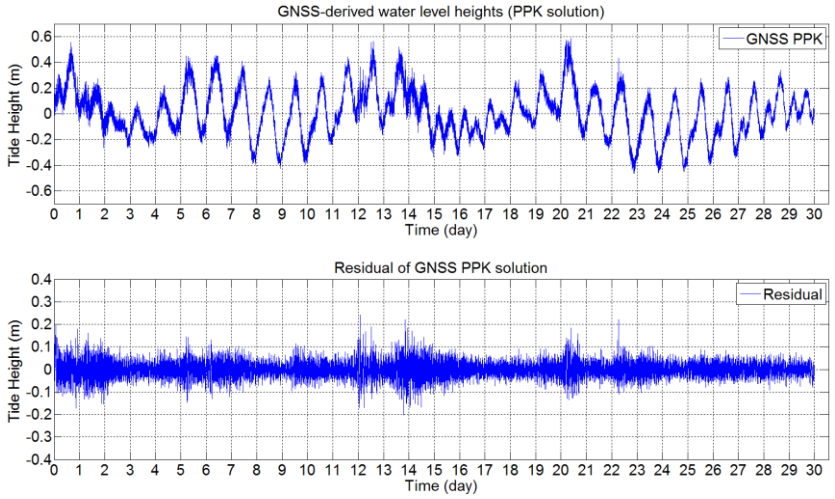

Figure 3.7: GNSS-derived water level heights based on PPK (upper panel). Difference between original heights and smoothed (using a low-pass filter) long-wavelength heights is shown in the lower panel

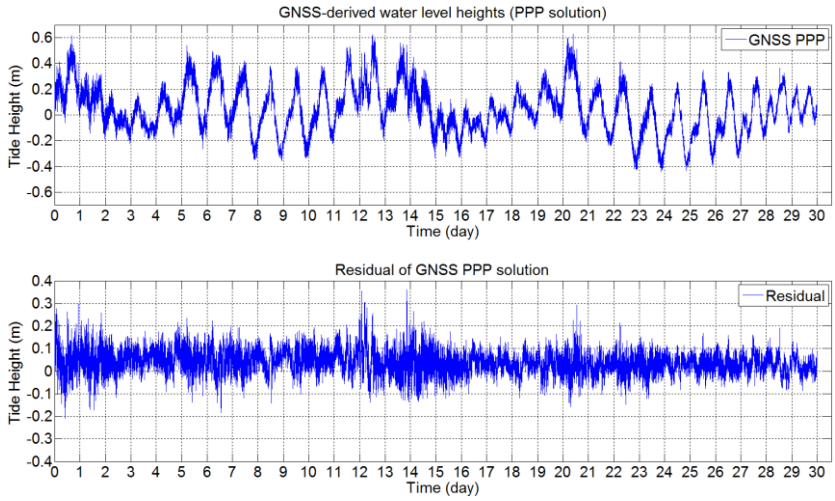

Figure 3.8: GNSS-derived water level heights based on PPP (upper panel). Difference between original heights and smoothed (using a low-pass filter) long-wavelength heights is shown in the lower panel

The distribution of the residuals for each of the PPK and PPP heights are illustrated in the form of histograms in Figure 3.9. The histogram for PPP (Figure 3.9 right) has a wider dispersion than for PPK (Figure 3.9 left), and shows the biases between the datasets, where the mean is not centred around zero. The standard deviations of the differences for PPK at the 2σ level (approximately at 95% confidence level) was ± 0.1 m, and the range for PPP is –0.1 m to 0.2 m, which indicates a higher precision for PPK. Both histograms closely resemble a normal distribution.

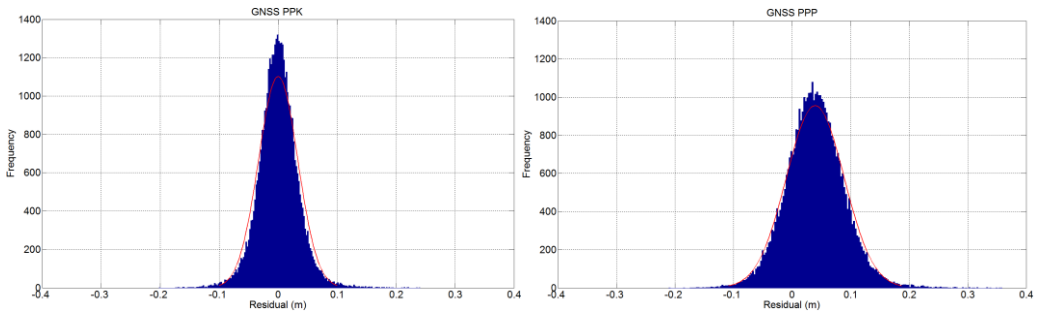

Figure 3.9: Histogram of height residuals for PPK (left) and PPP (right)

After removing the smoothed (long-wavelength) water level, the standard deviations of the residuals (denoted here as σ_{res}) are $\sigma_{res,PPK}$ = 2.9 cm and $\sigma_{res,PPP}$ = 3.7 cm for the GNSS-derived water level heights determined, respectively, by the PPK and PPP techniques. Comparing these values to those obtained for the baseline experiment (σ_{PPK} = 2.2 cm and σ_{PPP} = 3.1 cm; see Section 3.3.3), the increase in noise in the dynamic water height observed environment compared with the baseline case was quantified using the error budget model:

$$\sigma_{res}^2 = \sigma_{tech}^2 + \sigma_{dyn}^2 \tag{3.3}$$

where σ_{dyn} characterizes the additional noise due to exposing the GNSS antenna to the dynamic marine environment (e.g. short-term water level variations). This additional noise is quantified by rearranging terms in Eq. 3.3, such that:

$$\sigma_{dyn}^2 = \sqrt{\sigma_{res}^2 - \sigma_{tech}^2} \tag{3.4}$$

Thus, in the PPK and PPP case, the additional noise is $\sigma_{dyn,PPK}$ = 1.9 cm and $\sigma_{dyn,PPP}$ = 2 cm, respectively. Consequently, the additional noise in both cases are due to the dynamic environment is at a similar level of the positioning technique, i.e., for PPK and PPP these are σ_{PPK} = 2.2 cm vs. $\sigma_{dyn,PPK}$ = 1.9 cm and σ_{PPP} = 3.1 cm vs. $\sigma_{dyn,PPP}$ = 2 cm, respectively. Therefore, for both PPK and PPP, $\sigma_{res,PPK}$ has a similar impact of the dynamic environment and the positioning technique.

3.5.2 Comparison between GNSS-derived water level (by PPK and PPP) and tide gauge heights

To evaluate the quality of the GNSS-derived water level height estimates referred to AHD in Equation (3.1), a direct comparison with tide gauge observations referred to AHD in Equation (3.2) was performed. Overall, all three datasets (GNSS-derived water level heights based on PPK and PPP and the tide gauge heights) during the 30 days of testing, illustrated in Figure 3.10, agree rather well. All show the diurnal tide signals ranging approximately between + 0.6 m and - 0.4 m.

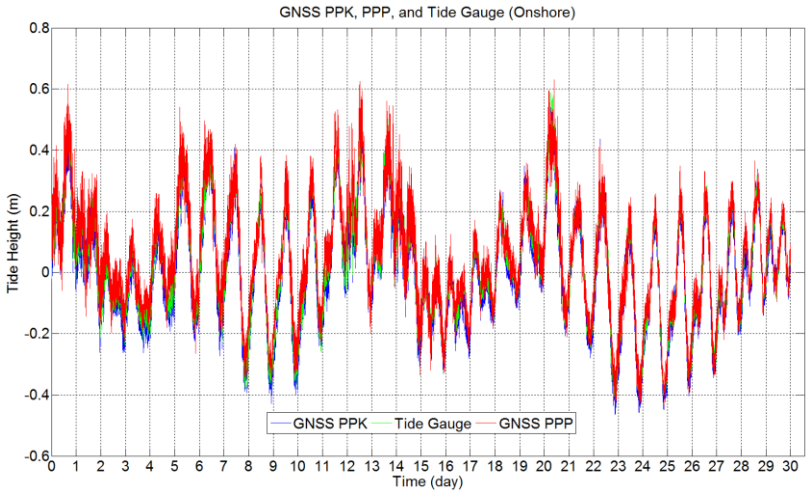

Figure 3.10: Comparison between GNSS-derived water level heights based on PPK (blue), PPP (red) and tide gauge heights (green)

Figure 3.11 depicts the results for one day (day of the year (DOY) 235, i.e. 22 August 2011). While the height values from each of the three solution results (PPK, PPP, and TG) show the diurnal tide, some small biases can be noticed between the datasets. Using the TG observations as a reference (as it is a widely used and accepted method) it appears that the PPK agree more closely with TG data than the PPP results. For the 30-day data record, the mean values are 0.8 cm, 4.8 cm and 2.2 cm for PPK, PPP and TG confirming the small biases between the data sets. The offsets between both PPK and PPP to TG may be an artefact of the geoid height used (i.e. offsets are within the error bounds of the geoid height). This may also demonstrate that the transformation of ellipsoidal heights to another height system (e.g. AHD) is highly dependent on the quality of the geoid height used.

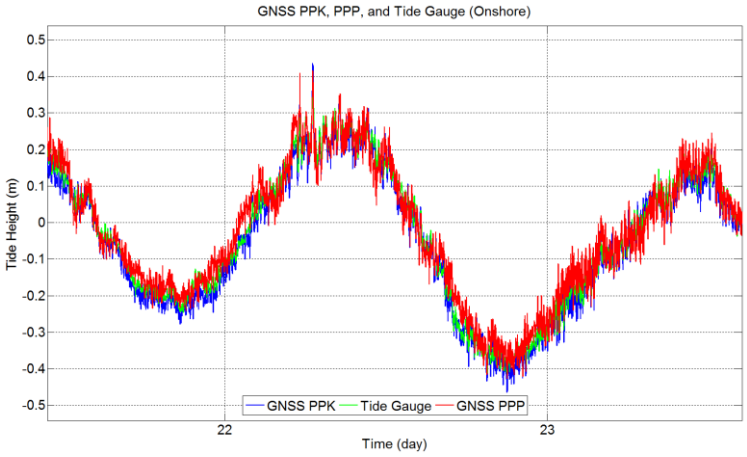

Figure 3.11: Agreement of water levels derived from PPK, PPP and TG centred around DOY 235 (22 August 2011)

As a first comparison, the agreement between the PPK, PPP and TG datasets was investigated in terms of the correlation coefficient *R* computed as:

$$R = \frac{\sum_{i=1}^{N}(x_i - \overline{x})\,(y_i - \overline{y})}{\sqrt{(x_i - \overline{x})^2\,(y_i - \overline{y})^2}} \tag{3.5}$$

where x_i is an observation of dataset X, e.g. PPK, y_i is the observation of data set Y, i.e. PPP, N is the number of observations, $\overline{x}$ is the mean of all observation in X and $\overline{y}$ is the mean of all observation in Y. Results show that both GNSS-derived water level heights (PPK and PPP) are highly correlated with the TG time series as demonstrated by correlation coefficients of 0.98 and 0.97, respectively, and a high correlation coefficient between the PPK and PPP time series of 0.96. This is confirmed by the slope coefficients of the quantiles for TG versus PPK, TG versus PPP and PPK versus PPP all being close to 1.0, (0.99, 0.97 and 0.96, respectively), which can be seen in the Quantile-Quantile (Q-Q) plots illustrated in Figures 3.12a, b and c used here for visually checking if the data are normal distributed.

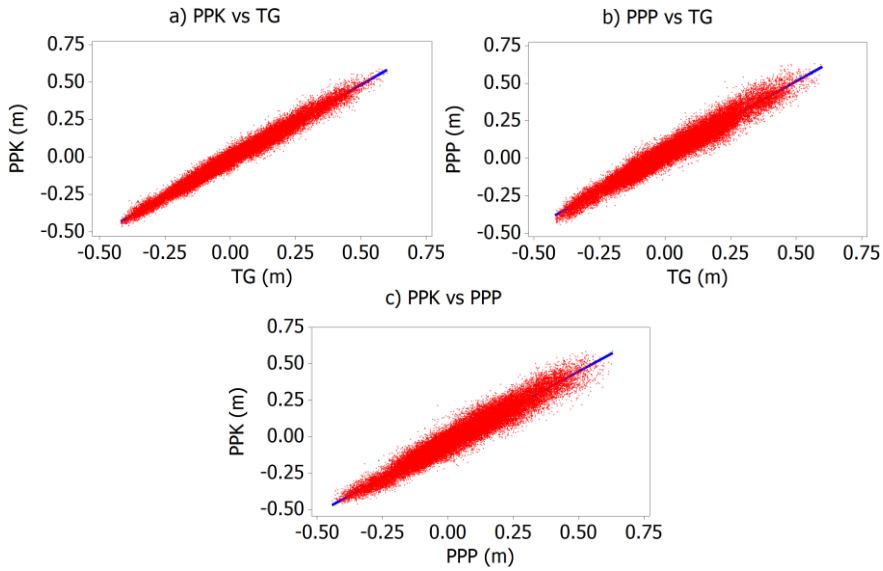

Figure 3.12: Q–Q plots of GNSS-PPK and GNSS-PPP with TG height time series, showing positive correlation for: (a) PPK vs. TG, (b) PPP vs. TG and (c) PPK vs. PPP. The Q-Q data are presented as dots (red), and least-squares fits of trends to the data are displayed as lines (blue)

For a further comparison, the differences were computed between various combinations of the three data sets, i.e. by subtracting PPK and PPP heights from TG heights and PPK from PPP heights, as shown in Figure 3.13. The PPK-TG differences have a standard deviation of 2.9 cm and a mean bias of –1.43 cm. For the PPP-TG differences, the standard deviation increases to 4.3 cm with a mean bias of 2.5 cm. Finally, the standard deviation of the PPK-PPP differences is 4.8 cm with a mean bias of 4 cm. This clearly indicates a higher variability (i.e. noisier) results of PPP with respect to the PPK heights and TG data.

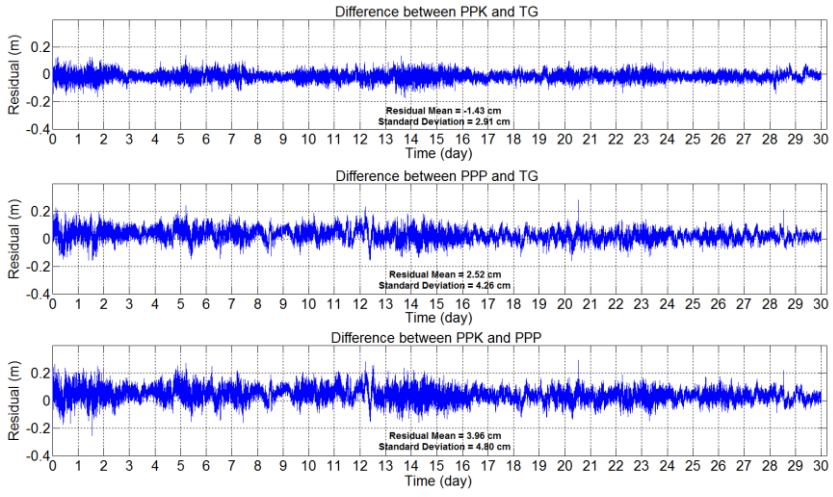

Figure 3.13: Difference between PPK, PPP and TG heights over 30 days

The fit between the PPK, PPP and TG data sets is further quantified by the root-mean-square error RMSE, computed as:

$$\text{RMSE} = \sqrt{\frac{\sum_{i=1}^{N}(y_i - x_i)^2}{N}} \tag{3.6}$$

where y_i represents either the PPK or PPP heights, and x_i is the TG heights. In relation to the standard deviations of residuals for each dataset presented in Section 3.5.1, the RMSE values also include the biases between the datasets. However, as the biases are relatively small, the RMSE values still show some good agreement with values of 3.25 cm for PPK-TG, 4.95 cm for PPP-TG and 6.22 cm for PPK-PPP.

The residuals between PPK, PPP and TG for each of the three combinations are shown by histograms in Figure 3.14. The residuals of PPK-TG Figure 3.14a demonstrate a stationary imprecision of approximately 6 cm as a standard deviation at approximately 2σ level (i.e. 95% confidence level) and the distribution of the PPP-TG difference indicate a lower precision when compared to the PPK-TG differences, confirmed by a lower precision (e.g. standard deviation at 95% confidence level) of approximately 15 cm (see Figure 3.14b). The PPK-PPP differences illustrated in Figure 3.14c show a considerably wider spread than the PPK-TG and PPP-TG differences, with a precision of 10 cm at the 95% confidence level. However, all residuals show that they are close to being normally distributed, with small biases between the datasets.

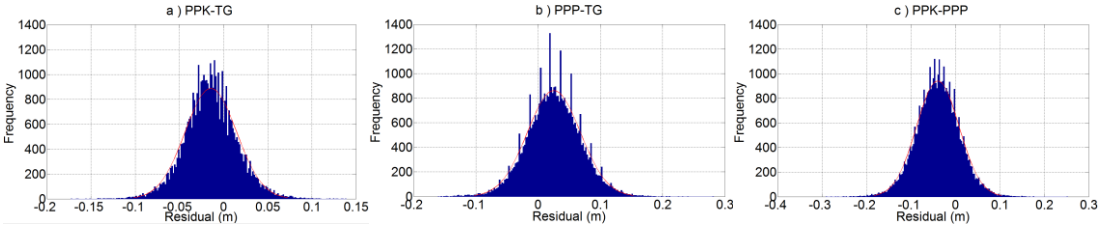

Figure 3.14: Histogram of residuals between PPK, PPP and TG, (a) PPK-TG; (b) PPP-TG; and (c) PPK-PPP heights

Further tests were performed to comprehensively analys the differences between the PPK, PPP and TG heights for the 30 days of data. Since the differences proved to be normally distributed as shown above, the Z-test was computed for testing the mean differences of the residuals as follows:

$$z = \frac{\bar{x} - \mu}{\sigma/\sqrt{n}} \tag{3.7}$$

where $\bar{x}$ is the mean difference tested, and μ is the true mean (i.e., assumed to be ideally zero). When the null hypothesis is accepted, it can be assumed that there is statistically no significant bias between the two datasets; σ is the standard deviation of the differences, and n is the number of water level height differences. The results of the Z-test for the three differences are listed in Table 3.1. The p-value results of PPK-TG, PPP-TG were larger than 0.05, indicating no significant bias between PPK, PPP and TG heights (see Table 3.1).

Table 3.1: Z-test analysis

Z-test	P value
PPK - TG	0.67
PPP - TG	0.62
PPK - PPP	0.93

3.6 Extracting tidal signals through spectral analysis

In the previous sections the noise levels of the GNSS-derived water level heights and their agreement with TG observations has been analysed. In this section and following sections the focus is on the extraction of tide signals from GNSS-derived water level heights and comparing them with tide signals extracted from TG observations.

Because the tide is a periodic phenomenon, it can be modeled by a series of periodic functions such as sinusoidal functions. Therefore, a reliable tidal analysis and prediction requires knowledge of the main tidal frequencies. Different tidal frequencies have been listed by many researchers based on studies of tidal theory (Doodson, 1921; Cartwright and Edden, 1973; Cartwright and Tayler, 1971; Hartmann and Wenzel, 1994, 1995; Kudryavtsev, 2004; Roosbeek, 1996; Tamura, 1987; Xi & Hou, 1987). They usually expand the tide-generating process harmonically using the plural of ephemeris of major celestial bodies (e.g., Moon and Sun) using different methods as discussed in Chapter 2. The main methods to analysis tide signals are either based on harmonic analysis (e.g. modelling in the time domain) or spectral analysis (e.g. modelling in the spectral domain).

3.6.1 Spectral analysis

In this section, spectral analysis is used to extract the main tidal constituents. Spectral analysis was applied to the GNSS-derived water level heights (both PPK and PPP solutions) and TG height observation to confirm the main tidal constituents present during the time of observation and to extract the amplitude and phase of main tidal harmonic constituents from the respective frequency spectra. In this study, the four major tidal harmonic constituents (i.e. M2, S2, K1 and O1) that represent a combination of the lunar and solar tide were confirmed as the main tidal constituents (see Figure 3.15). The variation in tidal forces due to the elliptical shape of the moon's orbit from apogee to perigee are represented by M2 and S2, while the diurnal variation in tidal forces due to the changing declination of the moon (i.e., the moon being to the north then to the south of the equator) are represented by two tidal constituents K1 and O1 in combination with M2 (Parker, 2007).

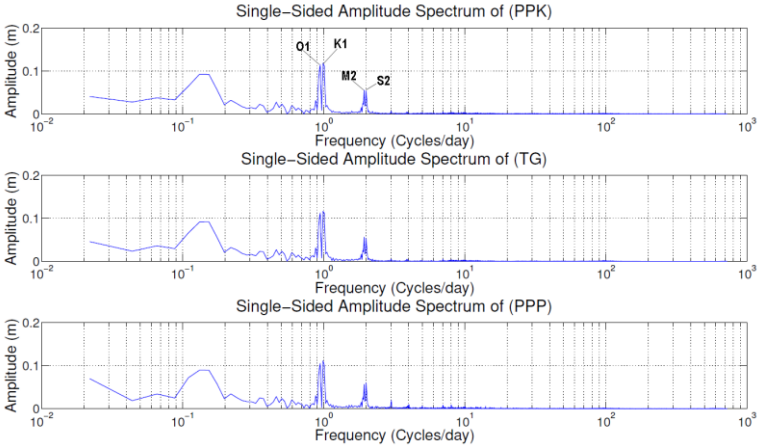

Figure 3.15: Power spectra for the PPK (top), PPP (middle) and TG (bottom) heights

In order to extract the amplitude and phase of the main tidal constituents (i.e., diurnal and semi-diurnal), each time series (PPK, PPP and TG) was transformed to its frequency spectrum by fast Fourier transform (FFT). The main tidal constituents can be identified in the frequency (or power) spectrum by the Fourier coefficients that have a significantly higher amplitude than the noise level of the signal. The continuous Fourier series can be written as:

$$f(t) = \sum_{i=1}^{\infty} A_i \, sin(\omega_i t + \varphi_i) \tag{3.8}$$

where $f(t)$ is the tidal time series; A_i is amplitude; ω_i is angular frequency; t is time; φ_i is phase; and i denotes the harmonic constituent.

The above equation can be expressed in terms of Fourier coefficients a_i and b_i

$$a_i = A_i \cos \varphi_i \tag{3.9}$$

$$b_i = A_i \sin \varphi_i \tag{3.10}$$

such that:

$$f(t) = \sum_{i=1}^{\infty} \left(a_i \cos\left(\frac{2\pi t}{P_i}\right) + b_i \sin\left(\frac{2\pi t}{P_i}\right) \right) \tag{3.11}$$

where, P_i is the period of the constituent.

The respective frequency spectra obtained from the FFT of *f(t)* for the PPK, PPP and TG time series, illustrated in Figure 3.15, clearly show that all-time series are dominated by the diurnal (K1 and O1), and semi-diurnal (M2 and S2) tidal harmonic constituents. The diurnal constituents K1 and O1 have the highest amplitudes in all spectra while the semi-diurnal constituents M2 and S2 have considerably lower amplitude. Apart from some increased power spectrum on an approximately weekly period, the frequency spectra also shows that the M2, S2, K1 and O1 tidal constituents are the only tidal constituents with amplitudes that are significantly higher than the noise level (see Figure 3.15). Therefore, the following analysis considers only those harmonic constituents as a good representation of short-term (several days) tidal variations at the study site.

The amplitudes of the four main tidal harmonic constituents of the PPK, PPP and TG time series extracted from the respective frequency spectra were almost identical (at the mm level) as shown in Table 3.2. From the table, it can be seen that the tidal signal at the test site is dominated by a daily variation where the amplitudes of the diurnal constituents are significantly higher than those of the semi-diurnal constituents. In addition, the agreement between the amplitudes determined from the GNSS water level heights using PPK method and tide gauge heights was slightly better for the semi-diurnal constituents (within ~1 mm) than for the diurnal constituents (within ~2 mm).

On the other hand, the amplitudes derived from the PPP solutions were somewhat larger for the semi-diurnal constituents (~4 mm) and the diurnal constituents (~6 mm), this is possibly an artefact of the increased noise level for the PPP data. Moreover, the extracted amplitude was generally consistent with published values, (Australian National Tide Tables (ANTT), 2004), although the published values given in Table 3.2 are based on much longer-term average values.

Table 3.2: The amplitude of tidal harmonic constituents determined by PPK, PPP solution and TG

Const.	Period (hr)	Freq. in cycle (cycle/day)	Amplitude (m) - published (ANTT, 2004)	Amplitude (m) - derived		
				PPK	PPP	TG
M2	12.421	1.9323	0.053	0.056	0.057	0.056
S2	12.000	2	0.046	0.054	0.060	0.053
K1	23.934	1	0.171	0.118	0.112	0.116
O1	25.819	0.9333	0.121	0.115	0.105	0.113

3.7 Extracting tidal signals from low-pass filtered water-level heights at the nearshore site

The water level height observed by GNSS or tide gauge stations contain both low- and high-frequency variations. The high-frequency variations may predominantly be caused by waves, dynamic draft variations and measurement uncertainties during the data collection. The high-frequency variations are considered here as noise when focusing on the low-frequency signals representing the tide with predominantly semi-diurnal and diurnal periods. To extract the low-frequency tide signal and suppress the high-frequency noise from GNSS-derived water-level heights or tide gauge observations, low-pass filters were used, which pass low-frequency (passband) and suppress high-frequency signals (stopband) from the time series. In this research, GNSS-derived water level and tide gauge heights were filtered using four commonly used filters, i.e. moving average, Savitzky-Golay, Gaussian and Butterworth low-pass filters. A more detailed discussion of each filter is given in the following sections.

The performance analysis of the filtering techniques is one of the main objectives of this research that is to analyse the filters ability to eliminate high-frequency signals while maintaining the lower-frequency tidal signal. The ideal filter would be one that optimises the flat amplitude response and has zero phase distortion (Wert, et al., 2004). The flat amplitude response is important, since it inhibits contaminating effects (in this

study on the low-frequency signal) from entering the filtered time series. Zero phase is important so that there is no delay or phase offsets that would create errors when reconstructing the tide signal (Equation (3.11)) in both the hydrographic height determinations and oceanographic constituent analysis. Apart from filter type, filter performance also depends on filter length as a function of the total time series length. In this research, the filter properties were assessed by their ability to correctly recover the amplitudes and phases of the major tidal harmonic constituents M2, S2, K1 and O1 through spectral analysis, and their ability to suppress high-frequency signals. The phase values were calculated for each tidal constituent using all filters and were found not to be affected by the filtering techniques; therefore, in this thesis the focus is on the amplitudes of the tidal constituents only.

Two evaluations were performed to examine the performance of the selected filters in relation to the window length: (1) the agreement between filtered GNSS-derived water level height and tide gauge time series, and (2) the damping (i.e. signal loss) effect on the major tidal harmonic constituents. For the former, the GNSS-derived water level height and tide gauge time series were filtered and compared to each other. The quality of the fit was quantified by the standard deviation (at 68% and 95% confidence level) and maximum values of the differences. This evaluation is summarised in the flowchart illustrated in Figure 3.16.

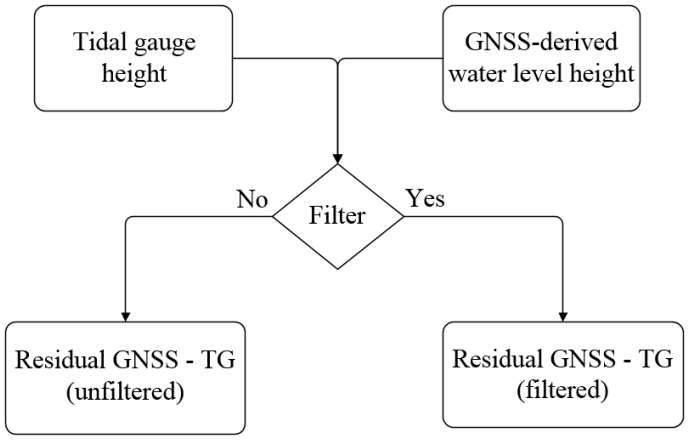

Figure 3.16: Flowchart of the filtering process

For the damping effect, only the GNSS-derived water level heights were examined, as results of the tide gauge provided similar results. For quantification of the damping effect, the amplitudes of the major tidal constituents were extracted from both the unfiltered and filtered time series. Based on the extracted amplitudes, the tide signals

were reconstructed for the unfiltered (taken as a reference) and filtered cases and subsequently the reconstructed signals were compared. The differences were quantified in terms of the standard deviation (at 68% and 95% confidence level) and maximum values of the differences. This process is summarised in the following three-steps (Alsaaq, Kuhn, El-Mowafy & Kennedy, 2016):

1. Extract the major tidal harmonic constituents (M2, S2, K1 and O1) from both the unfiltered and filtered GNSS-derived water level height time series.
2. Reconstruct the unfiltered and filtered tidal signals from the major tidal harmonic constituents estimated from step (1). The reconstruction superposes the harmonic signals as outlined in Equation (3.11).
3. Analyse the differences between the unfiltered and filtered reconstructed tidal signal from step (2), which shows the effect of filtering, and compute the standard deviations and maximum values of these differences.

In the above procedure, any differences between the unfiltered and filtered reconstructed tidal signals present in step (2) are caused only by the application of the filter with the selected window length. Therefore, the differences analysed in step (3) can be used to assess the performance of the different filters, e.g. retaining the low-frequency signal while removing the high-frequency noise.

In the following sections, each filter is briefly described and applied to the GNSS-derived water level heights, and the results are presented and discussed.

3.7.1 Moving average filter

The moving average filter is a simple low-pass filter that is commonly used to smooth sampled time-series data (Shenoi, 2006). It is good for reducing random noise while retaining the sharpest step response (Smith, 2013). As the response to a step change is linear, this filter has the advantage of responding completely with no residual effect within its response time, which is equal to the window length divided by the 1 minute sampling rate. This makes it a premier filter for time-domain encoded signals. However, the moving average is the worst filter for frequency-domain encoded signals, with little ability to separate one band of frequencies from another (Smith, 2013). This would have a direct impact on the extraction of tidal signals from water

level time series; nevertheless, the moving average filter has been included in this study since it is the most commonly used filter in digital signal processing.

A moving average filter operates by averaging a number of successive or neighbouring values or points from the input signal (i.e. contained within the applied window length in a time series) to produce corresponding values in the output signal. The moving average filter for an odd number of values is represented by (Smith, 2013):

$$y\,[\,n + (M-1)/2\,] = \frac{1}{M}\sum_{n=0}^{M-1} x\,[\,n + M] \tag{3.12}$$

where $x[n + m]$ is the input signal (the time series) containing $n = 1, \ldots, N$ discrete values (e.g., 1 min water level values in this case); $y[n]$ is the output signal (the smoothed time series) containing $n = (M-1)/2, \ldots, N-(M-1)/2$ values; and M is the number of values used in the moving average window length.

The smoothed average is centred with the window used, e.g. using $(M-1)/2$ previous values and $(M-1)/2$ values following the value with the index n. Seen as a filter, the moving average performs a convolution of the input sequence $x[n]$ with a rectangular pulse of length M and height $1/M$ (to make the area of the pulse, and hence, the gain of the filter). In practice, for a time series the index n identifies the time of observation (t) such that $t = n\Delta t$, where Δt is the sampling interval (1 minute in this case), where the time for the output value in in Equation (3.12) is referred to as the centre of the window length used.

The amplitudes of the semidiurnal (M2 and S2) and diurnal (K1 and O1) tidal constituents extracted from the filtered PPK, PPP and TG time series using window lengths from 10 to 360 minutes are listed in Table 3.3 (upper value in each row). In addition, the differences between the amplitudes extracted from the unfiltered and filtered PPK, PPP and TG time series are listed in the lower value in each row in Table 3.3. The damping property was assessed in more detail by applying a series of different window lengths (10, 30, 60, 80, 100, 120, 150, 180, 220, 260, 300 and 360 minutes), all considerably shorter than the target periods (e.g. diurnal and semi-diurnal). From the difference between the original tidal constituents and the filtered tidal constituents, the property of the moving average filter is clearly demonstrated by increased damping of the tidal constituents' amplitudes for increased window lengths (i.e. increased

smoothing). The results demonstrate that the damping effect relative to the amplitude of the unfiltered signal for a maximum window length of 360 minutes results in considerable differences. In this case, the damping of the amplitudes is between 37% and 38% for the M2 and S2 tidal constituents and between 10% and 11% for the K1 and O1 tidal constituents. Interestingly, the damping effects are very similar for the PPK, PPP and TG time series.

Table 3.3: Performances of the moving average filter to extract the amplitudes of the major tidal harmonic constituents (M2, S2, K1, O1) from the filtered PPK, PPP and TG time series in relation to the window lengths (WL). The upper value in each row indicates the extracted amplitude after applying the filter. The lower value in each row gives the difference between the amplitudes extracted from the original PPK, PPP and TG time series (see Table 3.2) and the filtered time series

	Amplitudes (m) / Residuals (m)											
	PPK				**PPP**				**TG**			
WL	**M2**	**S2**	**K1**	**O1**	**M2**	**S2**	**K1**	**O1**	**M2**	**S2**	**K1**	**O1**
10	0.056	0.054	0.118	0.115	0.057	0.060	0.112	0.105	0.056	0.060	0.112	0.113
	0.000	0.000	0.000	0.000	0.000	0.000	0.000	0.000	0.000	0.000	0.000	0.000
30	0.056	0.054	0.118	0.115	0.057	0.059	0.111	0.105	0.056	0.059	0.059	0.112
	0.000	0.000	0.000	0.000	0.000	0.000	0.000	0.000	0.000	0.000	0.000	0.000
60	0.056	0.053	0.118	0.114	0.056	0.059	0.111	0.105	0.056	0.059	0.059	0.112
	0.001	0.001	0.000	0.000	0.000	0.001	0.000	0.001	0.001	0.001	0.000	0.000
80	0.055	0.053	0.117	0.114	0.056	0.058	0.111	0.105	0.055	0.058	0.058	0.112
	0.001	0.001	0.001	0.001	0.001	0.001	0.001	0.001	0.001	0.001	0.001	0.001
100	0.054	0.052	0.117	0.114	0.055	0.057	0.110	0.104	0.055	0.057	0.057	0.112
	0.002	0.002	0.001	0.001	0.001	0.001	0.001	0.001	0.002	0.002	0.001	0.001
120	0.053	0.051	0.117	0.113	0.054	0.056	0.110	0.104	0.054	0.056	0.056	0.111
	0.002	0.003	0.002	0.002	0.002	0.003	0.002	0.002	0.002	0.003	0.001	0.002
150	0.052	0.050	0.116	0.113	0.053	0.055	0.109	0.103	0.052	0.055	0.055	0.110
	0.004	0.004	0.002	0.002	0.004	0.005	0.002	0.002	0.004	0.004	0.002	0.002
180	0.050	0.048	0.115	0.112	0.051	0.053	0.108	0.102	0.051	0.053	0.053	0.109
	0.006	0.006	0.003	0.003	0.006	0.007	0.003	0.003	0.006	0.006	0.003	0.003
220	0.047	0.045	0.113	0.110	0.048	0.050	0.107	0.101	0.048	0.050	0.050	0.108
	0.008	0.009	0.005	0.005	0.008	0.010	0.005	0.005	0.008	0.009	0.005	0.005
260	0.044	0.042	0.111	0.108	0.045	0.046	0.105	0.099	0.045	0.046	0.046	0.106
	0.011	0.012	0.007	0.006	0.012	0.013	0.007	0.006	0.011	0.012	0.010	0.006
300	0.041	0.039	0.109	0.106	0.041	0.043	0.102	0.097	0.041	0.038	0.043	0.104
	0.015	0.015	0.009	0.009	0.015	0.017	0.009	0.008	0.015	0.015	0.009	0.008
360	0.035	0.033	0.105	0.103	0.036	0.037	0.099	0.094	0.036	0.038	0.037	0.101
	0.020	0.021	0.013	0.012	0.021	0.023	0.013	0.011	0.021	0.020	0.013	0.012

As an example, the frequency spectra for the unfiltered and smoothed GNSS-derived water level heights (PPK and PPP) for a window length of 100 minutes are illustrated in Figures 3.17 and 3.18, which demonstrate the general properties of the low-pass filter used. The frequency spectra for all remaining window lengths are provided in Appendix A. The frequency spectra in Figures 3.17 and 3.18 clearly depict the four major tidal harmonic constituents. Figures 3.17c and 3.18c show the frequency

spectrum of the differences between the filtered and unfiltered tide signals, which clearly shows the low-pass filter properties by filtering out high-frequency signals and leaving low-frequency signals largely unchanged. However, it is important to point out that lower-frequency constituents are not completely left unchanged but to some extent damped. This is visible by the presence of residual amplitudes in mostly the diurnal (K1 and O1) and semi-diurnal (M2 and S2) tidal harmonic constituents (cf. Figures 3.17c and 3.18c) which should be zero when considering an ideal low-pass filter that perfectly separates high-frequency form low-frequency signals at the cut-off frequency (e.g. defined by the applied window length). This damping phenomenon is common for any practical filter that always has some gradual transition at the cut-off frequency. The amount of damping can be quantified using the frequency response of the filter describing how much the amplitude and phase of any input signal is changed through the application of the filter (e.g. Smith 2013). As the transition of the frequency response from the low-frequency (long-period) stopband to the high-frequency (short-period) passband at the cut-off frequency is gradual (e.g. from almost unchanged to complete elimination) lower-frequency signals closer to the cut-off frequency will be damped much more than those that are further away. This behaviour can clearly be seen by a much larger damping effect for the semi-diurnal than the diurnal tidal harmonic constituents (cf. Figures 3.17c and 3.18c), e.g. semi-diurnal signals have a higher frequency (e.g. closer to the cut-off frequency) than diurnal signals. For example, based on the response factors for a moving average filter with a window length of 360 minutes (e.g. cut-off frequency of 4 day^{-1}) the dampening effect is about 36% for semi-diurnal signals (frequency 2 day^{-1}) and only 10% for diurnal signals (frequency 1 day^{-1}), which is consistent with the amplitude reductions detailed in Table 3.3.

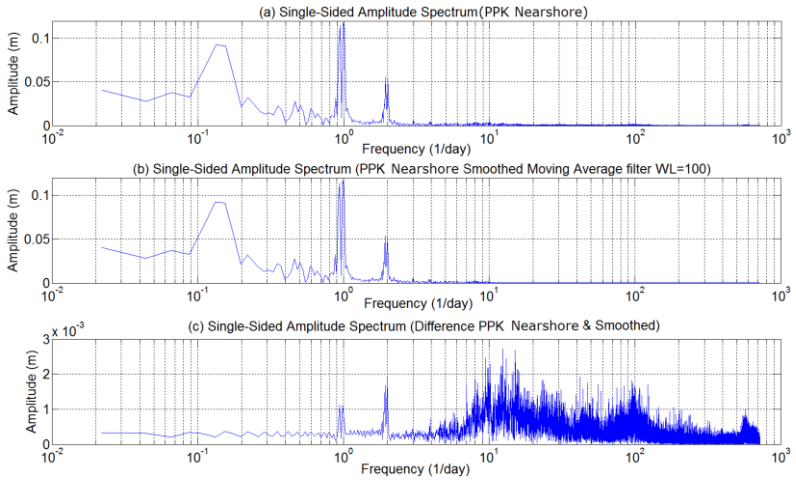

Figure 3.17: Single-sided frequency spectra of the moving average filter for PPK nearshore. (a) unfiltered GNSS-derived water level height signal (PPK); (b) GNSS-derived water level height signal (PPK) signal smoothed by the moving average filter with a 100-minute window length; and (c) differences between filtered and unfiltered GNSS-derived water level height signal

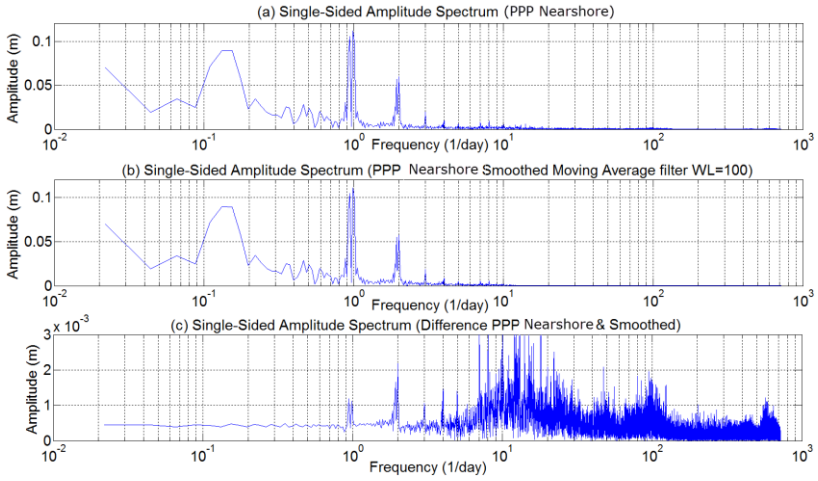

Figure 3.18: Single-sided frequency spectra of the moving average filter for PPP nearshore. (a) unfiltered GNSS-derived water level height signal (PPP); (b) GNSS-derived water level height signal (PPP) smoothed by the moving average filter with a 100-minute window length; and (c) differences between filtered and unfiltered GNSS-derived water level height signal

The application of the moving average filter evidently demonstrates that the amplitudes of tidal constituents extracted from the filtered signal are considerably damped with respect to the unfiltered signal. Following the evaluation procedure outlined earlier, the amplitudes of the M2, S2, K1 and O1 tidal constituents extracted from the unfiltered and filtered PPK and PPP time series (Tables 3.2 and 3.3) were used to reconstruct the tidal signal according to Equation (3.11). The reconstructed

signals were compared and the differences were quantified in terms of the standard deviation (at 68% and 95% confidence level) and maximum values. The results for the moving average filter for the PPK and PPP solutions are shown in Figures 3.19 and 3.20, respectively.

As a result of the moving average filter for PPK or PPP time series show (see Figures 3.19 and 3.20), the standard deviation of the differences between filtered PPK or PPP and TG time series (at 68% and 95% confidence level) and maximum differences decrease with the increase in window length. This demonstrates that a large part of the differences is indeed caused by the higher-frequency variations that were supressed by applying the filter. However, analysing the differences between the reconstructed filtered and unfiltered PPK and PPP time series revealed some significant differences in terms of damping the amplitudes of the four major tidal harmonic constituents. It can be clearly seen that the damping effect is considerably larger for an increasing window length with a standard deviation of the differences at a 68% and 95% confidence level and maximum difference of 2.4 cm, 4.6 cm and 6 cm, respectively for the PPK solutions for the longest window length of 360 minutes. These values were obtained by using all the differences between the reconstructed tidal signals based on the smoothed (i.e. dampened) and unsmoothed signals over the entire 30-day datasets.

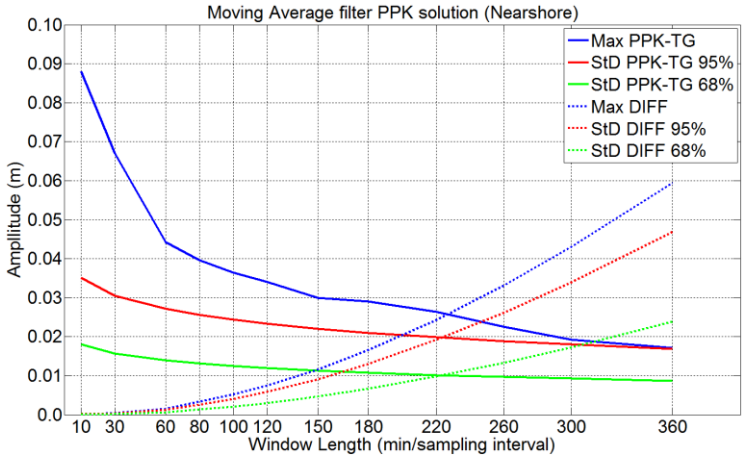

Figure 3.19: Performance of the moving average filter for PPK nearshore in relation to various window lengths. Differences between the filtered GNSS-derived water level heights (PPK) and tide gauge observation (TG) time series are denoted by PPK-TG and are shown by solid lines. Damping effects as manifested by differences in the reconstructed tide signals (DIFF) are shown by dotted lines. The standard deviations of differences (StD DIFF) are given at 68% and 95% confidence levels

The performance of the moving average filter when applied to the PPP solutions shows a very similar behaviour to that for the PPK solutions (cf. Figures 3.19 and 3.20), although the agreement between the filtered PPP and TG series is at a lower level. For the same maximum window length of 360 minutes, the standard deviation of the differences between the reconstructed filtered and unfiltered PPP time series at the 68% and 95% confidence level are 2.5 cm and 4.9 cm, whereas the maximum difference is 6.2 cm. These values are very similar to that of the PPK case (Figure 3.19). Thus the damping effect is similar, regardless of the noise level of the data.

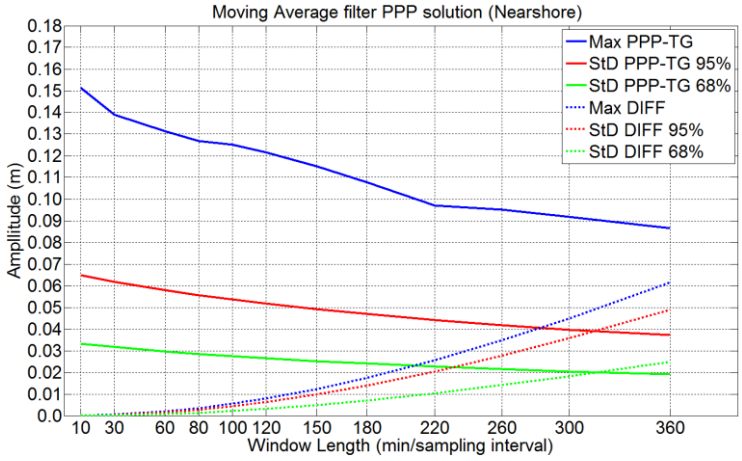

Figure 3.20: Performance of the moving average filter for PPP nearshore in relation to various window lengths. Differences between the filtered GNSS-derived water level heights (PPP) and tide gauge observation (TG) time series are denoted by PPP-TG and are shown by solid lines. Damping effects as manifested by differences in the reconstructed tide signals (DIFF) are shown by dotted lines. The standard deviations of differences (StD DIFF) are given at 68% and 95% confidence levels

3.7.2 Savitzky–Golay filter

The Savitzky–Golay filter effectively removes local noise while keeping the shape of the signal (i.e., minimally degrading the signal's information content) (Savitzky & Golay, 1964). For a time series, the Savitzky–Golay filter smoothes the signal locally by fitting a polynomial, in the least-squares sense, to a sliding window of data. The degree of the polynomial and the length of the sliding window are the filter's two parameters. A second degree polynomial is used (n=2) and k is the number of values

in the sliding window (i.e. the window length), the condition for the polynomial degree that can be resolved is:

$$n < k - 1 \tag{3.13}$$

For the case of $n = 0$, the Savitzy–Golay filter degenerates to a moving average filter, which is useful for removing white noise but is poor for preserving peak shape (higher-order moments) as demonstrated by the moving average filter results (see Section 3.7.1). For $n = 1$, the filter does a linear least-squares fit of the windowed data to a line. If $n = k - 1$, the polynomial exactly fits the data points in the window, and so no filtering takes place.

The method of the Savitzky–Golay filter is to consider a group of M samples f_n, where $n = 1, \ldots, M$ are linearly combined to form a filtered value h_j given by:

$$h_j = \sum_{i=-n_L}^{n_R} c_i \, f_{j+i} \tag{3.14}$$

where n_L is the number of points to the left of the centre and n_R is the number of points to its right of the centre index j. Notice that the moving average smoothing corresponds to the case where all coefficients c_n are equal, with $c_n = 1/(n_L + n_R + 1)$. The Savitzky–Golay filter creates a linear regression of a polynomial to the $n_L + n_R + 1$ samples in the window around sample j, and then evaluates this polynomial for every sample, for all j from 1 to M.

Similarly to the moving average filter, the Savitzky–Golay filter was applied to the PPK, PPP and TG time series for different window lengths. As in Table 3.3, the respective amplitudes of the semidiurnal (M2 and S2) and diurnal (K2 and O2) tidal constituents extracted from the filtered PPK, PPP and TG time series are listed as upper values in each row in Table 3.4, where the differences between the amplitudes extracted from the unfiltered and filtered PPK, PPP and TG time series are listed as the lower value in each row.

The results show the ability of the Savitzky–Golay filter to extract low-frequency tide variations and suppress high-frequency signals with considerably less damping effect of the tidal harmonic constituents than the moving average filter (cf. Tables 3.3 and

3.4). Table 3.4 shows that the damping effects are very small relative to the amplitude of the unfiltered signal for a maximum window length of 360 minutes. The relative change is about 2% for the M2 and S2 tidal harmonic constituents independent of the PPK, PPP and TG time series considered. The effect on the K1 and O1 tidal constituents for all window lengths is always smaller than 1 mm, and thus are considered to be negligible.

Table 3.4: Performances of Savitzky–Golay filter to extract the amplitudes of the major tidal harmonic constituents (M2, S2, K1, O1) from the filtered PPK, PPP and TG time series in relation to the window lengths (WL). The upper value in each row gives the extracted amplitude after applying the filter while the lower values in each row indicate the difference between the amplitudes extracted from the original PPK, PPP and TG time series (see Table 3.2) and the filtering time series

	Amplitudes (m) / Residuals (m)											
	PPK				**PPP**				**TG**			
WL	**M2**	**S2**	**K1**	**O1**	**M2**	**S2**	**K1**	**O1**	**M2**	**S2**	**K1**	**O1**
10	0.056	0.054	0.118	0.115	0.057	0.060	0.112	0.105	0.056	0.053	0.116	0.113
	0.000	0.000	0.000	0.000	0.000	0.000	0.000	0.000	0.000	0.000	0.000	0.000
30	0.056	0.054	0.118	0.115	0.057	0.060	0.112	0.105	0.056	0.053	0.116	0.113
	0.000	0.000	0.000	0.000	0.000	0.000	0.000	0.000	0.000	0.000	0.000	0.000
60	0.056	0.054	0.118	0.115	0.057	0.060	0.112	0.105	0.056	0.053	0.116	0.113
	0.000	0.000	0.000	0.000	0.000	0.000	0.000	0.000	0.000	0.000	0.000	0.000
80	0.056	0.054	0.118	0.115	0.057	0.060	0.112	0.105	0.056	0.053	0.116	0.113
	0.000	0.000	0.000	0.000	0.000	0.000	0.000	0.000	0.000	0.000	0.000	0.000
100	0.056	0.054	0.118	0.115	0.057	0.060	0.112	0.105	0.056	0.053	0.116	0.113
	0.000	0.000	0.000	0.000	0.000	0.000	0.000	0.000	0.000	0.000	0.000	0.000
120	0.056	0.054	0.118	0.115	0.057	0.060	0.111	0.105	0.056	0.053	0.116	0.113
	0.000	0.000	0.000	0.000	0.000	0.000	0.000	0.000	0.000	0.000	0.000	0.000
150	0.056	0.054	0.118	0.115	0.057	0.060	0.111	0.105	0.056	0.053	0.116	0.113
	0.000	0.000	0.000	0.000	0.000	0.000	0.000	0.000	0.000	0.000	0.000	0.000
180	0.056	0.054	0.118	0.115	0.057	0.060	0.111	0.105	0.056	0.053	0.116	0.113
	0.000	0.000	0.000	0.000	0.000	0.000	0.000	0.000	0.000	0.000	0.000	0.000
220	0.055	0.054	0.118	0.115	0.057	0.059	0.111	0.105	0.056	0.053	0.116	0.113
	0.000	0.000	0.050	0.000	0.008	0.009	0.005	0.005	0.000	0.000	0.000	0.000
260	0.055	0.053	0.118	0.115	0.056	0.059	0.111	0.105	0.056	0.052	0.116	0.113
	0.000	0.000	0.000	0.000	0.000	0.000	0.000	0.000	0.000	0.000	0.000	0.000
300	0.055	0.053	0.118	0.115	0.056	0.059	0.111	0.105	0.056	0.052	0.116	0.113
	0.000	0.001	0.000	0.000	0.000	0.000	0.000	0.000	0.001	0.001	0.000	0.000
360	0.055	0.053	0.118	0.115	0.056	0.058	0.111	0.105	0.055	0.052	0.116	0.112
	0.001	0.001	0.000	0.000	0.000	0.000	0.000	0.000	0.001	0.001	0.000	0.000

As an example, the frequency spectra for the unfiltered heights of PPK and PPP are illustrated in Figures 3.21a and 3.22a. The smoothed GNSS-derived water level heights of PPK and PPP after applying the Savitzky–Golay filter with a window length of 100 minutes are shown in Figures 3.21b and 3.22b. The frequency spectra clearly represent the four major tidal harmonic constituents. The difference between the filtered and unfiltered PPK and PPP time series in Figures 3.21c and 3.22c show insignificant damping effects in the spectrum of the residuals considered to be

negligible. This demonstrates that the Savitzky-Golay filter has a much steeper transition from the low-frequency (long-period) stopband to the high-frequency (short-period) passband (e.g. fast change from almost no damping to complete damping) at the cut-off frequency.

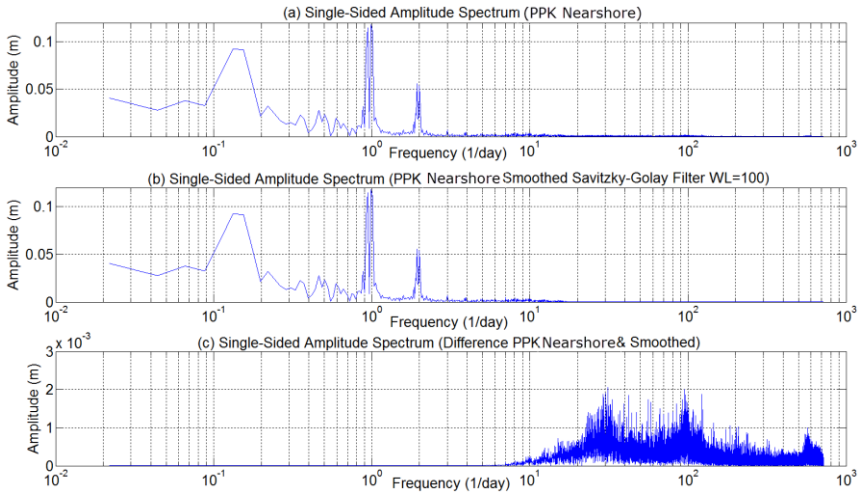

Figure 3.21: Single-sided frequency spectra of the Savitzky–Golay filter for PPK nearshore. (a) the unfiltered GNSS-derived water level height signal (PPK); (b) the GNSS-derived water level height (PPK) signal smoothed by the Savitzky–Golay filter with a 100-minute window length; and (c) the differences between the filtered and unfiltered GNSS-derived water level height signal

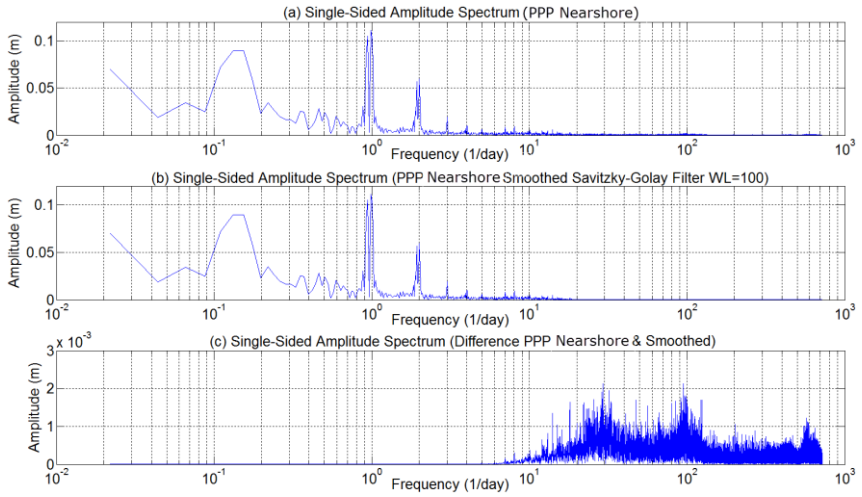

Figure 3.22: Single-sided frequency spectra of the Savitzky–Golay filter for PPP nearshore. (a) the unfiltered GNSS-derived water level height signal (PPP); (b) the GNSS-derived water level height (PPP) signal smoothed by the Savitzky–Golay filter with a 100-minute window length; and (c) the differences between the filtered and unfiltered GNSS-derived water level water height signal

The standard deviation of the differences between the filtered PPK and TG water level time series (at 68% and 95% confidence level) and the maximum differences when applying the Savitzky–Golay filter on the PPK time series are shown in Figure 3.23. It was found that a large part of the differences was due to higher-frequency variations, as the values significantly decreased with increase in window length. The damping effect was considerably smaller for the Savitzky–Golay filter when compared with the moving average filter in terms of the standard deviations at the 68% and 95% confidence level of the differences, with the maximum difference being between 1 and 2 mm for the maximum window length of 360 minutes. Again, these values are very similar to those of the PPP case (see Figure 3.24), which confirms that the damping effect is similar irrespective to the noise level of the data.

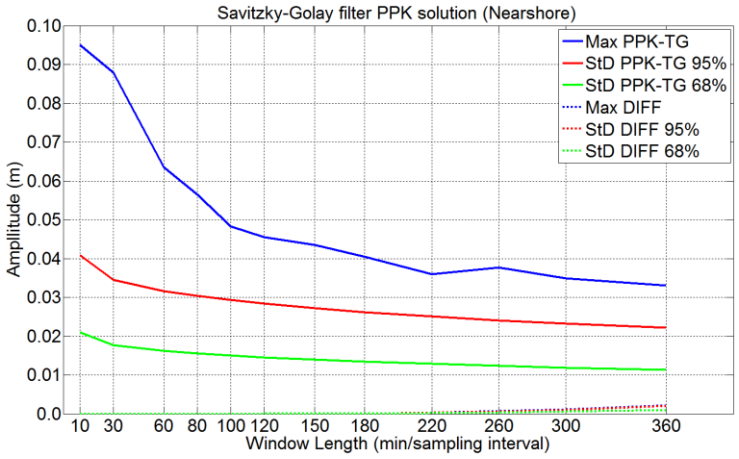

Figure 3.23: Performance of the Savitzky–Golay filter for PPK nearshore in relation to various window lengths. Differences between the filtered GNSS-derived water level heights (PPK) and tide gauge observation (TG) time series are denoted by PPK-TG and are shown by solid lines. Damping effects as manifested by differences in the reconstructed tide signals are shown by dotted lines and denoted by DIFF. The standard deviations of differences (StD DIFF) are shown for 68% and 95% confidence levels

Similar to the moving average filter, the performance of the Savitzky–Golay filter when applied to the PPP solutions shows behaviour consistent with that of the PPK solutions (cf. Figures 3.23 and 3.24), although the noisier PPP data led to larger differences between the filtered PPP and TG series. In Figure 3.24, it can be clearly seen that the impact of the noisier PPP data again led to larger PPP-TG difference values (for both the maximum and standard deviation of the differences between filtered PPP and TG data) as compared to the PPK solution (cf. Figure 3.23).

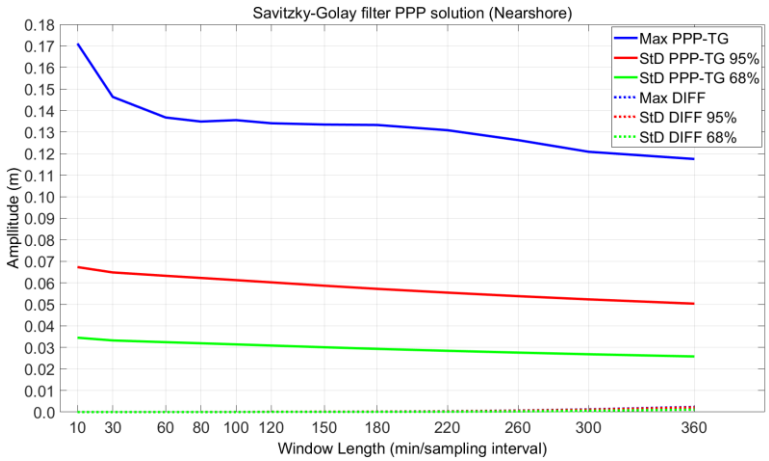

Figure 3.24: Performance of the Savitzky–Golay filter for PPP nearshore in relation to various window lengths used. Differences between the filtered GNSS-derived water level heights (PPP) and tide gauge observation (TG) time series are denoted by PPP-TG and are shown by solid lines. Damping effects as manifested by differences in the reconstructed tide signals are shown by dotted lines and denoted by DIFF. The standard deviations of differences (StD DIFF) are shown for 68% and 95% confidence levels

3.7.3 Gaussian filter

In this study, one-dimensional Gaussian filtering was used to represent water level heights, using the Gaussian function. It is parameterised by its mean and variance (Kopparapu & Satish, 2011).

In the frequency domain, the Gaussian filter $G(\omega)$ is given by:

$$G(\omega) = \exp\left(\frac{-\omega^2\,\sigma_f^2}{2}\right) \tag{3.15}$$

where ω is the water level height time series, and σ_f^2 is the variance based on the noise affecting the signal. The properties of the Gaussian filter can be illustrated for the signal X contaminated by added white Gaussian noise (AWGN) N as given by

$$X_N\,(\omega) = X\,(\omega) + N\,(\omega) \tag{3.16}$$

The estimate of the signal $\hat{X}_N(\omega)$ after filtering by the Gaussian filter is obtained as:

$$\hat{X}_N(\omega) = X(\omega)G(\omega) + N(\omega)G(\omega) \tag{3.17}$$

And the error in the filtered output, denoted as E(ω), is given by

$$\begin{aligned} E(\omega) &= X(\omega) - \hat{X}_N(\omega) \\ &= X(\omega)\,[1 - \mathrm{G}(\omega)] + N(\omega)G(\omega) \end{aligned} \tag{3.18}$$

As seen in Equation (3.18), the error in the filtered output ($E(\omega)$) due to filtering has two components: one due to distortion of the signal $X(\omega)$ [1− G(ω)], and the second due to the residual noise $N(\omega)G(\omega)$ in the signal filtering. Let *P* denote the power in the signal, then input and output signal to noise (*S*) ratios are given by:

$$\begin{aligned} S_i &= \frac{P_X}{P_N} \\ S_o &= \frac{P_X}{P_X - P_{\hat{X}}} = \frac{P_X}{P_E} \end{aligned} \tag{3.19}$$

Similar to the above presentation of the moving average and Savitzky–Golay filters, the amplitudes of the M2, S2, K1 and O1 extracted from the filtered PPK, PPP and TG time series and their differences from those extracted from the PPK, PPP and TG time series are listed in Table 3.5 using the Gaussian filter. Examining the difference between the extracted amplitudes from the unfiltered and filtered PPK, PPP and TG time series (lower value in each row of Table 3.5), the Gaussian filter shows increased damping of low-frequency tidal harmonic constituents when the window length is increased. The numerical results for the Gaussian filter show that the damping effects for the PPK, PPP and TG time series are between 15% and 17% for the M2 and S2 tidal constituents and about 4% for the K1 and O1 tidal harmonic constituents for a maximum window length of 360 minutes.

Table 3.5: Performances of Gaussian filter to extract the amplitudes of the major tidal harmonic constituents (M2, S2, K1, O1) from the filtered PPK, PPP and TG time series in relation to the window lengths (WL). In each row, the upper value is the extracted amplitude after applying the filter; the lower value is the difference between the amplitudes extracted from the original PPK, PPP and TG time series (see Table 3.2) and the filtering time series

	Amplitudes (m) / Residuals (m)											
	PPK				**PPP**				**TG**			
WL	**M2**	**S2**	**K1**	**O1**	**M2**	**S2**	**K1**	**O1**	**M2**	**S2**	**K1**	**O1**
10	0.056	0.054	0.118	0.115	0.057	0.060	0.112	0.105	0.056	0.053	0.116	0.113
	0.000	0.000	0.000	0.000	0.000	0.000	0.001	0.000	0.000	0.000	0.000	0.000
30	0.056	0.054	0.118	0.115	0.056	0.059	0.111	0.105	0.056	0.053	0.116	0.113
	0.000	0.000	0.000	0.000	0.001	0.001	0.001	0.000	0.001	0.001	0.000	0.000
60	0.055	0.054	0.118	0.115	0.056	0.059	0.111	0.105	0.056	0.052	0.116	0.112
	0.000	0.000	0.000	0.000	0.001	0.001	0.001	0.000	0.001	0.001	0.000	0.000
80	0.055	0.053	0.118	0.115	0.056	0.059	0.111	0.105	0.056	0.052	0.116	0.112
	0.000	0.000	0.000	0.000	0.001	0.001	0.001	0.000	0.002	0.001	0.000	0.000
100	0.055	0.053	0.118	0.114	0.056	0.059	0.111	0.105	0.056	0.052	0.116	0.112
	0.001	0.001	0.000	0.000	0.001	0.001	0.001	0.000	0.001	0.001	0.000	0.000
120	0.055	0.053	0.118	0.114	0.056	0.058	0.111	0.105	0.055	0.052	0.116	0.112
	0.001	0.001	0.001	0.001	0.001	0.002	0.001	0.001	0.001	0.001	0.001	0.001
150	0.054	0.052	0.117	0.114	0.055	0.058	0.111	0.105	0.055	0.051	0.116	0.112
	0.002	0.002	0.001	0.001	0.002	0.002	0.001	0.001	0.002	0.002	0.001	0.001
180	0.053	0.051	0.117	0.114	0.054	0.057	0.110	0.104	0.054	0.050	0.115	0.111
	0.002	0.002	0.001	0.001	0.003	0.003	0.002	0.001	0.002	0.002	0.001	0.001
220	0.052	0.050	0.116	0.113	0.053	0.056	0.110	0.104	0.053	0.049	0.115	0.111
	0.003	0.003	0.002	0.002	0.004	0.004	0.002	0.002	0.003	0.003	0.002	0.002
260	0.051	0.049	0.115	0.112	0.052	0.054	0.109	0.103	0.052	0.048	0.114	0.110
	0.005	0.005	0.003	0.002	0.005	0.006	0.003	0.002	0.005	0.005	0.003	0.002
300	0.050	0.048	0.115	0.112	0.051	0.053	0.108	0.102	0.050	0.047	0.113	0.109
	0.006	0.006	0.003	0.003	0.006	0.007	0.004	0.003	0.006	0.006	0.003	0.003
360	0.047	0.045	0.113	0.110	0.048	0.050	0.107	0.101	0.048	0.044	0.111	0.108
	0.009	0.009	0.005	0.005	0.009	0.010	0.005	0.004	0.009	0.009	0.005	0.005

Similar to the previous filters, Figures 3.25a and 3.26a show the frequency spectra of the unfiltered PPK and PPP time series, respectively, which again clearly depict the four major tidal harmonic constituents (M2, S2 K1, and O1). After applying the Gaussian filter for a 100-minute window length, the frequency spectra of the smoothed PPK and PPP time series are shown in Figures 3.25b and 3.26b, respectively. Figures 3.25c and 3.26c show the frequency spectra of the differences between the filtered and unfiltered PPK and PPP time series, where the dampening effect can again be seen as residual magnitudes between unfiltered and filtered signals for the M2, S2, K1 and O1 tidal constituents. Like for the moving average filter, the damping is explained by the frequency response of the filter as explained in section 3.7.1.

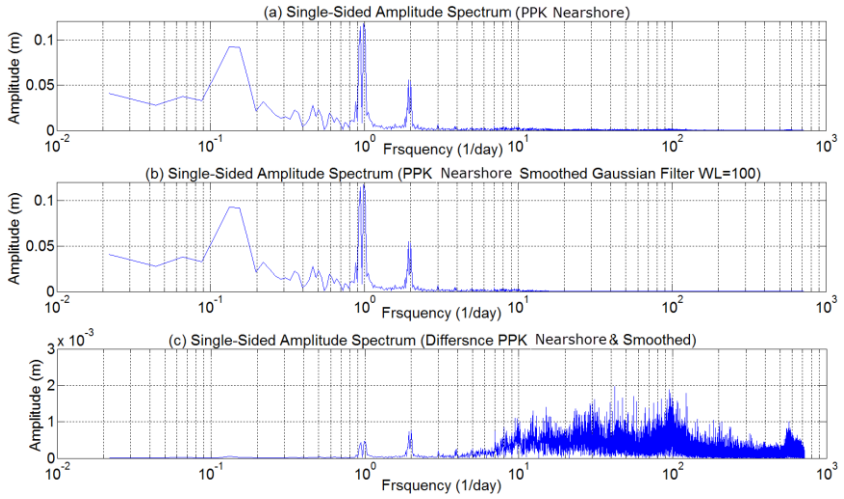

Figure 3.25: Single-sided frequency spectra of the Gaussian filter for PPK nearshore. (a) the unfiltered GNSS-derived water level height signal (PPK); (b) the GNSS-derived water level height (PPK) signal smoothed by the Gaussian filter with a 100-minute window length; and (c) the differences between the filtered and unfiltered GNSS-derived water level height signal

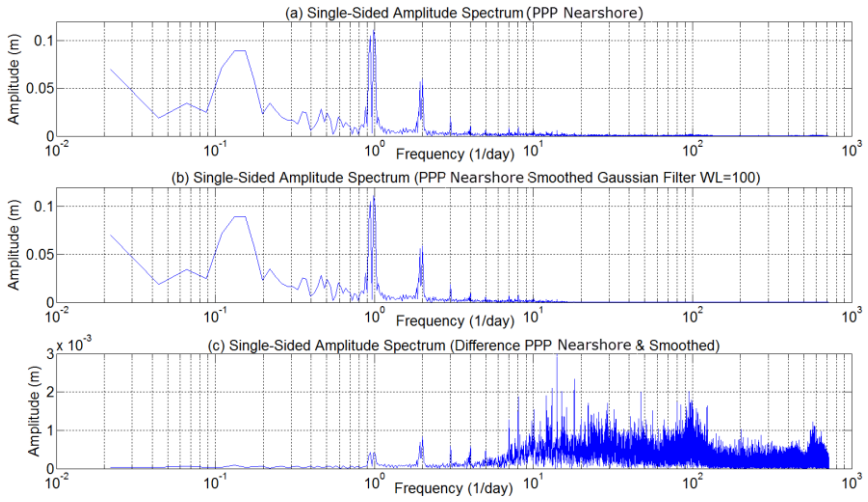

Figure 3.26: Single-sided frequency spectra of the Gaussian filter for PPP nearshore. (a) the unfiltered GNSS-derived water level height signal (PPP); (b) the GNSS-derived water level height (PPP) signal smoothed by the Gaussian filter with a 100-minute window length; and (c) the differences between the filtered and unfiltered GNSS-derived water level height signal

Figures 3.27 and 3.28 show the results when applying the Gaussian filter to the PPK, PPP and TG time series. Again the standard deviation of the differences between the unfiltered and filtered PPK and TG time series (at 68% and 95% confidence level) and the maximum differences decreased with increased window length, confirming

previous findings that a large part of the differences was due to higher-frequency variations. For a maximum window length of 360 minutes, the standard deviations (at 68% and 95% confidence level) and maximum differences for the PPK-TG were 1 cm, 1.9 cm and 2.5 cm, respectively. Further, it can be clearly seen that the damping effect was considerably smaller than for the moving average filter but considerably larger than for the Savitzky–Golay filter. Again, these values are very similar for the PPK and PPP time series, regardless of the noise level in the data.

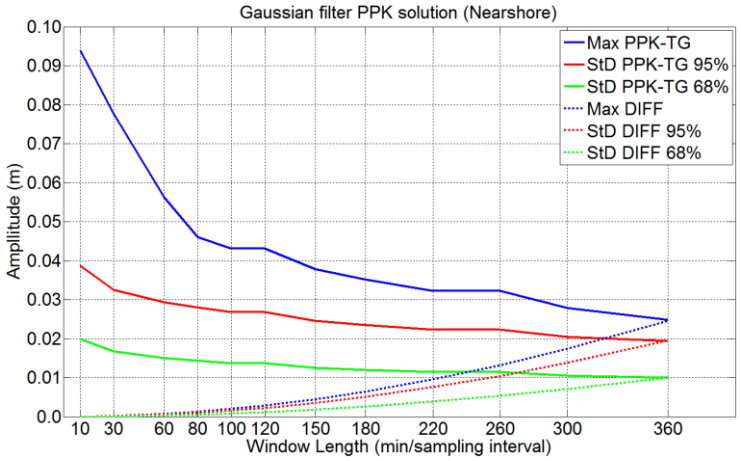

Figure 3.27: Performance of the Gaussian filter for PPK nearshore in relation to various window lengths. Differences between the filtered GNSS-derived water level heights (PPK) and tide gauge observation (TG) time series are denoted by PPK-TG and are shown by solid lines. Damping effects as manifested by differences in the reconstructed tide signals are shown by dotted lines and denoted by DIFF. The standard deviations of differences (StD DIFF) are given at 68% and 95% confidence levels

In Figure 3.28, as expected the noisier PPP data using the Gaussian filter led to larger differences between the PPP and TG time series than for PPK-TG (Figure 3.27), while the damping effect was effectively the same as PPK. For the maximum window length of 360 minutes, the maximum difference of PPP-TG is 9.5 cm and the standard deviations of the differences for a 68% and 95% confidence level are 2.2 cm and 4.3 cm respectively, while the respective values for the damping effect of PPP are 2.5 cm for the maximum difference and 1 cm and 2 cm for the standard deviations at 68% and 95% confidence levels, respectively.

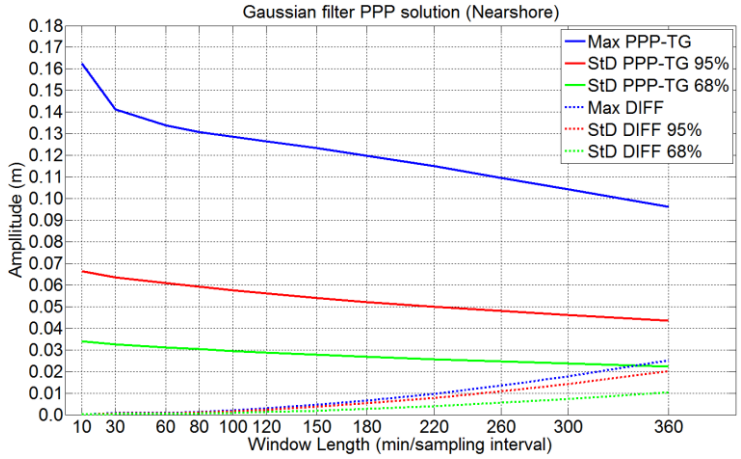

Figure 3.28: Performance of the Gaussian filter for PPP nearshore in relation to various window lengths. Differences between the filtered GNSS-derived water level heights (PPP) and tide gauge observation (TG) time series are denoted by PPP-TG and are shown by solid lines. Damping effects as manifested by differences in the reconstructed tide signals are shown by dotted lines and denoted by DIFF. The standard deviations of differences (StD DIFF) are given at 68% and 95% confidence levels

3.7.4 Butterworth filter

The Butterworth filter is maximally flat in the passband and produces virtually no distortion of the low-frequency signal component (Roberts & Roberts, 1978). The filter has a maximally flat response in the passband and rolls off towards zero in the stopband (Podder, Hasan, Islam, & Sayeed, 2014).

The general equation for a Butterworth filter's amplitude response is

$$H(\omega) = \frac{1}{1 + \left(\frac{\omega}{\omega_c}\right)^{2N}} \tag{3.20}$$

where ω_c is the cut-off frequency, and N is the number of order of the filter. The frequency response magnitude is monotonically decreasing, with $H(\omega) = 1$ at $\omega = 0$ and $H(\omega) = 0$ at Nyquist frequency $\omega = \pi$. At the cut-off frequency ω_c, the gain is $H(\omega) = 1/\sqrt{2}$. Increasing filter order N results in a steeper transition from passband to stopband.

Table 3.6 lists the results of M2, S2, K1 and O1 amplitude after applying Butterworth filtering with the residuals between the original time series and the filtered time series

in the PPK, PPP and TG records. The filtered PPK, PPP and TG amplitudes of each constituent decrease as the window length increases; therefore the residual increases, where the TG and PPP are 34% and 36% of the low frequency of the M2 and S2 tidal constituents, and 10% and 9% of S2 and O1 respectively for the longest window length of 360 minutes.

Table 3.6: Performances of Butterworth filter to extract the amplitudes of the major tidal harmonic constituents (M2, S2, K1, and O1) from the filtered PPK, PPP and TG time series in relation to the window lengths (WL). In each row, the upper value is the extracted amplitude after applying the filter, and the lower value is the difference between the amplitudes extracted from the original PPK, PPP and TG time series (Table 3.2) and the filtering time series

	Filtered (m) / Residual (m)											
	PPK				**PPP**				**TG**			
WL	**M2**	**S2**	**K1**	**O1**	**M2**	**S2**	**K1**	**O1**	**M2**	**S2**	**K1**	**O1**
10	0.056	0.054	0.118	0.115	0.057	0.053	0.116	0.113	0.056	0.053	0.116	0.113
	0.000	0.000	0.000	0.000	0.000	0.000	0.000	0.000	0.000	0.000	0.000	0.000
30	0.055	0.054	0.118	0.115	0.057	0.053	0.116	0.113	0.056	0.053	0.116	0.113
	0.000	0.000	0.000	0.000	0.000	0.000	0.000	0.000	0.000	0.000	0.000	0.000
60	0.055	0.053	0.118	0.115	0.056	0.052	0.116	0.112	0.056	0.052	0.116	0.112
	0.001	0.001	0.000	0.000	0.001	0.001	0.000	0.000	0.001	0.001	0.000	0.000
80	0.055	0.053	0.117	0.114	0.056	0.052	0.116	0.112	0.055	0.052	0.116	0.112
	0.001	0.001	0.001	0.001	0.001	0.001	0.001	0.001	0.001	0.001	0.001	0.001
100	0.054	0.052	0.117	0.114	0.055	0.051	0.116	0.112	0.055	0.051	0.116	0.112
	0.002	0.002	0.001	0.001	0.002	0.002	0.001	0.001	0.002	0.002	0.001	0.001
120	0.053	0.051	0.117	0.114	0.054	0.050	0.115	0.111	0.054	0.050	0.115	0.111
	0.002	0.002	0.001	0.001	0.002	0.003	0.001	0.001	0.002	0.002	0.001	0.001
150	0.052	0.050	0.116	0.113	0.053	0.049	0.114	0.111	0.053	0.049	0.114	0.111
	0.004	0.004	0.002	0.002	0.004	0.004	0.002	0.002	0.004	0.004	0.002	0.002
180	0.050	0.048	0.115	0.112	0.051	0.047	0.113	0.110	0.051	0.047	0.113	0.110
	0.005	0.005	0.003	0.003	0.005	0.006	0.003	0.002	0.005	0.005	0.003	0.003
220	0.048	0.046	0.114	0.111	0.049	0.045	0.112	0.109	0.049	0.045	0.112	0.109
	0.008	0.008	0.004	0.004	0.008	0.009	0.004	0.003	0.008	0.008	0.004	0.004
260	0.045	0.043	0.112	0.109	0.046	0.042	0.110	0.107	0.046	0.042	0.110	0.107
	0.011	0.011	0.006	0.005	0.011	0.012	0.006	0.005	0.011	0.011	0.005	0.005
300	0.042	0.040	0.110	0.108	0.043	0.039	0.108	0.106	0.042	0.039	0.108	0.106
	0.014	0.014	0.008	0.007	0.014	0.016	0.008	0.007	0.014	0.014	0.007	0.007
360	0.036	0.034	0.106	0.105	0.037	0.034	0.105	0.108	0.037	0.034	0.105	0.108
	0.019	0.020	0.012	0.010	0.019	0.022	0.011	0.009	0.019	0.019	0.005	0.005

Figures 3.29a and 3.30a show the unfiltered GNSS-derived water level heights for PPK and PPP. Again the residual magnitudes corresponding to the dampening effect of the semi-diurnal and diurnal tidal constituents is clearly visible with similar magnitudes as for the moving average filter (cf. section 3.7.1). Figures 3.29b and 3.30b show the smoothed GNSS-derived level heights for PPK and PPP after applying the Butterworth filter. It is evident that the high-frequency signals have been filtered out and the low-frequency signals have been retained with residual magnitudes for the diurnal and semi-diurnal tidal constituents clearly visible in Figures 3.29c and 3.30c.

Again, the residuals express the difference in magnitude between unfiltered and filtered signals showing the dampening effect for diurnal and semi-diurnal tidal constituents.

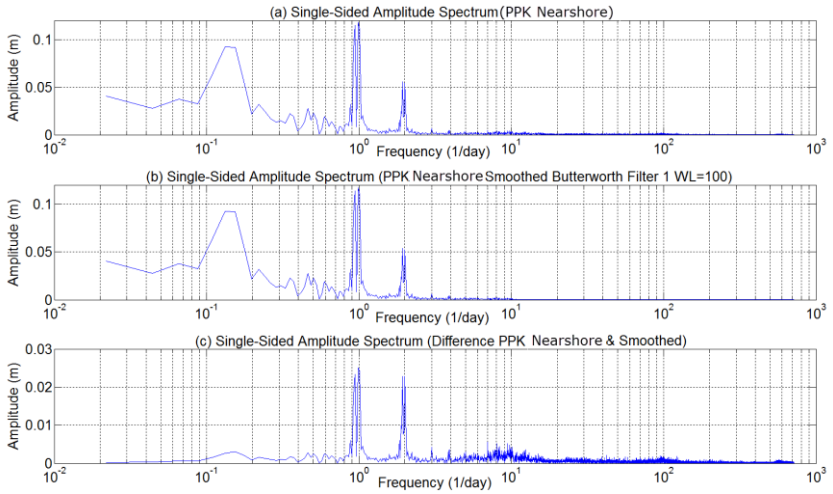

Figure 3.29: Single-sided frequency spectra of the Butterworth filter for PPK nearshore. Single-sided frequency spectra for (a) the unfiltered GNSS-derived water level height signal (PPK); (b) the GNSS-derived water level height (PPK) signal smoothed by the Butterworth filter with a 100-minute over 30 days window length; and (c) the differences between filtered and unfiltered GNSS-derived water level height signal

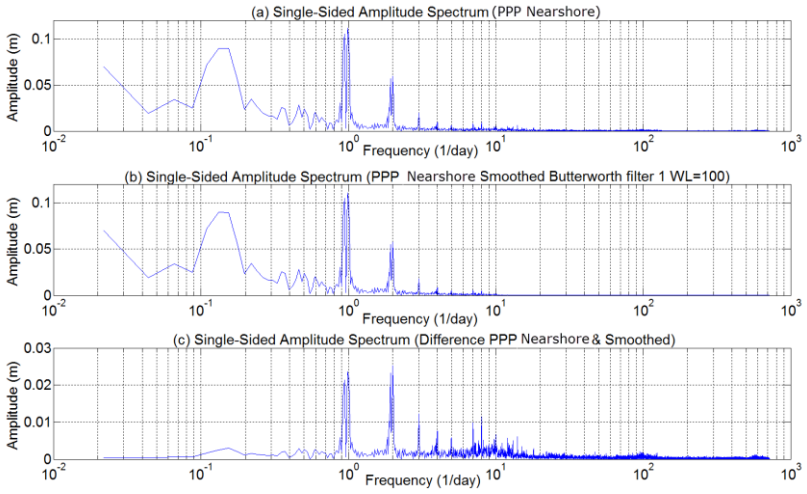

Figure 3.30: Single-sided frequency spectra of the Butterworth filter for PPP nearshore. Single-sided frequency spectra for (a) the unfiltered GNSS-derived water level height signal (PPP); (b) the GNSS-derived water level height (PPP) signal smoothed by the Butterworth filter with a 100 minute over 30 days window length; and (c) the differences between the filtered and unfiltered GNSS-derived water level height signal

The Butterworth filter results were quite similar to those of the moving average filter for the differences between PPK-TG and PPP-TG, when comparing the values of the standard deviations of the differences at the 68% and 95% confidence levels and the maximum differences. The respective values for the longest window length of 360 minutes for PPK-TG are 2.2 cm, 4.4 cm and 5.6 cm, while the corresponding values obtained for the moving average filter are 2.3 cm, 4.6 cm and 6 cm. In the case of PPP-TG the respective values are 2.2 cm, 4.5 cm and 5.6 cm for the Butterworth filter and 2.5 cm, 4.9 cm and 6.1 cm for the moving average filter.

For the PPK and PPP time series the application of the Butterworth filter confirms that the differences PPP-TG were considerably larger than for PPK-TG, demonstrating the impact of the noisier PPP data. Again, the damping effect was very similar for both the PPK and PPP time series, and is somewhat independent of the noise level of the data (see Figures 3.31 and 3.32).

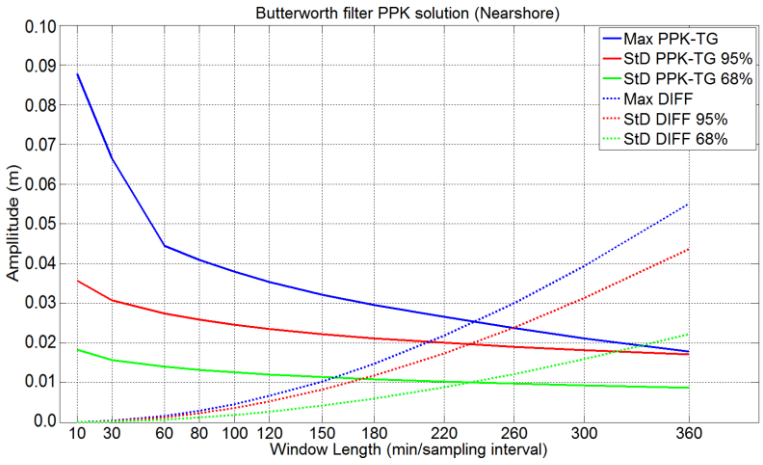

Figure 3.31: Performance of the Butterworth filter for PPK nearshore in relation to various window lengths. Differences between the filtered GNSS-derived water level heights (PPK) and tide gauge observation (TG) time series are denoted by PPK-TG and are shown by solid lines. Damping effects as manifested by differences in the reconstructed tide signals are shown by dotted lines and denoted by DIFF. The standard deviations of differences (StD DIFF) are given at the 68% and 95% confidence levels

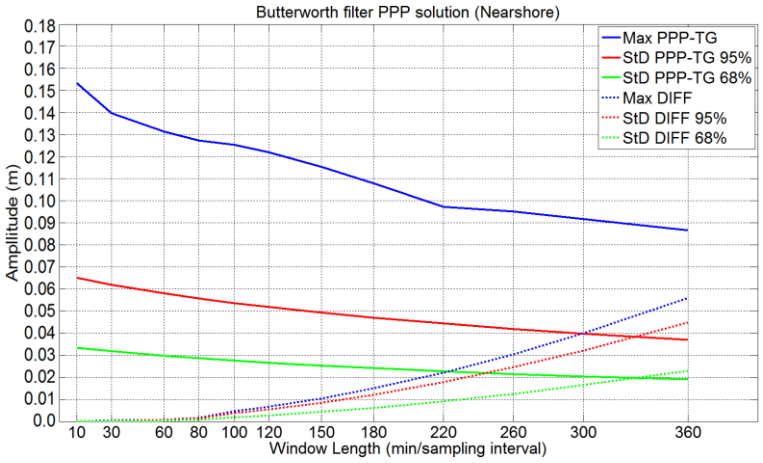

Figure 3.32: Performance of the Butterworth filter for PPP nearshore in relation to various window lengths. Differences between the filtered GNSS-derived water level heights (PPP) and tide gauge observation (TG) time series are denoted by PPP-TG and are shown by solid lines. Damping effects as manifested by differences in the reconstructed tide signals are shown by dotted lines and denoted by DIFF. The standard deviations of differences (StD DIFF) are given at the 68% and 95% confidence levels

3.8 Comparison of the performance of the filtering techniques and their capability in meeting IHO standards

The International Hydrographic Organization (IHO), states in its standard on positioning requirements (Special Publication 44: IHO, 2008) that the tide measured at a tide gauge in the immediate vicinity of the survey area must have a standard deviation not greater than ± 5 cm at the 95% confidence level. This level of positioning is commensurate with IHO Special Order Surveys for tidal analysis and for the determination of a vertical datum. For other orders, ± 10 cm at 95% confidence level should not be exceeded (cf. Section 2.5).

The presented filtering methods are used to eliminate high-frequency signals while maintaining the lower frequency tidal signal. Their damping effect has to be considered in reaching the accuracies noted above. This section assesses the suitability of the four types of filtering methods considered here (moving average, Savitzy–Golay, Gaussian and Butterworth) to extract the tide signal from GNSS-derived water level height observations.

All of these filters were shown to be capable of extracting low-frequency tide variations and suppress high-frequency signals. Considering the damping effect, the

Savitzy–Golay filter was found to better preserve the low-frequency tidal harmonic constituents with almost negligible damping effects (a few millimetres only) as demonstrated by the standard deviation of the differences between the reconstructed unfiltered and filtered tide signals for both the PPK and PPP time series for a reasonably long window length of 360 minutes. Therefore, consideration of damping effects for the Savitzy–Golay filter can be neglected, at least for window lengths of up to 360 minutes, when quantifying an error budget for GNSS-derived tide signals. The Gaussian filter demonstrated increased smoothing that led to increase damping of the low-frequency tidal harmonic constituents. However, the effect of damping as expressed by the standard deviation of the differences between the reconstructed unfiltered and filtered tide signals remained well below the 5 cm level (95% confidence level), which meets current IHO standards for a Special Order Survey using either the PPK or the PPP methods if the damping effect is considered the only error source. In terms of the damping effect, the moving average and Butterworth filters showed similar effects for both the PPK and PPP time series. Both filters showed much stronger smoothing of low-frequency tidal harmonic constituents than the Savitzky–Golay and Gaussian filters, though their maximum damping effects remained still below ± 10 cm for a window length of 360 minutes. Therefore, for a long window length, use of these filters does not meet IHO standards for Special Order Surveys but they do meet the standards for other surveys that specify an accuracy of ± 10 cm if the damping effect is considered the only error source.

Considering the agreement between tidal signals extracted from GNSS-derived water level heights and tide gauge observations, the standard deviation of the differences decreases when increasing window lengths. The difference between PPK and TG, signals for all window lengths, including unfiltered signals, give standard deviations of less than ± 5 cm at 95% confidence level, thus meeting IHO standards for Special Order Surveys. However, for the PPP-TG differences, the standard deviations are larger than ± 5 cm for small window lengths but fall below ±5 cm for longer window lengths. Therefore, the PPP solutions would still meet IHO standards for Special Order Surveys with increased smoothing by the moving average, Gaussian and Butterworth filters, but not for the Savitzky–Golay filter for which the standard deviation remained above ± 5 cm for the maximum window length of 360 minutes. However, all filters would satisfy IHO standards for other surveys requiring an accuracy of ± 10 cm.

In summary, both effects need to be considered when forming an error budget model. Taking their respective standard deviations as a quality measure of the filtering methods that were tested, a combined standard deviation can be built from:

$$\sigma_{filter} = \sqrt{\sigma_{GNSS-TG}^2 + \sigma_{damp}^2} \tag{3.21}$$

As $\sigma_{GMSS-TG}$ and σ_{damp} behave in an opposite manner, the combined effect (σ_{filt}) has to be considered in order to find acceptable performance of the filter type and window length. The standard deviation of the difference between GNSS (using PPK and PPP) and TG $\sigma_{GNSS-TG}$ indicate corresponding amplitudes of the differences between the filtered GNSS signal and TG, whereas σ_{damp} is the damping effect as manifested by the differences in the reconstructed tide signals. The focus in this study is the standard deviation at 95% confidence level to achieve a total measurement error for tidal height that meets IHO standards. From Equation (3.21) can be estimated the optimum window length for each filter. When the $\sigma_{GNSS-TG}$ and σ_{damp} are intersected, that means the combined standard deviation (cf. Equation 3.21) will be at a minimum. Thus, the window length corresponding to the intersection can be considered as an optimum window length for which the low-frequency tidal signals are retained and the high-frequency signals are filtered out and the effect introduced by the filter will be at a minimum.

For the moving average filter, the optimum window length is around 220 minutes for PPK and 315 minutes for PPP resulting in a combined filter effect (cf. Equation 3.21) of ±3.2 cm and ±5.6 cm, respectively. Using the Savitzky–Golay filter for PPK and PPP, $\sigma_{GNSS-TG}$ does not intersect σ_{damp} up until the longest window length considered. In absence of an intersection, in this study the minimum combined effect (cf. Equation 3.21) of the Savitzky–Golay filter is given for the longest window length by ±2.3 cm and ±5 cm, respectively for PPK and PPP. For the Gaussian filter the optimum window length is 360 minutes for PPK and the same behaviour as for the Savitzky–Golay filter for PPP (e.g. no intersection). Again, in this study the minimum combined effect (cf. Equation 3.21) of the Gaussian filter is given for the longest window length by ±2.8 cm and ±4.8 cm, respectively for PPK and PPP. Finally, for the optimum window length for the Butterworth filter was obtained by 235 minutes

for PPK and 330 minutes for PPP resulting in a combined filter effect of ±3.2 cm and ±6.1 cm, respectively.

3.9 Chapter summary

This chapter described the process used to extract tidal height signals from GNSS-derived water level height observations in nearshore sheltered areas. The study area was a pontoon in a controlled environment where no vessels were moored and the effects of sea swell and vessel motion were largely reduced. The tide observations of a SeaFreame tide gauge station in the study area were used as a reference for the GNSS-derived water level heights. Since data was collected prior to conducting this study, two post-processing GNSS-positioning techniques, the PPK and PPP were used to process GNSS height data. The PPK mode used an IGS station at Curtin University located approximately 25 km away as reference station; PPP was processed in a kinematic mode using the CSRS-PPP service.

To compare GNSS-derived water level heights with traditional tide gauge records, they should be reduced to a common datum. GNSS-derived water level heights are computed as ellipsoidal heights relative to the WGS84 ellipsoid. Tide gauge heights are measured relative to the chart datum used at Hillarys Boat Harbour. In this study, the Australian Height Datum (AHD) was used as the common reference datum for the heights obtained both from GNSS and tide gauge observations. In order to validate the accuracy levels of the PPK and PPP positioning techniques, they were applied relative to a static base line approximately the same length as the distance between the harbour and the reference station. The data was processed in kinematic mode in exactly the same way as the GNSS-derived water level observations. The additional noise due to the dynamic environment was characterized as $\sigma_{dyn,PPK}$ = 1.9 cm for PPK and $\sigma_{dyn,PPP}$ = 2 cm for PPP. When comparing these values to the precision values obtaiened for both position techniques it can be seen that the precision for both PPK and PPP is mostly dominated by the added noise due to the dynamic environment. The respective values are σ_{PPK} = 2.2 cm vs. $\sigma_{dyn,PPK}$ = 1.9 cm for PPK and σ_{PPP} = 3.1 cm vs. $\sigma_{dyn,PPP}$ = 2 cm for PPP.

The comparison between GNSS-derived water level heights based on PPK and PPP and tide gauge heights agreed closely with the diurnal tide, with small biases noticed between the datasets. Spectral analysis based on the Fourier transform was used to

compute the amplitude and phase of four major tidal harmonic constituents, representing the combination of lunar and solar tides. The phase values were calculated for each constituent in all filtering processes, and it was found that there was no impact from the filtering techniques on the original phase values; and therefore, only the tidal amplitudes for each filter was the focus.

The four different types of low-pass filters used in this study, namely the moving average, Savitzy–Golay, Gaussian and Butterworth filters were described. To assess the filter performance for a range of window lengths, the amplitudes and phases of the four major tidal harmonic constituents (M2, S2, K1 and O1) were determined and compared to the unfiltered tide information obtained by GNSS using PPK and PPP and the tide gauge. The results indicated that all filters were able to extract low-frequency tide variations and filter out high-frequency signals. The Savitzy–Golay filter was found to best retain the low-frequency tidal harmonic constituents in the PPK solution with a damping effect of only a few millimetres for the longest window length of 360 minutes. For the Gaussian filter the maximum dampening effect for the longest window length of 360 minutes was 2.5 cm for PPK. For the Butterworth and moving average filters the maximum dampening effect for the longest window length of 360 minutes was considerably higher and reached values of 5.5 cm and 6 cm for PPK. Overall, all filters would meet current IHO standards for Special Order Surveys when the dampening effect is considered the only error source. Considering PPP the dampening effects were slightly higher than for PPK reaching maximum values for the longest window length of 360 minutes of a few millimetres cm for the Savitzy–Golay filter and 2.5 cm, 5.6 cm and 6.2 cm for the Gaussian, Butterworth and moving average filters, respectively.

As a general result, the study shows that GNSS height measurement can replace tide gauge observations and provide tide information with sufficiently high accuracy to meet IHO standards for any survey order and a special order survey for most scenarios considered using both PPK and PPP methods.

The next chapter discusses the measurement of tide heights from GNSS height observations taken from a survey vessel in an offshore area. The GNSS data will be processed using the NRCan Canada Spatial Reference System (CSRS) Precise Point Positioning (PPP) service. To investigate the accuracy of the PPP height measurement

technique offshore, PPP will be compared with the PPP solution in sheltered coastal waters area. In addition, the offshore data will be used in conjunction with all the filters in the same manner as the sheltered coastal waters data to produce filtered tidal signals.

Chapter 4:

Offshore GNSS-derived Water Level Heights

4.1 Introduction

This chapter focuses on the analysis of GNSS-derived water level heights observed from a survey vessel in an offshore environment. The survey site is located in the Indian Ocean approximately 2700 km from the Western Australian coast. Due to the long distance from shore, the use of reference stations in a relative-baseline approach (e.g. PPK) was not considered. Hence, only the PPP method was implemented to obtain water level height estimates from GNSS observations. PPP does not require a local base station, but rather it uses precise satellite orbits and clock estimates such as those provided by the International GNSS Service (IGS) (http://www.igs.org/) or in real time by IGS-RTS (http://www.igs.org/rts).

The main aim of this chapter is to: (1) assess the accuracy and variability of GNSS-PPP water level height estimates in an offshore environment; (2) assess the ability to extract water level/tide information from the GNSS-PPP water level heights using filtering techniques in this environment; and (3) compare statistical results for GNSS-PPP water level heights estimated offshore with those from the nearshore experiment described in Chapter 3 to demonstrate the benefits of using GNSS for offshore applications.

The chapter starts with a discussion of the challenges in the offshore environment compared with onshore surveys and estimates the extent to which the dynamic

environment affects GNSS-PPP water level height estimation and extraction of tide information. The dynamic environment of a survey vessel is affected by ‘non-tidal’ processes such as surface wave activity and the attitude of the vessel (roll, pitch, heave and dynamic draft) during GNSS height observations. As in Chapter 3, this chapter also addresses the filtering techniques that are available to extract low-frequency tide variations and suppress high-frequency noise. It also studies the effect of damping on the four major tidal harmonic constituents.

This chapter compares the effectiveness of GNSS-PPP water level height measurement in nearshore and offshore environments. Particular focus is on the precision of PPP solutions and the variability added to the GNSS-PPP water level heights due to the more dynamic character of the offshore environment. In addition, the obtained results are compared and discussed in relation to IHO standards.

4.2 Possible vertical positioning uncertainty in the offshore environment

Vertical uncertainty refers here to the uncertainty in GNSS-PPP water level height determined when mounting the GNSS antenna on a survey vessel. All causes were investigated: tides, draft, roll, pitch and heave of the vessel. ‘Uncertainty propagation’ is the combined effects of measurement uncertainties from several sources with the uncertainties in the derivation or calculation of parameters (Beaudoin et al., 2009; Calder 2006, 2013; Schmitt et al., 2008). With focus on the vertical, sources of uncertainty in horizontal positioning and heading (Hare et al., 2011) are not relevant to this study. For the determination of the total vertical uncertainty (TVU), all contributing measurement uncertainties, both random and systematic, were included in the propagated error budget.

Vertical uncertainty is to be understood as the uncertainty of the reduced water level height. All uncertainties should be combined statistically to obtain a TVU (IHO, 2008). The measurement uncertainties propagate directly into the GNSS-derived water level height; these include the uncertainty in the GNSS vertical position of the antenna phase centre; the measurement of the three-dimensional offsets between the phase centre and the reference point of the vessel (RP), taking into account the effects of vessel motion; and uncertainty related to the geoid model, which is usually provided with an imprecise estimate. Contributing factors to the vertical uncertainty include:

- GNSS-positioning related factors (e.g., observation quality, positioning technique, processing algorithm, orbit, clock, ionospheric, tropospheric, and multipath).
- Vertical change of the RP due to the movements of the vessel (roll, pitch, heave) and GNSS antenna measurements.
- Ellipsoidal/vertical datum separation (uncertainty related to the geoid model) if a transfer from ellipsoidal heights to geoid-based height system is required.

Apart from identifying outliers during GNSS-PPP processing, filter techniques may also be used to reduce observation noise and, to some extent, reduce the impact of large errors, depending on their magnitude. The effect of uncertainties in the PPP solution and those due to high-frequency water level variations, combined with the values obtained from the static setup, underlines the uncertainties in the final water level height. The main observation or conclusion is that for the nearshore experiment, the high-frequency variability in the GNSS-estimated water level heights is due to both processing and variations in water level, while in the offshore environment the high-frequency variability is mostly due to water movement.

The offset of the GNSS antenna, roll, pitch and heave of the vessel, and the WL were measured with respect to the vessel's RP. The GNSS antenna was measured from the antenna phase centre to the RP of the vessel as *x*, *y*, *z* coordinates (x = –2.74 m, y = 5.40 m, z = 20.45 m). All heave, roll, pitch, and heading values obtained from motion sensors on-board of the vessel were applied relative to the RP in real time during the survey. Heave was recorded in real time by the motion sensors, then corrected to GNSS heights during the data analysis. The distance between WL and RP (5.33 m) was not applied during the merge process, but it was applied when the vessel was at anchor.

The separation (SEP) between the reference surface used for the GNSS height (e.g. reference ellipsoid) and the chart datum changed spatially. Water level measurements are still required to establish the chart datum over the survey area. In absence of a chart datum in the offshore environment, in this study the geoid (approx. MSL) was used as the chart datum. A model is then needed to correct the ellipsoidal height values to the chart datum. The Earth Gravitational Model 2008 (EGM2008) was used in this study to convert the GNSS-based ellipsoidal heights to geoid-based orthometric heights.

Figure 2.9 in Chapter 2 shows the relationship between the reference ellipsoid, the survey vessel, and MSL. The GNSS antenna height refers to its distance from the waterline (WL), considering all heave, roll, pitch and dynamic draft of the vessel. The GNSS height determination at the antenna is referenced to the vessel RP. Combining these provides a direct measurement from the ellipsoid to the antenna, then to the RP.

4.3 Impact of vertical motions on water level heights

Correcting the GNSS-derived water level height for the effect of the superimposed vessel motion is perhaps the most difficult aspect of hydrographic surveying, since all conditions may occur simultaneously or over different time periods. The height of the ellipsoid obtained from the shipborne GNSS antenna must be corrected for all motions of the platform. In the following sections the effects of roll, pitch, heave and squat on the ellipsoidal height are described in more detail.

4.3.1 Roll and pitch effect

In this study, the vessel's motion caused by wave action (roll, pitch and heave) was measured by on-board motion sensors. Respective corrections are defined as changes of the height above the RP (neglecting deflections from the vertical). The corrected height above the RP, H_{corr}, including the combined effect from roll, pitch and heave, are given by (De Loach, 1996):

$$H_{corr} = h_{GNSS} - (z_0 - z_{rot}) - \delta d_i \tag{4.1}$$

where H_{corr} is the GNSS antenna height after correction for pitch, roll and heave; h_{GNSS} is the uncorrected GNSS antenna height (here the height above chart datum) from the GNSS positioning solution; z_0 is the GNSS antenna height in the vessel's body frame; z_{rot} is the GNSS antenna height in the vessel's body frame after correction for rotation due to pitch and roll as shown in Figure 4.1; and δd_i is the heave. The heave correction is a simple vertical translation of the GNSS antenna; more details are given in the next section.

The impact of roll and pitch is combined in z_{rot}, which is derived from the Δ_{roll} and Δ_{pitch} rotation matrices as follows:

$$\begin{bmatrix} x \\ y \\ z \end{bmatrix}_{rot} = \Delta_{pitch} \cdot \Delta_{roll} \cdot \begin{bmatrix} x \\ y \\ z \end{bmatrix}_0 =$$

$$\begin{bmatrix} \cos(pitch) & 0 & -\sin(pitch) \\ 0 & 1 & 0 \\ \sin(pitch) & 0 & \cos(pitch) \end{bmatrix} \cdot \begin{bmatrix} 1 & 0 & 0 \\ \cos(roll) & 0 & \sin(roll) \\ -\sin(roll) & 0 & \cos(roll) \end{bmatrix} \cdot \begin{bmatrix} x \\ y \\ z \end{bmatrix}_0 \quad (4.2)$$

When the roll and pitch axes coincide with the x and y body coordinate axes, respectively, $\begin{bmatrix} x \\ y \\ z \end{bmatrix}_0$ is the position of the GNSS antenna phase centre in the body frame coordinate system, and $\begin{bmatrix} x \\ y \\ z \end{bmatrix}_{rot}$ is the position of GNSS antenna phase centre after correction for pitch and roll using the rotation matrices Δ_{pitch} and Δ_{roll}.

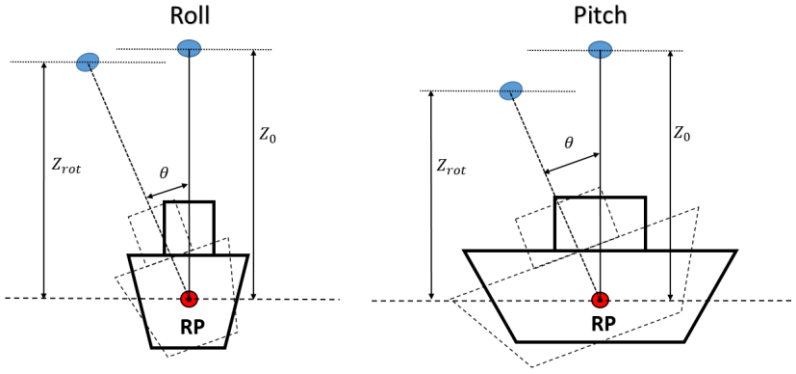

Figure 4.1: Effect of vessel roll and pitch on the estimated height at the GNSS antenna above the vessel reference point (RP)

4.3.2 Squat and draft variations

As the vessel moves through the water, the fixed antenna height and the hydrostatic correction due to draft changes must be accounted for. The motion of the vessel produces a wave system of displaced water around the hull which extends over a considerable area of influence, leading to an apparent change of draft and trim of the vessel. Therefore, a GNSS antenna aboard a vessel changes its height above the undisturbed water level significantly due to the hydrodynamic effect (the 'squat'). Essentially, the amount of squat depends on the vessel's speed through the water, the size, weight and shape of the vessel's hull, and the cross-section of the waterway. The squat may be estimated by empirical or analytical methods based on fluid dynamics computations (Briggs, 2009; Jachowski, 2008).

The variation of the vessel's load during a mission (due to fuel consumption, for example) alters the vessel's draft. The vessel's speed changes its attitude; for example, if it is travelling faster than 3 m/s, water level height errors of 5 to 10 cm occur (Guo, et al., 2016). The vessel's squat can therefore be treated as speed-dependent only. When the speed remains at or less than 3 m/s, the GNSS water level height error is generally less than 1 cm (Bonnefond et al., 2003; Reinking, Härting, & Bastos, 2012).

4.3.3 Heave corrections

'Heave' mostly refers to the short, periodic vertical movements of a vessel due to waves that are mainly caused by disturbing factors such as meteorological effects. Therefore, any short-term vertical motion predominantly due to waves is considered to be heave, and was removed from the GNSS height observations.

The effect of heave, δd_i, may reach several decimetres, and waves of several metres height may occur. In this study, the vessel heave effect observed by the motion sensors was removed from the GNSS water level heights. Heave is related to the ellipsoidal height by:

$$\delta d_i = h_i - h_{WL_i} \tag{4.3}$$

where h_i is the instantaneous (i.e., uncorrected) ellipsoidal height obtained from GNSS, and h_{WL_i} is the ellipsoidal height of the undisturbed (static) water level.

4.4 Compensation for vessel motion

During vessel calibration tests, the vessel motion was measured, then removed. Calibration is an essential procedure that consists of determining the composite offset angles (pitch, roll and yaw) due to the vessel motion by motion sensors and apply corrections to the estimated water level by GNSS. Inertial sensors or inertial measurement units (IMU) are the most commonly used sensors in hydrography to measure roll, pitch and heave of floating platforms. The IMU comprise a set of three orthogonal accelerometers (linear acceleration sensors) and three gyroscopes (angular rate sensors). These are placed in the same vessel frame, and thus they sense the same motion as the vessel itself (strap-down system) or in a stabilised platform (gimballed system) (Deurloo, 2011).

In this study, the vessel movements were recorded by two sets of measurements: actual location of the vessel was determined by two GNSS antennas, and relative movement (pitch and roll) by an Octopus F180 IMU. The accuracies of IMU measurements were: roll ± 0.1°; pitch ± 0.1°; heave: ± 5 cm. The IMU measures the combined effect of all accelerations caused by all forces acting on the vessel, including external forces due to wave and wind action. The data from the accelerometers uses low-pass filters to remove high-frequency variations due to wave action, quick turns and sudden speed variations to provide an estimate of the gravity vector. The direction from which the angular changes occur (roll and pitch) are also measured. The heave is determined by double integration of the linear accelerations sensed in the vertical direction (IHO, 2005).

4.5 Offshore GNSS data processing

4.5.1 Description of offshore hydrographic survey

The data used in this study were collected by the vessel *Fugro Equator* built specifically for survey operations on the high seas (Figure 4.2, right). It is 65 m long, with a beam of 15 m. It was fitted with a hull-mounted Kongsberg EM302 multibeam echo sounder (MBES) capable of acquiring bathymetric, backscatter and water column data down to water depths of 7000 m, and a Kongsberg SBP-300 pinger sub-bottom profiler (SBP). The data collected by this vessel had been used in support of the search for the wreckage of the MH370 aircraft which disappeared on 08 March 2014 and is thought to have ended its journey in an area of the Indian Ocean. The farthest distance from the Western Australian coast in this study was about 2700 km (Figure 4.2, left). The mean ocean depth in the survey area was about 570 m. Waves up to 6 m were experienced during the survey.

Figure 4.2: Survey area of GNSS observations (left). *Fugro Equator* survey ship (right)

4.5.2 Offshore GNSS data collection

A Fugro StarPack GNSS receiver on board the *Equator* was used to collect kinematic GNSS observations. The raw dual-frequency pseudorange and carrier-phase observations for GPS and GLONASS were collected continuously for 30 days from 17 November to 17 December 2014 (321 DOY – 351 DOY) at a rate of 1 Hz. The receiver is a high-precision positioning system that stores all GNSS raw data in SPM binary format to an internal flash card. SPM files contain GNSS observations, receiver configuration details and all information required to create RINEX files. The raw GNSS observations were extracted from SPM files by using a special routine. Once extracted, all SPM files were converted to RINEX files using the Trimble RINEX converter software. The RINEX conversion was performed for each day separately over the entire 30-day period.

4.5.3 Offshore GNSS PPP processing

The accuracy of traditional differential GNSS positioning (e.g. PPK) depends on the baseline length, since the method assumes that both ends of the baseline have similar ionosphere and troposphere conditions. Therefore, shipborne GNSS data cannot be processed accurately too far from land when using an on-land reference station (Fund et al., 2013). PPP offers an alternative approach for locations remote from land. In this study the GNSS data was post-processed in kinematic mode using the NRCan CSRS-PPP online tool. The Geodetic Reference System 1980 (GRS80) ellipsoid was employed, since it is practically identical to the WGS84 reference system (NRCAN, 2016).

In this study, the satellite elevation cut-off angles were set at 10° to eliminate possible multipath from the ocean surface. The GNSS data was processed at 1 Hz, and also resampled at 1 minute for comparison with the nearshore results (Section 3). A 15-min to 25-min initialisation period was needed for carrier-phase ambiguities of PPP to converge to almost constant values and reach a stable precision level. PPP convergence depends on a number of factors: the number and geometry of visible satellites, user environment and dynamics, observation quality, and sampling rate (Kouba, 2009).

4.6 Offshore GNSS water level height determination

Since PPP processing of GNSS data provides the ellipsoidal height. A geoid height is applied to reduce the ellipsoidal height to the geoid (e.g. MSL or chart datum). Accordingly, the GNSS water level height is the distance between the geoid (e.g. chart datum or MSL) and the water surface, taking the GNSS antenna offset into account.

An equipotential surface model is generally used to represent MSL in waters more than 200 m deep (Dodd & Mills, 2010). The EGM2008 model was used as a tool for interpolating the geoid height across the survey area. For depths greater than 200 m, it can be used as the chart datum, because tidal variations become relatively small in relation to the large depths. This gravitational model is complete to spherical harmonic degree and order 2160 (Pavlis, Holmes, Kenyon, & Factor 2012). In this study, a 1 × 1 arc-minute grid of the geoid height relative to the WGS 84 ellipsoid was used. These difference values at the location of each GNSS observation were then added to the ellipsoidal height at the GNSS observations to determine the water level height with respect to the EGM2008 geoid.

Figure 4.3 illustrates the GNSS-PPP water level height obtained offshore for the vessel over the 30-day survey period. Roll and pitch corrections were applied to the original GNSS observations during survey operations, while the heave correction obtained from the motion sensor was applied by subtracting it from the original GNSS-PPP water level heights. As Figure 4.3 shows, the offshore GNSS-PPP water level height contains more noise than the nearshore GNSS height estimates, indicating much greater wave activity. Even though the PPP estimates contained large high-frequency variations, they were still able to capture the main tide signals, as shown in Figure 4.4 illustrating the tide signature of the semidiurnal tides for example on days 6 to 8 (22–24 November 2014), with a tidal range of about ± 0.5 m.

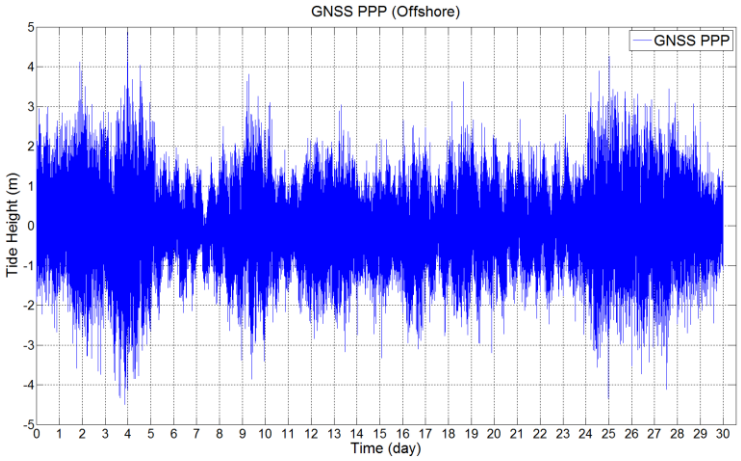

Figure 4.3: GNSS-PPP water level heights

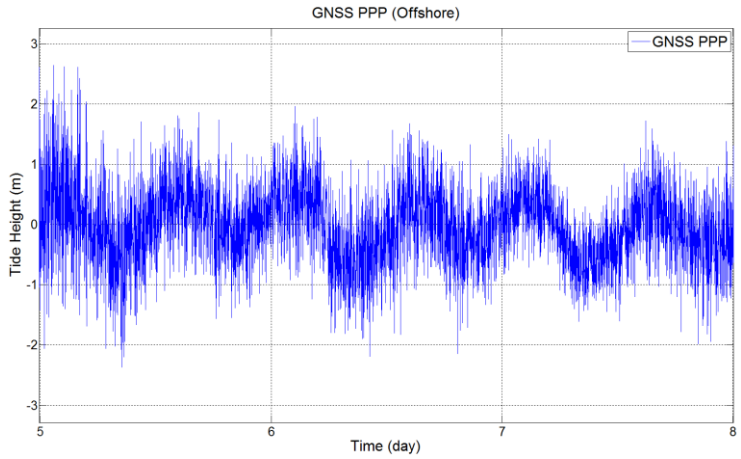

Figure 4.4: Computed tidal heights for days 6, 7 and 8 (22, 23 and 24 November 2014)

4.6.1 Variability of offshore GNSS-PPP water level heights

To assess the characteristic of the estimated shipborne GNSS-PPP water level heights, the Savitzky–Golay filter with 100 min window length was applied to separate the high-frequency variations from the low-frequency tide signal. This filter was used based on results of Chapter 3, as the best performing filter (e.g. least damping). Figure 4.5a shows the GNSS water level heights, and the difference between the original and smoothed water level heights are illustrated in Figure 4.5b. The standard deviation of the residual between the unfiltered and filtered water level heights is 78.3 cm with a mean of 0.11 cm. The distribution of the residual is shown as a histogram in Figure 4.6. The figure shows that the residuals are normally distributed.

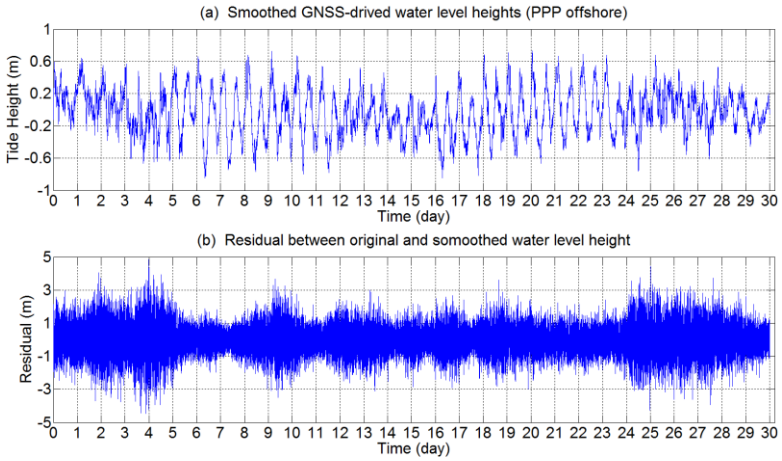

Figure 4.5: GNSS-derived water level heights based on PPP offshore: (a) Shipborne GNSS-derived water level heights; (b) Residual between original and smoothed data using the Savitzky–Golay filter with 100 min window length

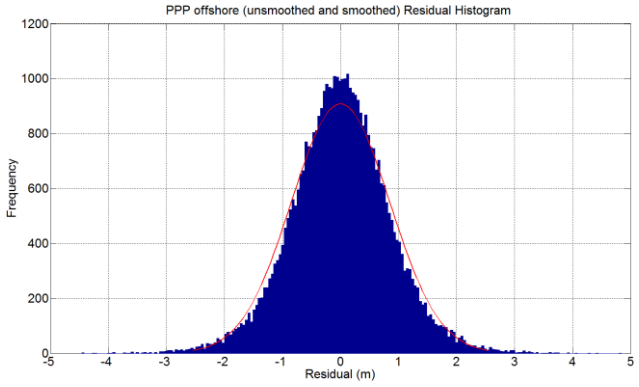

Figure 4.6: The distribution of the residual for ship-borne GNSS water level heights

4.6.2 Spectral analysis of offshore GNSS-PPP water level heights

As in Chapter 3, the frequency spectrums of the original GNSS-PPP water level heights for the offshore test were derived, and the main tidal frequencies were extracted. The original GNSS-PPP water level heights were transformed to their frequency spectrum by using the Fast Fourier transform. The amplitudes of the major tidal harmonic constituents M2, S2, K1 and O1 were extracted, and are presented in Table 4.1. From the table, and Figure 4.7, it is clear that the tidal signal was predominantly semidiurnal.

Table 4.1: Major tidal constituents extracted from the frequency spectrum of offshore GNSS-PPP water level heights

Constituents	Period (hr)	PPP Amplitude (m)
M2	12.421	0.259
S2	12.000	0.129
K1	23.934	0.077
O1	25.819	0.058

The frequency spectrum of the original GNSS-PPP heights shown in Figure 4.7 clearly depicts the semidiurnal (M2 and S2) and diurnal (K1 and O1) tidal constituents. The semidiurnal constituents M2 and S2 have the largest amplitudes; the amplitudes of the diurnal constituents K1 and O1 are much lower (~8 cm compared to ~26 cm). Figure 4.7 also shows the high-frequency variations that were filtered out.

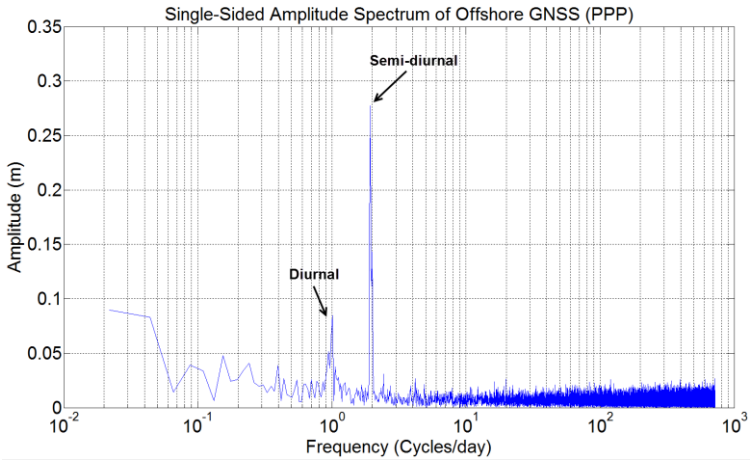

Figure 4.7: Power spectra for the offshore GNSS-PPP water level heights

4.7 Extracting tidal signals from low-pass filtered offshore water level heights

Following the same procedure as described in Chapter 3 for nearshore GNSS-derived water level height measurements, the four low-pass filtering techniques (moving average, Savitzky–Golay, Gaussian and Butterworth filter) were again assessed for their suitability for extracting tidal signals from the offshore GNSS-derived water level heights. As described in sections 4.3.1 and 4.3.2, roll, pitch and squat and their corrections were applied on the original GNSS observations during data collection. The heave correction was applied directly to the GNSS-PPP water level heights. As in

the nearshore environment, the GNSS-PPP heights were filtered to reveal the low-frequency tidal variations. GNSS heights determined by kinematic PPP (i.e., the single-epoch solution) contain both high-frequency variations (induced by waves and the attitude and motion of the vessel) and low-frequency tidal variations. In order to remove the high-frequency variations and extract the low-frequency tidal signals, the low-pass filters were applied to the GNSS-PPP water level height estimates. As in the nearshore data analysis procedure (cf. Chapter 3), in the following sections the performances of the low-pass filters were evaluated in relation to window length. The major tidal harmonic constituents were extracted from both the unfiltered and filtered (smoothed) time series and the differences between the respective unfiltered and filtered reconstructed tidal signals were analysed (refer to Figure 3.16 in Chapter 3). Unlike the case in the nearshore experiment, no tide gauge data was available, thus no comparison could be made. Therefore, the analysis is restricted to the damping effect only.

As defined in Chapter 3, an optimal filter is the filter that retains the amplitudes of the major tidal harmonic constituents, and filters out high-frequency content. As in the nearshore experiment, in the offshore environment the four major tidal harmonic constituents were extracted from the unfiltered and filtered GNSS-PPP signals. The respective tidal signals were reconstructed based on superposition of the extracted tidal harmonic constituents. The differences between the unfiltered and filtered reconstructed tidal signals were quantified by their standard deviations at the 68% and 95% confidence levels, and the maximum values of the differences. This indicates the damping effect of the filters on the tidal constituents. To assess the properties of each filter, window lengths of 10, 30, 60, 80, 100, 120, 150, 180, 220, 260, 300 and 360 minutes were applied. A more detailed description of each filter is provided in Chapter 3; in the following sections the results for the four filters in the offshore environment are given.

4.7.1 Moving average filter applied to offshore water level heights

The moving average filter methodology is described in Section 3.7.1. The frequency spectra for the unfiltered, filtered and difference between the filtered and unfiltered tide signals of the offshore GNSS-PPP water level heights were derived using the Fast Fourier transform method. An example is illustrated in Figure 4.8 for a window length

of 100 minutes. The frequency spectra for all remaining window lengths are provided in Appendix B. The spectra clearly show the four major tidal harmonic constituents (Figure 4.8a, b) and the extent to which the filter has removed high-frequency variations and retained low-frequency tidal signals. The damping effect of the filter is seen in Figure 4.8c, which shows differences between filtered and unfiltered GNSS water level heights, illustrating the residual amplitudes for the semidiurnal tidal constituents M2 and S2. By comparison with the nearshore environment, Figure 4.8c also shows increased amplitudes (cm rather than mm) for the high-frequency constituents of the spectra (for instance, by comparing Figures 3.18c and 4.8c).

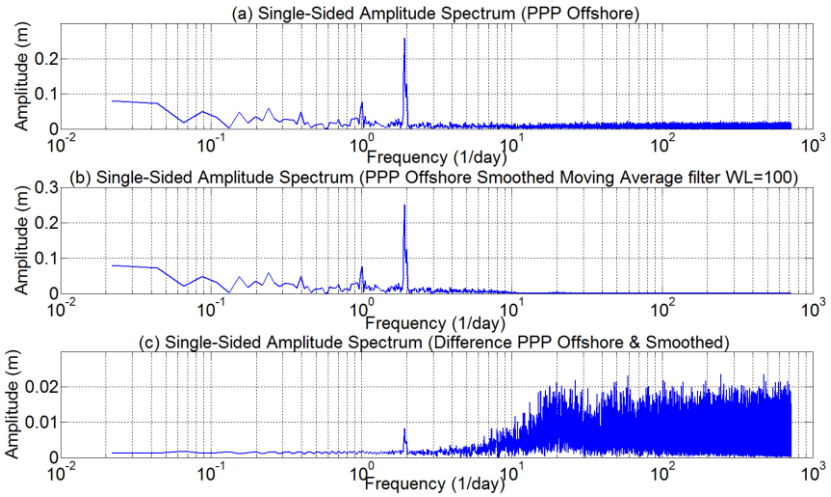

Figure 4.8: Single-sided frequency spectra of the moving average filter for PPP offshore: (a) unfiltered GNSS-PPP; (b) GNSS-PPP smoothed by the moving average filter with a 100-minute window length; and (c) differences between filtered and unfiltered GNSS-PPP water level heights

Following the procedure described in Chapter 3, the damping effect of the moving average filter based on the window length for the offshore GNSS-PPP water level heights is shown in Figure 4.9. The difference between the reconstructed tidal signals based on the tidal constituents extracted from the filtered and unfiltered GNSS-PPP water level height time series reveals significant differences to results of Chapter 3 for amplitude damping of the four major tidal harmonic constituents see Figure 3.19. It is clear that the damping effect increased considerably with increasing window length for the moving average filter, with standard deviations of the differences 7 cm and 14 cm at the 68% and 95% confidence level, respectively. A maximum difference of 14.8 cm was estimated for the longest window length of 360 minutes. These values were

obtained by analysing the differences between the reconstructed tidal signals based on the smoothed (damped) and unsmoothed signals over the entire 30-day dataset. Table 4.2 in Section 4.7.5 contains a summary of the damping effect for all window lengths.

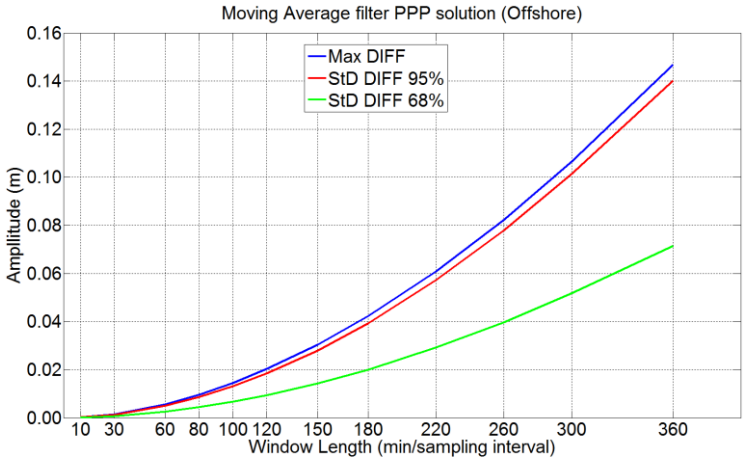

Figure 4.9: Performance of the moving average filter in relation to various window lengths used. Damping effects, as manifested by differences in the reconstructed tide signals, are shown by dotted lines and denoted by DIFF. The standard deviations of the differences (StD DIFF) are given at 68% and 95% confidence levels

4.7.2 Savitzky–Golay filter applied to offshore water level heights

The method of the Savitzky–Golay filter is described in Section 3.7.2. Figure 4.10a and b show the frequency spectra for the unfiltered and filtered offshore GNSS-PPP water level heights when this filter was applied with a window length of 100 minutes, as an example. These spectra clearly show the semidiurnal (M2, S2) and diurnal (K2, O2) tidal constituents. The frequency spectrum for the differences between the reconstructed tide signals based on the constituents extracted from the unfiltered and filtered GNSS-PPP heights is shown in Figure 4.10c; this indicates a better performance than the case for the moving average filter, since it does not show any damping effects, i.e. no residual effects for the main tidal harmonic constituents.

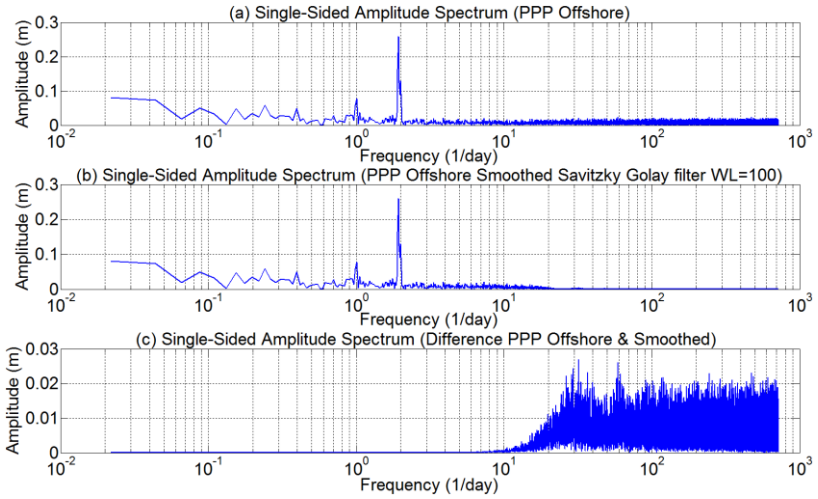

Figure 4.10: Single-sided frequency spectra of the Savitzky–Golay filter for PPP offshore: (a) unfiltered GNSS-PPP; (b) GNSS-PPP signal smoothed by the Savitzky–Golay filter for a 100-minute window length; and (c) differences between the filtered and unfiltered offshore GNSS-PPP water level heights

Similar to the moving average filter (Section 4.7.1), the standard deviations (68% and 95% confidence level) of the differences between the reconstructed tidal signals obtained from the tidal harmonic constituents extracted from unfiltered and filtered offshore GNSS-PPP water level height time series and maximum differences increased with increasing window length as depicted in Figure 4.11, but at a much reduced level. The damping effect was considerably less for the Savitzky–Golay filter, with standard deviations at 68% and 95% confidence levels of 0.4 cm and 0.7 cm, respectively, while the maximum difference was at the same level as the standard deviation at the 95% confidence level up to the maximum window length of 360 minutes. Thus, the damping effect was similar to that for the nearshore GNSS water level height described in Chapter 3, despite the high noise level of the data in the longest window length of 360 minutes. A summary of the damping effect for all window lengths is given in Table 4.2 in Section 4.7.5.

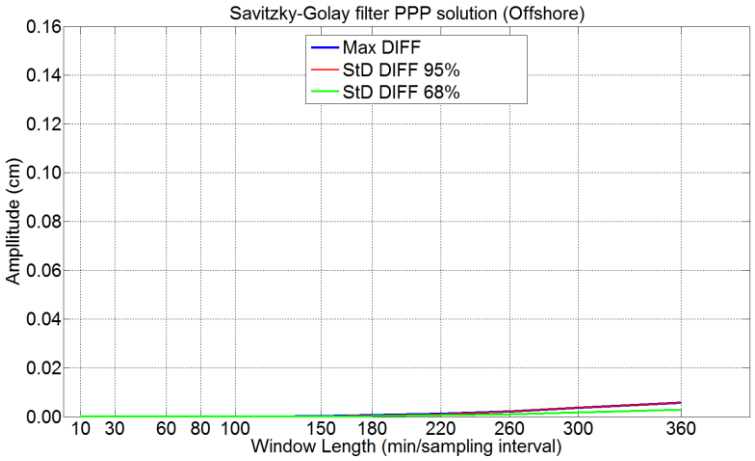

Figure 4.11: Performance of the Savitzky–Golay filter in relation to various window lengths. Damping effects, as manifested by differences in the reconstructed tide signals, are shown by dotted lines and denoted by DIFF. The standard deviations of the differences (StD DIFF) are given at 68% and 95% confidence levels

4.7.3 Gaussian filter applied to offshore water level heights

The methodology of the Gaussian filter was described in Section 3.7.3. The tidal constituents M2, S2, K1 and O1 when applying this filter are illustrated in Figure 4.12a and b for the unfiltered and filtered heights respectively. As for the previous two filters, the Gaussian filter was able to eliminate high-frequency variations and retain low-frequency tidal signals. Figure 4.12c shows the frequency spectrum of the differences between unfiltered and filtered data. Again, residual magnitudes between the unfiltered and filtered signals can be seen that relate to the damping effects on M2 and S2, which are largest for the moving average filter and smallest for the Savitzky-Golay filter.

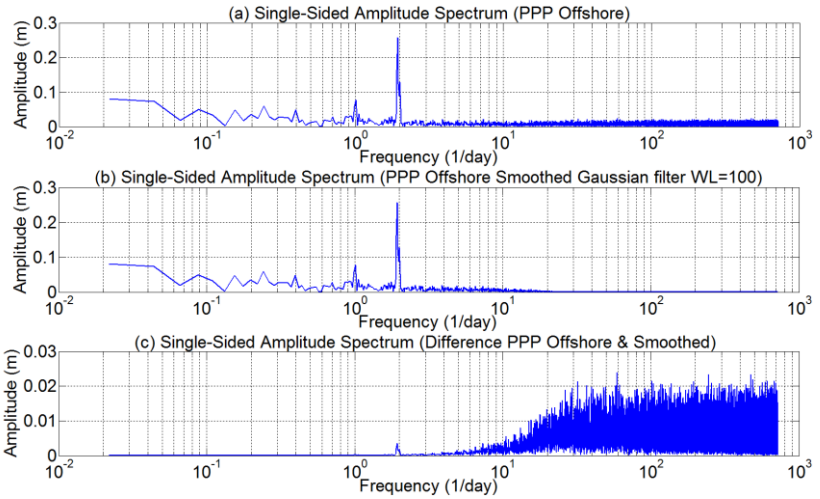

Figure 4.12: Single-sided frequency spectra of the Savitzky–Golay filter for PPP offshore: (a) unfiltered GNSS-PPP; (b) GNSS-PPP signal smoothed by the Gaussian filter with a 100-minute window length; and (c) differences between the filtered and unfiltered offshore GNSS-PPP water level heights

Figure 4.13 confirms the inference that the damping effect for the Gaussian filter was larger than for the Savitzky–Golay filter but smaller than that for the moving average filter. For the Gaussian filter, the maximum damping effect with standard deviations at 68% and 95% confidence levels were 3.2 cm and 6.4 cm, respectively, with a maximum difference of 6.8 cm for the maximum window length of 360 minutes. Table 4.2 in Section 4.7.5 presents a summary of the damping effect for all window lengths for the Gaussian filter.

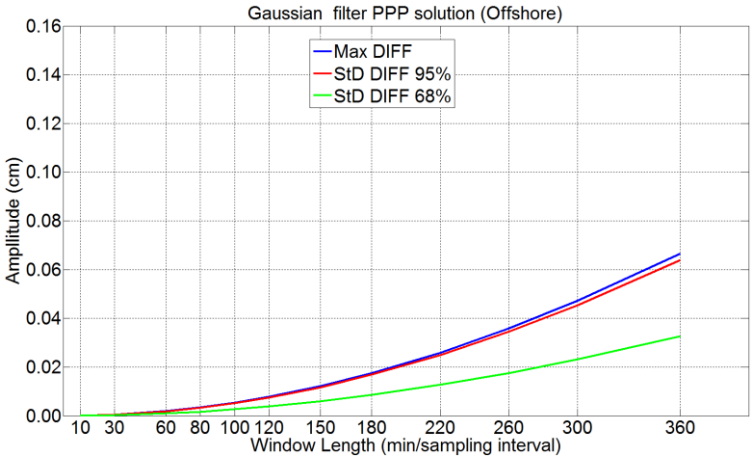

Figure 4.13: Performance of the Gaussian filter in relation to various window lengths. Damping effects, as manifested by differences in the reconstructed tide signals, are shown by dotted lines denoted by DIFF. The standard deviations of the differences (StD DIFF) are given at the 68% and 95% confidence levels

4.7.4 Butterworth filter applied to offshore water level heights

The Butterworth filter method is described in Section 3.7.4. The behaviour of the Butterworth filter is very similar to the moving average filter, in that it exhibits a large damping effect on the semidiurnal tidal harmonic constituents as illustrated in Figure 4.14. Again the frequency spectra for the unfiltered and filtered GNSS-PPP water level height time series clearly show the semidiurnal (M2, S2) and diurnal (K2, O2) tidal constituents for a window length of 100 minutes (shown in Figure 4.14a, b). The damping effect is clearly seen in Figure 4.14c showing the frequency spectrum of the differences between the unfiltered and filtered GNSS-PPP water level height time series as residual magnitudes in the amplitude of the semidiurnal tidal constituents (see more details in Section 3.7.1.

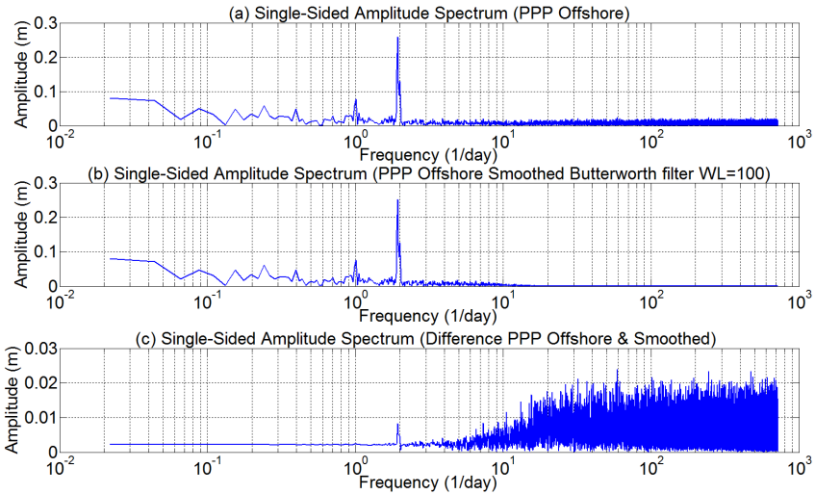

Figure 4.14: Single-sided frequency spectra of the Gaussian filter for PPK offshore: (a) unfiltered GNSS-PPP; (b) GNSS-PPP smoothed by the Butterworth filter for a 100-minute window length; and (c) differences between the filtered and unfiltered offshore GNSS-PPP water level heights

Figure 4.15 confirms that the results for the Butterworth filter show a quite similar behaviour to those for the moving average filter when applied to the offshore GNSS-PPP water level height time series. It is clear that the damping effect is considerably larger than for either the Savitzky–Golay or Gaussian filters, but similar to the moving average filter damping performance. The standard deviations at 68% and 95% confidence levels obtained from the differences between the reconstructed tidal signals based on the tidal constituents extracted from the unfiltered and filtered GNSS PPP

water level heights are 7.2 cm and 14 cm, respectively, for the longest window length of 360 minutes. For the same window length, the maximum difference between the reconstructed tidal signals based on the filtered (damped) and unfiltered signals is 14.8 cm. A summary of the damping effect for all window lengths is given in Table 4.2, Section 4.7.5.

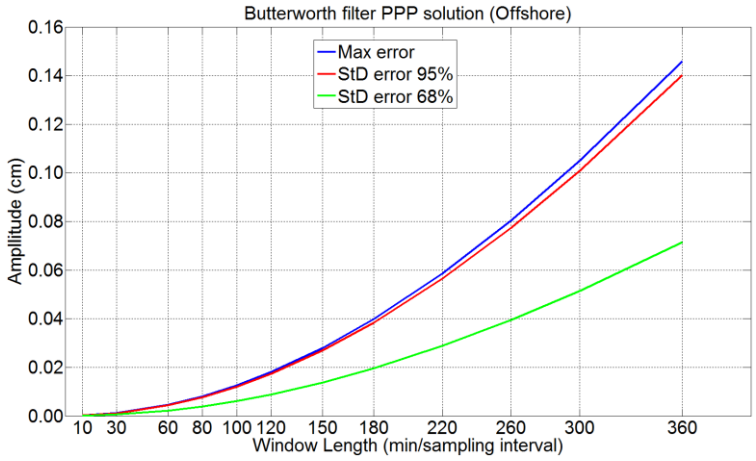

Figure 4.15: Performance of the Butterworth filter for different window lengths. Damping effects, as manifested by differences in the reconstructed tide signals, are shown by dotted lines and denoted by DIFF. The standard deviations of the differences (StD DIFF) are given at 68% and 95% confidence levels

4.7.5 Comparison of filter results

The amplitudes of the major semidiurnal (M2, S2) and diurnal (K1, O1) tidal harmonic constituents extracted from the filtered offshore GNSS-PPP water level height time series using different window lengths are listed in Table 4.2 (upper value in each row). In addition, the differences between the amplitudes extracted from the unfiltered and filtered GNSS-PPP time series are listed in Table 4.2 by the lower value in each row. From the difference between the original tidal constituents and the filtered tidal constituents, the properties of all filters are clearly demonstrated by an increased damping of the tidal constituents' amplitudes at longer window lengths (i.e., increased smoothing). The moving average and Butterworth filters produced the largest damping effects of 34% and 37%, respectively, for the maximum window length of 360 minutes for the M2 and S2 tidal constituents and 11% and 10% for K1 and O1.

Results for the Savitzky–Golay filter showed much lower damping of the tidal harmonic constituents than either the moving average or Butterworth filters. The

maximum damping effect relative to the amplitude of the unfiltered signal for the maximum window length of 360 minutes was only 2% for the semidiurnal tidal constituents, and was negligible for the diurnal tidal constituents.

The damping effects for the Gaussian filter lay between those of the other filters. The damping effects are smaller than for the moving average and Butterworth filters, but considerably larger than for the Savitzky–Golay filter. The results for the Gaussian filter showed maximum damping effects of 16% relative to the amplitude of the unfiltered signal for the maximum window length of 360 minutes for both the M2 and S2 tidal constituents, and 5% for K1 and O1.

Table 4.2: Performances of all four filters in extracting the amplitudes of the major tidal constituents (M2, S2, K1, O1) from the filtered PPP time series relative to window length (WL). The upper value in each row is the extracted amplitude after applying the filter; the lower value in each row is the difference between the amplitudes extracted from the original offshore PPP time series (given in Table 4.1) and the filter time series

	Amplitudes (m) / Residual (m)															
	Moving Average				**Savitzky–Golay**				**Gaussian**				**Butterworth**			
WL	**M2**	**S2**	**K1**	**O1**	**M2**	**S2**	**K1**	**O1**	**M2**	**S2**	**K1**	**O1**	**M2**	**S2**	**K1**	**O1**
10	0.26	0.13	0.08	0.06	0.26	0.13	0.08	0.06	0.26	0.13	0.08	0.06	0.26	0.13	0.08	0.06
	0.00	0.00	0.00	0.00	0.00	0.00	0.00	0.00	0.00	0.00	0.00	0.00	0.00	0.00	0.00	0.00
30	0.26	0.13	0.08	0.06	0.26	0.13	0.08	0.06	0.26	0.13	0.08	0.06	0.26	0.13	0.08	0.06
	0.00	0.00	0.00	0.00	0.00	0.00	0.00	0.00	0.00	0.00	0.00	0.00	0.00	0.00	0.00	0.00
60	0.26	0.13	0.08	0.06	0.26	0.13	0.08	0.06	0.26	0.13	0.08	0.06	0.26	0.13	0.08	0.06
	0.00	0.00	0.00	0.00	0.00	0.00	0.00	0.00	0.00	0.00	0.00	0.00	0.00	0.00	0.00	0.00
80	0.25	0.13	0.08	0.06	0.26	0.13	0.08	0.06	0.26	0.13	0.08	0.06	0.25	0.13	0.08	0.06
	0.01	0.00	0.00	0.00	0.00	0.00	0.00	0.00	0.00	0.00	0.00	0.00	0.00	0.00	0.00	0.00
100	0.25	0.13	0.08	0.06	0.26	0.13	0.08	0.06	0.26	0.13	0.08	0.06	0.25	0.13	0.08	0.06
	0.01	0.00	0.00	0.00	0.00	0.00	0.00	0.00	0.00	0.00	0.00	0.00	0.01	0.00	0.00	0.00
120	0.25	0.12	0.08	0.06	0.26	0.13	0.08	0.06	0.25	0.13	0.08	0.06	0.25	0.12	0.08	0.06
	0.01	0.00	0.00	0.00	0.00	0.00	0.00	0.00	0.00	0.00	0.00	0.00	0.01	0.01	0.00	0.00
150	0.24	0.12	0.07	0.06	0.26	0.13	0.08	0.06	0.25	0.13	0.08	0.06	0.24	0.12	0.08	0.06
	0.02	0.00	0.00	0.00	0.00	0.00	0.00	0.00	0.01	0.00	0.00	0.00	0.02	0.01	0.00	0.00
180	0.24	0.12	0.07	0.06	0.26	0.13	0.08	0.06	0.25	0.12	0.08	0.06	0.24	0.12	0.08	0.06
	0.02	0.00	0.00	0.00	0.00	0.00	0.00	0.00	0.01	0.01	0.00	0.00	0.02	0.01	0.00	0.00
220	0.22	0.11	0.07	0.06	0.26	0.13	0.08	0.06	0.24	0.12	0.08	0.06	0.24	0.11	0.07	0.06
	0.40	0.00	0.05	0.00	0.00	0.00	0.00	0.00	0.02	0.01	0.00	0.00	0.04	0.02	0.00	0.00
260	0.21	0.10	0.07	0.06	0.26	0.13	0.08	0.06	0.24	0.12	0.08	0.06	0.21	0.10	0.07	0.06
	0.05	0.01	0.00	0.00	0.00	0.00	0.01	0.00	0.02	0.01	0.00	0.00	0.05	0.03	0.00	0.00
300	0.20	0.09	0.07	0.05	0.26	0.13	0.08	0.06	0.23	0.11	0.08	0.06	0.20	0.10	0.07	0.06
	0.06	0.01	0.00	0.00	0.00	0.00	0.00	0.00	0.03	0.02	0.00	0.00	0.06	0.03	0.01	0.00
360	0.17	0.08	0.07	0.05	0.25	0.13	0.08	0.06	0.22	0.11	0.07	0.06	0.17	0.08	0.07	0.06
	0.09	0.02	0.01	0.01	0.01	0.00	0.00	0.00	0.04	0.02	0.00	0.00	0.09	0.05	0.01	0.01

4.8 Comparison of filter results with IHO standards

The aim has been to find the optimal filter method to use for filtering GNSS heights. In this section, the performances of the four filters are compared in terms of meeting IHO standards. As described in Section 3.9, tide measurement errors must lie within a standard deviation not exceeding ± 5 cm at the 95% confidence level to meet IHO Special Order surveys, and not exceeding ± 10 cm at the 95% confidence level for any other order. As in Chapter 3 for a nearshore environment, the four filters discussed in sections 4.7.1 to 4.7.4 are assessed for their suitability for extracting the tide signal from GNSS-PPP water level height observations in an offshore environment. Unlike the case of nearshore environment, where tide gauge data is available, no such information is available offshore. Therefore, in this case only the damping effect due to filtering (smoothing) of the GNSS-PPP water level height may be compared to IHO specifications. In this case, the maximum window lengths of 360 minutes for each filter were derived for which the damping effect meets IHO specifications of ±10 cm at 95% confidence level.

The four filters considered in this study, namely: the moving average, Savitzky–Golay, Gaussian and Butterworth filters were able to eliminate high-frequency signals and maintain the lower-frequency tidal signal contained in the GNSS-PPP water level heights. They also showed considerable damping effects at increased window lengths. The moving average and Butterworth filters produced very similar damping, reaching a standard deviation (at 95% confidence level) of ±14 cm for the longest window length of 360 minutes. Therefore, for these filters, very long window lengths are to be avoided in order to keep the damping effect below the maximum tide accuracy of ±10 cm (95% confidence level) specified by the IHO for any order except for special order surveys. To keep the damping effects below ±10 cm, the window length for these filters should not exceed approximately 300 minutes. With standard deviations of ±6.4 cm (at 95% confidence level) the damping effects of the Gaussian filter was well within the IHO standard for any order except for special order surveys. With regards to the dampening performance, only the Savitzky-Golay filter was well within the IHO standard for any order also including special order surveys for all window lengths up to the maximum of 360 minutes.

Taking offshore GNSS-PPP water level height estimates as representative for nearshore hydrographic surveys on board a small vessel that is exposed to high dynamics, the above considerations change when the IHO standards for Special Order surveys, e.g. ±5 cm at 95% confidence level should not be exceeded. In this situation only the the Savitzky-Golay filter can provide acceptable results in reducing the high-frequency noise but leaving the low-frequency tide signal largely unchanged.

4.9 Comparison between GNSS-PPP performance in nearshore and offshore environments

This section evaluates the performance of the PPP technique and its potential use for both nearshore and offshore hydrographic surveys. In this study the nearshore GNSS observations were collected on a floating pontoon within a sheltered harbour area, thus can be considered as a hydrographic survey in rather sheltered conditions. On the other hand, the offshore environment in the middle of the Indian Ocean is an example of a highly dynamic environment.

For the two surveys, Figure 4.16 illustrates the daily averages of the visible GPS and GLONASS satellites over the 30-day study period. Note that the time periods for the nearshore experiment (1 to 31 August 2011) and offshore experiment (17 November to 17 December 2014) were different. For the nearshore experiment, the GNSS receiver observed only an average of 7 to 9 GPS satellites during the first 13 days, then observed on average 13 to 15 GPS and GLONASS satellites for the remainder of the study period as shown in Figure 4.16. Unfortunately, there was no record of the reason for switching off GLONASS during the first period, noting that the nearshore data was collected a few years before commencement of this study. For the offshore study both GPS and GLONASS satellites were tracked throughout the whole study period, with the daily average number of satellites varying between 11 and 15.

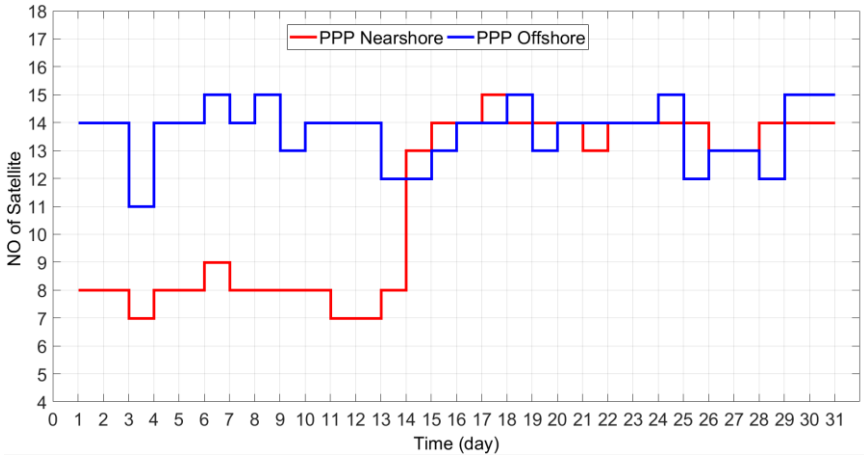

Figure 4.16: Daily average number of visible GNSS satellites during the nearshore (red) and offshore (blue) surveys

The accuracy of the PPP method is primarily limited by the quality of observations, the precision of available precise orbit and clock products and the effects of unmodelled biases and error sources, such as multipath errors. Under ideal conditions, PPP is able to provide horizontal and vertical positions at an accuracy level of a few centimetres when operated in static mode. The accuracy level decreases to the decimetre-level when operated in kinematic mode (Bisnath & Gao, 2009). Figures 4.17 and 4.18 illustrate the daily average accuracy of the PPP solutions for the nearshore and offshore studies, as obtained by CSRS Canada PPP online processing software after solution conversion. For the nearshore study, Figure 4.17 shows a height accuracy level of about ± 5 cm for the first 13 days, followed by an improvement to just below ± 4 cm for the remainder of the study period, which seems to have been related to the number of satellites tracked shown in Figure 4.16. For the offshore study the height accuracy level is generally between ± 4 cm and ± 5 cm throughout the study period. While the height accuracy levels for both the nearshore and offshore studies are at the few-cm level, except for the last few days of the offshore study, it can be seen that the height accuracy was consistently lower for the nearshore study for the period when both GPS and GLONASS satellites were tracked (by comparing the period between days 14 and 26 in Figures 4.17 and 4.18). Similar behaviour can be seen for the horizontal positions, though at a level between 1 cm and 2 cm.

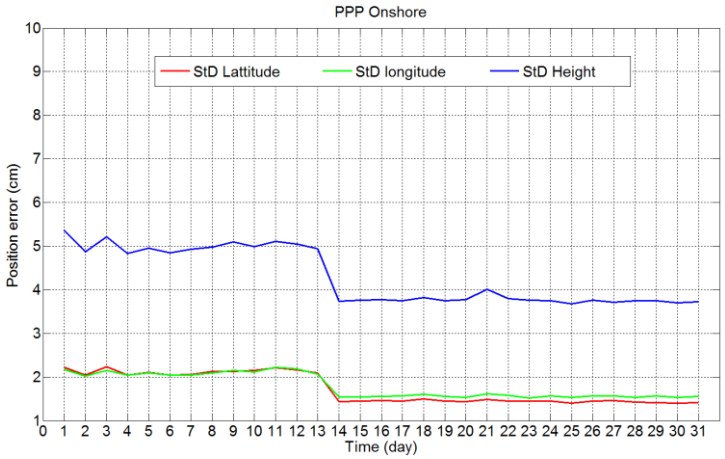

Figure 4.17: Daily average latitude, longitude and height errors at 95% confidence level for the PPP nearshore study as obtained by CSRS PPP software

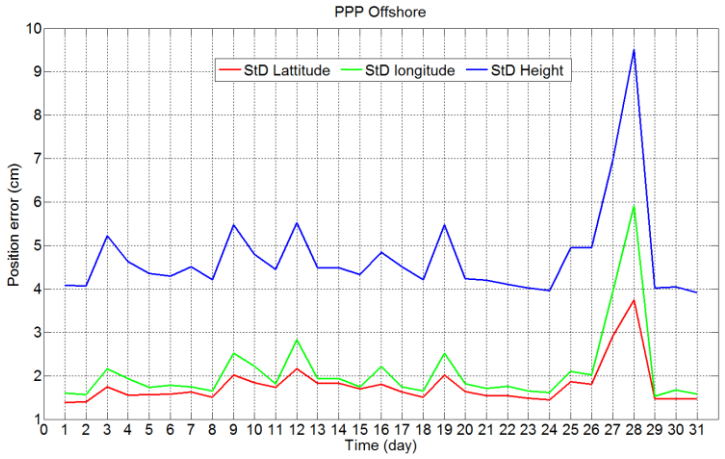

Figure 4.18: Daily average latitude, longitude and height errors at 95% confidence level for the PPP offshore study as obtained by CSRS PPP software

The average standard deviation (STD) of the PPP horizontal and vertical coordinates taken over the 30-day study periods for the nearshore and offshore study are given in Tables 4.3 and 4.4. The standard deviations indicate the precision of the surveys conducted in both cases. Comparing the average values of the standard deviations, it can be seen that the height precision for both are at a similar level of 4 – 5 cm, although the nearshore study on average shows slightly smaller STD , thus implies a slightly higher precision. This, together with the error values for the offshore study, show that the more dynamic offshore environment produced slight reductions in positioning precision, both horizontally and vertically.

Table 4.3: PPP nearshore positioning STD

Nearshore	Latitude (cm)	Longitude (cm)	Height (cm)
Mean	1.73	1.79	4.29
Max	2.24	2.22	5.37
RMS	1.76	1.81	4.33

Table 4.4: PPP offshore positioning STD

Offshore	Latitude (cm)	Longitude (cm)	Height (cm)
Mean	1.77	2.09	4.74
Max	3.74	5.92	9.51
RMS	1.82	2.25	4.86

Furthermore, the variability of GNSS-PPP water level height observations in both the nearshore and offshore environments were analysed by studying the residuals obtained by subtracting the smoothed signals using the moving average filter, as an example, with a window length of 100 minutes from the original observations. The standard deviation of these residuals with respect to the mean values for the offshore environment ($\sigma_{res,PPP}$) was 78.3 cm. Comparing this value to that corresponding quantity obtained in the nearshore environment, $\sigma_{res,PPP}$ = 2 cm and the standard deviation of the static baselines $\sigma_{tech,PPP}$ = 3.1 cm (refer to Section 3.5.1, Chapter 3) it is seen that the offshore environment added considerable variability to the estimated water level height. Applying the error budget model given in Equations (3.3) and (3.4) in Chapter 3, the additional variability due to the dynamic variations ($\sigma_{dyn,PPP}$) in the offshore environment can be quantified when using $\sigma_{tech,PPP}$ = 3.1 cm as a measure of variables for the PPP solution. The additional variability in the offshore environment, after applying the propagation of variance, becomes $\sigma_{dyn,PPP}$ = 78.24 cm, which is considerably larger than the $\sigma_{dyn,PPP}$ = 2 cm value obtained for the nearshore environment.

4.10 Chapter summary

The fundamental aim of this chapter is to investigate the performance of GNSS-PPP water level height estimation in a kinematic mode for the purpose of extracting the tidal signals offshore. The findings indicate that shipborne GNSS measurements can

be used for precise observation of tide signals if (i) appropriate corrections due to vessel motion are made and (ii) low-pass filtering is applied. The effects of vessel motion including roll, pitch, squat, draft variations and heave on tidal height as well as the application of the four low-pass filters (moving average, Savitzky-Golay, Gaussian and Butterworth) have been described.

As presented in Chapter 3 (for the nearshore environment), similar filter testing methodology was applied here to extract the four major tidal harmonic constituents (M2, S2, K1, O1) of the offshore GNSS-PPP water level height signal from unfiltered and filtered time series. Based on the extracted major tidal harmonic constituents the unfiltered and filtered tidal signals are reconstructed and compared by quantifying the standard deviation at 68% and 95% confidence level and the maximum values of the differences.

Despite much larger variability of the GNSS-PPP water level heights, filtering results in this chapter showed again the ability of the discussed filters to separate low-frequency tide variations from high-frequency motion, considered here as noise. They also showed considerable damping effects as window lengths increased. The Savitzky–Golay filter was found to best maintain the low-frequency tidal harmonic constituents in the PPP solution than a Gaussian filter, the maximum dampening effect of Savitzky–Golay and Gaussian filters for the longest window length of 360 minutes was 0.7 cm, and 6.8 cm, respectively. However, both filters produced maximum residual errors that would meet IHO Order 2 survey standards applicable to offshore areas. The maximum effects of the Savitzky–Golay filter met Special Order standards, while the maximum effect of the Gaussian filter met specifications for other orders. For the moving average and Butterworth filters the maximum dampening effect for the longest window length of 360 minutes was considerably higher and both reached values of 14.8 cm. As a result, the maximum effect and standard deviation at 95% confidence level did not meet IHO standards.

The GNSS-PPP height depends on quality of observations, accuracy of the precise orbits and satellite clock offsets, and the number of satellites in view. The variability in the offshore environment was much greater than nearshore due to the dynamic environment, with height estimation precision in terms of the standard deviations of 4 cm to 5 cm by PPP, both in nearshore and offshore environments.

The next chapter presents tidal predictions based on the harmonic constituents extracted from GNSS water level height estimation. The precision of all prediction methods depends upon the precision of the observed readings used to generate the necessary tidal harmonic constituents.

Chapter 5:

Short-Term Tide Modelling and Prediction Using GNSS Heights

5.1 Introduction

This chapter focuses on short-term, i.e., days, tide modelling and prediction using GNSS heights in place of traditional tide observations, such as readings from tide gauge stations. Tide modelling and prediction is frequently used for the purpose of safe navigation, e.g. to provide mariners with water level information (Bowditch, 2002), enabling water depth to be determined at any given time. For hydrographic surveys, tide information is crucial for reducing observed water depths to a selected datum, e.g. the chart datum (IHO, 2011). Tide information is also important for managing and planning tasks within the coastal zone.

GNSS has become a common cost effective tool for vertical positioning at sea. As demonstrated in Chapters 3 and 4, GNSS is also used to provide water level height information, either in real time or in post-mission mode, from which the tide signal can be extracted. This makes GNSS positioning very attractive, as it provides both vertical positioning and tide information during the course of a hydrographic survey. Ultimately, GNSS-derived water level heights may well be an efficient replacement for tide gauge observations, and is already of particular interest in offshore areas where traditional tide gauge stations are not available. In such areas, a GNSS system operated on a survey vessel or a buoy can provide an instant height measurement of the water surface. Also in nearshore environments, GNSS is a simple means of obtaining tide

information that is less reliant on traditional tide gauge stations. Importantly, GNSS can operate in a similar way to a traditional tide gauge when it is in a fixed location, e.g. on an anchored buoy. Otherwise, GNSS can be operated in a kinematic mode, as on a survey vessel, and is thus quite versatile. Apart from the extraction of tide information for hydrographic surveys in nearshore and offshore areas, GNSS heights for short-term tide modelling and prediction is also particularly useful for detecting and monitoring anomalous sea-level variations, such as those caused by a tsunami.

This chapter investigates short-term tide modelling and prediction using GNSS-derived water level heights in both nearshore and offshore environments. To this end, the PPK and PPP solutions described in Chapter 3 for a nearshore environment and the PPP solutions described in Chapter 4 for an offshore environment are used. Based on the GNSS-derived water level heights, the four major tidal harmonic constituents M2, S2, K1 and O1, which represent the combined effect of the lunar and solar tides, are extracted and used for short-term tide modelling and prediction. As demonstrated in Chapters 3 and 4, the four major tidal harmonic constituents capture most of the tidal signal in both the nearshore and offshore areas, and thus are considered to be sufficient for this investigation.

The numerical modelling in this chapter is based on harmonic analysis using the MATLAB routine T_TIDE, which derives the amplitude and phase of the tidal harmonic constituents. In this study, the tidal harmonic constituents were used to model and ultimately predict the tide for data records from 1 to 30 days in length.
As described in Chapters 3 and 4, low-pass filters are applied to remove high-frequency noise from the raw GNSS-derived water levels. Particular focus in this chapter is given to the impact of the filters on the quality of short-term tide prediction.

5.2 Tide modelling

The methods of tide modelling are classed as either harmonic or nonharmonic. The harmonic method models the tide through fundamental tidal constituents, represented as harmonic constants combined into a composite tide. The nonharmonic method is based on lunitidal intervals, ranges and inequalities derived directly from high- and low-water estimates without regard to the harmonic constituents of the tide (Parker, 2007). The harmonic analysis method was used in this study for tide modelling. This approach is based on reconstructing the tidal signature over a given area and for a

given time using tidal harmonic constituents, each of which is estimated from the amplitudes and phase lags in the tide (see Section 2.2.6).

Traditionally, tide predictions are available only at major ports with tide gauges that provide long-term data records. The tides recorded in this way may be broken down into their harmonic constituents that are then used to reconstruct the main tide signal, enabling future tides to be predicted as depicted in the simple flowchart shown in Figure 5.1.

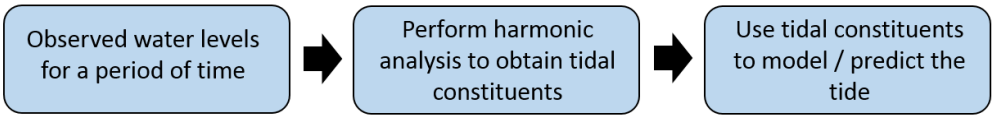

Figure 5.1: Flowchart of modelling and predicting the tide using the harmonic method

To model the tide, it is necessary to know the harmonic constants (amplitude and phase lag) for the tidal harmonic constituents. Once the constituents are known, it is simply a matter of combining the effects of all of them (adding, in this case) and thereby build a model of the tide. Traditionally, the constituents of the tide are obtained from harmonic analysis of tide gauge observations (Hicks & Szabados, 2006). Today, GNSS-derived water level height observations can be used. This has the added benefit of removing the need for tide gauges and, especially in offshore areas, allows the hydrographer to reference water level heights directly to the GNSS ellipsoid or the geoid if the geoid height is known. This is also an important advantage for tsunami early warning systems (see Section 5.5).

The harmonic modelling technique for computing the tide height at a given time *t* is expressed by the sum of the harmonic terms as in the harmonic analysis equation (see Equation 2.3 in Chapter 2.2.6), which describes how the astronomical tidal harmonic constituents are combined to represent tidal motion as a function of time. The equation allows for a static datum shift, and sums the tidal harmonic constituents as cosines with known frequencies (e.g. M2 = 1/12.4206 cycle per hour) and estimated amplitudes and phases.

The height of the tide at any given time may be expanded according to Equation 2.3 as a harmonic series using trigonometric identities (Doodson & Warburg, 1941;

Dronkers, 1975; Foreman, 1996; Najibi, Abedini, & Sheibani, 2013; Okenwa, 1978; Foreman & Neufeld, 1991; Okwuashi & Ndehedehe, 2017):

$$h(t) = z_o + \sum_{i=1}^{n} f_i\, H_i\, cos\,(\omega_i t)\cos((v_i + u_i) - \varphi_i) - \sum_{i=1}^{n} f_i\, H_i\, \sin(\omega_i t)\sin((v_i + u_i) - \varphi_i) \quad (5.1)$$

The parametersf_i, v_i, u_i, $h\,(t)$, φ_i and t are known; z_o, H_i and φ_i are unknown.

Let

$$a_i = f_i\ H_i \cos\,[(v_i + u_i) - \ \varphi_i] \quad (5.2)$$

and

$$b_i = f_i\ H_i \sin\,[(v_i + u_i) - \ \varphi_i] \quad (5.3)$$

where H_i and φ_i are unknown for the amplitude and phase of constituent *i*.

The amplitude is derived as

$$H_i = \sqrt{a_i^2 + \ b_i^2} \quad (5.4)$$

The phase value is derived by dividing (5.3) by (5.2) as

$$\tan\ \ [(v_i + u_i) - \varphi_i] = \ b_i / \ a_i \quad (5.5)$$

where a_i and b_i are called the constituent constants.

Introducing Equations (5.2) and (5.3) into Equation (5.1) yields

$$h(t) = z_o + \sum_{i=1}^{n} a_i\ \cos(\omega_i t)\ + \sum_{i=1}^{n} b_i\ \ \sin(\omega_i t) \quad (5.6)$$

Assuming equal weight observations, the least-squares solution for a_i and b_i is given as

$$\hat{X} = (A^T\ A)^{-1}\ A^T \hat{L} \quad (5.7)$$

Applying the principle of least squares to estimate a_i and b_i, the design matrix **A** (also known as the Vandermonde (pattern) matrix, e.g. Leffler & Jay, 2009), the vector of measured heights *L* of size *m* and vector of the unknowns *X* are:

$$\mathbf{A} = \begin{vmatrix} 1 & \cos\omega_1 t_1 & \sin\omega_i t_1 \; . \; . \; . & \cos\omega_n t_1 & \sin\omega_n t_1 \\ 1 & \cos\omega_1 t_2 & \sin\omega_1 t_2 \; . \; . \; . & \cos\omega_n t_2 & \sin\omega_n t_2 \\ . & . & . & . & . \\ . & . & . & . & . \\ . & . & . & . & . \\ 1 & \cos\omega_1 t_m & \sin\omega_1 t_m \; . \; . \; . & \cos\omega_n t_m & \sin\omega_n t_m \end{vmatrix} \tag{5.8}$$

$$\hat{L} = |\, h\,(t_1),\;\; h\,(t_2),\; h\,(t_3),\; \ldots,\;\; h\,(t_m)\,|^{\,T} \tag{5.9}$$

and

$$\hat{X} = |z_o,\; a_1\,,\;\; b_1,\;\; \ldots,\;\; a_n,\;\; b_n\,|^{\,T} \tag{5.10}$$

As stated in Section 5.1, the MATLAB routine T_TIDE was used to determine the amplitude H_i and phase φ_i of selected tidal harmonic constituents from GNSS-derived water level heights. T_TIDE was developed by (Pawlowicz, Beardsley, & Lentz, 2002) as a modified version of the Tidal Package originally developed at the Institute of Ocean Sciences (IOS) (Foreman & Neufeld, 1991). It is a package of routines for performing classical harmonic analyses with nodal corrections. More detailed information on the development of confidence intervals for the harmonic constituents can be found in (Pawlowicz, et al., 2002).

For tidal analysis in this study, the 30-day GNSS-derived water level height data for the nearshore and offshore environments (see Chapters 3 and 4) were used to derive the harmonic constituents and develop a model for predicting short-term tide variations.

5.2.1 Nearshore tidal model

This section describes tidal modelling for 30 days of filtered PPK and PPP GNSS-derived water level height observations in the nearshore environment (see Chapter 3), using the Savitzky–Golay low-pass filter, as the best performing filter, and 100 min window length as a medium window length. The results of tide predictions for different filters are set out in Section 5.3. Based on the input tide time series, T_TIDE was used to determine the amplitudes and phases of the four principal diurnal and semidiurnal tidal harmonic constituents M2, S2, K1 and O1. These are listed in Table 5.1.

Comparison of the amplitudes and phases obtained for the PPK and PPP solutions reveal a reasonably close fit, implying that the choice of GNSS positioning method has a small impact on the harmonic analysis and consequent prediction.

For the phase results, there is generally only a small difference between the PPK and PPP solutions for the dominant tidal harmonic constituents (i.e., those with larger amplitudes). Therefore, it would be expected that the constituent values would be almost the same for the two methods, since both datasets were for the same period.

Table 5.1: Tidal harmonic constituents derived from the nearshore 30-day GNSS-derived PPK and PPP water level height solutions using T_TIDE software

Tide	PPK solution		PPP solution		Differences	
	Amp (m)	Phase (deg)	Amp (m)	Phase (deg)	Amp (m)	Phase (deg)
M2	0.055	61.31	0.057	62.24	– 0.001	– 0.93
S2	0.054	74.71	0.060	67.63	– 0.006	7.08
K1	0.142	203.32	0.130	203.00	0.012	0.32
O1	0.123	178.41	0.115	177.35	0.008	1.06

Figure 5.2 shows the tide model based on the filtered GNSS-PPK water level heights in the upper panel, and the GNSS-PPP water level heights in the middle panel, over the 30 days. The figure shows that the modelled tide using the two methods yielded the same pattern and similar results. This is confirmed in the lower panel of Figure 5.2 illustrating the tide models obtained from the two methods and the model residuals between both results. The comparison reveals a high level of agreement; RMSE values computed from the differences between the tide model values and the corresponding filtered water level heights for PPK and PPP were 11.4 cm and 12.2 cm respectively. The difference between the PPK and PPP models shows an RMSE value of 4.1 cm and a correlation coefficient of 0.99.

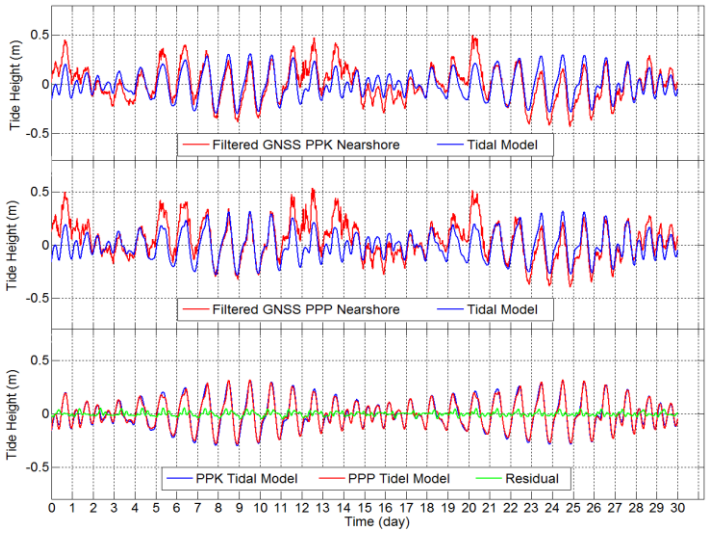

Figure 5.2: Nearshore tidal model results: Tide model obtained from GNSS-PPK water level heights (PPK tide mode, upper panel); tide model obtained from GNSS-PPP water level heights (middle panel). Comparison between both tide models (lower panel) (Note: Savitzky–Golay filter with 100 min window length has been used)

5.2.2 Offshore tidal model

Similar to the methodology implemented in the nearshore environment, the filtered GNSS-derived water level heights were processed using T_Tide in the offshore survey using the Savitzky–Golay filter with 100 min window length. The offshore results of the GNSS-derived water level heights were compared to the nearshore results to evaluate the possibility of predicting tides from offshore tidal data. As discussed in Chapter 4, the tidal data was collected during a 30-day survey in the Indian Ocean. The extracted amplitudes and phases using the PPP solution for the four tide constituents (M2, S2, K1, O1) for the offshore survey using T_Tide software are given in Table 5.2. The amplitudes and phases of the constituents differed from the nearshore environment results due to the fluctuating water heights at the different locations.

Table 5.2: Offshore environment: Tidal harmonic constituents obtained from GNSS-PPP water level heights

Const.	PPP solution	
	Amp (m)	Phase (deg)
M2	0.258	286.50
S2	0.131	192.68
K1	0.095	55.98
O1	0.051	127.29

The tidal model obtained from the filtered GNSS-PPP water level heights over 30 days is shown in Figure 5.3 (upper panel). The residual between the PPP tide model and the filtered GNSS-PPP water level heights measured from the same tide datum are shown in the lower panel of Figure 5.3. The magnitudes of the residuals are much higher, which was to be expected due to the larger fluctuation of the GNSS-derived water level height and the medium window length used (PCTMSL, 2005; <www.transport.wa.gov.au>). The RMSE of the differences between the modelled and observed water level heights increased to 17.9 cm due to the noisier offshore data. This is likely to be a result of the more dynamic effect of the offshore environment on the shipborne GNSS antenna.

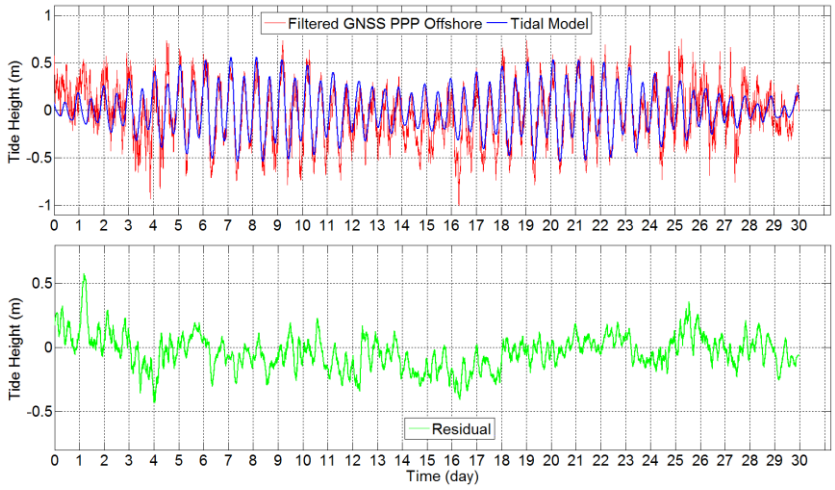

Figure 5.3: Offshore tidal model results: Tide model obtained from the GNSS-PPP water level heights (PPP tide model, upper panel); Residual between the PPP tide model and filtered GNSS-PPP water level heights (lower panel) (Savitzky–Golay filter with 100 min window length has been used)

Figures 5.2 and 5.3 show that the agreement between the modelled tide and the (filtered) water level heights varied over time. They are generally in much better agreement around the time of the Spring tide because of the greater tide variation caused by the constructive superposition of the lunar and solar tides, and the agreement is generally worse during neap tides (destructive superposition of lunar and solar tides). The residuals in the figures reflect this behaviour. Importantly, this behaviour also explains the general trend seen in the tide models, with the better modelling around the Spring tide on a 14-day cycle (and correspondingly poorer modelling around neap tide).

5.3 Tide prediction

The main focus in this section is on short-term prediction of tides based on the PPK and PPP solutions of the GNSS-derived water level heights in the nearshore and offshore environments. A particular focus is on the application of low-pass filters to reduce high-frequency noise in the GNSS-derived water level heights, and their influence on short-term tide predictions. In this section, the four principal harmonic constituents were used in modelling and predicting the tide. For a given data period, e.g. between 1 and 29 days, the harmonic constituents were derived using the T_TIDE routine, then subsequently predicted beyond the data period used to derive the tidal harmonic constituents.

Based on a maximum period of 30 days of GNSS observations, various data prediction periods from 1 to 29 days at one-day intervals were tested. These data periods were used to derive the tidal harmonic constituents, which were then used for prediction of the tide beyond the used data period. That is, based on the extracted tidal harmonic constituents from a selected number of days D, between 1 and 29 days, predictions were performed for the reminder of the month, i.e. for up to (30 – D) days. For example, the tidal harmonic constituents were derived for 7 days, and predictions are applied for a period of up to 23 days. In order to quantify the accuracy of prediction, the RMSE for the data of a particular day were derived from the residuals between the predicted tide signal and the smoothed GNSS water level heights estimated for that day.

To study the impact of high-frequency variations on tide predictions—thus indirectly investigate the possible need for smoothing—tide predictions were applied for the original (unsmoothed) and smoothed GNSS-derived water level heights (both PPK and PPP), using the four filtering techniques discussed in Chapters 3 and 4. To exemplify the impact of filtering, moderate smoothing for a 100 min window-length was examined. Prediction was applied for both environments, nearshore using PPK and PPP methods, and offshore using PPP method.

Figure 5.4a shows the daily average RMSE values (e.g. difference between predicted and given data) for unsmoothed nearshore GNSS-PPK water level height for all possible sets of observation days (used to derive the tidal harmonic constituents) and prediction days (following the observation days). The equivalent results are shown in

Figure 5.4b–e for the smoothed water levels using the four filtering techniques discussed in Chapters 3 and 4 all applying a 100 minute window length, as an example. Further, Figure 5.5 shows the equivalent results but using the unsmoothed nearshore GNSS-PPP water level height. Overall, the results in Figures 5.4 and 5.5 are very similar, thus indicating that predictions based on PPK and PPP are of similar quality.

The RMSE values clearly show that at least a few days of data are required to obtain a reasonable fit with RMSE < 10 cm. For example using only the first few days of data results in RMSE values generally larger than ±10 cm and in some cases larger than ±30 cm. To some extent the RMSE values decreased with increasing amounts of observational data as the diurnal constituents were better estimated. This is in particular the case for all smoothed data (cf. Figures 5.4b to 5.4e and 5.5b to 5.5e). The moving average filter (Figures 5.4b and 5.5b) and the Butterworth filter (Figures 5.4e and 5.5e) performed well in removing high-frequency signals and retaining the low-frequency signals, and the results from the Savitzky–Golay filter were similar to those using the Gaussian filter (cf. Section 3.7). The 'banded' structures in Figures 5.4 and 5.5 indicate some periods for which predictions are somewhat better (e.g. RMSE values below ±10 cm) and other periods that preformed slightly worse (e.g. RMSE values larger than ±10 cm). To some extent, this is related to the spring and neap tides with generally better predictions around spring tides than neap tides (see also Figure 5.7).

Figure 5.6 illustrates the RMSE values for the unsmoothed and smoothed offshore GNSS-PPP water level heights. Due to the more dynamic nature of the offshore environment it can now be seen that filtering becomes important as the RMSE values related to the unsmoothed data are generally above ±50 cm while dropping to values well below ±30 cm after applying filtering.

Overall, the results for the filtered signals show considerably more occasions when the RMSE values fall below ±10 cm e.g. indicate the overall improvements due to filtering. While the improvement of the prediction is rather modest in the nearshore environment, e.g. there are a few more occasions when the RMSE value is greater than 30 cm for the unsmoothed data than the smoothed data the improvement is considerable for the offshore environment. Regarding the choice of filter technique for the prediction, it seems that all filters perform in a very similar way.

Comparing nearshore with offshore, the average of the RMSE values (all combinations of observation and prediction periods) of the four filters for nearshore PPK and PPP are ±13.5 cm and ±14.1 cm, respectively. Meanwhile, the average of RMSE values for offshore PPP is ±24 cm. Again this documents the noisier data in the offshore environment. Also, the use of PPK and PPP is of lesser importance for the nearshore area as documented by very similarly performance of the predictions. For the offshore area, it shows that filtering the data is more important for tidal prediction. This is further documented by the average of the RMSE values of unsmoothed GNSS-PPP water level heights of ±81 cm and the average of the RMSE value of smoothed data for all four filters drops significantly to ±24 cm.

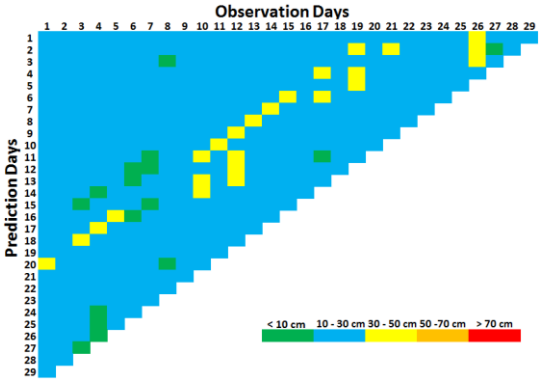

(a)

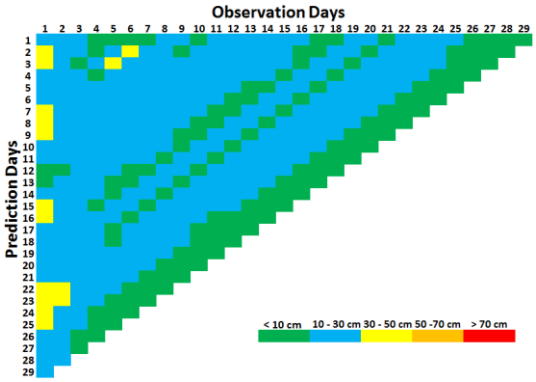

(b)

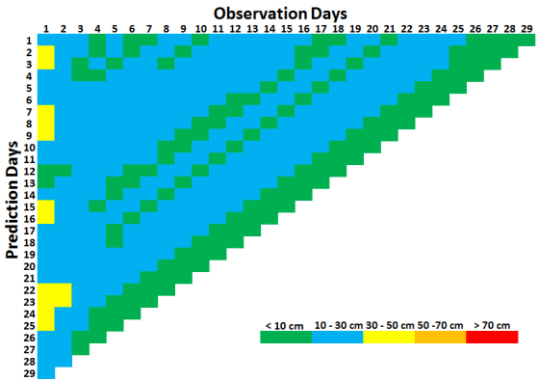

(c)

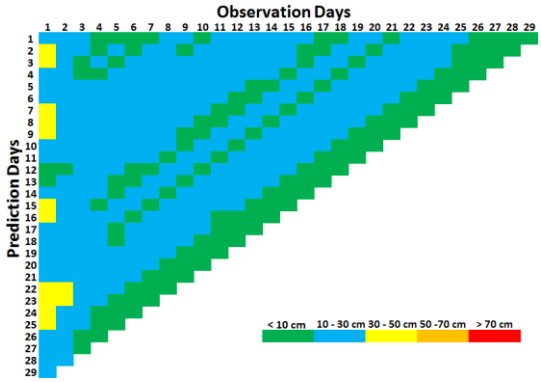

(d)

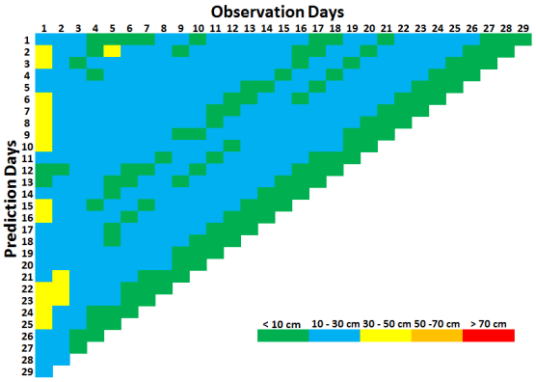

(e)

Figure 5.4 : RMSE values for various daily combinations of the predicted tide for the nearshore GNSS-PPK water level heights for the following cases: (a) Unsmoothed GNSS-PPK water level height; (b) moving average filter; (c) Savitzky–Golay filter; (d) Gaussian filter; (e) Butterworth filter. Days indicate the number of days used to derive the tidal harmonic constituents. Prediction days indicate the number of days for which the tide signal has been predicted beyond the used observation days

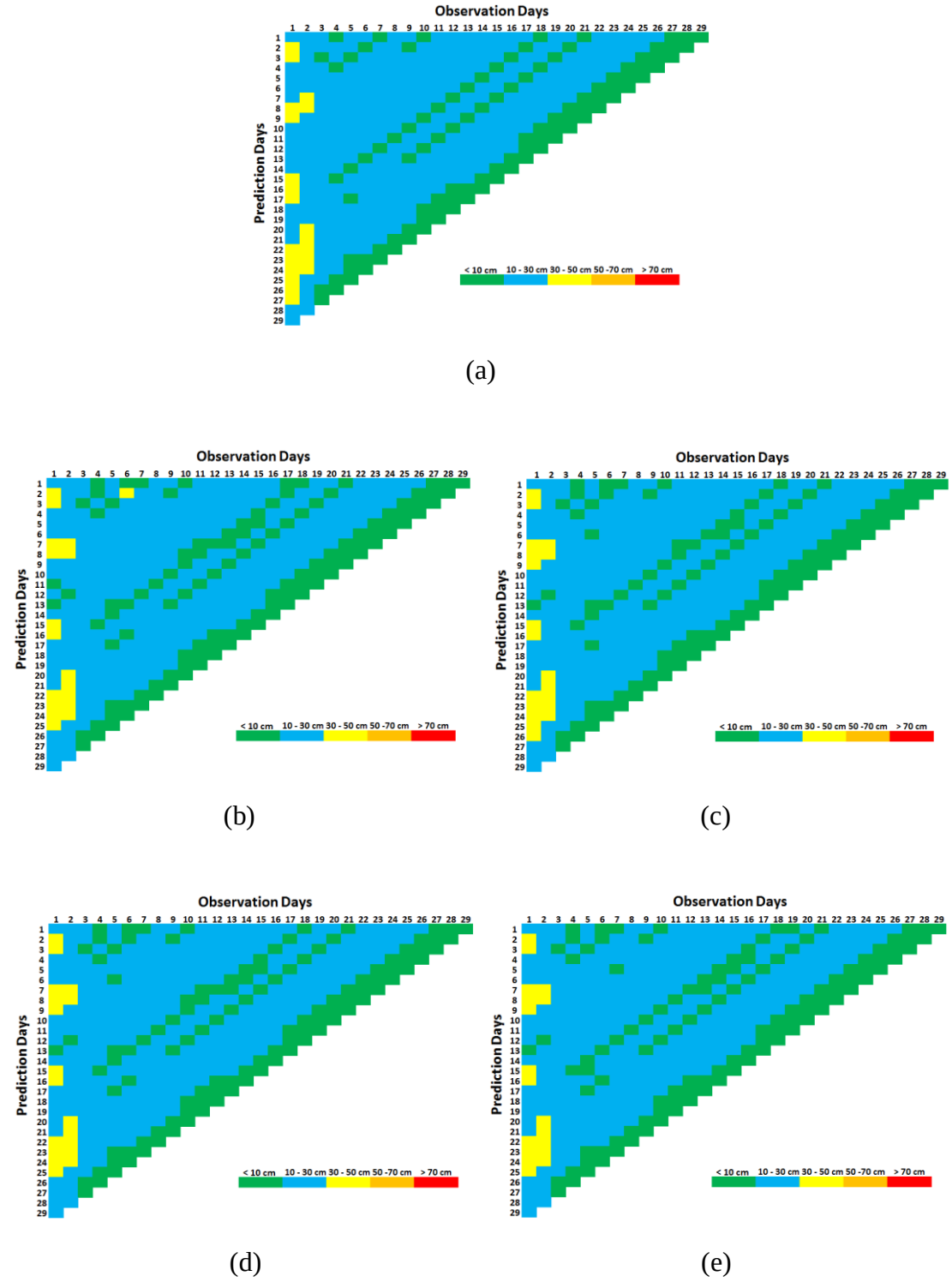

Figure 5.5: RMSE values for various daily combinations of the predicted tide for the nearshore GNSS-PPP water level heights for the following cases: (a) Unsmoothed GNSS-PPP water level height; (b) moving average filter; (c) Savitzky–Golay filter; (d) Gaussian filter; (e) Butterworth filter. Days indicate the number of days used to derive the tidalharmonic constituents. Prediction days indicate the number of days for which the tide signal has been predicted beyond the used observation days

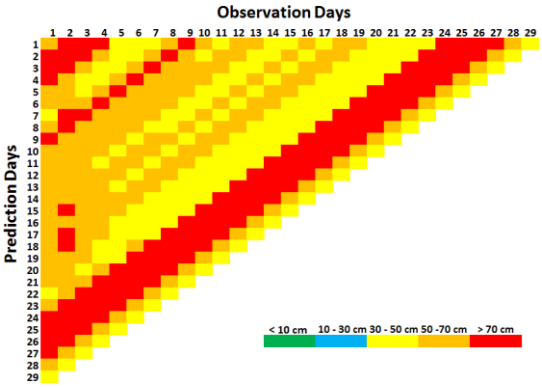

(a)

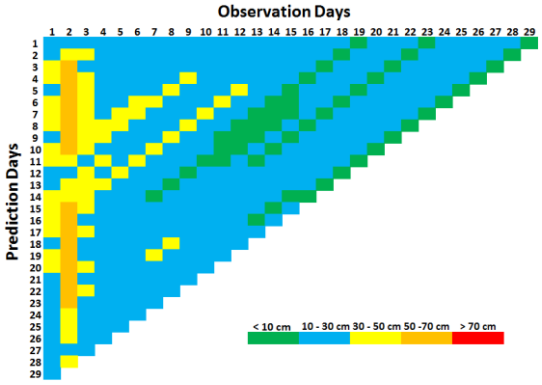

(b)

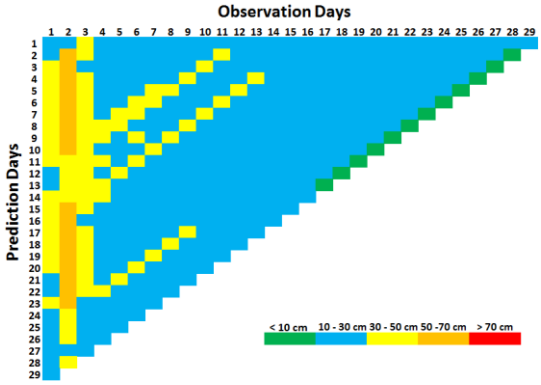

(c)

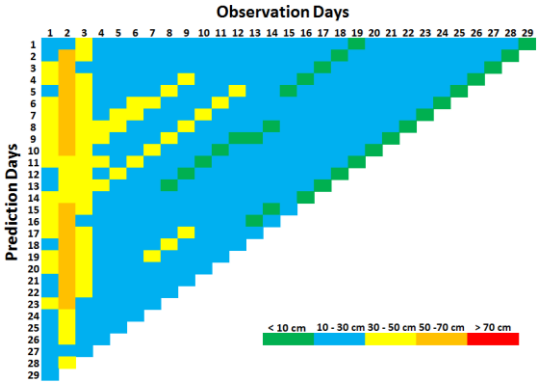

(d)

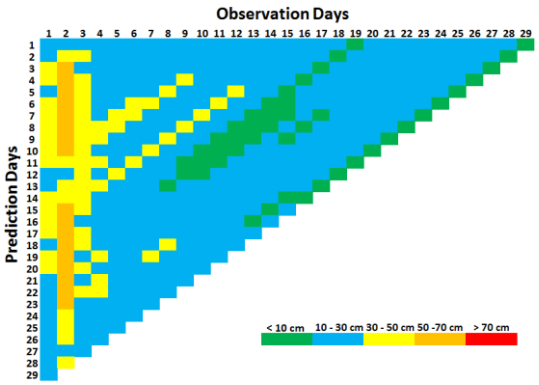

(e)

Figure 5.6: RMSE values for various daily combinations of the predicted tide for the offshore GNSS-PPP water level heights for the following cases: (a) Unsmoothed GNSS-PPP water level height; (b) moving average filter; (c) Savitzky–Golay filter; (d) Gaussian filter; (e) Butterworth filter. Days indicate the number of days used to derive the tidal harmonic constituents. Prediction days indicate the number of days for which the tide signal has been predicted beyond the used observation days

The smoothed and unsmoothed offshore GNSS-PPP water level heights are shown in Figure 5.6. The colour scale shows that all days had an RMSE between 10 cm and 30 cm, attributable to the dynamic environment (data noise). Again, the prediction accuracy increased with increasing the period of the observational tide data. Thus, tidal prediction accuracy was reasonable, with low RMSE, especially for predictions four days ahead of tide observation, both for nearshore and offshore GNSS-derived water level heights.

As an example, Table 5.3 shows the prediction RMSE for nearshore PPK and PPP and offshore PPP using selected periods of 5-days, 15-days and 23-days of observational data used to derive the tidal harmonic constituents. The RMSE values noted in Table 5.3 clearly show that the RMSE decreased with increasing length of the observation period and consequently decreasing prediction period. Figure 5.7 shows the filtered GNSS water level height using the moving average filter with 100 min window length as an example for (a) nearshore GNSS-PPK water level height, (b) nearshore GNSS-PPP water level height, and (c) offshore GNSS-PPP water level height. It is clear that the predictions based on only five days of data varies more from the filtered data than using 15 and 23 days.

Table 5.3: Selected RMSE for the nearshore (PPK and PPP) tide models and offshore PPP tide model using different length of observation data. The RMSE values are based on the difference between the predicted tide and smoothed GNSS-derived water level heights for the remainder of the 30-day data period

Length of observations (days)	Prediction period (days)	PPK nearshore (cm)	PPP nearshore (cm)	PPP offshore (cm)
5	25	12.1	13	20.4
15	15	11.8	12.6	16.6
23	7	11.5	11.9	15.3

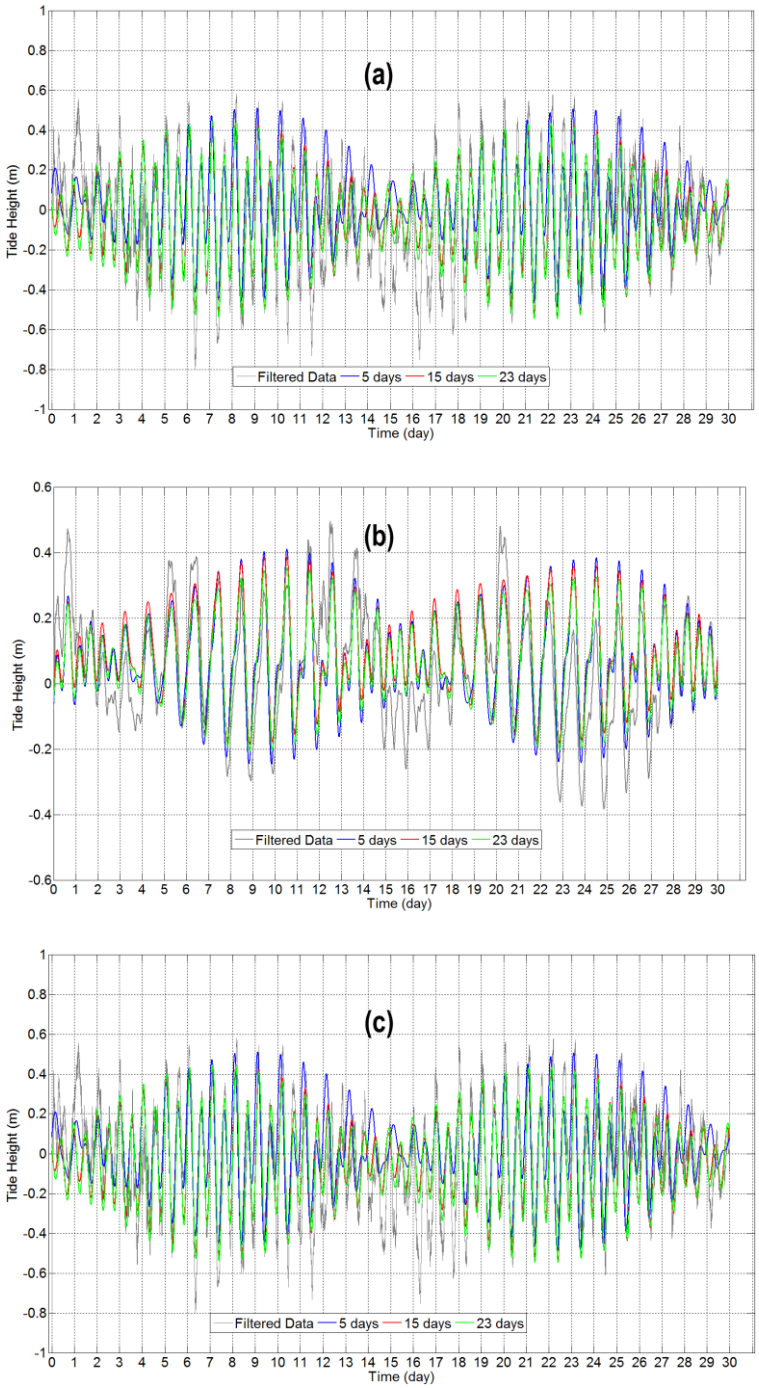

Figure 5.7: Comparison between selected prediction scenarios using different periods of observation data (5, 15 and 23 days) and filtered GNSS-derived water level height data (cf. Table 5.3). (a) Nearshore GNSS-PPK; (b) nearshore GNSS-PPP; and (c) offshore GNSS-PPP (Note: Moving average filter with 100 min window length has been applied as an example)

According to the IHO standards, the tide must be known to within ± 5 cm at the 95% confidence level for Special Order surveys, and must not to exceed ± 10 cm for any other order at the tide gauges for nearshore applications (e.g. shallow waters). In

offshore environments, the accuracy level requirement is less stringent, depending on the water depth. Thus, in practice, tidal variations are often neglected. From the RMSE values, the orders that can be assigned may be determined by the predicted tide based on the observational data period, as detailed above. The nearshore GNSS water level height determined by using PPK and PPP meet Order 1 in some cases (e.g. RMSE < ±10 cm), while offshore GNSS-PPP water level height meets Order 2 in only a few cases (e.g. RMSE < ±10 cm). On the other hand, both predictions for PPK and PPP in the nearshore and PPP in the offshore environments do not satisfy IHO standards for special order surveys (e.g. RMSE < ±10 cm). This situation may improve when using longer data periods, as stipulated by the IHO, setting a limit of no less than 30 days of data for the production of tide tables (IHO, 2008). In this study, the improvement can be seen when using 29 days of observation data and only one day of prediction leading to consistently small RMSE values (e.g. in all but one case RMSE < ±10 cm, cf. Figures 5.4, 5.5 and 5.6).

5.4 The benefits of GNSS offshore

The advantages of using GNSS in offshore areas can be summarised as follows:

- GNSS allows precise positioning in extensive ocean areas where it was not previously possible.
- GNSS has the potential to reduce costs and time of positioning offshore.
- It can be used to estimate the height of the water level for tide information in real time for hydrographic surveying, marine geodesy, and physical oceanography. Tide information is very important for hydrographic surveying, for sounding reductions to a common datum (e.g. chart datum). Moreover, it can indirectly improve meteorological modelling and weather forecasting.
- It can also improve the reliability and availability of positioning/navigation in maritime activities with improved safety of navigation and reduced risk of maritime accidents and oil spills. There are also benefits of GNSS in offshore oil and gas operations and in bathymetry (Acil Allen consulting, 2013).
- Using GNSS receivers on a vessel or buoy offshore to obtain wave data using the PPP technique to observe high-frequency sea level variations could be used in natural weather warning systems, such as to identify anomalous sea level variations produced by a tsunami. This will be further discussed in the next section.

5.5 Tsunami early warning system by using GNSS

The results in Section 5.3 show that the use of kinematic GNSS heights for precise short-term tide prediction may be limited, but could have important applications in areas of poor tide gauge coverage or in the open ocean where the IHO standards are less stringent than in shallow waters. For example, it may serve as an additional sensor for the detection of anomalous sea-level variations, such as may be caused by a tsunami. The PPP technique facilitates centimetre-level accuracy positioning using carrier phase observable with real-time precise satellite orbits and clock corrections as external information (El-Mowafy and Deo, 2017). PPP requires no reference station and is not limited by a baseline length, unlike other precise positioning methods such as RTK or DGPS. It is necessary to use PPP for long periods of time for conversion and initialisation of carrier phase ambiguities. For tsunami early warning systems, observations over long periods are possible because GNSS operate continuously. Nearfield tsunami early warning systems for coastal regions should be able to provide a warning as early as 5 to 10 min (Hoechner, Ge, Babeyko, & Sobolev, 2013). Some practical examples are the Jet Propulsion Laboratory's GPS Real Time Earthquake and Tsunami Alert project (GREAT) (http://www.gdgps.net/products/great-alert.html); Real-Time Earthquake Analysis for Disaster mitigation network (READI) (http://sopac.ucsd.edu/readi.shtml); NASA-NOAA GPS-Aided Tsunami Early Detection (GATED) system (https://appliedsciences.nasa.gov/content/11-disaster11d-0021); Earthquake Early Warning and Tsunami Warning of Japan (http://www.jma.go.jp/en/tsunami/), and the German Indonesian Tsunami Early Warning System (GITEWS) (http://www.gitews.org/en/). These systems use a dense network of GNSS receivers at Continuous Operating Reference stations (CORS) and sea buoys, set up at strategic locations for monitoring land displacement and sea level fluctuations. The use of GNSS on board of ships at anchor was also proposed for disaster prevention and sea monitoring (Saito and Kubo, 2016).

As mentioned in Chapter 2, external information of precise satellite orbits and clock data is necessary for real time kinematic PPP analysis. In the offshore area, this external information is typically not acquired by the Internet; rather, commercial services, e.g., Fugro Starfix, Trimble RTX and StarFire provide precise orbit and clock corrections for PPP corrections in real time. The objective is to achieve real-time PPP with less than 10 cm error in the vertical plane (El-Mowafy, Deo, & Kubo, 2017).

Fugro Sarfix utilises PPP technology, which differs from the traditional differential approach insofar as satellite errors are not aggregated but are estimated at source on each satellite. The GNSS orbit and clock corrections are computed separately, free of ionospheric and tropospheric effects, with errors of 10 cm (2σ level) Dixon, 2006; Inazu et al., 2016; Sharpe, Hatch, & Nelson, 2000).

The core of using GNSS for tsunami early warning could be based on the constant prediction of the tide over a relatively short period (e.g. minutes to hours) based on preceding (smoothed) water level observations and instantaneous comparison with new (smoothed) water level observations. For early warning of a tsunami, short-term tide predictions, e.g. minutes to hours (e.g. RMSE values for all predictions considered in Section 5.3 are between 2 cm and 8 cm), can serve as a threshold for recognising fluctuation of the water level. Investigations have shown that the actual propagation of a tsunami can be monitored by checking the amplitude of the filtered signal against a prescribed threshold (Consoli, Recupero, & Zavarella., 2014). In the absence of a tsunami or other anomalous conditions (e.g., storm surge), the predicted tide signal should fit the actual water level within the limits illustrated in Section 5.3, which can then be used to define a meaningful threshold at a particular location. With better predictions, by improved filtering performance for example, a lower threshold could be prescribed, which would enable smaller tsunamis to be detected, and then tsunami warning is triggered to initiate the required response measures on land (Inazu et al., 2016).

A result of this study is that improved filtering techniques to reduce signal noise and measurement error and/or prediction models (e.g. accounting for an increased number of tidal constituents) are needed. With improved estimation accuracy and satellite corrections, GNSS water level height observations can be used to replace tide gauge data for tide prediction in offshore areas, which might not be available for this purpose, and incidentally improve early detection of offshore tsunamis in real time.

5.6 Chapter summary

In this chapter, a tide model was used to extract the four major tidal constituents M2, S2, K1 and O1 for nearshore areas using PPK and PPP and offshore using PPP. The tidal model compares unsmoothed and smoothed water level heights using the Savitzky–Golay filter with 100 min window length over a 30-day period (nearshore

and offshore). The RMSE determined from the difference between the observed data and the nearshore tidal model was 11.6 cm for PPK and 13 cm for PPP, with a correlation coefficient of 0.99 for both. The RMSE between the offshore tidal model and observed values increased to 17.9 cm because of the noisier data in the more dynamic offshore environment.

The four major tidal constituents M2, S2, K1 and O1 were used to predict the tide. The GNSS observations taken over various combinations of data prediction periods were tested. The four low-pass filtering techniques, namely: moving average, Savitzky–Golay, Gaussian and Butterworth were used to show the impact of high-frequency variations on the tide prediction.

The results show the benefit of using GNSS-derived water level heights to detect anomalous sea level variations such those caused by a tsunami. GNSS methods can be used for a tsunami early warning system through monitoring actual water level observations and comparing them with short-term tide predictions (e.g. minutes to hours) where a threshold based on the RMSE values between 2 and 8 cm can be set. Moreover, GNSS methods can play a main role as a replacement for tide gauges. Finally, it is possible to use GNSS height-estimate tide information in offshore areas for real time applications such as hydrographic surveying, marine geodesy and physical oceanography.

Chapter 6:

Conclusions and Recommendations

Information and predictions of tide heights are of great importance in marine hydrographic surveys to reduce raw water-depth observations to a common datum, e.g. chart datum. Continuous tide measurements are needed and recorded at stations around the world wherever there is marine activity, for instance for port and harbour operations, marine navigation, dredging and other shoreline engineering, management and maintenance works. Any activity that requires highly accurate and continuous knowledge of water depths must be able to access tidal information at any time. Traditionally, tide variations are determined from an analysis of long-term sea-level data. Furthermore, sea-level change has recently been suggested as one of the most sensitive indicators of climate change, and it is predicted to have a significant impact on the socioeconomic development of many countries. Some 2.5 billion people live less than 60 km from the sea, and this zone supports the greatest biological diversity worldwide (Schöne, 2011). Assessment of rising sea levels associated with climate change requires very accurate tide information for efficient coastal management.

For many decades, it has only been possible to measure water levels by means of tide gauges fixed at points convenient to the observer. Needless to say, such observations give a limited view of true global and regional movements in the overall sea level. Moreover, two main issues relating to tide gauge measurement are that (i) it must be corrected for vertical land movement, and (ii) it relies on its relation to benchmarks on land.

In the last two decades, GNSS observations have come into common usage in hydrographic surveying, due in part to the ease of horizontal positioning that the method offers. In addition, the height of the water surface during a survey can be measured in real time using GNSS, a feature that is not possible using traditional tide gauge stations. GNSS is easy to install and use on a floating platform such as a vessel or buoy. It is beneficial in hydrographic surveying in other ways—in particular, offering lower cost and greater efficiency. In this regard, multi-GNSS has several advantages for tide determination over traditional relative positioning methods using one GNSS only (e.g., GPS), especially in the offshore environment. In addition, GNSS may act as an additional sensor for detecting unusually large changes in the mean sea surface height or slope (such as that associated with a tsunami, as discussed) in order to promptly alert local communities and minimise human losses and to respond adequately to provide the required humanitarian aid.

This chapter summarises the research activities in this thesis and its outcomes in terms of tide height determination using GNSS, and suggests recommendations for improvements and further research. The objectives and questions for this thesis are reiterated to show how these were achieved.

Research in this thesis dealt with tide height determination using GNSS methodology to derive water level heights over space and time. Four objectives were stated at the beginning of the study in Chapter 1. These objectives were achieved in a number of steps: the clear understanding of tide determination from GNSS-derived water level heights at sea in terms of its definition and difficulties are illustrated in Chapter 2. Chapter 3 provides an outline of the research methodology, presenting the GNSS positioning techniques PPK and PPP that were used to estimate water level heights, and the different types of low-pass filters for extracting the low-frequency tide variations and filtering out high-frequency noise from the GNSS signal in sheltered coastal waters (nearshore). Tide gauge observations were used as an independent reference for GNSS-derived water level heights in the nearshore study area.

The challenges in an offshore environment, including the effect of the dynamic environment on GNSS water level height estimation and subsequent extraction of tide information, are addressed in Chapter 4: in particular, the effect of non-tidal processes on a survey vessel, such as wave activity and the attitude of the vessel itself (roll, pitch,

heave and dynamic draft) during GNSS height observations. In addition to presenting and discussing the results, Chapters 3 and 4 also review the results in relation to IHO standards.

Based on the findings of Chapters 3 and 4, Chapter 5 examines the feasibility of short-term tide modelling and prediction from GNSS-derived water level heights as an alternative to the traditional approach of using observations at tide gauge stations. In particular, the performance of short-term tide predictions is assessed for various periods of data, and performance of four filtering techniques are discussed. Finally, the use of GNSS for significant applications, such as monitoring anomalous sea level variations due to tsunamis is discussed.

6.1 Conclusions

The following points provide brief summaries of the studies described in Chapters 3, 4 and 5, and present the main findings and conclusions derived upon them.

- Chapter 3 presented the analysis and results of a 30-day period of continuous GNSS-derived water level heights determined at Hillarys Boat Harbour in Western Australia. The location is a sheltered harbour site (i.e., nearshore), with a GNSS receiver mounted on a pontoon in a controlled environment with no boat traffic in the near vicinity (i.e., no vessels being moored). Thus, the effects of sea swell and vessel motion were mostly not present. Tide readings at a tide gauge station located approximately 348 m from the GNSS antenna were used as an independent reference for GNSS-derived water level heights. Two GNSS positioning techniques were used in the processing of GNSS code and carrier phase observables and for estimating height at each epoch of the observations. Post-processed kinematic (PPK) approach was carried out using the IGS station CUT0, located approximately 25 km from the test site, as a reference station. In addition, precise point positioning (PPP) was processed using the CSRS-PPP service. Both solutions were evaluated as to their ability and performance in extracting the tide signal.

  Tide gauge observations and GNSS data were reduced to a common datum to enable the two methods to be directly compared. The GNSS-derived water level heights were computed as ellipsoidal heights relative to the WGS84 ellipsoid. Tide gauge heights were related to the chart datum used at Hillarys

Boat Harbour. The Australian Height Datum (AHD) was used as the common reference for both and hence their results were reduced to this datum. The results showed that both the PPK and PPP GNSS-derived water level heights were closely correlated with the tide gauge time series, a finding that was confirmed by correlation coefficients of 0.98 and 0.97, respectively, and a high correlation coefficient between the PPK and PPP time series of 0.96. The standard deviations of the PPK–tide gauge differences and PPP–tide gauge differences were 2.9 cm and 4.3 cm, respectively. The difference is due to that PPP was processed in a float ambiguity solution whereas PPK processing applies a fixed ambiguity resolution in addition to any small biases not modelled with high accuracy in PPP processing (e.g. high-order ionosphere, etc.). The standard deviation of the PPK–PPP differences was 4.8 cm, with indications that the PPP results were the more highly variable of the two. Based on these comparisons, each of the GNSS techniques was considered to be a workable alternative to tide gauge observations.

For the purpose of validating the precision of the GNSS-derived water level heights using the PPK and PPP positioning techniques, a static baseline with a similar distance to the reference station was measured by GNSS and processed in the kinematic mode in exactly the same way as the water levels were estimated. Signal noise in PPP mode was 3.1 cm, and 2.2 cm for PPK.

Four low-pass statistical filters (moving average, Savitzky–Golay, Gaussian and Butterworth) are described in detail in Chapter 3. The purpose of these were to separate the low-frequency water level tide signals from the high-frequency signals generated by surface waves together with observation errors. To assess the performance of each of the filters over several window lengths (i.e., the degree of smoothing), the amplitudes and phases of the four major tidal harmonic constituents M2, S2, K1 and O1 were first determined by the fast Fourier transform method. Because these four constituents dominate the tide behaviour and magnitude, they were considered to be sufficient for testing the capabilities of the filters. The constituents derived from the filtered tide information obtained by GNSS (PPK and PPP) and tide gauge observations were compared. The results indicated that, while all of the filters successfully

removed the high-frequency signals, some damped the amplitude of the low-frequency tide signal excessively.

The Savitzky–Golay filter was found to best maintain the low-frequency tidal harmonic constituents of the PPK signal, with 1 mm damping effect. The Gaussian filter produced 2.2 cm damping over the longest (360-minute) window length. The maximum damping by the Savitzky–Golay filter for PPP was 2 mm (cf. 2.5 cm for the Gaussian filter). The maximum damping effect of both filters meet current IHO standards for a Special Order surveys. The moving average and Butterworth filters performed similarly, but produced stronger damping of the low-frequency tidal constituents. Nonetheless, the maximum damping by both of these filters was 6 cm and 5.6 cm respectively for PPK at a window length of 360 minutes, and 6.2 cm and 6.1 cm for PPP. These filters therefore also meet lower IHO standards (< 10 cm) and thus deem appropriate for other Survey Orders.

- Chapter 4 outlined the approach and results of the offshore GNSS-derived water level heights by GNSS-PPP measured on a survey vessel in the open ocean. Considerably more variation was found in the observed water level heights due to the more dynamic character of the offshore environment. The challenges and factors that have an impact on measuring GNSS-derived water level heights in offshore surveys were discussed, together with their correction for wave activity and attitude of the vessel (roll, pitch, heave) and draft. The procedure for assessing filter performance offshore was identical to that in Chapter 3 for the same four types of low-pass filter, used with different window lengths to extract the amplitudes and phases of the four major tidal harmonic constituents as before. Again the results showed the ability of all filters to extract low-frequency tide variations and filter out high-frequency variations.

  The filters also showed considerable damping effects over longer window lengths. Damping by the moving average and Butterworth filters was very similar, reaching a standard deviation (95% confidence) of 14.8 cm for the longest window length of 360 minutes. The damping effect of the Savitzky–Golay and Gaussian filters for a maximum window length of 360 minutes was 0.7 cm and 6.8 cm respectively, still within the IHO standard requirement of ±10 cm at 95% confidence level.

The accuracy of the offshore GNSS-PPP processing was variable, with larger errors than for the nearshore environment. The additional variability in the offshore environment after applying propagation of variance came to 78.2 cm, much larger than the 2 cm for the nearshore environment due to the dynamic variations. The quality of height estimation was found to depend on the location (geometry) and the number of satellites in view.

- Chapter 5 investigated short-term tide modelling and prediction using GNSS-derived water level heights in both nearshore and offshore environments. Short-term tide modelling and prediction utilised the GNSS-derived water level heights determined by PPK and PPP in the nearshore environment (described in Chapter 3), and by PPP offshore (given in Chapter 4). As in Chapters 3 and 4, since the four tidal harmonic constituents capture the majority of the tidal signal in both the nearshore and offshore areas, they were considered to be sufficient for this investigation.

  The harmonic constituents M2, S2, K1 and O1 were derived by the T_TIDE routine in MATLAB and used to model and predict the tide for a given data period. Various combinations of data prediction periods selected from the 30-day GNSS observations were tested for periods from 1 to 29 days, increasing by one-day intervals, to derive the tidal harmonic constituents.

  Finally, the use of GNSS-PPP water heights for modelling and predicting tides in the offshore environment was presented for the important applications of (i) detecting anomalous sea level variations that are caused by tsunami or a storm surge, and (ii) replacing tide gauge observations by GNSS height measurements to obtain tide information. To perceive a tsunami, the system needs to predict the next occurring tide signal and compare it with the observed tide signal within the same time interval. If the difference between the two signals exceeds a certain threshold, and occurs several times consecutively, then it is likely that a tsunami is occurring in the observed zone and the tsunami warning is triggered to initiate the required response measures on land. The tidal analysis and prediction methodologies and the best low-pass filtering techniques are presented in this chapter. These are the crucial elements needed to provide a high probability and a correct tsunami warning.

6.2 Recommendations

In this research, the two GNSS, e.g. GPS and GLONASS were used. Therefore, further studies would benefit from combining observations from several multi-GNSS constellations. For example, using GPS, GLONASS, Galileo and BeiDou signals together would significantly increase the number of observations in a combined phase-delay analysis, improving redundancy and precision, increase the potential for improve positioning accuracy and obtaining GNSS water level height estimates. Further testing in both nearshore and offshore environments is recommended that include more advanced PPP methods once evidently well established, such as PPP with integer ambiguity resolution and what is known as PPP-RTK. Application of these methods in real-time when available will give more insight into the capability of these techniques for tide estimation and real-time monitoring of fluctuations of the sea surface.

To optimise the usefulness of the original data series, it is possible to use the entire dataset to compute the spectrum of both the tidal constituents and the motion of the vessel. In this research, only heave corrections were recorded and removed from GNSS-derived water level heights; other information (heading pitch and roll determined during calibration time, and composite angle offset from IMU from the local vertical in the transverse plane of the vessel) were applied to the original GNSS observations during survey operations in this study. In order to meet the higher standards of accuracy demanded for many applications, the motion data must be determined and removed from the data.

Although four types of low-pass filters were rigorously tested, further studies are required to include other filtering techniques, together with optimal window lengths, to remove high-frequency noise and retain the low-frequency tide signal. It can be envisaged that the GNSS water level height is capable of greater accuracy and improved capabilities.

The four major tidal harmonic constituents M2, S2, K1 and O1, representing the combined lunar and solar tides, were acquired in this research. It is recommended that future studies include more or all tidal harmonic constituents to give more robust uncertainty estimates, which are then propagated by the prediction computations. This would give an improved estimate of the GNSS-derived water level height and enhance

tidal model identification and prediction using GNSS heights in offshore environments, and provide a reliable method of tsunami detection. In the nearshore environment, GNSS systems might well replace traditional tide gauges.

References

Aarup, T., Merrifield, M., Perez, B., Vassie, I., & Woodworth, P. (2006). *Manual on sea-level measurements and interpretation, volume IV: An update to 2006*. JCOMM Technical Report No. 31. Paris: Intergovernmental Oceanographic Commission of UNESCO.

Abd Rabbou, M. and El-Rabbany, A. (2015). PPP accuracy enhancement using gps/glonass observations in kinematic mode. *Positioning*, 6, 1-6.

Acil Allen consulting. (2013). Precise positioning services in the maritime sector. Accessed from www.ignss.org/LinkClick.aspx?fileticket=b%2F3x6KEaFS4%3D&tabid=56

Alsaaq, F., Kuhn, M., El-Mowafy, A., & Kennedy, P. (2016). Filtering methods to extract the tide height from Global Navigation Satellite Systems (GNSS) signals for hydrographic applications. Paper presented at the *IFHS hydro conference 2016: State of the art GNSS techniques, 08–10 November, Rostock, Germany*.

Amiri-Simkooei, A., Zaminpardaz, S., & Sharifi, M. (2014). Extracting tidal frequencies using multivariate harmonic analysis of sea level height time series. *Journal of Geodesy*, 88(10), 975–988.

Awange, J. L. (2012). *Environmental monitoring using GNSS: Global navigation satellite systems*. Heidelberg: Springer.

Beaudoin, J., Calder, B., Hiebert, J., & Imahori, G. (2009). Estimation of sounding uncertainty from measurements of water mass variability. *International Hydrographic Review*, 2, 20–38.

Bisnath, S., & Gao, Y. (2009). Current state of precise point positioning and future prospects and limitations. In M. G. Sideris (Ed.), *Observing our changing earth: Proceedings of the 2007 IAG General Assembly, Perugia, Italy, 2–13 July* (pp. 615–623). Berlin: Springer.

Bisnath, S., Wells, D., Howden, S., Dodd, D., Wiesenburg, D., & Stone, G. (2004). Development of an operational RTK GPS-equipped buoy for tidal datum determination. *The International Hydrographic Review*, 5(1), 54 –64.

Bonnefond, P., Exertier, P., Laurain, O., Ménard, Y., Orsoni, A., Jeansou, E., … Born, G. (2003). Leveling the sea surface using a GPS-catamaran special issue: Jason-1 calibration/validation. *Marine Geodesy*, 26(3–4), 319–334.

Bouin, M.-N., Ballu, V., Calmant, S., & Pelletier, B. (2009). Improving resolution and accuracy of mean sea surface from kinematic GPS, Vanuatu subduction zone. *Journal of Geodesy*, 83(11), 1017–1030.

Bowditch, N. (2002). *The American practical navigator: An epitome of navigation* (Bicentennial edition). Bethesda, MD: National Imagery and Mapping Association.

Briggs, M. (2009). *Ankudinov ship squat predictions–Part I: Theory and FORTRAN programs.* Coastal and Hydraulics Engineering technical note ERDC/CHL CHETN-IX-19. Vicksburg, MS: US Army Engineer Research and Development Center.

Brown, N., Featherstone, W., Hu, G., & Johnston, G. (2011). AUSGeoid09: A more direct and more accurate model for converting ellipsoidal heights to AHD heights. *Journal of Spatial Science*, 56(1), 27–37.

Bureau of Meteorology (BOM), 2015. Australian baseline sea level monitoring project hourly sea level and meteorological data. Accessed from http://www.bom.gov.au/oceanography/projects/abslmp/data/ (March. 3, 2015).

Capuano, P., De Lauro, E., De Martino, S., & Falanga, M. (2011). Water level oscillations in the Adriatic Sea as coherent self-oscillations inferred by independent component analysis. *Progress in oceanography*, 91(4), 447–460.

CARIS 2009. *Hips and sips 7.0 user guide.* Caris Company. Assessed on-line June 2016 http://www.caris.com/Documentation\CARIS HIPS & SIPS 7.0 Users Guide.pdf

Cartwright, D. E. (2000). *Tides: A scientific history*. Cambridge, UK: Cambridge University Press.

Cartwright, D., & Edden, A. C. (1973). Corrected tables of tidal harmonics. *Geophysical Journal International*, 33(3), 253–264.

Cartwright, D., & Tayler, R. (1971). New computations of the tide-generating potential. *Geophysical Journal International*, 23(1), 45–73.

Calder, B. (2006). On the uncertainty of archive hydrographic data sets. *IEEE Journal of Oceanic Engineering* 31(2), 249–265.

Calder, B., (2013). Distribution-free, variable resolution depth estimation with composite uncertainty, in *Proceedings of the U.S. Hydro Conference, 26–28 March, New Orleans, Louisiana*.

Chang, C. C., Lee, H. W., & Tsui, I. F. (2002). Preliminary test of tide-independent bathymetric measurement based on GPS. *Geomatics Research Australasia*, 76, 23–36.

Cheng, K.-c. (2004). Radar altimeter absolute calibration using GPS water level measurements. Retrieved from https://kb.osu.edu/dspace/handle/1811/78647

Chia-chyang, C., & Hsing-wei, L. (2003). Evaluation of GPS-based attitude parameters applied to bathymetric measurements. *Wuhan University Journal of Natural Sciences*, 8(2), 685–692.

Church, I. (2008). *Developing a nested finite-element hydrodynamic model to predict phase and amplitude modification of the tide within narrow fjords.* (Unpublished masters dissertation). University of New Brunswick, Frederickton, NB.

Consoli, S., Recupero, D. R., & Zavarella, V. (2014). A survey on tidal analysis and forecasting methods for tsunami detection. *Science of Tsunami Hazards*, 33(1), 1–56.

Dawidowicz, K. (2014). Sea level changes monitoring using GNSS technology: A review of recent efforts. *Acta Adriatica*, 55(2), 145-161.

DeLoach, S. R. (1995). *GPS tides: A project to determine tidal datums with the global positioning system* (No. TEC-0071). Alexandria, VA: Army Topographic Engineering Center.

Deurloo, R. (2011). *Development of a Kalman filter integrating system and measurement models for a low-cost strapdown airborne gravimetry system.* (Unpublished doctoral dissertation). University of Porto, Porto, Portugal.

Dixon, K. (2006). StarFire: A global SBAS for sub-decimeter precise point positioning. Paper presented at *The 19th International Technical Meeting of the Satellite Division of The Institute of Navigation (ION GNSS 2006) September 26–29 2006*, Fort Worth, TX.

Dodd, D., & Mills, J. (2011). Ellipsoidally referenced surveys: Issues and solutions. *The International Hydrographic Review* (6), 19–30.

Dodd, D., Mills, J., Battilana, D., & Gourley, M. (2010). Hydrographic surveying using the ellipsoid as the vertical reference surface. Paper presented at the *FIG Congress 2010: Facing the Challenges – Building the Capacity, Sydney, Australia, 11–16 April.*

Doodson, A. T. (1921). The harmonic development of the tide-generating potential. Proceedings of the Royal Society of London. *Series A, containing papers of a Mathematical and Physical Character*, 100(704), 305–329.

Doodson, A. T., & Warburg, H. D. (1941). *Admiralty manual of tides*. London: HM Stationery Office for the Hydrographic Department, Admiralty.

Dronkers, J. (1975). *Tidal theory and computations*. New York: Academic Press.

Ducarme B, Venedikov AP, Arnoso J, Vieira R (2006b) Analysis and prediction of ocean tides by the computer program VAV. In: *Proceedings of the 15th international symposium on earth tides, Journal of Geodynamics* 41, 119–127

El-Mowafy, A. (2000). Performance analysis of the RTK technique in an urban environment. *Australian Surveyor*, 45(1), 47–54.

El-Mowafy, A., (2012). Precise real-time positioning using network RTK, in S. Jin (Ed.), Global Navigation Satellite Systems: Signal, Theory and Applications (pp. 161–188). Croatia: InTech.

El-Mowafy A. & Deo, M (2017). Bridging real-time precise point positioning in natural hazard warning systems during outages of MADOCA corrections. In Proceedings of ION Pacific PNT-2017, Honolulu, Hawaii, May 2017, (pp. 514–525). Manassas, VA: ION.

El-Mowafy, A., Deo, M., & Kubo, N. (2017). Maintaining real-time precise point positioning during outages of orbit and clock corrections. *GPS Solutions*, 21(3), 937–947.

El-Mowafy, A., Deo, M., & Rizos, C. (2016). On biases in precise point positioning with multi-constellation and multi-frequency GNSS data. Measurement Science and Technology, 27(3). doi: 10.1088/0957-0233/27/3/035102

El-Rabbany, A. (2002). *Introduction to GPS: The Global Positioning System*. London: Artech House.

European Commission. (2016). Open service signal-in-space interface control document. OS-SIS-GALILEO-ICD. Available from: https://www.gsc-europa.eu/system/files/ galileo_documents/Galileo-OS-SIS-ICD.pdf

Fernandes, M. J., Lazaro, C., Nunes, A. L., Pires, N., Bastos, L., & Mendes, V. B. (2010). GNSS-derived path delay: An approach to compute the wet tropospheric correction for coastal altimetry. *IEEE Geoscience and Remote Sensing Letters*, 7(3), 596–600.

Flinchem, E., & Jay, D. (2000). An introduction to wavelet transform tidal analysis methods. *Estuarine, Coastal and Shelf Science*, 51(2), 177–200.

Fok, H. S. (2012). *Ocean tides modeling using satellite altimetry*. (unpublished doctoral dissertation). Columbus, OH: The Ohio State University.

Foreman, M. G., & Neufeld, E. (1991). Harmonic tidal analysis of long time series. *The International Hydrographic Review*, 68(1), 85-108

Foreman, M.G.G., 1996. Manual for tidal heights analysis and prediction, *Pacific Marine Science Report* 77–10. Sidney, BC: Institute of Ocean Sciences.

Fu, L. L., Christensen, E. J., Yamarone, C. A., Lefebvre, M., Menard, Y., Dorrer, M., & Escudier, P. (1994). TOPEX/POSEIDON mission overview. *Journal of Geophysical Research: Oceans*, 99(C12), 24369–24381.

Fu, L.-L., & Cazenave, A. (Eds.) (2000). *Satellite altimetry and earth sciences: A handbook of techniques and applications, Vol. 69*. Cambridge, MA: Academic Press.

Gill, S. K., & Schultz, J. R. (Eds.). (2001). *Tidal datums and their applications*. Silver Spring, MD: National Oceanic and Atmospheric Administration.

Guo, J., Dong, Z., Tan, Z., Liu, X., Chen, C., & Hwang, C. (2016). A crossover adjustment for improving sea surface height mapping from in-situ high rate ship-borne GNSS data using PPP technique. *Continental Shelf Research*, 125, 54–60.

Gurtner, W., & Estey, L. (2013). RINEX: The Receiver Independent Exchange Format Version 3.02. Retrieved from ftp://igs.org/pub/data/format/rinex302.pdf

Hare, R., Eakins, B., Amante, C., & Taylor, L. A. 2011. Modelling bathymetric uncertainty. Paper presented at the *US HYDRO 2011 Conference, April 25–28, Tampa, Florida*.

Haigh, I. D. (2017). Tides and Water Levels. *Encyclopedia of Maritime and Offshore Engineering*. DOI: 10.1002/9781118476406.emoe122.

Harting, A., & Reinking, J. (2002). Ships: A new method for efficient full-scale ship squat determination. Paper presented at *the 30th PIANC-AIPCN Congress 2002*. Sydney, NSW: Institution of Engineers.

Härting, A., Berndt, T., & Reinking, J. (2007). Squat related effects on small surveying craft. Paper presented at the Hydrographic Technical Awareness Seminar TAS07, 19–21 June, Cape Town, Republic of South Africa.

Hartmann, T., & Wenzel, H. G. (1994). The harmonic development of the earth tide generating potential due to the direct effect of the planets. *Geophysical Research Letters*, 21(18), 1991–1993.

Hein, G., Landau, H., and Blomenhofer, H. (1990). Determination of instantaneous sea surface, wave heights, and ocean currents using satellite observations of the Global Positioning System. *Marine Geodesy*, 14(1), 217–224.

Hicks, S. D., & Szabados, M. W. (2006). *Understanding tides*. US Department of Commerce, National Oceanic and Atmospheric Administration, National Ocean Service. Hoechner, A., Ge, M., Babeyko, A., & Sobolev, S. (2013). Instant tsunami early warning based on real-time GPS—Tohoku 2011 case study. *Natural Hazards and Earth System Sciences*, 13(5), 1285–1292.

Hoechner, A., Ge, M., Babeyko, A., & Sobolev, S. (2013). Instant tsunami early warning based on real-time GPS—Tohoku 2011 case study. *Natural Hazards and Earth System Sciences*, 13(5), 1285–1292.

Hofmann-Wellenhof, B., Lichtenegger, H., & Collins, J. (2012). *Global positioning system: Theory and practice*. Berlin: Springer Science & Business Media.

Hofman-Wellenhof, B., Lichtenegger, H., & Wasle, E. (2008). *GNSS—global navigation satellite systems, GPS, GLONASS, Galileo and more*. Vienna: Springer-Verlag.

Hyvärinen, A., Karhunen, J., & Oja, E. (2004). *Independent component analysis*. Hoboken, NJ: John Wiley & Sons.

Inazu, D., Waseda, T., Hibiya, T., & Ohta, Y. (2016). Assessment of GNSS-based height data of multiple ships for measuring and forecasting great tsunamis. *Geoscience Letters*, 3(1), 3-25.

Intergovernmental Oceanographic Commission. (IOC) (2006). *Manual on sea-level measurements and interpretation (vol. IV): An update to 2006*. Paris: UNESCO/.

International Hydrographic Organization. (2005). *IHO Manual on Hydrography* (1st Ed.). Monaco: International Hydrographic Bureau.

International Hydrographic Organization. (2008). *IHO Standards for Hydrographic Surveys* (5th Ed.). Monaco: International Hydrographic Bureau.

International Hydrographic Organization. (2011). *Resolutions of the International Hydrographic Organization* (2nd Ed.). Monaco: International Hydrographic Bureau.

Jachowski, J. (2008). Assessment of ship squat in shallow water using CFD. *Archives of Civil and Mechanical Engineering*, 8(1), 27–36.

Jay, D. A., & Kukulka, T. (2003). Revising the paradigm of tidal analysis–the uses of non-stationary data. *Ocean Dynamics*, 53(3), 110–125.

Jürgenson, H., Liibusk, A., & Ellmann, A. (2008). Geoid profiles in the Baltic Sea determined using GPS and sea level surface. *Geodezija ir Kartografija*, 34(4), 109–115.

Kato, T., Terada, Y., Ito, K., Hattori, R., Abe, T., Miyake, T., … Nagai, T. (2005). Tsunami due to the 2004 September 5th off the Kii peninsula earthquake, Japan, recorded by a new GPS buoy. *Earth, Planets and Space*, 57(4), 297–301.

Kennedy, P. (2011). Hillary's GNSS Tide Trials. (Fugro technical report) Fugro Survey Pty Ltd (Australia) [accessed 7 April 2017. https://sft.fugro.com/courier/web/.

Kopparapu, S. K., & Satish, M. (2011). Identifying optimal Gaussian filter for Gaussian noise removal. Paper presented at *the third national Conference on Computer Vision, Pattern Recognition, Image Processing and Graphics, 15-17 Dec*. Karnataka, India.

Kouba, J. (2009) A Guide to Using International GNSS Service (IGS) Products http://igscb.jpl.nasa.gov/igscb/resource/pubs/UsingIGSProductsVer21.pdf

Kouba, J., & Héroux, P. (2001). Precise point positioning using IGS orbit and clock products. GPS solutions, 5(2), 12-28.

Kudryavtsev, S. (2004). Improved harmonic development of the Earth tide-generating potential. *Journal of Geodesy*, 77(12), 829–838.

Kuo, C.-Y., Chiu, K.-W., Chiang, K.-W., Cheng, K.-C., Lin, L.-C., Tseng, H.-Z., Lin, H.-T. (2012). High-frequency sea level variations observed by GPS buoys using

precise point positioning technique. *Terrestrial, Atmospheric & Oceanic Sciences*, 23(2): 209.

Leffler, K. E., & Jay, D. A. (2009). Enhancing tidal harmonic analysis: Robust (hybrid L1/L2) solutions. *Continental Shelf Research*, 29(1), 78–88.

Marreiros, J. P. H. (2012). Kinematic GNSS precise point positioning: Application to Marine Platforms. (doctoral dissertation) Portugal: University of Portugal.

Melgar, D., & Bock, Y. (2013). Near-field tsunami models with rapid earthquake source inversions from land-and ocean-based observations: The potential for forecast and warning. *Journal of Geophysical Research: Solid Earth*, 118(11), 5939–5955.

Melgar, D., & Bock, Y. (2015). Kinematic earthquake source inversion and tsunami runup prediction with regional geophysical data. *Journal of Geophysical Research: Solid Earth*, 120(5), 3324–3349.

Misra, P., & Enge, P. (2006). *Global positioning system: Signals, Measurements, and Performance* (2nd ed.). MA: Ganga-Jamuna Press.

Montenbruck, O., Steigenberger, P., Prange, L., Deng, Z., Zhao, Q., Perosanz, F., Weber, G. (2017). The multi-GNSS experiment (MGEX) of the international GNSS service (IGS): Achievements, prospects and challenges. *Advances in Space Research*, 59(7), 1671–1697.

Najibi, N., Abedini, A., & Sheibani, R. A. (2013). Harmonic decomposition tidal analysis and prediction based on astronomical arguments and nodal corrections in Persian Gulf, Iran. *Research Journal of Environmental and Earth Sciences*, 5(7), 381–392.

National Oceanic and Atmospheric Administration (2001). *Tidal datums and their applications*. Silver Spring, MD: NOAA.

National Oceanic and Atmospheric Administration (2005). National Oceanic and Atmospheric Administration. Retrieved from http://oceanservice.noaa.gov/education/tutorial_tides/

NRCAN: Canadian Spatial Reference System. (2016). Accessed 24 January 2016 http://www.geod.nrcan.gc.ca/online_data_e.

Okenwa, E. G. (1978). *Automated tidal reduction of soundings*. Department of Surveying Engineering, University of New Brunswick, NB.

Okwuashi, O., & Ndehedehe, C. (2017). Tide modelling using support vector machine regression. *Journal of Spatial Science*, 62(1), 29–46.

Parker, B. B. (2007). *Tidal analysis and prediction*. Silver Spring, MD: US Department of Commerce.

Pavlis, N. K., Holmes, S. A., Kenyon, S. C., & Factor, J. K. (2012). The development and evaluation of the Earth Gravitational Model 2008 (EGM2008). *Journal of Geophysical Research: Solid Earth*, 117(B4), 1-38.

Pawlowicz, R., Beardsley, B., & Lentz, S. (2002). Classical tidal harmonic analysis including error estimates in MATLAB using T_TIDE. *Computers & Geosciences*, 28(8), 929–937.

Peltier, W. (2004). Global glacial isostasy and the surface of the ice-age Earth: the ICE-5G (VM2) model and GRACE. *Annual Reviews Earth & Planetary Science*, 32, 111–149.

PCTMSL: Permanent Committee on Tides and Mean Sea Level. (2005). The factors contributing to the level of confidence in the tidal predictions: Accuracy of tidal predictions. Retrieved from http://www.icsm.gov.au/tides/ Port_Tidal_Predictions-V0.4.pdf

Podder, P., Hasan, M. M., Islam, M. R., & Sayeed, M. (2014). Design and implementation of Butterworth, Chebyshev-I and elliptic filter for speech signal analysis. International Journal of Computer Applications, 98(7), 12-18.

Pugh, D. (1987). *Tides, surges and mean sea-level: A handbook for engineers and scientists*. Chichester, UK: John Wiley.

Pugh, D. T. (1996). *Tides, surges and mean sea-level*. Chichester: Wiley.

Pytharouli, S., & Stiros, S. (2012). Analysis of short and discontinuous tidal data: A case study from the Aegean Sea. *Survey Review*, 44(326), 239–246.

Qin-wen, X. (1989). The precision of the development of the tidal generating potential and some explanatory notes. *Bulletin d'Informations Marées Terrestres*, 105, 7396–7404.

Reinking, J., Härting, A., & Bastos, L. (2012). Determination of sea surface height from moving ships with dynamic corrections. *Journal of Geodetic Science*, 2(3), 172–187.

Roberts, J., & Roberts, T. D. (1978). Use of the Butterworth low-pass filter for oceanographic data. *Journal of Geophysical Research: Oceans*, 83(C11), 5510–5514.

Rodkin, M., & Tikhonov, I. (2014). Seismic regime in the vicinity of the 2011 Tohoku mega earthquake (Japan, Mw= 9). *Pure and Applied Geophysics*, 171(12), 3241–3255.

Roelse, A., Granger, H., & Graham, J. (1975). *The adjustment of the Australian levelling survey 1970–1971*. Canberra: Department of Minerals and Energy, Division of National Mapping.

Roosbeek, F. (1996). RATGP95: A harmonic development of the tide-generating potential using an analytical method. *Geophysical Journal International*, 126, 197–204.

Ross, D. (1995). *Power from the waves*. NY: Oxford University Press.

Ronai, B. (2006). The national Australian tide gauge network. Retreived from http://www.gloss-sealevel.org/publications/documents/australia_tgn_2001.pdf

Saito, E., & Kubo, N. (2016). Performance evaluation and a new disaster prevention system of precise point positioning at sea. In *Proceedings of the 29th International Technical Meeting of The Satellite Division of the Institute of Navigation (ION GNSS+ 2016), Portland, Oregon, September 2016*, pp. 3412–3432.

Sakamoto, Y., Ishiguro, M., & Kitagawa, G. (1986). *Akaike information criterion statistics*. Tokyo: D. Reidel Publishing.

Savitzky, A., & Golay, M. J. (1964). Smoothing and differentiation of data by simplified least squares procedures. *Analytical chemistry*, 36(8), 1627–1639.

Schmitt, T., Mitchell, N. C., & Ramsay, A. T. S. (2008). Characterizing uncertainties for quantifying bathymetry change between time-separated multibeam echo-sounder surveys. *Continental Shelf Research*, 28(9): 1166–1176.

Schöne, T., Illigner, J., Manurung, P., Subarya, C., Zech, C., & Galas, R. (2011). GPS-controlled tide gauges in Indonesia—a German contribution to Indonesia's Tsunami Early Warning System. *Natural Hazards and Earth System Sciences*, 11(3), 731–740.

Schone, T., Reigber, C., & Braun, A. (2003). GPS offshore buoys and continuous gps control of tide gauges. *The International Hydrographic Review*, 4(3), 64–70.

Schureman, P. (1958). *Manual of harmonic analysis and prediction of tides*. Washington, D.C.: US Government Printing Office.

Sharpe, T., Hatch, R., & Nelson, F. (2000). John Deere's StarFire System: WADGPS for precision agriculture. Paper presented at *the Proceedings of the 13th International Technical Meeting of the Satellite Division of The Institute of Navigation, September 19–22*, Salt Lake City, UT.

Shennan, I., & Horton, B. (2002). Holocene land- and sea-level changes in Great Britain. *Journal of Quaternary Science*, 17(5-6), 511–526.

Shenoi B.A. (2006), *Introduction to digital signal processing and filter design*. New York: John Wiley.

Smith, S. (2013). *Digital Signal Processing: A Practical Guide for Engineers and Scientists*: Elsevier Science.

Stewart, R. H. (2008). *Introduction to Physical Oceanography*: University Press of Florida.

Strang, G., & Borre, K. (1997). *Linear algebra, geodesy, and GPS*. Wellesley, MA: Wellesley–Cambridge Press.

Sumich, J. L., & Morrissey, J. F. (2004). *Introduction to the biology of marine life*. Sudbury, MA: Jones & Bartlett Learning.

Tamura, Y. (1987). A harmonic development of the tide-generating potential. *Bulletin d'Informations Marées Terrestres*, 99, 6813–6855.

Tamura, Y. (1993). Additional terms to the tidal harmonic tables. In H.-T. Hsu (Ed.), Proceedings *of the 12th International Symposium on Earth Tides, 4–8 August,* Beijing (pp. 6813-6855). Beijing: Science Press.

Tang, L., Titov, V. V., Bernard, E. N., Wei, Y., Chamberlin, C. D., Newman, J. C., … Moore, C. (2012). Direct energy estimation of the 2011 Japan tsunami using deep-ocean pressure measurements. *Journal of Geophysical Research: Oceans*, 117(C8), 1-28.

Tang, L., Titov, V., & Chamberlin, C. (2009). Development, testing, and applications of site-specific tsunami inundation models for real-time forecasting. *Journal of Geophysical Research: Oceans*, 114(C12), 1-22.

Tay, S., Coatanhay, A., Maussang, F., & Garello, R. (2010). A tracking algorithm for GNSS reflected signals on sea surface. Paper presented at *The Geoscience and Remote Sensing Symposium, 25-30 July*, Honolulu, HI.

Tomczak, M. (2007). *Australian Tides Manual*, Special Publication No. 9. [Assessed 13 June 2017. Available from http://www.icsm.gov.au/tides/SP9_v4.4_May2017.pdf

Tsushima, H., Hirata, K., Hayashi, Y., Tanioka, Y., Kimura, K., Sakai, S. I., ... & Maeda, K. (2011). Near-field tsunami forecasting using offshore tsunami data from the 2011 off the Pacific coast of Tohoku Earthquake. *Earth, Planets and Space*, 63(7), 821–826.

Tsushima, Y., Iga, S.-i., Tomita, H., Satoh, M., Noda, A. T., & Webb, M. J. (2014). High cloud increase in a perturbed SST experiment with a global nonhydrostatic

model including explicit convective processes. *Journal of Advances in Modeling Earth Systems*, 6(3), 571–585.

Venedikov, A. P., Arnoso, J., & Vieira, R. (2005). New version of program VAV for tidal data processing. *Computers & Geosciences*, 31(5), 667–669.

Vignudelli, S., Cipollini, P., Gommenginger, C., Gleason, S., Snaith, H. M., Coelho, H., … & Gómez-Enri, J. (2011). Satellite altimetry: Sailing closer to the coast. In DanLing Tang (Ed.), *Remote Sensing of the Changing Oceans* (pp. 217–238). Heidelberg: Springer.

Wells, D., & Beck, N. (1986). *Guide to GPS positioning* / prepared under the Leadership of David Wells; by Norman Beck ...[et at.]. Fredericton, N.B: Fredericton, N.B: Canadian GPS Associates.

Wert, T. D., Dare, P., & Clarke, J. H. (2004). *Tidal height retrieval using globally corrected GPS in the Amundsen Gulf region of the Canadian Arctic*. (Unpublished masters dissertation). Fredericton, NB: University of New Brunswick.

Wei, Y., Chamberlin, C., Titov, V. V., Tang, L., & Bernard, E. N. (2013). Modeling of the 2011 Japan tsunami: Lessons for near-field forecast. *Pure and Applied Geophysics*, 170(6–8), 13091331.

Xi, Q. W., & HOU, T. (1987). A new complete development of the tide-generating potential for the epoch J2000. 0. *Chinese Journal Geophysics*, 30(4), 349-362.

Appendix A

Frequency Spectra for Nearshore GNSS-derived Water Level Heights

This appendix provides a complete list of all frequency spectra for all window lengths (10, 30, 60, 80, 120, 150, 180, 220, 260, 300 and 360 minutes) for the nearshore GNSS-derived water level heights (see Chapter 3).

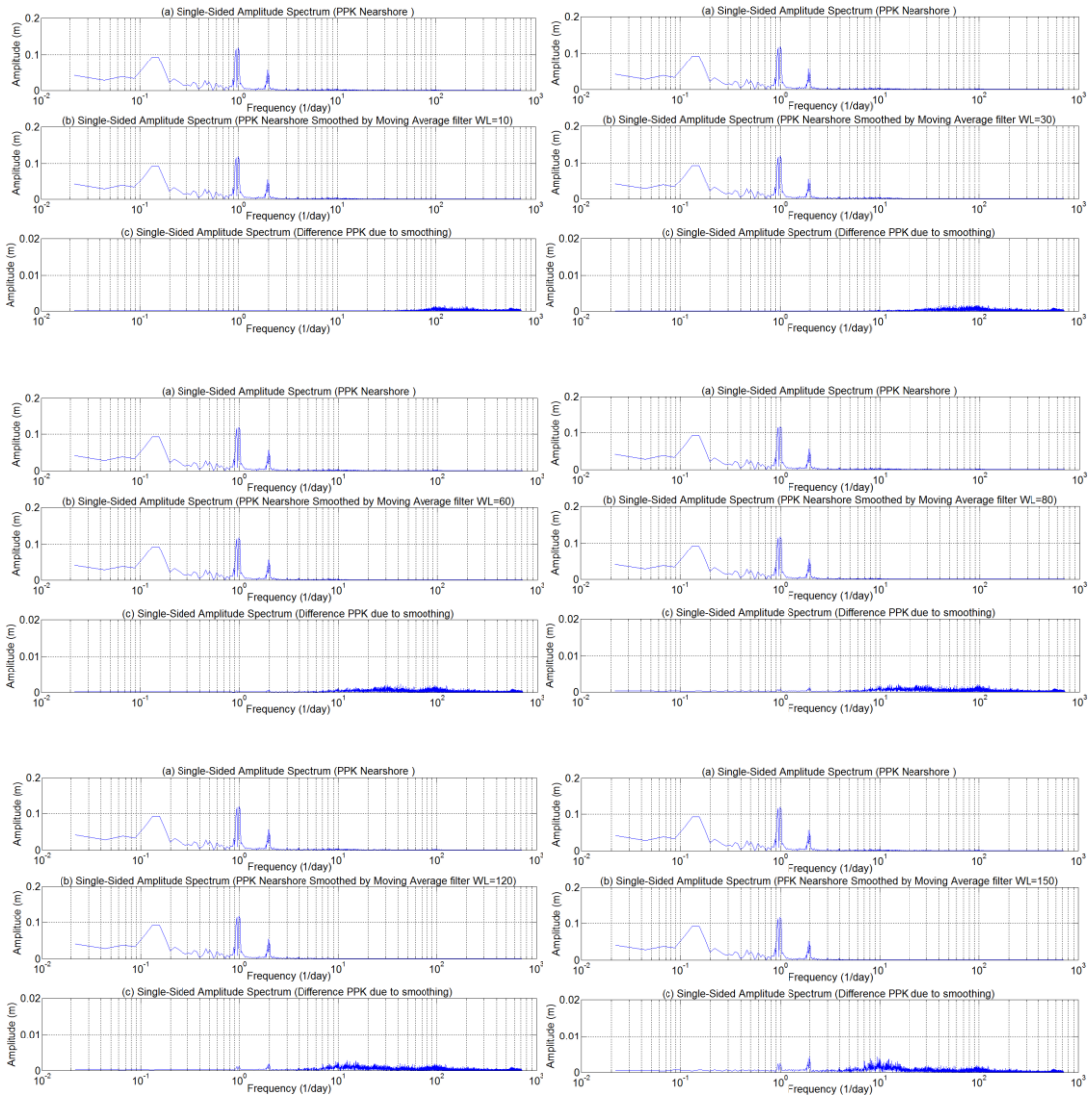

Figure A.1a: Single-sided frequency spectra of the moving average filter for PPK nearshore (10, 30, 60, 80, 120 and 150) WL: In each group of three plots, (a) PPK nearshore unfiltered; (b) PPK nearshore smoothed by the moving average filters for 10, 30, 60, 80, 120 and 150 minute window length; and (c) differences between filtered and unfiltered GNSS-derived water level height signals

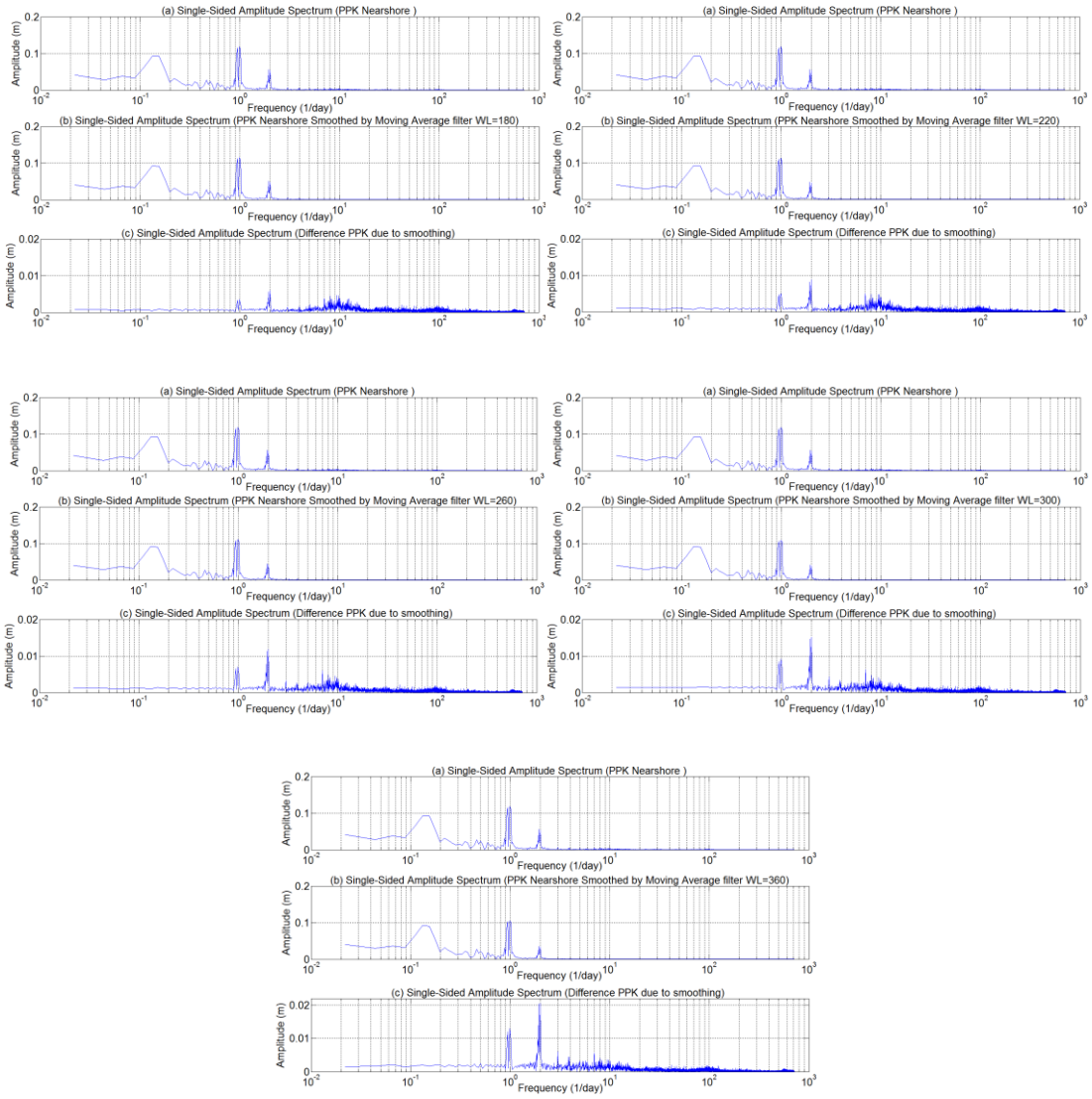

Figure A.1b: Single-sided frequency spectra of the moving average filter for PPK nearshore (180, 220, 260, 300 and 360) WL: In each group of three plots, (a) PPK nearshore unfiltered; (b) PPK nearshore smoothed by the moving average filters for 180, 220, 260, 300 and 360 minute window length; and (c) differences between filtered and unfiltered GNSS-derived water level height signals

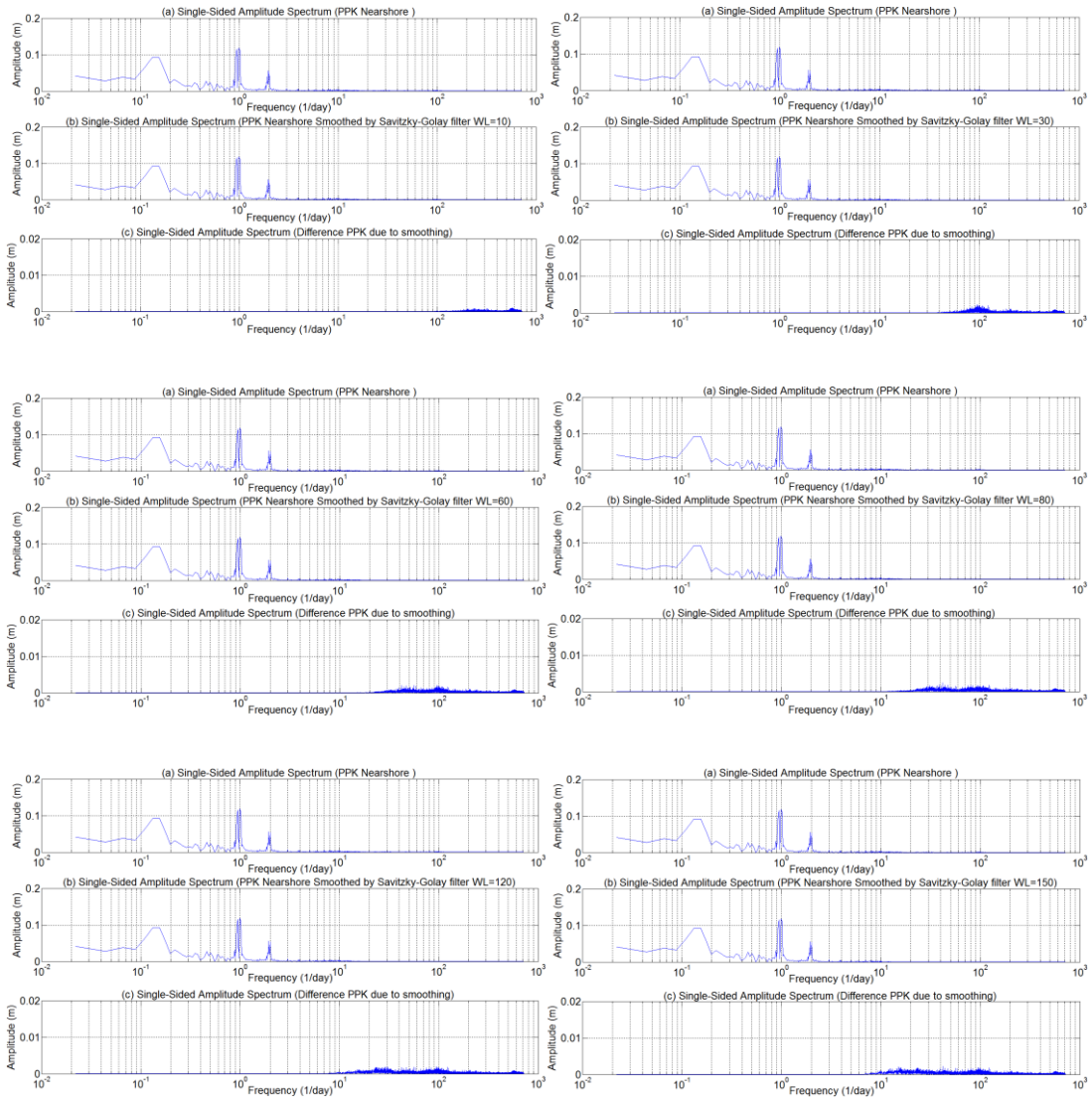

Figure A.2a: Single-sided frequency spectra of the Savitzky-Golay filter for PPK nearshore (10, 30, 60, 80, 120 and 150) WL: In each group of three plots, (a) PPK nearshore unfiltered; (b) PPK nearshore smoothed by the Savitzky-Golay filters for 10, 30, 60, 80, 120 and 150 minute window length; and (c) differences between filtered and unfiltered GNSS-derived water level height signals

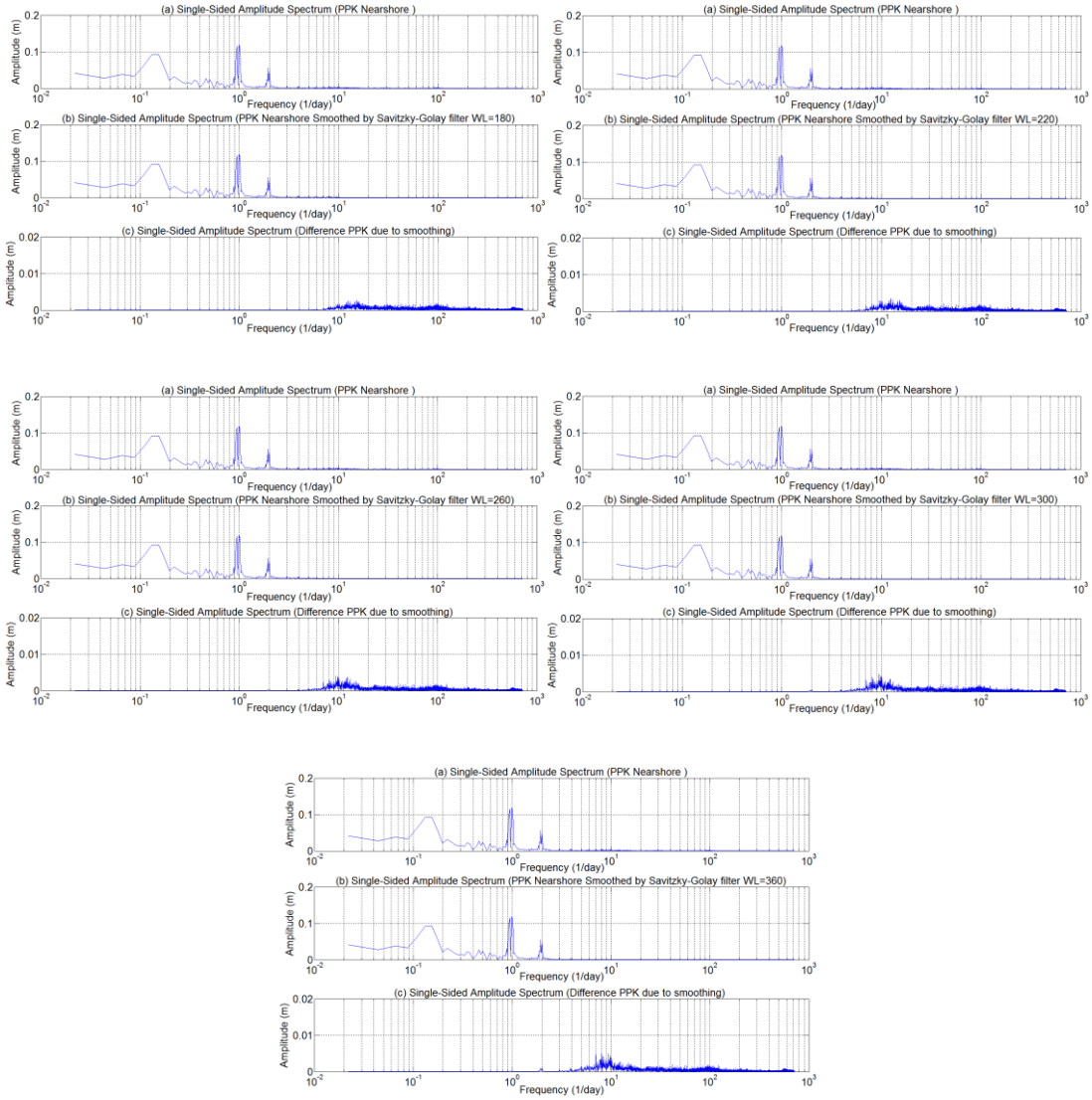

Figure A.2b: Single-sided frequency spectra of the Savitzky-Golay filter for PPK nearshore (180, 220, 260, 300 and 360) WL: In each group of three plots, (a) PPK nearshore unfiltered; (b) PPK nearshore smoothed by the Savitzky-Golay filters for 180, 220, 260, 300 and 360 minute window length; and (c) differences between filtered and unfiltered GNSS-derived water level height signals

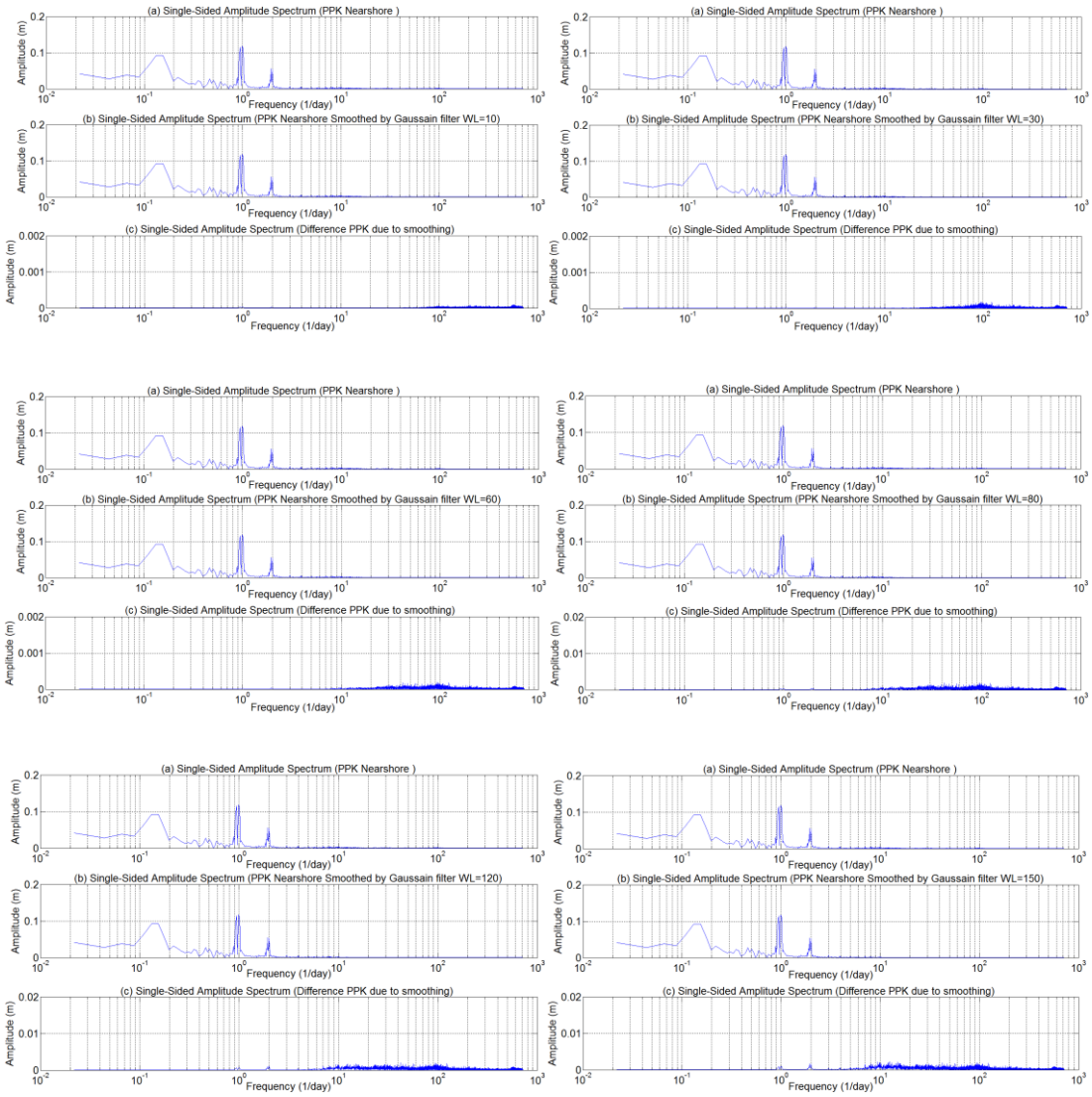

Figure A.3a: Single-sided frequency spectra of the Gaussain filter for PPK nearshore (10, 30, 60, 80, 120 and 150) WL: In each group of three plots, (a) PPK nearshore unfiltered; (b) PPK nearshore smoothed by the Gaussain filters for 10, 30, 60, 80, 120 and 150 minute window length; and (c) differences between filtered and unfiltered GNSS-derived water level height signals

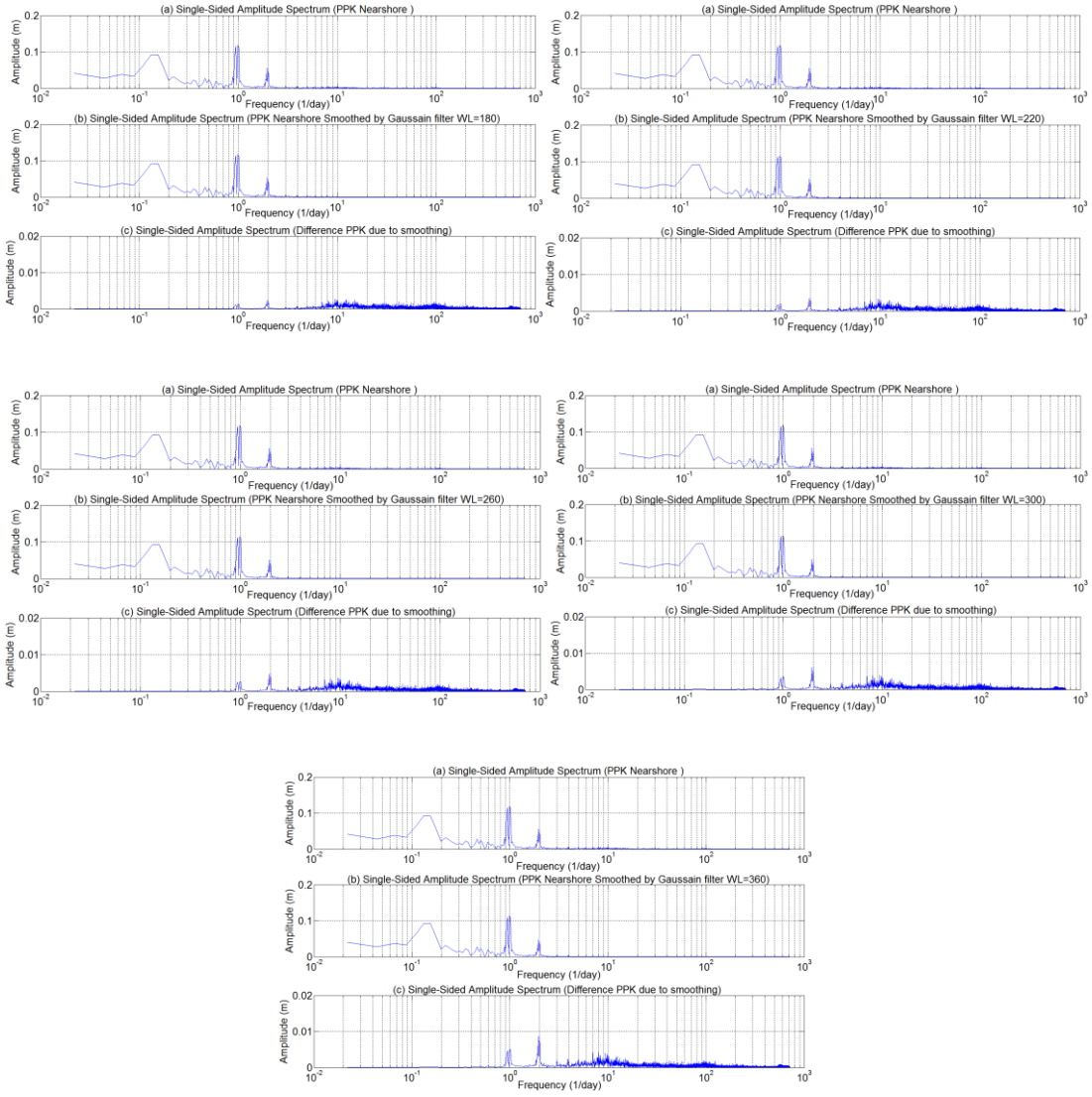

Figure A.3b: Single-sided frequency spectra of the Gaussain filter for PPK nearshore (180, 220, 260, 300 and 360) WL: In each group of three plots, (a) PPK nearshore unfiltered; (b) PPK nearshore smoothed by the Gaussain filters for 180, 220, 260, 300 and 360 minute window length; and (c) differences between filtered and unfiltered GNSS-derived water level height signals

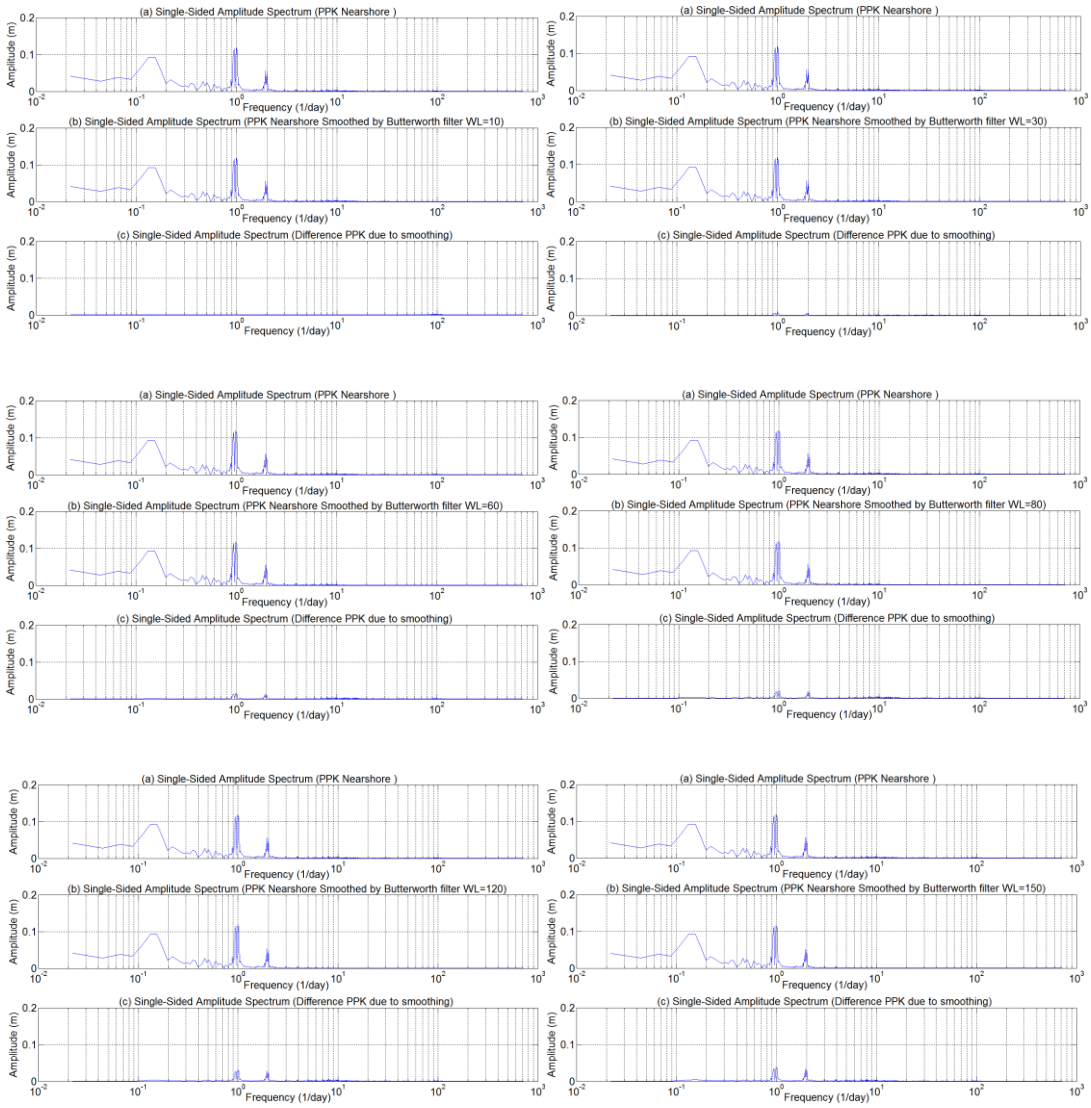

Figure A.4a: Single-sided frequency spectra of the Butterworth filter for PPK nearshore (10, 30, 60, 80, 120 and 150) WL: In each group of three plots, (a) PPK nearshore unfiltered; (b) PPK nearshore smoothed by the Butterworth filters for 10, 30, 60, 80, 120 and 150 minute window length; and (c) differences between filtered and unfiltered GNSS-derived water level height signals

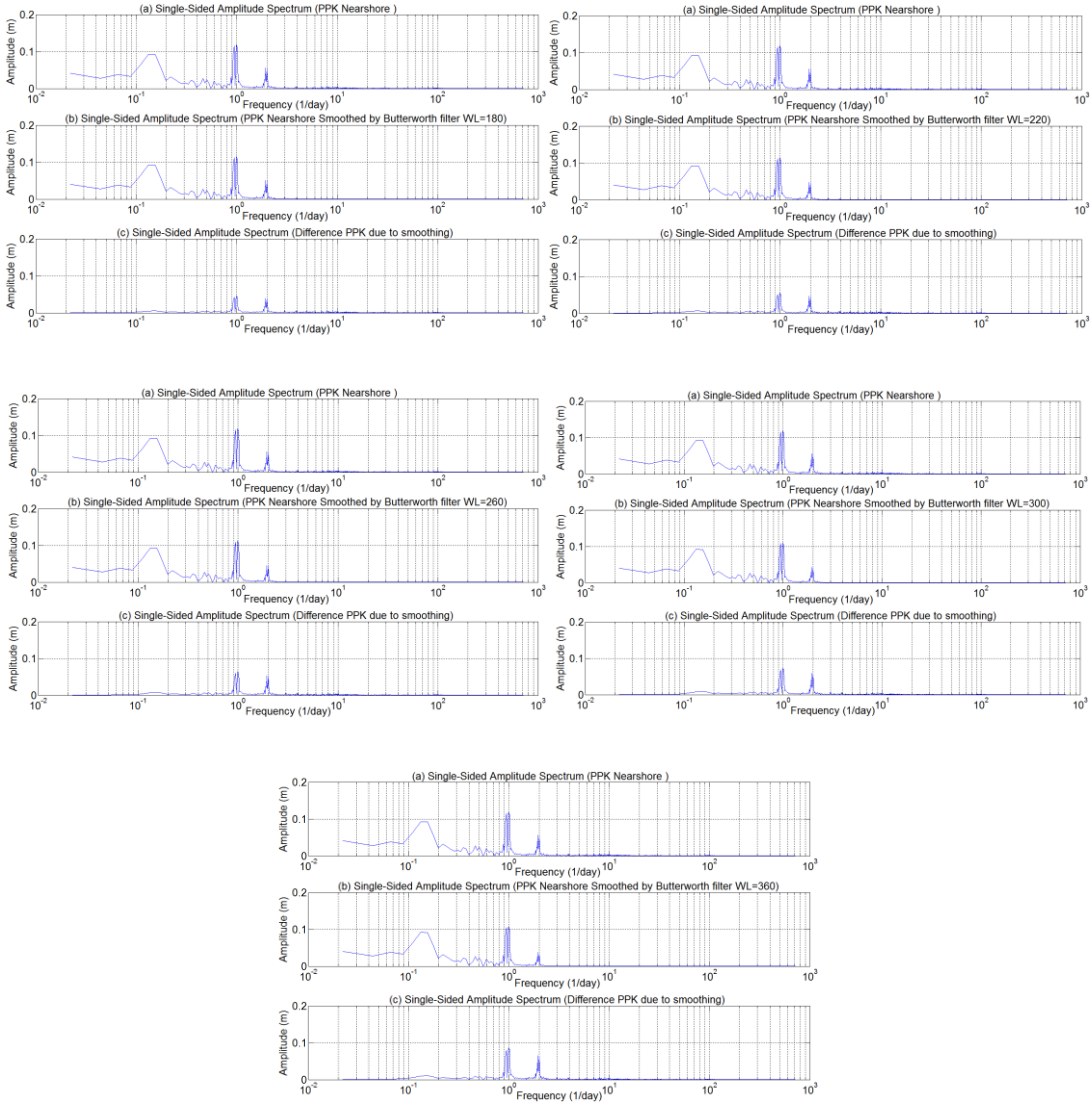

Figure A.4b: Single-sided frequency spectra of the Butterworth filter for PPK nearshore (180, 220, 260, 300 and 360) WL: In each group of three plots, (a) PPK nearshore unfiltered; (b) PPK nearshore smoothed by the Butterworth filters for 180, 220, 260, 300 and 360 minute window length; and (c) differences between filtered and unfiltered GNSS-derived water level height signals

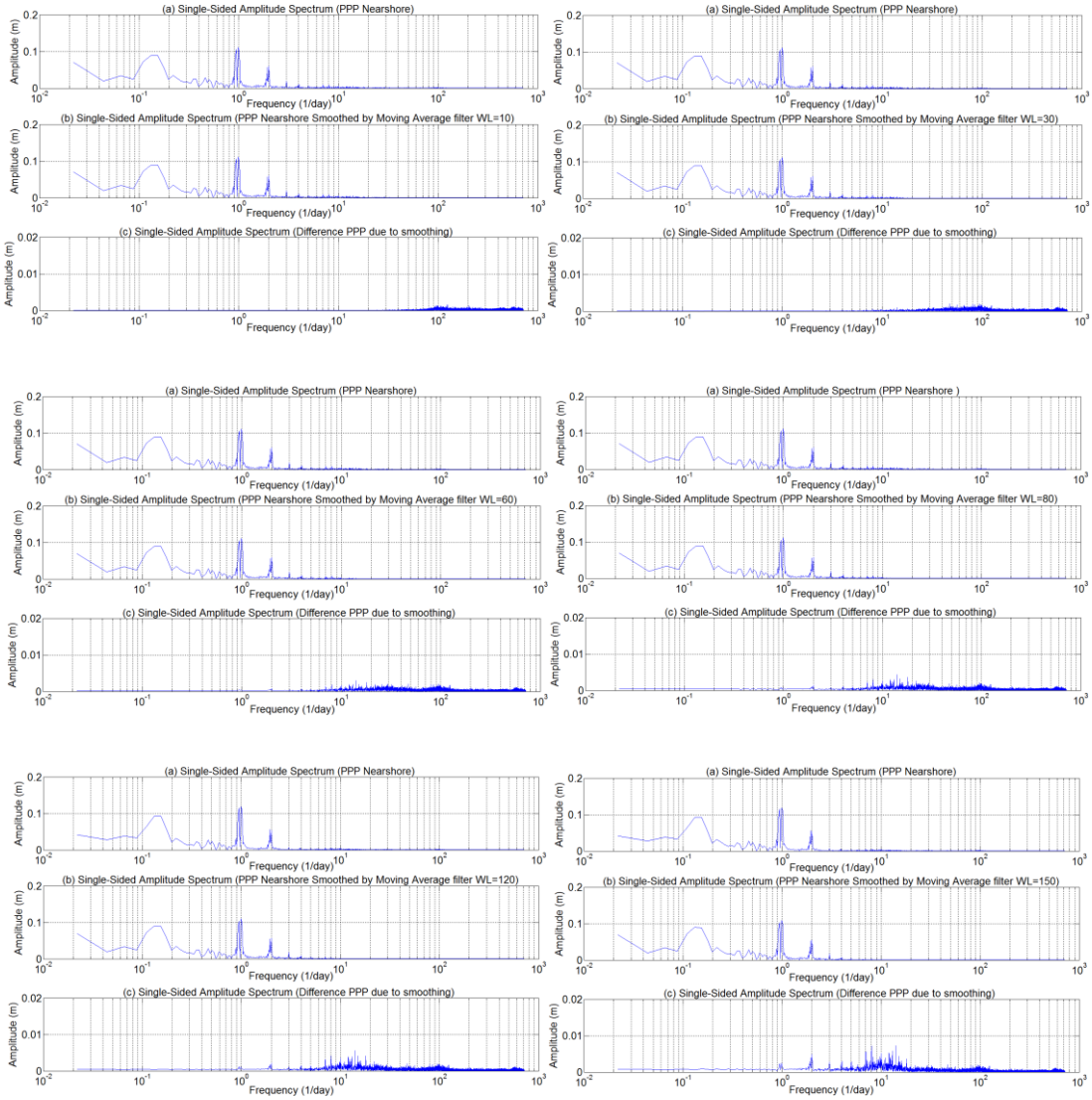

Figure A.5a: Single-sided frequency spectra of the moving average filter for PPP nearshore (10, 30, 60, 80, 120 and 150) WL: In each group of three plots, (a) PPP nearshore unfiltered; (b) PPP nearshore smoothed by the moving average filters for 10, 30, 60, 80, 120 and 150 minute window length; and (c) differences between filtered and unfiltered GNSS-derived water level height signals

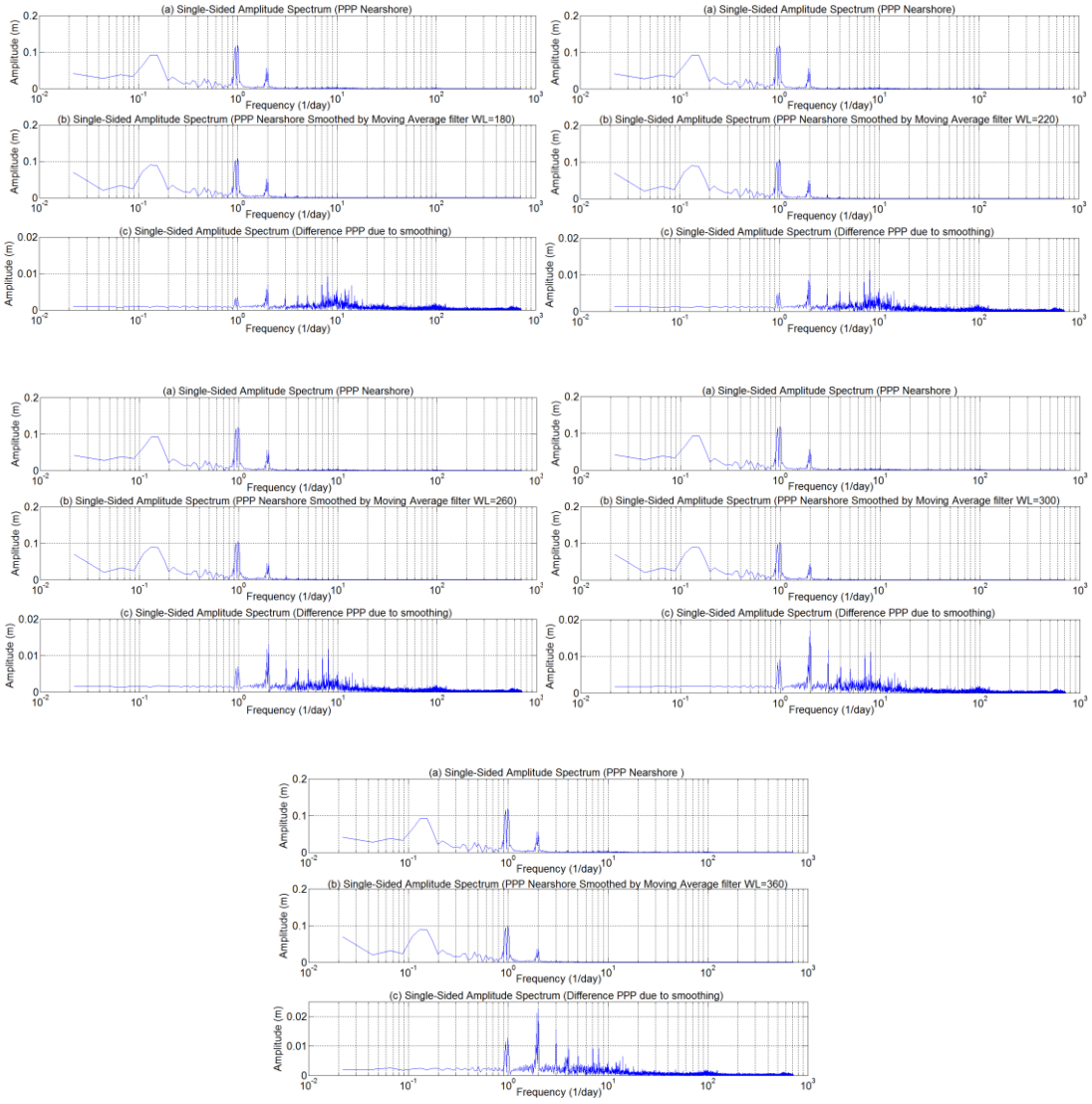

Figure A.5b: Single-sided frequency spectra of the moving average filter for PPP nearshore (180, 220, 260, 300 and 360) WL: In each group of three plots, (a) PPP nearshore unfiltered; (b) PPP nearshore smoothed by the moving average filters for 180, 220, 260, 300 and 360 minute window length; and (c) differences between filtered and unfiltered GNSS-derived water level height signals

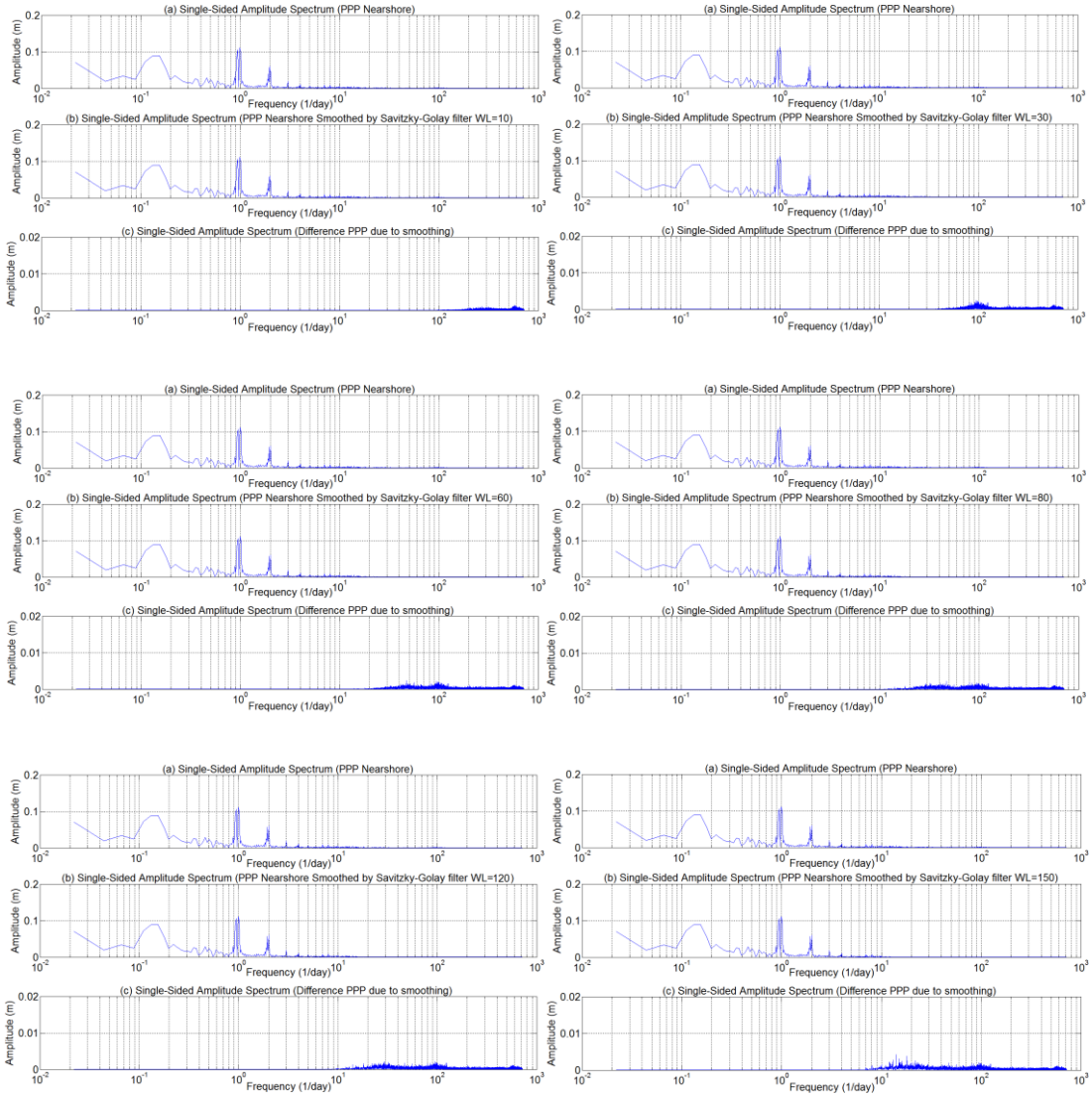

Figure A.6a: Single-sided frequency spectra of the Savitzky-Golay filter for PPP nearshore (10, 30, 60, 80, 120 and 150) WL: In each group of three plots, (a) PPP nearshore unfiltered; (b) PPP nearshore smoothed by the Savitzky-Golay filters for 10, 30, 60, 80, 120 and 150 minute window length; and (c) differences between filtered and unfiltered GNSS-derived water level height signals

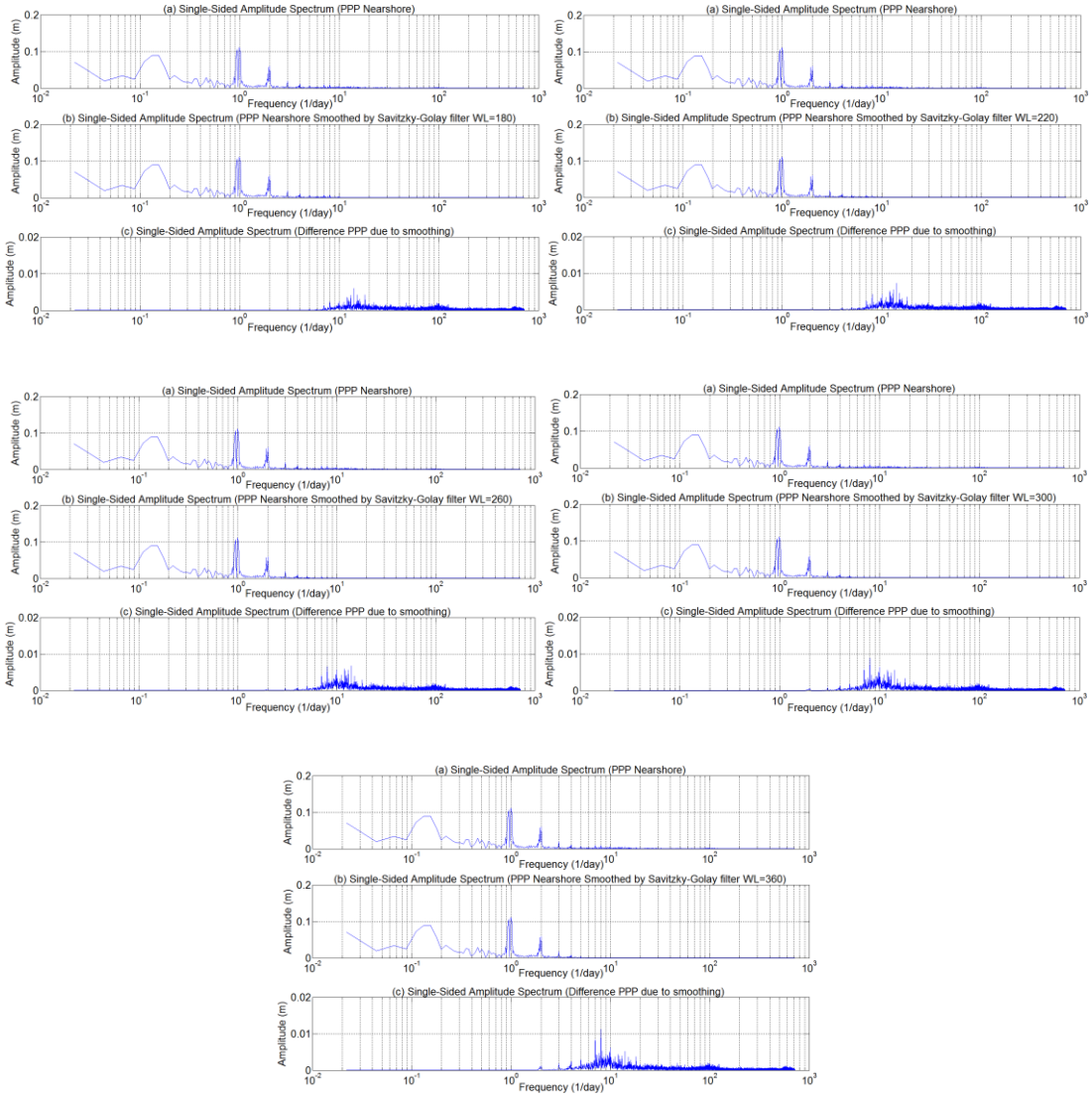

Figure A.6b: Single-sided frequency spectra of the Savitzky-Golay filter for PPP nearshore (180, 220, 260, 300 and 360) WL: In each group of three plots, (a) PPP nearshore unfiltered; (b) PPP nearshore smoothed by the Savitzky-Golay filters for 180, 220, 260, 300 and 360 minute window length; and (c) differences between filtered and unfiltered GNSS-derived water level height signals

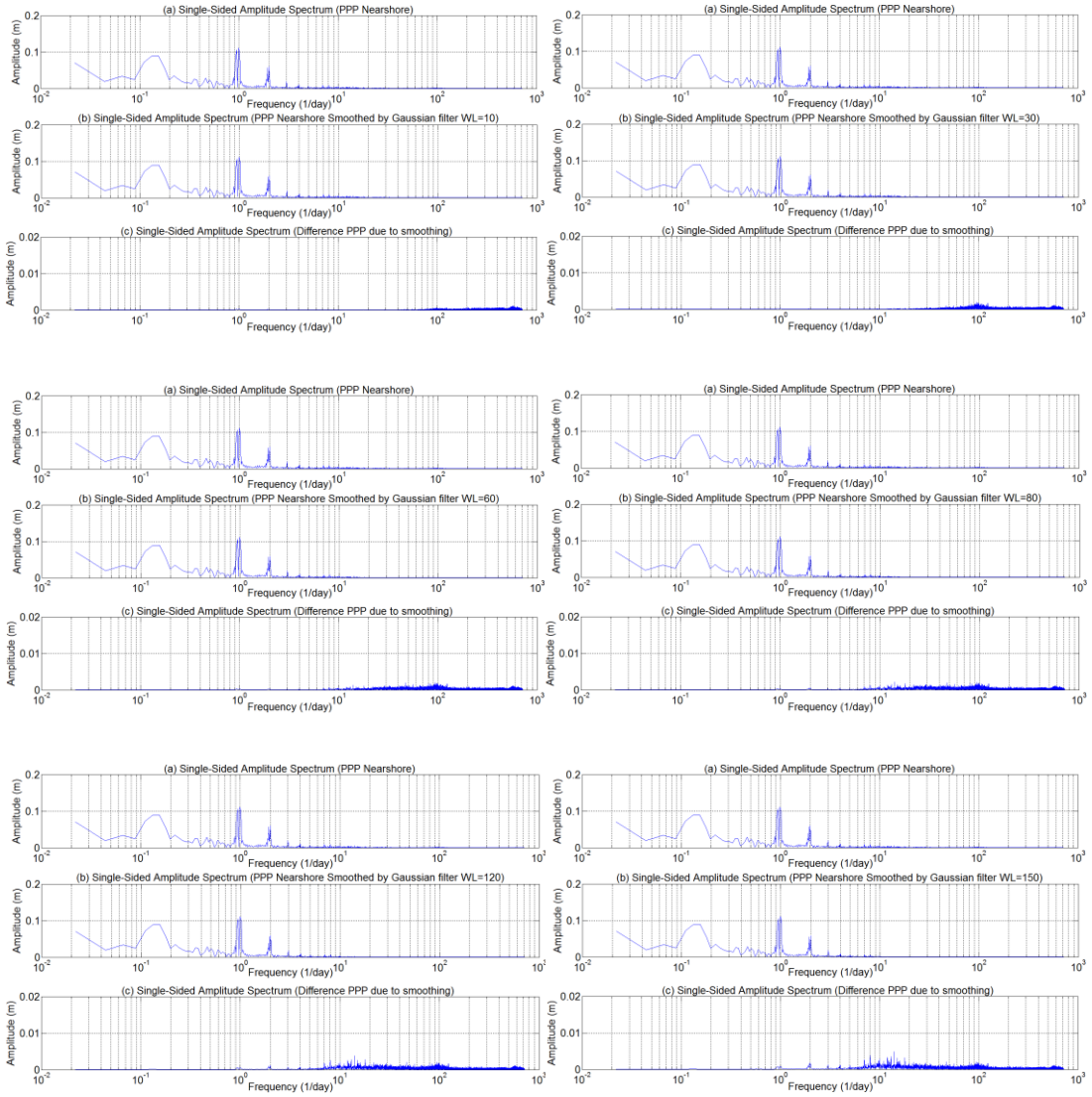

Figure A.7a: Single-sided frequency spectra of the Gaussain filter for PPP nearshore (10, 30, 60, 80, 120 and 150) WL: In each group of three plots, (a) PPP nearshore unfiltered; (b) PPP nearshore smoothed by the Gaussain filters for 10, 30, 60, 80, 120 and 150 minute window length; and (c) differences between filtered and unfiltered GNSS-derived water level height signals

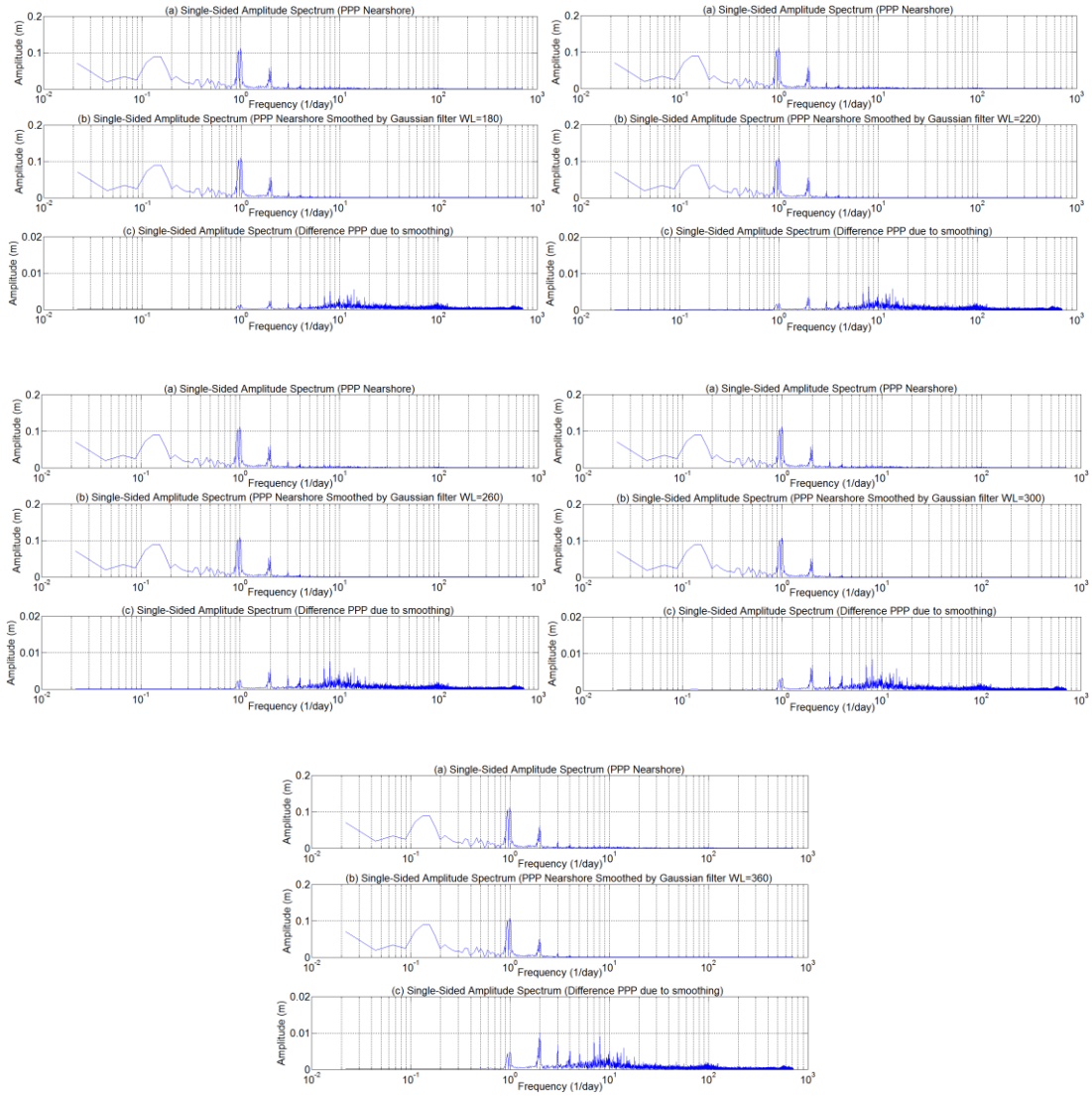

Figure A.7b: Single-sided frequency spectra of the Gaussain filter for PPP nearshore (180, 220, 260, 300 and 360) WL: In each group of three plots, (a) PPP nearshore unfiltered; (b) PPP nearshore smoothed by the Gaussain filters for 180, 220, 260, 300 and 360 minute window length; and (c) differences between filtered and unfiltered GNSS-derived water level height signals

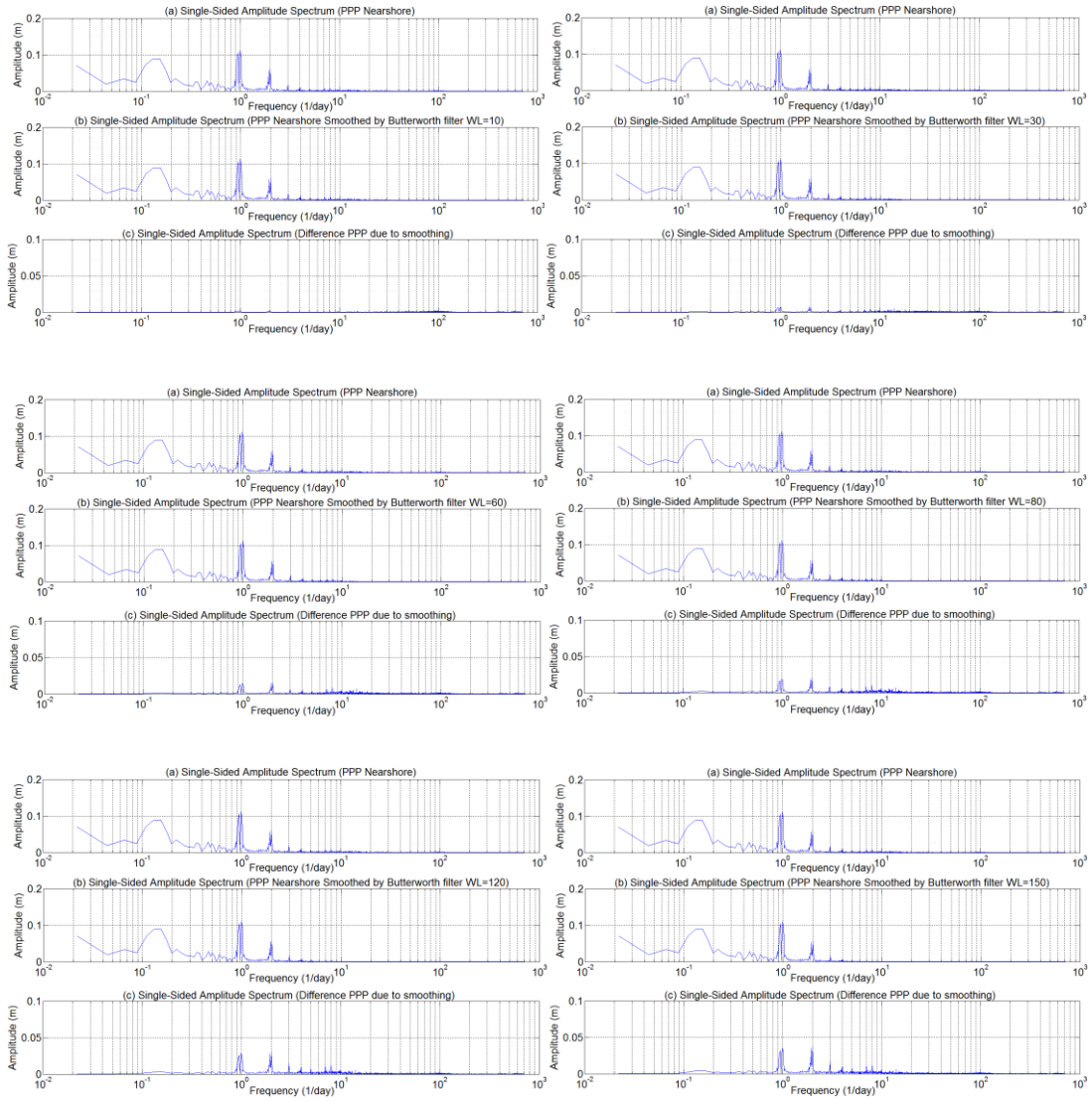

Figure A.8a: Single-sided frequency spectra of the Butterworth filter for PPP nearshore (10, 30, 60, 80, 120 and 150) WL: In each group of three plots, (a) PPP nearshore unfiltered; (b) PPP nearshore smoothed by the Butterworth filters for 10, 30, 60, 80, 120 and 150 minute window length; and (c) differences between filtered and unfiltered GNSS-derived water level height signals

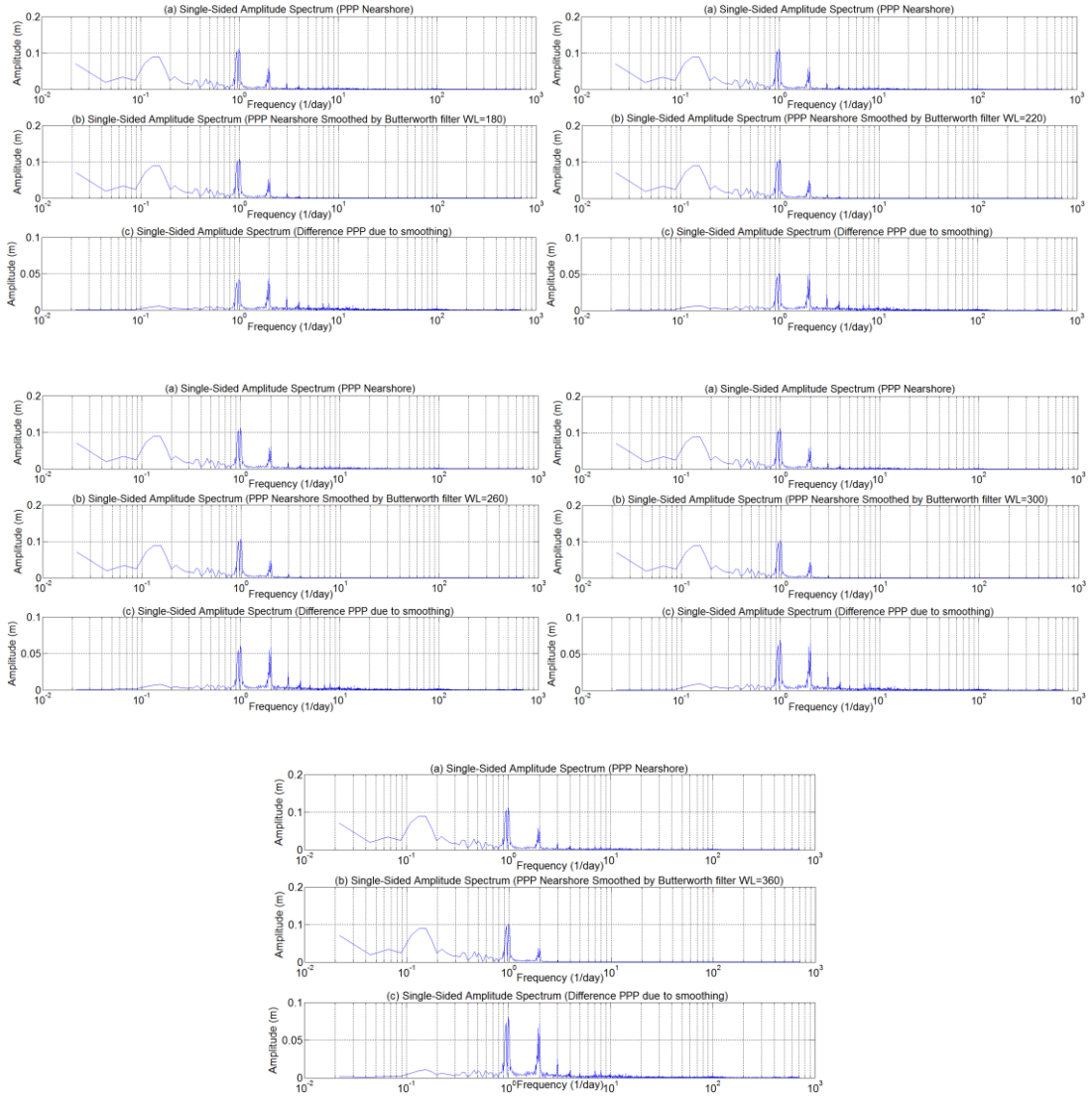

Figure A.8b: Single-sided frequency spectra of the Butterworth filter for PPP nearshore (180, 220, 260, 300 and 360) WL: In each group of three plots, (a) PPP nearshore unfiltered; (b) PPP nearshore smoothed by the Butterworth filters for 180, 220, 260, 300 and 360 minute window length; and (c) differences between filtered and unfiltered GNSS-derived water level height signals

Appendix B

Frequency Spectra for Offshore GNSS-derived Water Level Heights

This appendix provides a complete list of all frequency spectra for all window lengths (10, 30, 60, 80, 120, 150, 180, 220, 260, 300 and 360 minutes) for the offshore GNSS-derived water level heights (cf. Chapter 4).

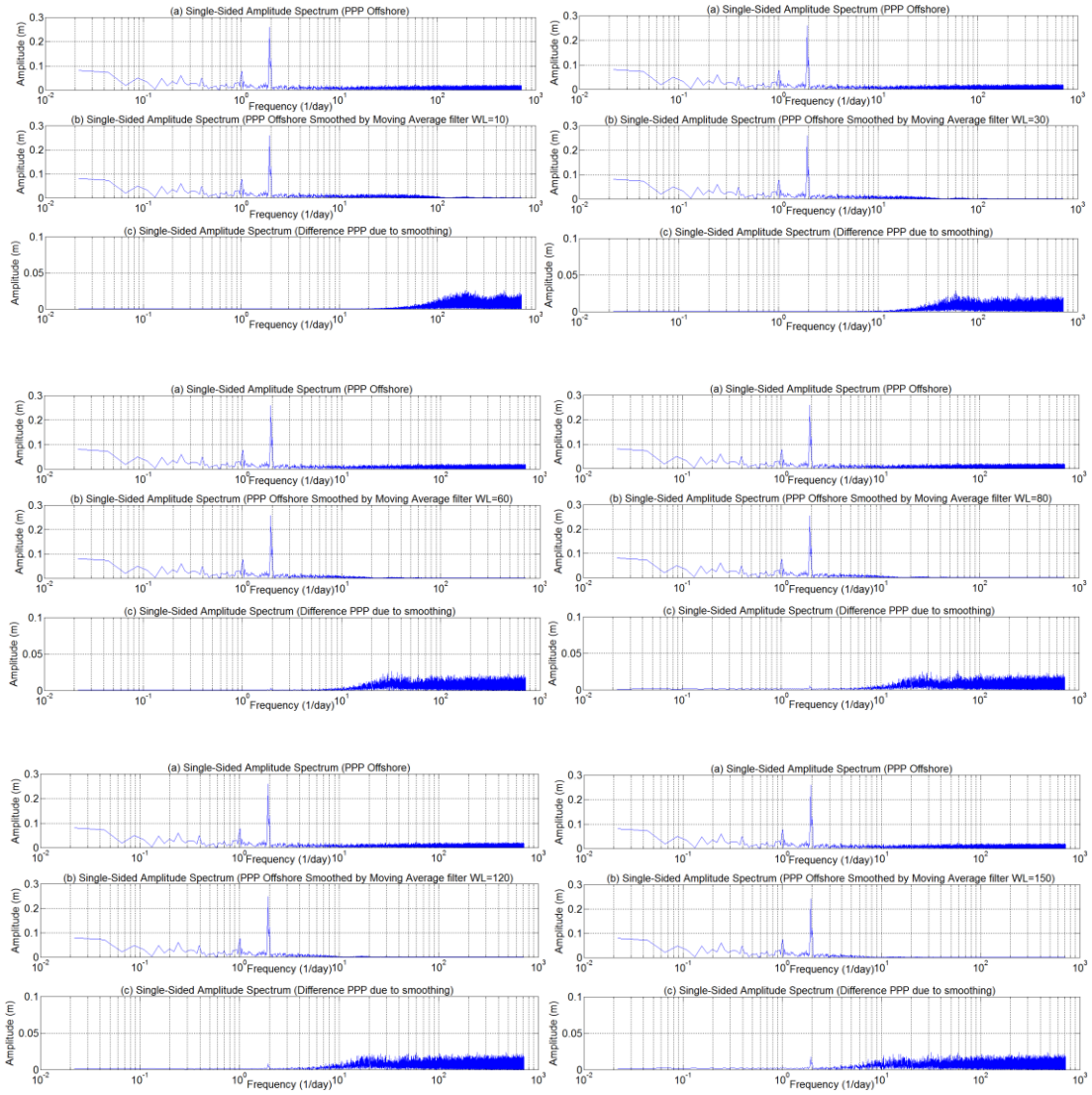

Figure B.1a: Single-sided frequency spectra of the moving average filter for PPP offshore (10, 30, 60, 80, 120 and 150) WL: In each group of three plots, (a) PPP offshore unfiltered; (b) PPP offshore smoothed by the moving average filters for 10, 30, 60, 80, 120 and 150 minute window length; and (c) differences between filtered and unfiltered GNSS-derived water level height signals

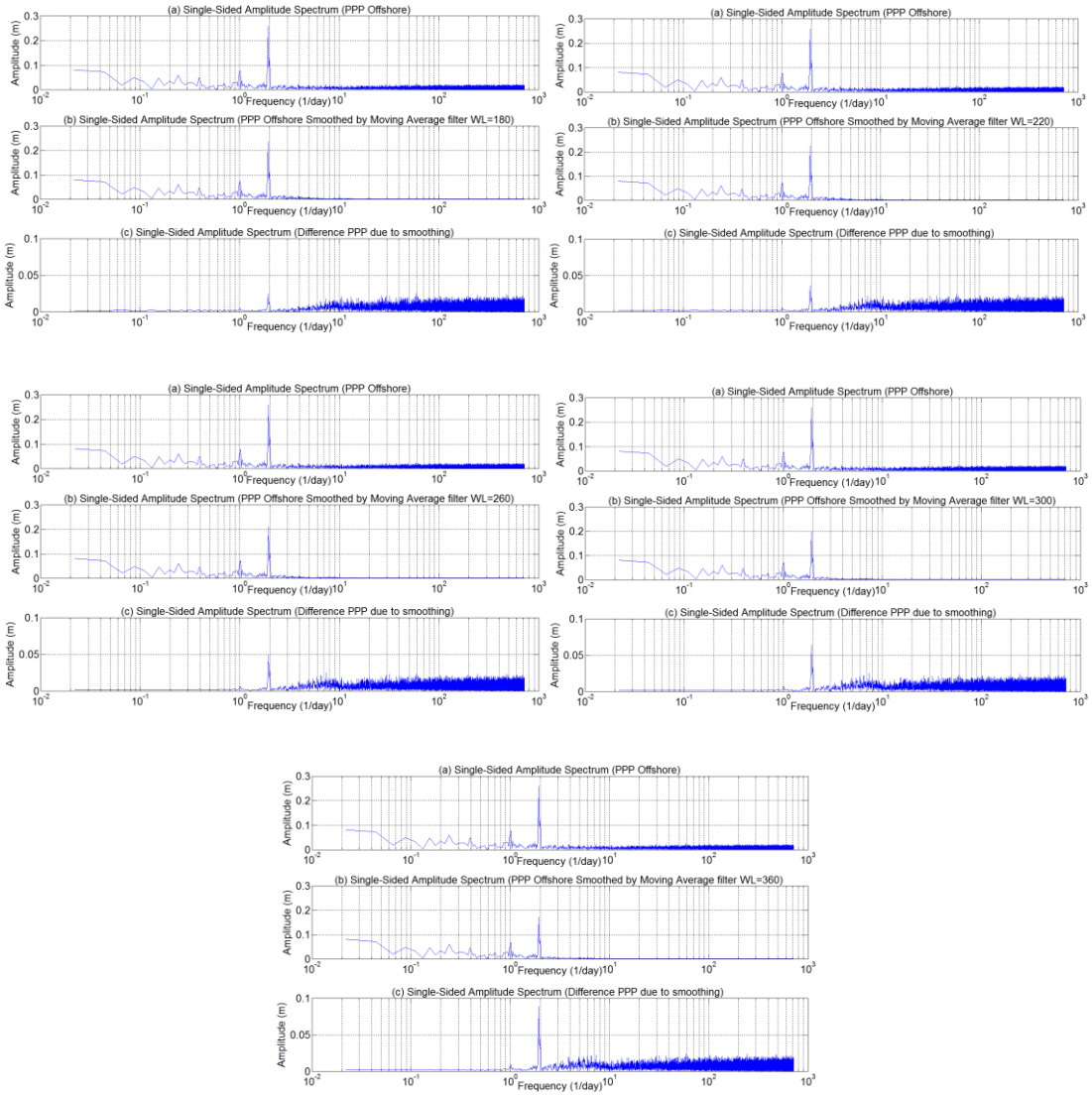

Figure B.1b: Single-sided frequency spectra of the moving average filter for PPP offshore (180, 220, 260, 300 and 360) WL: In each group of three plots, (a) PPP offshore unfiltered; (b) PPP offshore smoothed by the moving average filters for 180, 220, 260, 300 and 360 minute window length; and (c) differences between filtered and unfiltered GNSS-derived water level height signals

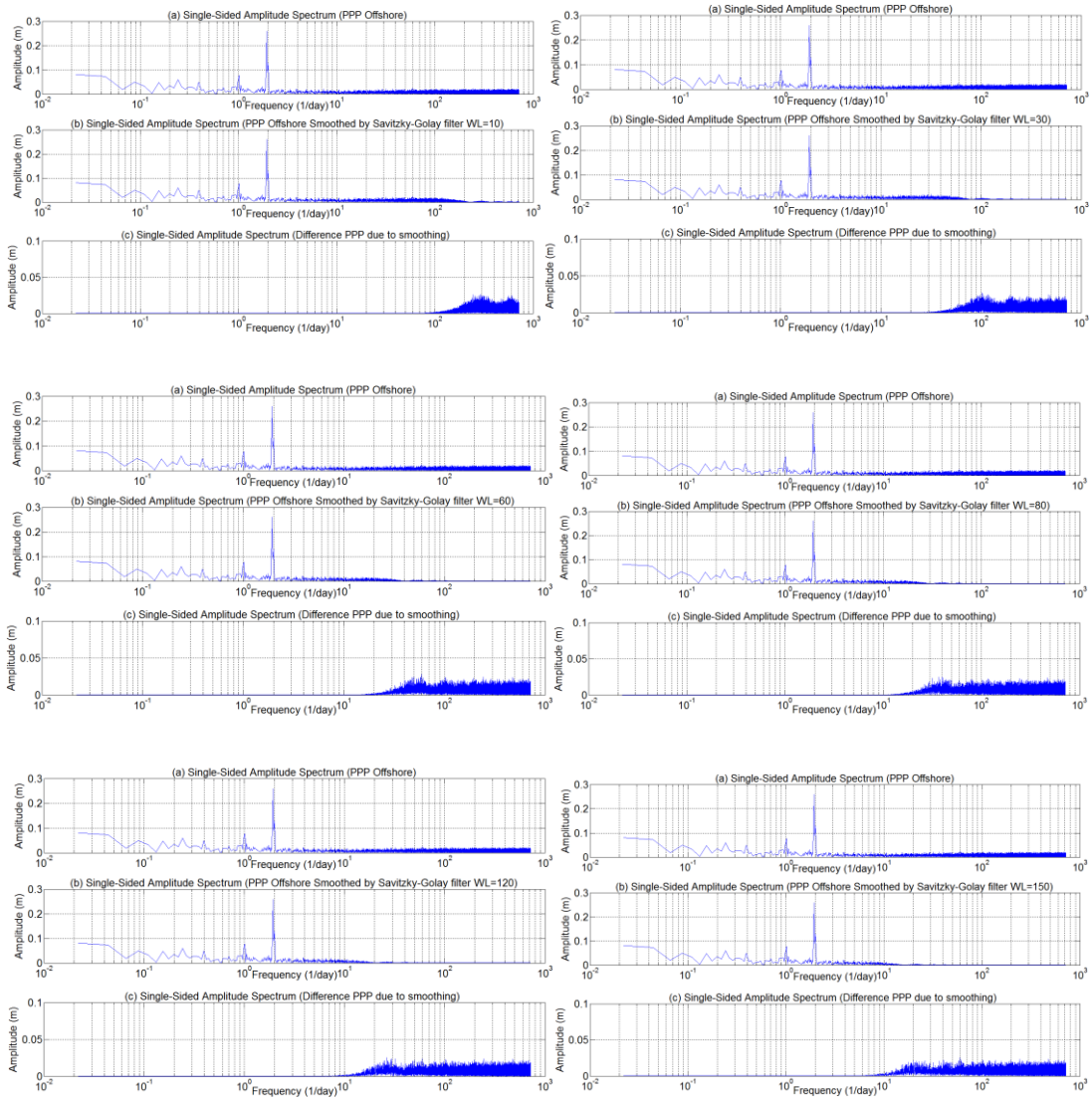

Figure B.2a: Single-sided frequency spectra of the Savitzky-Golay filter for PPP offshore (10, 30, 60, 80, 120 and 150) WL: In each group of three plots, (a) PPP offshore unfiltered; (b) PPP offshore smoothed by the Savitzky-Golay filters for 10, 30, 60, 80, 120 and 150 minute window length; and (c) differences between filtered and unfiltered GNSS-derived water level height signals

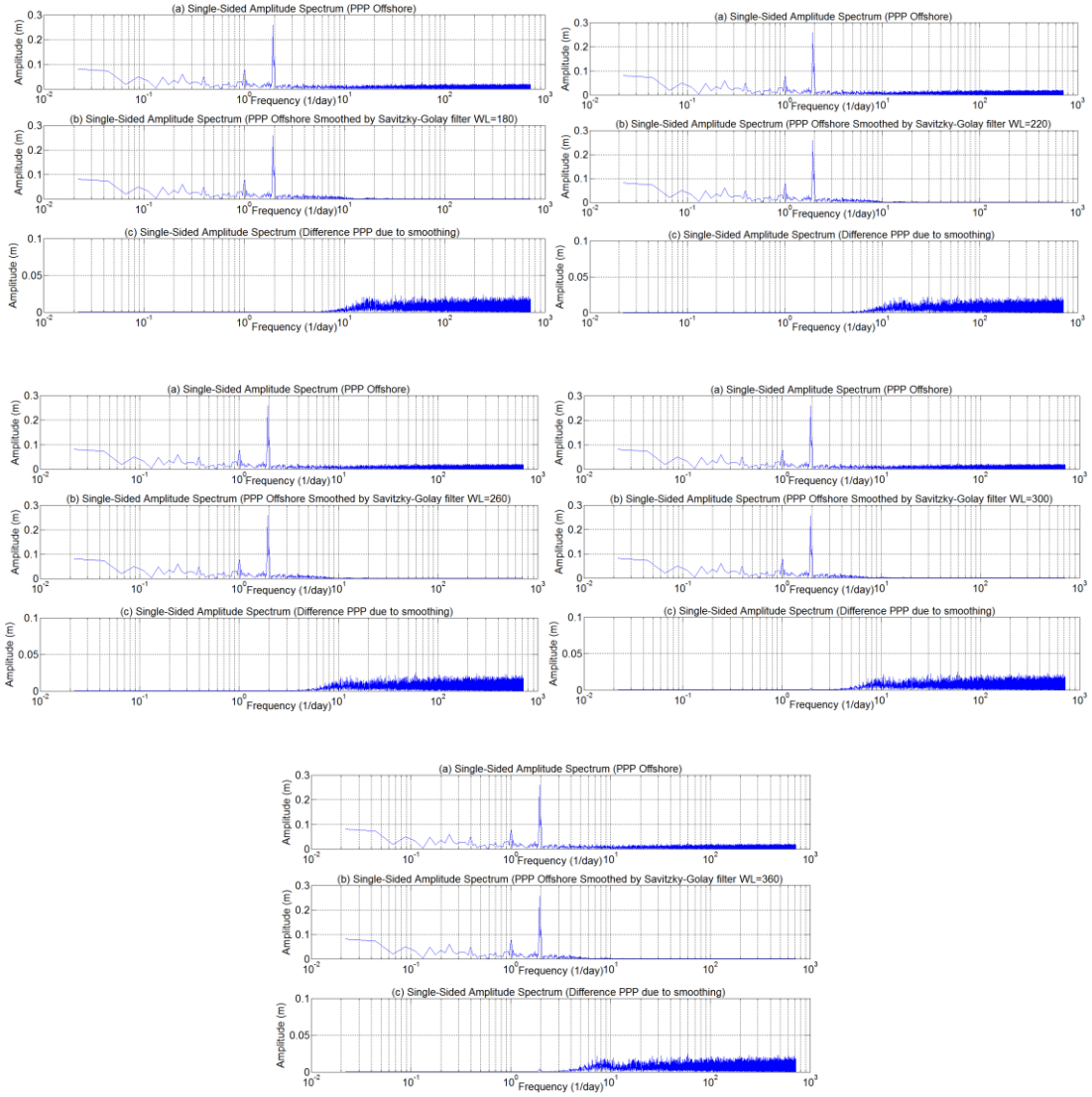

Figure B.2b: Single-sided frequency spectra of the Savitzky-Golay filter for PPP offshore (180, 220, 260, 300 and 360) WL: In each group of three plots, (a) PPP offshore unfiltered; (b) PPP offshore smoothed by the Savitzky-Golay filters for 180, 220, 260, 300 and 360 minute window length; and (c) differences between filtered and unfiltered GNSS-derived water level height signals

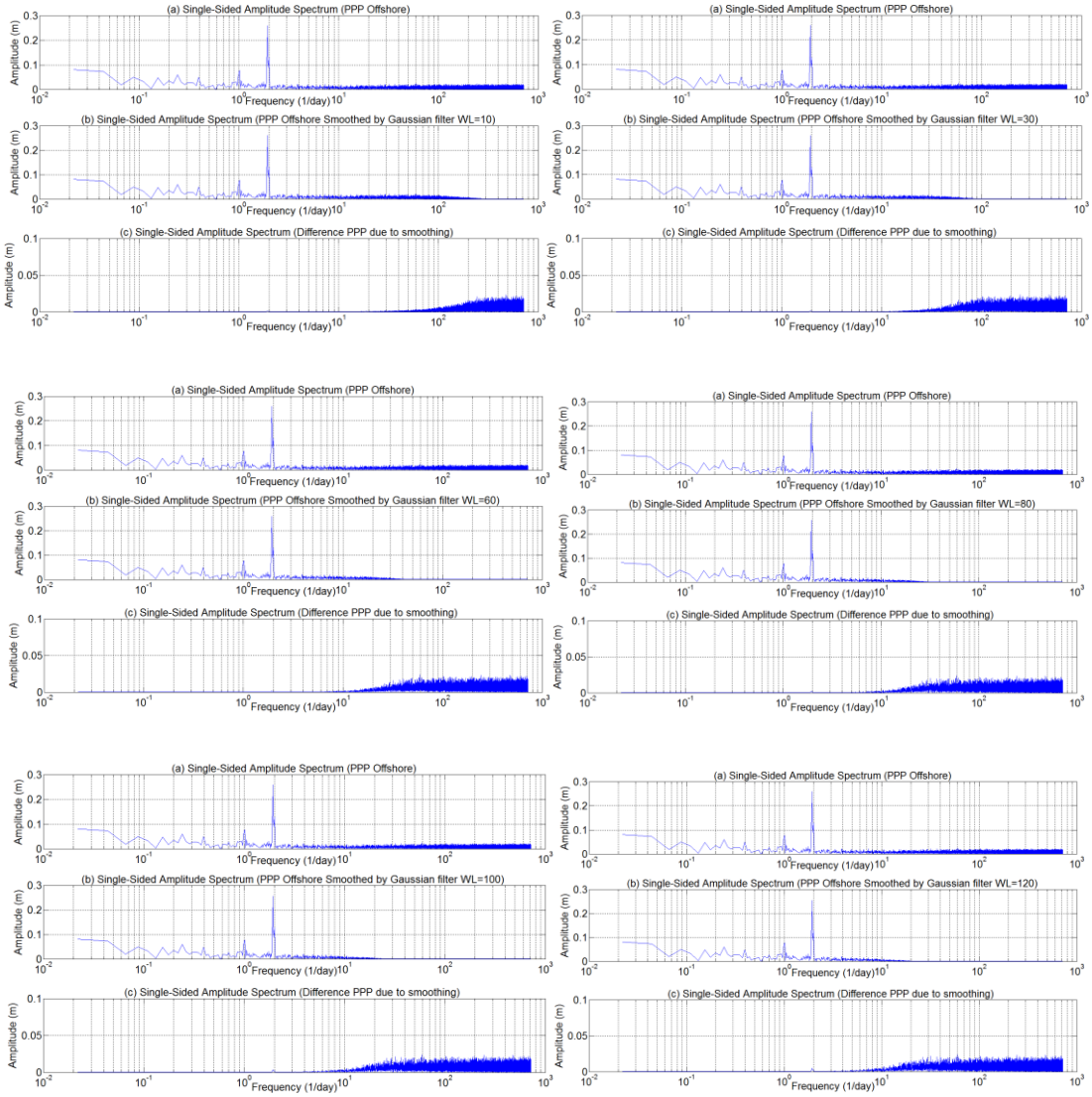

Figure B.3a: Single-sided frequency spectra of the Gaussain filter for PPP offshore (10, 30, 60, 80, 120 and 150) WL: In each group of three plots, (a) PPP offshore unfiltered; (b) PPP offshore smoothed by the Gaussain filters for 10, 30, 60, 80, 120 and 150 minute window length; and (c) differences between filtered and unfiltered GNSS-derived water level height signals

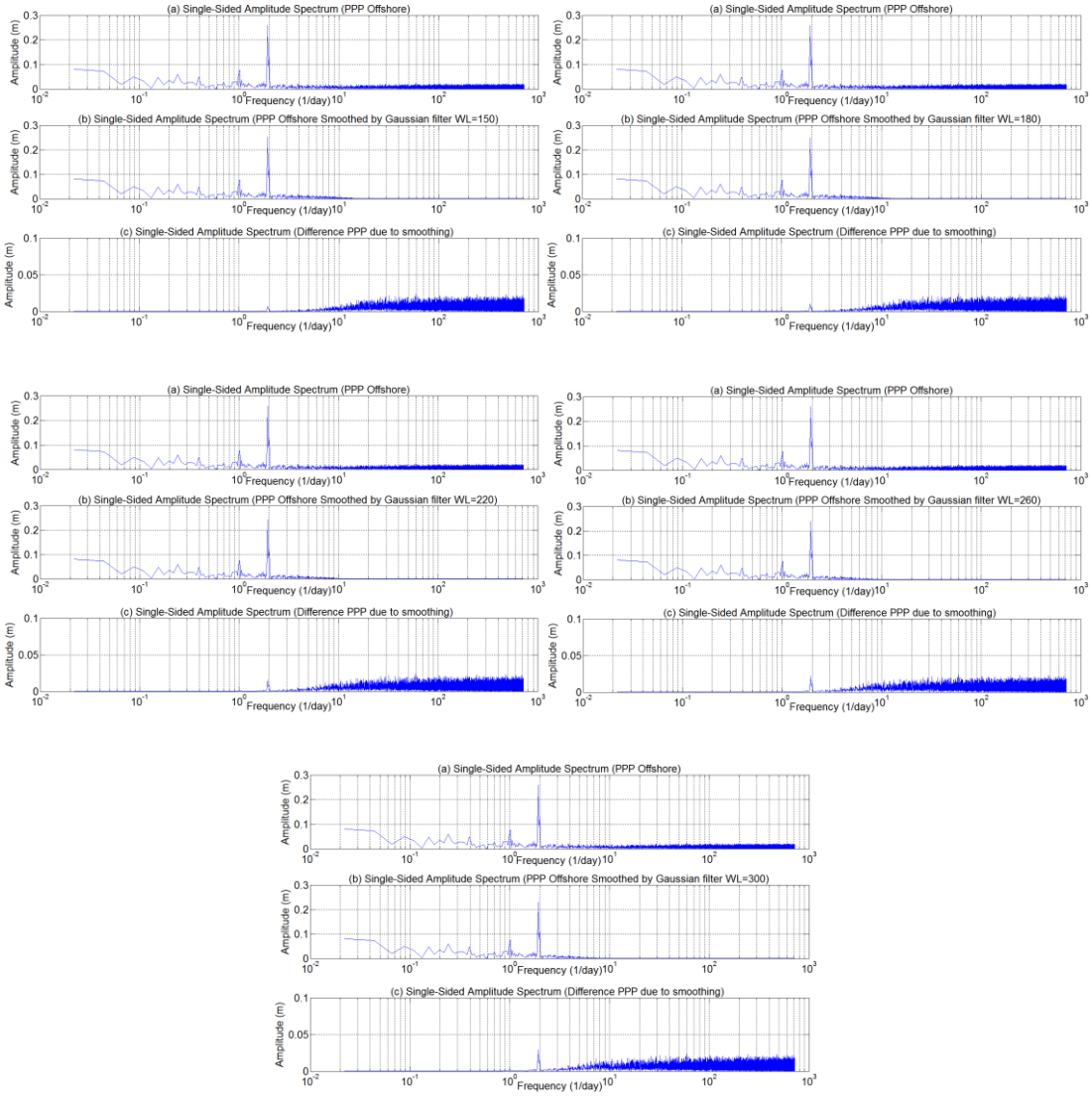

Figure B.3b: Single-sided frequency spectra of the Gaussain filter for PPP offshore (180, 220, 260, 300 and 360) WL: In each group of three plots, (a) PPP offshore unfiltered; (b) PPP offshore smoothed by the Gaussain filters for 180, 220, 260, 300 and 360 minute window length; and (c) differences between filtered and unfiltered GNSS-derived water level height signals

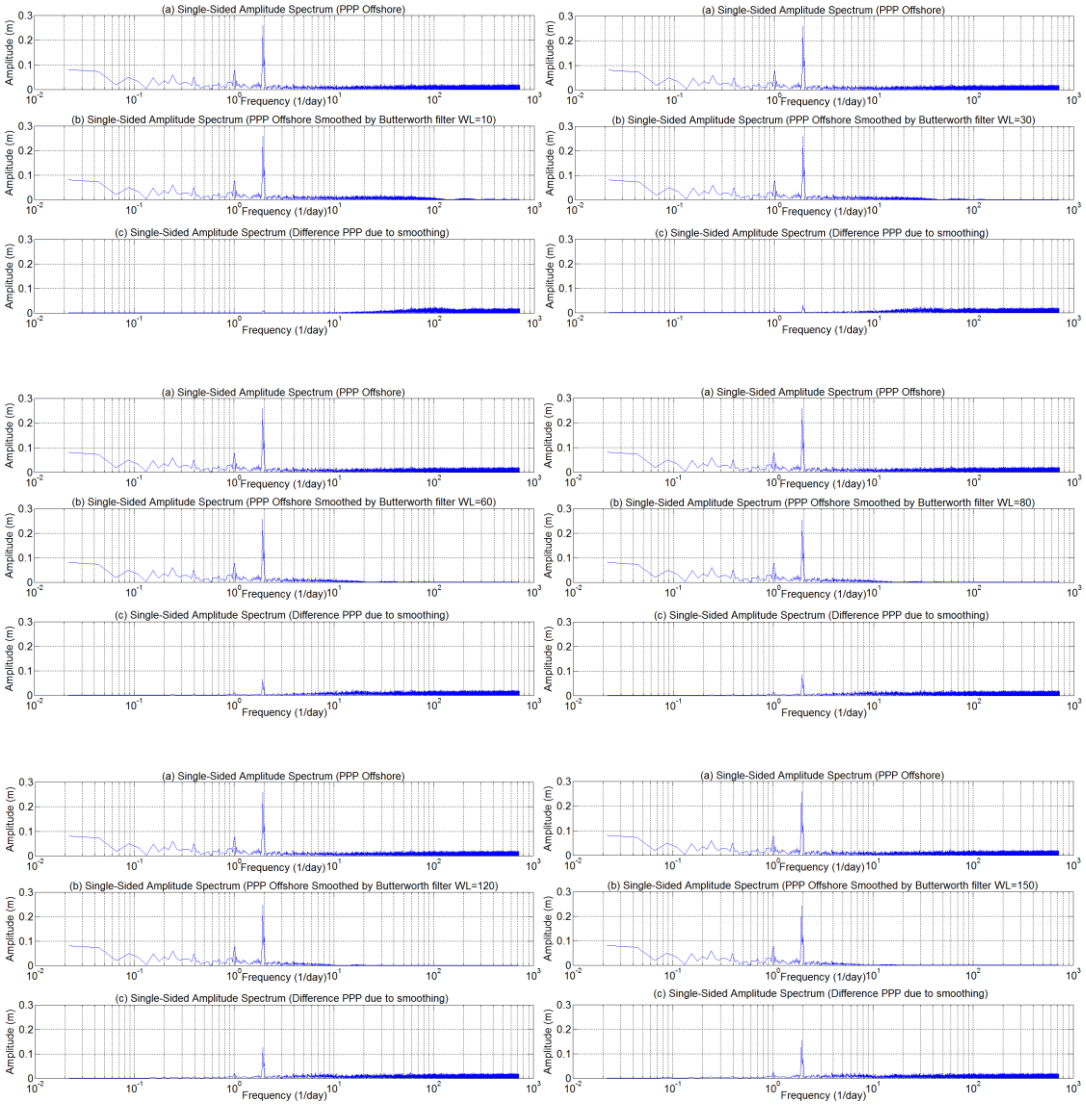

Figure B.4a: Single-sided frequency spectra of the Butterworth filter for PPP offshore (10, 30, 60, 80, 120 and 150) WL: In each group of three plots, (a) PPP offshore unfiltered; (b) PPP offshore smoothed by the Butterworth filters for 10, 30, 60, 80, 120 and 150 minute window length; and (c) differences between filtered and unfiltered GNSS-derived water level height signals

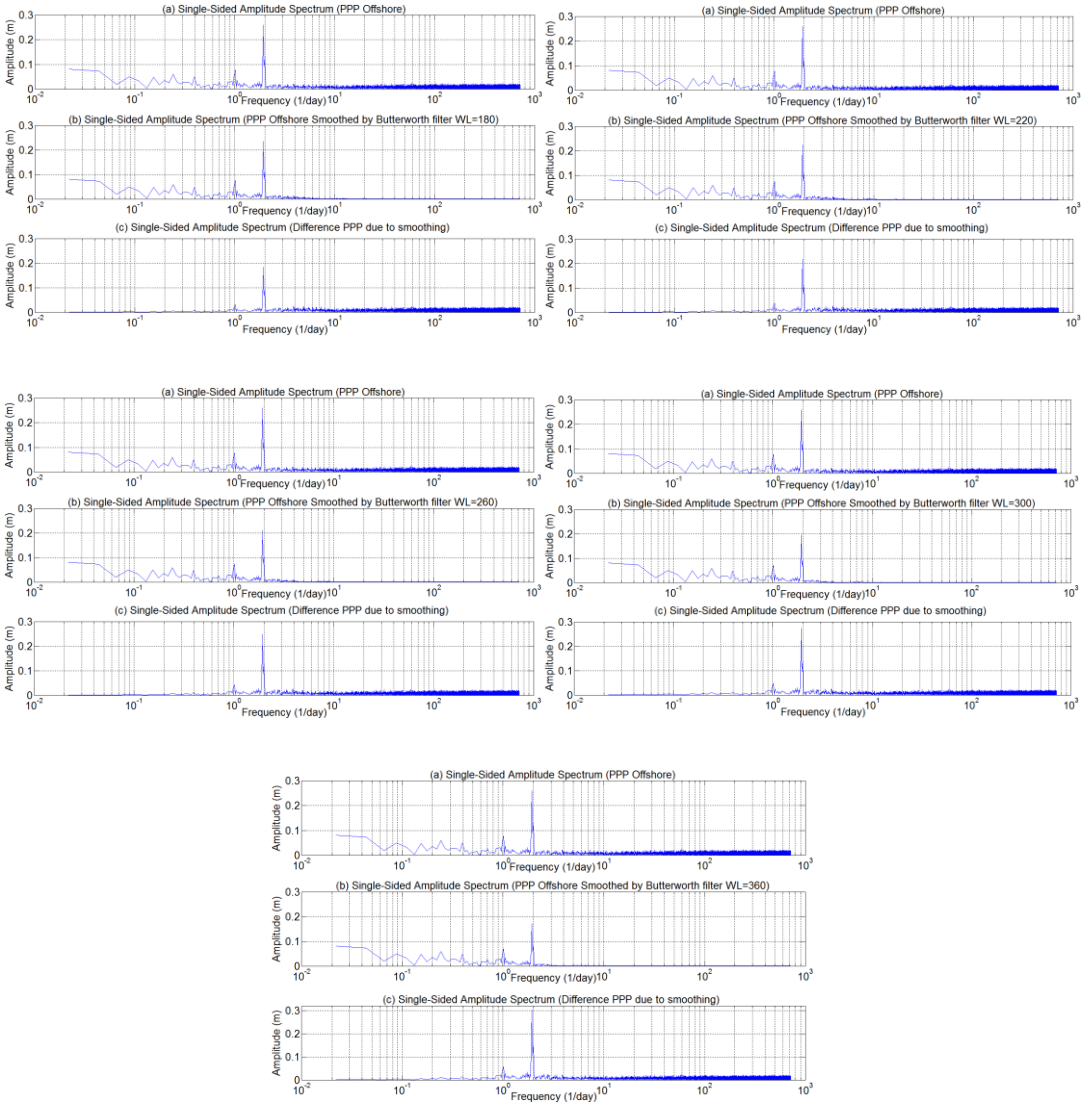

Figure B.4b: Single-sided frequency spectra of the Butterworth filter for PPP offshore (180, 220, 260, 300 and 360) WL: In each group of three plots, (a) PPP offshore unfiltered; (b) PPP offshore smoothed by the Butterworth filters for 180, 220, 260, 300 and 360 minute window length; and (c) differences between filtered and unfiltered GNSS-derived water level height signals